Static Fatigue: A Key Cause of Time Effects in Sand

by

Srinivasa S. Nadukuru

A dissertation submitted in partial fulfillment
of the requirements for the degree of
Doctor of Philosophy
(Civil Engineering)
in the University of Michigan
2013

Doctoral Committee:

Professor Radoslaw L. Michalowski, Chair
Professor James R. Barber
Professor Roman D. Hryciw
Assistant Professor Dimitrios Zekkos

DEDICATION

To my family

ACKNOWLEDGEMENTS

I owe a deep debt of gratitude to my advisor, Professor Radoslaw Michalowski for the continuous support of my PhD research, for his immense knowledge, enthusiasm, and motivation. His guidance, insights, long and fruitful discussions helped me in all research and writing of this thesis. I also would like to thank the other members of my dissertation committee, Professor J. Barber, Professor R. Hryciw, and Assistant Professor D. Zekkos, for their ideas, comments and invaluable advice.

Special thanks are to Mr. Bob Fischer and Mr. Rick Burch for their assistance in the design and construction of the laboratory devices. I also thank the other members of the civil engineering faculty, especially Professor R. Woods, Assistant Professor A. Athanasopoulos-Zekkos, and Associate Professor J. Lynch for making the classes during my study at UM more interesting and very educating. The knowledge I gained from these classes helped me tremendously during the course of my research.

I also gained tremendous insights into my research during the course of many discussions I had with several great friends I made during my time at Ann Arbor, in particular, Ravi Ranade and Sean O'Connor. I also thank my fellow geotechnical graduate students for sharing their friendship with me during my stay at UM.

I would like to acknowledge the research support from the National Science Foundation, Grants No. CMMI-1129009 and CMMI-0724022, the Rackham Pre-Doctoral fellowship, and the H.E. Riggs fellowship, without which this research would not have been possible.

Finally, I want to thank my parents, and my brother and sister-in-law for their confidence in me and dedicated support.

> *I do not know what I may appear to the world; but to myself I seem to have been only like a boy playing on the seashore, and diverting myself in now and then finding a smoother pebble or a prettier shell than ordinary, whilst the great ocean of truth lay all undiscovered before me.* – Sir Isaac Newton (1642 – 1727)

TABLE OF CONTENTS

LIST OF TABLES

LIST OF FIGURES

ABSTRACT

Freshly deposited or disturbed sands have a tendency to alter their mechanical properties. This is often seen after dynamic compaction of sand beds, where at first, the cone penetration resistance may not have increased, but in a matter of weeks and months the increase in resistance to penetration becomes evident. This time effect has been known for decades, but there is no universally accepted explanation as to what causes such time-delayed effects in sands. A hypothesis is postulated, which suggests that a key contributing factor behind time effects in sands is the delayed fracturing of the micro-morphological features present on surfaces of sand grains in contact. Experimental tests performed as part of this research support this hypothesis, and the numerical simulations indicate that the hypothesis is plausible. Experiments were performed using two custom-designed laboratory devices for testing of inter-granular sand contacts, and also tests were carried out on sand specimens, dry and wet. All experimental results are consistent with the hypothesis suggested. In addition, discrete element and finite element computations were performed as part of this study on aging of sand. Discrete element simulations were able to mimic the characteristics of the true (experimental) process when the static fatigue hypothesis was used. The model also predicted an increase in horizontal stress in sand subjected to sustained vertical load with restrained horizontal deformation, which is central to explaining the process of time-delayed increase in cone penetration resistance of sands after disturbance. Aging of sands under confined conditions leads to an increase in inter-granular contact stiffness, and thereby, to an increase in macroscopic elastic moduli, but the internal friction angle of sand remains nearly unchanged during aging.

Chapter 1

INTRODUCTION

1.1 Background and Motivation

Sands, like all soils in natural environment, change their properties over time: they "age". These *time effects* in sand are ubiquitous; they affect the behavior of soil deposits in geologic time scale as well as in the engineering scale: days to years. While some changes may be inconsequential, others might be very important. In geologic time scale, mechanical, chemical, thermal and microbial processes may cause compositional and structural changes to sand forming rock (lithification) or fine grained soil (by weathering). The geologic time effects in sand have been known to researchers for many decades. Over the past few decades researchers found out that the mechanical properties of freshly deposited, or disturbed sand can change in a span of days and months. Changes of sand properties were noticed in the past in both laboratory and field studies. These *time effects* are often referred to as *aging* in geotechnical literature.

Although the accounts of changes to mechanical properties of sand during aging were published in the 1960's through 1980's (Denisov and Reltov, 1961; Afifi and Woods, 1971; Daramola, 1980), particular attention to sand aging as an important process affecting engineering predictions in regard to cone penetration resistance of sand deposits was brought about by Mitchell and Solymar (1984). Since then, there has been an increasing body of evidence showing the prevalence of time effects in sand. Some of the mechanical properties of sand that are affected by aging include: shear modulus, small strain stiffness, and resistance to liquefaction. The practical significance of the change in sand properties during aging is quite apparent. Aging-related changes in the field are encountered quite often during and after ground improvement operations. For example, the cone penetration resistance of freshly deposited or

dynamically compacted can increase in time considerably (e.g., 50% in months). Driven piles (also called displacement piles) in sand often exhibit a significant increase in shaft bearing capacity (it can double in a matter of 4 months) with time. Despite having many well documented cases of aging, the reasons and mechanisms that cause this phenomenon are still not clear and the process was referred to recently as a continuing *enigma* (Mitchell, 2008). If the mechanisms and factors influencing aging become well understood, they could be incorporated into geotechnical engineering design and practice. The immediate need is in improvement of interpretation of field test results on freshly compacted soils, but the aging process is ubiquitous, and it affects many other problems, such as bearing capacity of driven piles, or the behavior of freshly deposited fills.

Over the years, there have been several hypotheses put forth by different researchers explaining the reasons behind aging in sands. These hypotheses can be broadly classified as chemical (mineral dissolution and precipitation at grain contacts), mechanical (particle rearrangement, secondary compression, force chain buckling, and sand grain crushing), and biological (microbial-assisted grain cementation). More recently, experimental and numerical evidence has pointed towards mechanical processes as being responsible for sand aging (Bowman and Soga, 2003; Mitchell, 2008). Many researchers now believe that aging in sand is due to grain re-arrangement leading to a granular structure with a more stable configuration. This time-dependent grain movement occurring in a granular assembly is often referred to as "creep". Although a lot of attention has been paid in recent years to improve understanding of the effects of "creep" on the entire granular assembly (Bowman and Soga, 2003; Mitchell and Soga, 2005; Kwok and Bolton 2010), an open question remains as to what causes the time-dependent grain rearrangement, and how this process propagates through the spatial scales to affect the properties of sand at the macroscopic (continuum) scale. The point is made here that term "creep" (manifestation of viscous properties) does not represent any specific mechanism, it is only a phenomenological term used to classify the type of macroscopic behavior of materials. Therefore, the concept of "creep" cannot be used as an explanation of the process occurring in sand. This thesis focuses on gaining evidence for pointing to a specific process being responsible for aging of sands.

The distinction is made between visco-elastic process, such as creep, and aging. The former is a rate-dependent process, whereas the latter is dependent on time alone. While this

distinction is clear at the level of phenomenological modeling, it is less obvious when the process is considered at different scales. The term "aging" is used in this thesis consistently with existing geotechnical literature.

The research described in this dissertation attempts to obtain evidence to support or disprove a recently postulated hypothesis responsible for sand aging (Michalowski and Nadukuru, 2012). The suggested hypothesis takes advantage of earlier research in material science and rock mechanics (Charles, 1958; Wiederhorn and Boltz, 1970; Scholz, 1978a). This hypothesis provides plausible explanation for the nature of aging in sand. It also indicates reasons for peculiar behavior of sand deposits after dynamic compaction, which is consistent with some earlier suggestions (Schmertman, 1987, 1991; and Mesri et al., 1990).

The topic of this thesis grew out of the research on the behavior of concrete segmented pipelines buried in sand, subjected to ground rupture. In particular, it was the behavior of the freshly deposited backfill that brought the topic of sand aging about. In the course of this study, predictions of the behavior of buried pipelines became a secondary matter; still, one of the chapters (Chapter VI) is devoted to this topic.

1.2 Scope and Outline

The purpose of this research is to identify reasons behind sand aging. For this, a hypothesis was postulated. This dissertation aims at obtaining experimental evidence supporting the hypothesis, and numerical simulations to further indicate the plausibility of the hypothesis. The extent of the study involves characterization of sand grain surfaces and experimental tests on both single inter-granular contacts and on specimens of sand (predominantly Ottawa 20-30 sand, from U.S. Silica Co.). Custom-designed laboratory devices were manufactured to perform some of the tests. Numerical simulations were performed using discrete element method (PFC^{3D}) and finite element method (ABAQUS).

This dissertation is organized into seven chapters. The current chapter (Chapter 1) introduces the topic of research. Chapter 2 provides the literature review with an overview of time effects in sand. This is a brief review of past research, some of the important case histories, and some previously suggested hypotheses. A full review of case studies was not attempted, as several excellent summaries are available (Human, 1992; Baxter, 1999; Saftner, 2011). The hypothesis postulated in this research is discussed in Chapter 3. The objectives of this

dissertation and specific methodology used to investigate the suggested hypothesis are also discussed in that chapter. Chapter 4 summarizes the experimental investigation part of the dissertation. First, an overview of grain surface morphology obtained from Atomic Force Microscopy and Scanning Electron Microscopy is presented. Micro and macro scale laboratory test results are discussed in the latter part of this chapter.

Results from the numerical investigation are presented in Chapter 5. First, a brief introduction of the numerical methods is provided, followed by description of simulations and results. This chapter includes a new discrete element model to simulate aging. Finite element simulations and explanation of the delayed changes to cone penetration resistance after sand disturbance is also provided in this chapter.

Chapter 6 contains simulations of the behavior of concrete segmented pipelines buried in sand, subjected to ground rupture. This is a secondary topic, but the main study in this thesis grew out of the interest in the behavior of the pipeline backfill. Funding for this research was, almost in its entirety, provided by the project on pipelines.

The summary of the accomplished work and achievements are provided in Chapter 7, along with the conclusions and recommendations for future work.

Chapter 2

LITERATURE REVIEW ON TIME EFFECTS IN SAND

2.1 Introduction

When subjected to prolonged loads, engineering properties of sand change in time. Over the last three decades, there has been increasing evidence collected from the field and laboratory measurements showing time dependency of mechanical properties of sand. These changes affect, for instance, the small strain stiffness (Afifi and Woods 1971, Anderson and Stoke 1978, Wu and Woods 1987), cone penetration resistance (Mitchell and Solymar 1984, Hryciw 1986), liquefaction resistance (Seed 1979), or the pile setup (Chow et al. 1998).

This section provides an overview of findings available in the literature and plausible explanations/mechanisms causing the time effects as provided in the literature. The observations of time effects related to soil properties are grouped into those coming from field measurements and those from laboratory studies. The mechanisms proposed by various researchers to explain the time-dependent phenomena are also discussed in this chapter.

2.2 Field Measurements of Changes

There are numerous case histories in the literature indicating changes to in-situ sand properties over time. These changes were noticed, for instance, following compaction or deposition operations. In many cases, the penetration resistance measured by the Standard Penetration test (SPT) blow count (N value) or Cone Penetration Test (CPT) tip resistance was changing in time. Other in-situ changes include the changes in bearing capacity of driven piles and increase in liquefaction resistance. Some of the case studies illustrating time effects are presented in this section.

2.2.1 Changes to Cone Penetration Test (CPT) Resistance

Mitchell and Solymar (1984) presented evidence for time-dependent changes to cone penetration resistance after dynamic compaction of sand at the Jebba Hydroelectric Development project in Nigeria. The dam, a 42 m high earth and rock fill dam on the Niger River in Nigeria was located on alluvial sand deposits, formed by medium to coarse sub-rounded to round silica sand. To densify the soil deposits, vibrocompaction was carried out at depths less than 25 m and blasting was carried out at the depth of 25 to 40 m. Blasting was found to reduce the penetration resistance immediately afterward, even though the densification was evident by the surface subsidence. Nine days after blasting, the static cone resistance was still slightly lower than before blasting, but a considerable increase in penetration resistance was found after 11 weeks. A similar effect was found in soils after vibrocompaction, Fig. 2.1. Increase in penetration resistance was also observed after placement of a 10 m hydraulic fill to be used as a construction platform at the dam site. A chemical mechanism was cited to be the reason behind the observed time-dependent changes. The authors hypothesized that precipitation of silica or other materials from pore fluid could cause cementation between particle contacts thereby gradually increasing the cone penetration resistance.

Dumas and Beaton (1988) reported on a field study where the CPT tip resistance almost doubled after dynamic compaction. The site was a part of Port Canada's Pointe Noire deep-sea harbor development project at Sept-Iles, Quebec. A thick sand fill was placed by end dumping clean sand in a loose state into the sea. Dynamic compaction was carried out to densify a 6 to 17 m thick deposit of medium to coarse grained sand fill. CPT tip resistance almost doubled 18 days after compaction. They also suggested that the time dependent increase in tip resistance was related to the level of dynamic stresses at a given depth; they observed a greater increase in tip resistance near the surface than that at larger depth, indicating the influence of attenuation of the dynamic process with depth. Figure 2.2. shows the increase in CPT tip resistance observed by the authors.

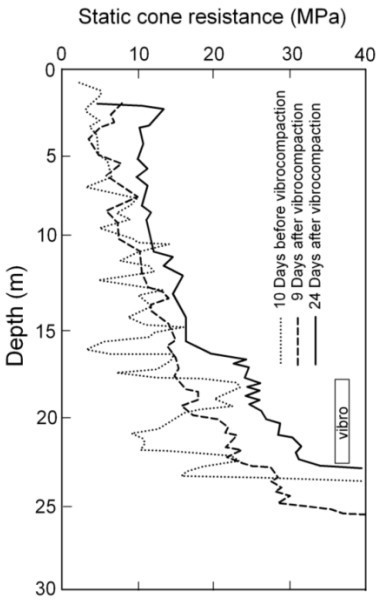

Figure 2.1. Increase in cone penetration resistance after vibro compaction; Jebba Dam site (redrawn from Mitchell, 2008).

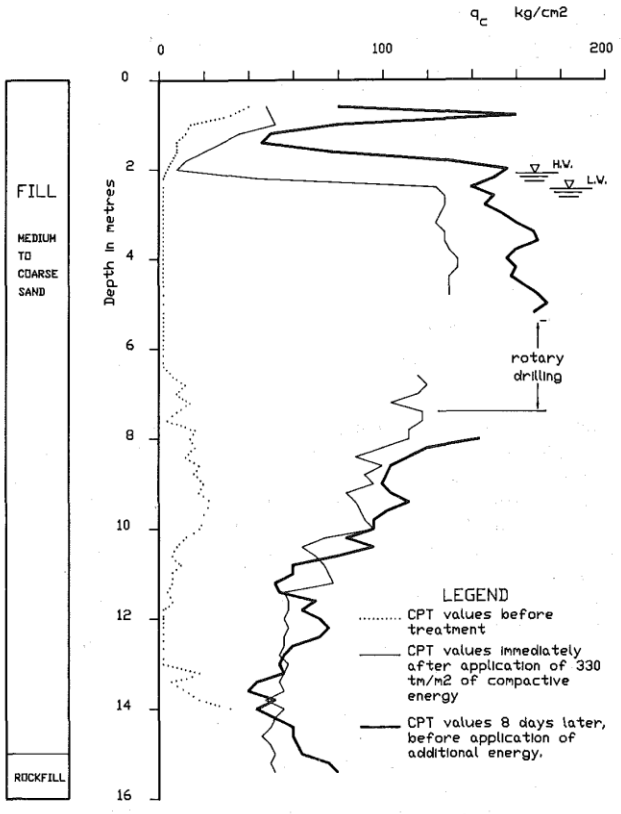

Figure 2.2. Increase in CPT tip resistance after dynamic compaction at Port Canada, Quebec (from Dumas and Beaton, 1988).

Skempton (1986) showed that the ratio of the Standard Penetration Test (SPT) N-value normalized to 1 atm and soil's relative density increased from 35 on laboratory test samples (aged for 10^{-2} years, ie., about 3.5 days), to 40 for recent fills (10 years), to 55 for natural deposits (> 100 years).

Hryciw (1986) discussed a project where the CPT resistance decreased after 2 days following explosive densification and did not show any improvement even after 30 days. The tests were carried out in southeastern Georgia off the Atlantic coast. The site consisted of 3 to 9 m of loose sand. Blasting was performed at a depth of 7 m. The initial decrease of penetration resistance occurred despite the clear evidence of compaction indicated by surface settlements. Loss of cementation between grains during blasting was thought to be the reason behind CPT resistance being lower than the pre-blast value.

Handford (1988) reports an increase in SPT N-value from pre-blast values within days of explosive densification at an oil-sand mine tailings dam at Fort McMurray, Canada. While, all of the SPT results showed an increasing trend following the blast, one of the SPT result showed an initial decrease followed by an increase in the blow count after blasting. Fordham et al. (1991) described a project near the same area, designed to decrease the risk of liquefaction in oil sand tailings. CPT results immediately after blast densification failed to meet the minimum requirements. However, after four months, CPT tip resistance increased to an acceptable level. Re-establishment of intergranular frictional contacts between sand grains was thought to be the reason behind the observed time effects.

Schmertmann (1991) observed an increase in static-cone penetration resistance over a period of 70 days after deep dynamic compaction of a 10 m thick silty sand layer in Jacksonville, Florida. The number of drops used during the deep dynamic compaction operations seemed to affect the magnitude of increase in cone penetration resistance. Schmertmann attributed the observed changes to an increase in particle interlocking due to small slippage between particles resulting in a stronger soil skeleton. He also suggested that an increase in horizontal stress may have contributed to the observed changes in penetration resistance.

Following the 1989 Loma Prieta earthquake, Human (1992) reported on CPT results on a man-made hydraulically filled Bay Farm Island in Alameda, California. After the earthquake, sand boils were seen above the silty sand fill. Cone penetration resistance values 4 days after the earthquake showed no change when compared to pre-earthquake values. Although there was a

slight increase in CPT resistance performed later, Human concluded that the increase was within the natural variability of the soil.

Charlie et al. (1992) carried out blast densification on a 1.5 m thick layer of poorly graded medium-to-fine sand overlaying a 3.6 m thick layer of dense poorly graded gravely sand with a relative density between 70% and 85%. A layer of inorganic silt was beneath the gravely sand layer. The site was located in Greeeley, Colorado. One week after blasting, CPT tip resistance and sleeve friction were less than pre-blast values. After 18 weeks, CPT tip resistance increased by 18% and sleeve friction decreased by 39% compared to the 1 week values. However, they were both less than the pre-blast value. After 5.5 years, the penetration resistance increased to a value greater than pre-blast value; the tip resistance increased by 210% and sleeve friction decreased 42% with respect to the one week values. The authors also compiled data from previous tests from other researchers and concluded that rate of aging is faster in hotter climates than for colder climates.

Jefferies and Rogers (1993) present a study of changes to CPT resistance during the construction of a mobile caisson, the Molikpaq, to be used for offshore hydrocarbon drilling in the Arctic during the winter season. The caisson was filled with hydraulically placed sand and had an octagonal shape, with a width of 100 m and a 70 m by 70 m square open center. The caisson was deployed at different sites. It should be noted that most of the caisson was below sea water. At one of the site, the caisson was filled with blast densified hydraulically placed sand to provide additional protection against ice loading expected at the site. Following blasting, 1 m of settlement was observed. No increase in CPT tip resistance was observed 2 ~ 12 hours after blasting. However after 2 ~ 5 days, a substantial increase in CPT resistance was observed. It was noted that the increase in CPT tip resistance continued at a decreasing rate. At another site, the Molikpaq was filled with clean sand without any form of densification. CPT tip resistances were constant at this site for over 10 months. For both sites, the sand came from the same borrow source. The authors suggested that bonding between sand grain contacts might not be a plausible explanation as both sites had identical chemical environments and aging was observed only in the mechanically disturbed situation.

Ashford et al. (2004) observed changes to CPT tip resistance following explosive densification. The tests were carried out at Treasure Island in San Francisco Bay. Treasure Island is a manmade island consisting of loose fine sand and silty sand. The researchers were testing

pile performance during liquefaction by carrying out 3 blasts. CPT performed after 2 days from the second blast, showed a drop in the penetration resistance despite the ground settling by 10 cm. 42 days after the third blast, average penetration resistance between 2 and 5 m depth had almost doubled from the preblast value.

Narsilio et al. (2009) carried out blast densification on a site, 35 miles west of Charleston, South Carolina. Four blast events were carried out over a period of 8 months. Following each blast event, ground settlement was observed with a decreasing trend. After every blast, the cone penetration resistance decreased. After the final blast, it took about a year for the tip resistance to increase to the preblast value. CPT performed after 2 years from the final blast showed an increase in tip resistance beyond the one year value.

Saftner (2011) observed increases to CPT resistance following blast densification at Griffin, IN. However vibroseis shaking at the same site didn't show any aging effects. The tests performed by Saftner shows the importance of disturbance energy on aging. The researcher used his data along with data from previous projects that showed aging effects, and showed that increase in CPT resistance is the largest in soils saturated with salt water, soil with fresh water and dry soil in that order. Saftner developed empirical equations to predict the increase in cone penetration resistance following vibratory disturbance methods (explosive densification, placement of hydraulic fill, earthquakes, and vibroseis shaking) and compactive disturbance methods (impact piers, vibro-compaction, and deep dynamic compaction). Equation (2.1) was suggested by Saftner to be used for vibratory compactive methods and Equation (2.2) for compactive disturbance methods.

$$\frac{q_c(t)}{q_{c,\,fresh}} = 1 + 0.25e^{-0.75\frac{\sigma'_v}{\sigma_{atm}}}\log(t) \tag{2.1}$$

$$\frac{q_c(t)}{q_{c,\,fresh}} = 1 + 0.16\log(t) \tag{2.2}$$

where,
$q_c(t)$ is the CPT tip resistance at time t
$q_{c,fresh}$ is the initial post-disturbance tip resistance
σ'_v is the vertical effective stress at a particular location.
σ_{atm} is the atmospheric pressure.

2.2.2 Pile Setup

When a pile is driven through sand, excess pore pressure dissipation due to pile driving is expected within a few hours, after which the ultimate load capacity is measured by performing load tests. However, field data indicates that the pile load capacity is time-dependent and may increase significantly over several months. This is called pile set-up. The following section presents some of the pile-set up cases from the literature.

Based on observations from 45 load tests on driven concrete piles into uniform medium sand, Tavenas and Audy (1972) concluded that the bearing capacities of piles in sand are time-dependent. The tests were conducted near the St. Charles river site in Quebec City, Canada. They observed that the ultimate bearing capacity increased by about 70% in 15 to 20 days over the 12 hour values. Figure 2.3 shows the results obtained by the researchers. Since the sand at the site was so pervious ($k = 10^{-2}$ cm/sec), it was suggested that the increase in bearing capacity must be related to changes occurring in the sand structure around the pile.

Skov and Denver (1988) used stress wave measurements to evaluate pile-set up using the Case Pile Wave Analysis Program (CAPWAP) on a pipe pile driven into clean sand and gravel. After 30 days, they observed that the setup occurred in the medium to fine sand layers with very little setup occurring in the coarse sand and fine gravel strata, Fig. 2.4. They suggested a logarithmic relation between pile-setup and time.

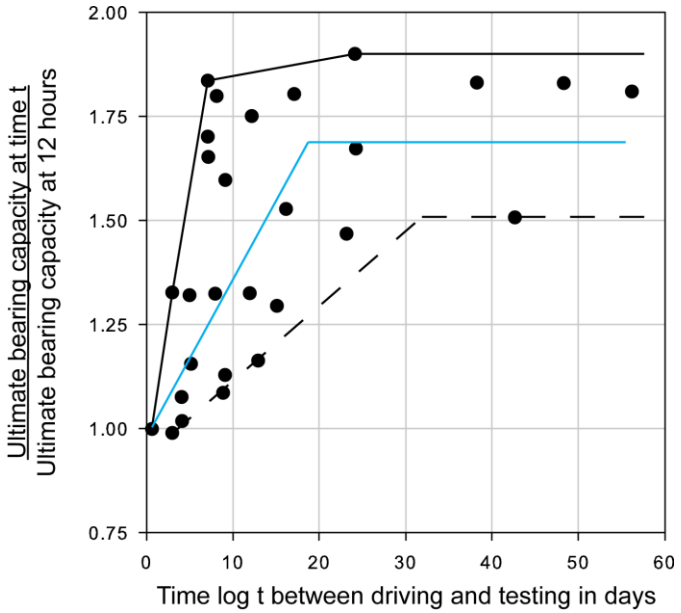

Figure 2.3. Increase in bearing capacity of driven concrete piles over time (redrawn from Tavenas and Audy, 1972).

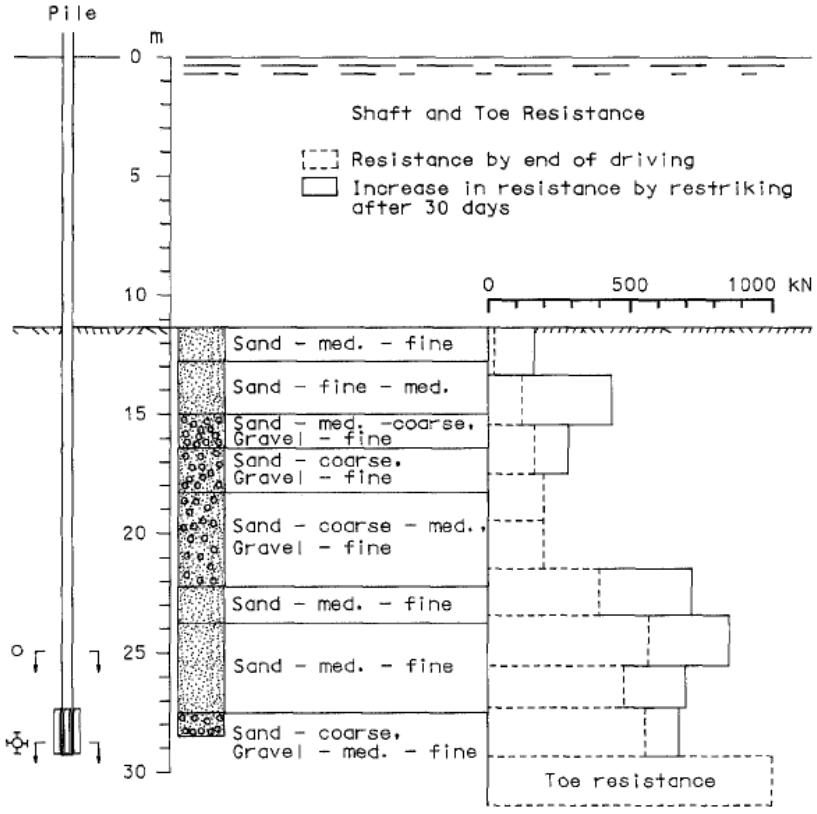

Figure 2.4. Changes to pile resistance during driving and restriking of pile calculated from CAPWAP analyses (from Skov and Denver, 1988).

York et al. (1994) reported on pile-setup encountered during the construction of John F. Kennedy International Airport. The airport is situated on the south shore of Long Island adjacent to Jamaica Bay in the Borough of Queens, New York city. The site consisted of 3 ~ 4.6 m thick hydraulically placed fill from the bay bottom on top of a 1 to 3.4 m thick marshy shore. Underlying the marshy soil was a 40 m thick stratum of glacial sand. They observed a 40 ~ 80 % increase in load capacity. They also noted that the setup approached a maximum value after 15 ~ 25 days after which there was not that much of a change in time. They suggested redistribution of stresses to be the cause of pile-setup.

Chow et al. (1998) performed tests on open ended piles to investigate the pile behavior in dense marine sand. They observed an 85% increase in shaft capacity between 6 months and five years after installation. For bored piles in sand, they did not find any setup. Based on their observations, the authors suggested that during pile driving, a circumferential arching occurs, which reduces the radial stresses on the pile shaft. Over time, creep occurring in the soil leads to the breakdown of the arching stresses, causing an increase in radial stress and leading to pile-setup. They also suggested that increased dilation caused by sand aging can also cause pile setup.

To study pile-setup, Axelsson (2000) performed field tests near Fittja Straits at Varby, 20 km south-west of Stockholm, Sweden. The site consisted of a 2.5 m thick clay layer underlain by silty sand to gravely sand and sandy deposits. The groundwater table was 2 m below the ground surface. The sand consisted of mainly quartz and feldspars. Square concrete piles (235 mm) were driven into loose to medium dense sand. By performing a CAPWAP analysis, the author noticed a linear increase in pile bearing capacity. He noticed a 30-50% increase in total capacity per log cycle of time, Fig. 2.5. One hour after pile driving, Axelsson observed very low horizontal effective stress ratios of 0.05 to 0.08 on the pile shaft. After 72 days the stress ratio increased to 0.10 ~ 0.15. Based on these results, the author suggested that during pile driving, a soil arch is developed and the arch deteriorates with time, leading to an increase in horizontal stress on the pile. This explanation is in agreement with the one proposed by Chow et al. (1998).

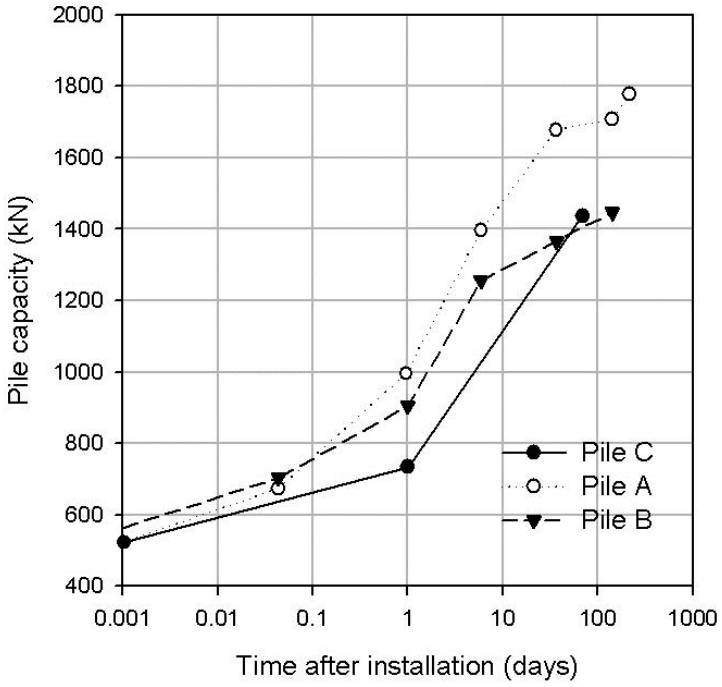

Figure 2.5. Increase in the total capacity of three piles with time (redrawn from Axelsson, 2000).

2.3 Laboratory Measurements of Time Effects

Changes to engineering properties of sand occurring in time were also measured in laboratory tests. The following section gives a brief overview of the observed time-dependent changes in sands after disturbance.

2.3.1 Penetration Resistance

In a laboratory test to simulate blast densification, Dowding and Hryciw (1986) used blasting caps as explosives in a large cylindrical liquefaction tank (107 cm in diameter and 102 cm high) filled with saturated Evanston Beach sand. Before the start of the test, water was pumped upwards to liquefy the sand in the tank. This resulted in an initial relative density of about 50%. The blasting caps were placed at the center of the tank. After blasting, relative density of the sand was 60% ~ 78%. Immediately after the blast, they observed a drop in mini-cone penetration resistance compared to the pre-blast value. After a few days, the penetration resistance increased to beyond the pre-blast values. The largest increase was found near the blast location. It is interesting to note that, the authors also found an increase in penetration resistance in time even without blasting. Figure 2.6 shows the results obtained by Dowding and Hryciw (1986).

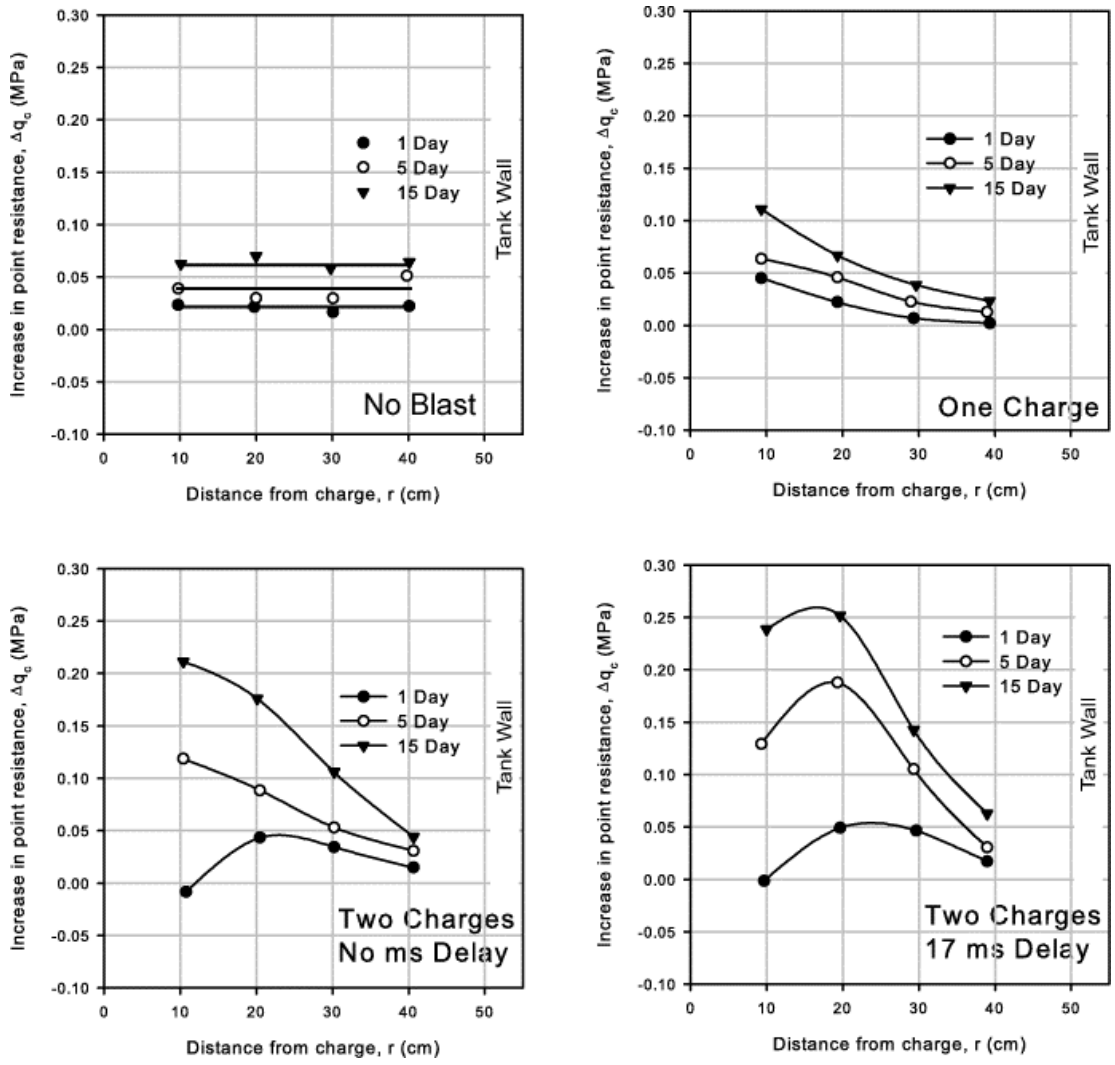

Figure 2.6. Change in penetration resistance of blast densified Evanston Beach sand (redrawn from Dowding and Hryciw, 1986).

To understand the effects of sand aging on penetration resistance, Joshi et al. (1995) performed laboratory tests by pushing 1 cm diameter probes into river and Beaufort Sea sand under different environmental conditions aged to up to 2 years. The sands were placed in PVC pipes, 360 mm inner diameter, 20 mm thick and 370 mm high. All sands were loaded with 100 kPa vertical stress. Tests were conducted on dry sand, and, sands saturated with distilled and simulated sea water (pH = 8). All penetration tests showed an increasing trend of probe resistance with time. The largest increase in penetration resistance was observed in samples submerged under sea water, followed by river water, and then dry sand. Figure 2.7. shows the changes to probe resistance over time for river sand in distilled water.

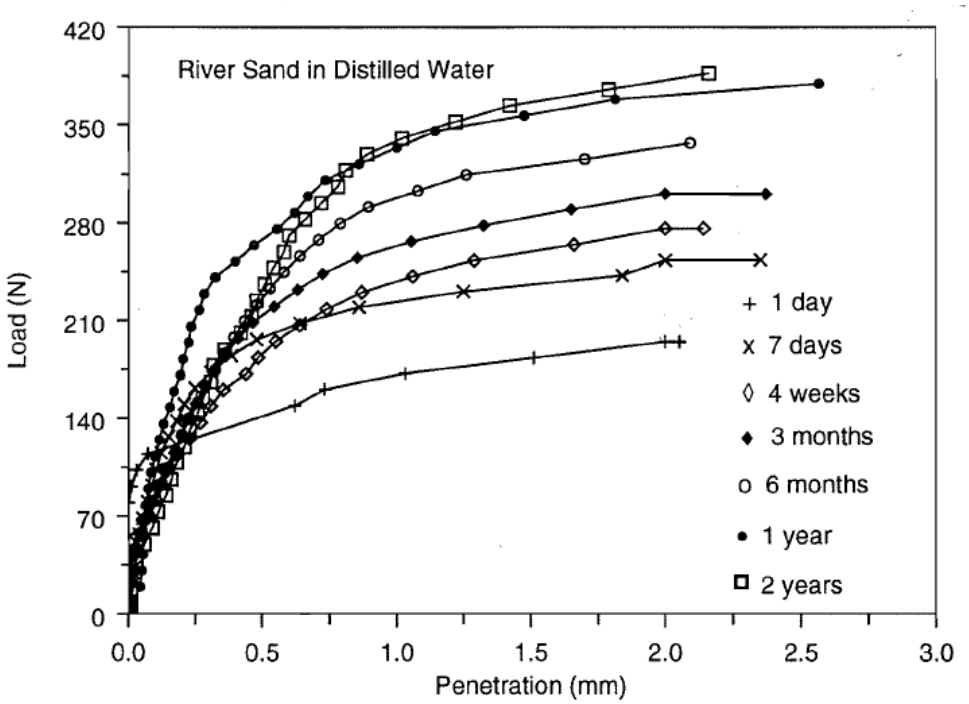

Figure 2.7 Changes to penetration resistance of river sand submerged in distilled water (from Joshi et al., 1995).

Baxter and Mitchell (2004) measured changes to small strain shear modulus, electrical conductivity and minicone penetration resistance after aging of sands. Testing was carried out on Evanston Beach sand and Density sand, with 100 kPa vertical stress, and four different pore fluids (air, distilled water, ethylene glycol & CO_2 water). Chemical analysis performed on Evanston Beach sand before the test showed the presence of mainly quartz along with some soluble fractions of carbonate material. While the small strain shear modulus of Evanston beach sand in all four pore fluids increased in time, the corresponding values for Density sand decreased in time. Electrical conductivity of Evanston beach sand in carbondioxide-saturated water decreased in time. In all other tests, the conductivity increased with time. It is interesting to note that although changes in small strain shear modulus were observed in the tests, there was no measurable increase in mini-cone penetration resistance.

2.3.2 Soil stiffness

The time-dependent changes in sand affect the small-strain shear modulus. Afifi and Woods (1971) performed resonant column tests on sand after different confinement durations. They observed a linear increase of small strain shear modulus with logarithm of time. There was no

measurable change in vertical strain for the duration of the testing. Based on their results, the researchers concluded that some mechanism or combination of mechanisms other than changes to void ratio is responsible for the time dependent change in shear modulus. For air-dry Ottawa sand (30-50), the shear modulus was found to increase approximately 2 to 5% per log cycle of time. From testing different sands with different grain size, they concluded that the rate of increase in shear modulus is higher for smaller sized sands. Figure 2.8. shows the changes in shear modulus observed by the researchers for Ottawa sand. Similar results were reported by Anderson and Stoke (1978). They expressed the change of shear modulus with time as per Equations (2.3) & (2.4).

$$I_G = \frac{\Delta G}{\log_{10}\left(\frac{t_2}{t_1}\right)} \tag{2.3}$$

$$N_G = \left(\frac{I_G}{G_{1000}}\right)100\% \tag{2.4}$$

where I_G is the coefficient of shear modulus increase with time, ΔG is the change in small strain shear modulus from time t_1 to t_2 after primary consolidation, G_{1000} is the small strain shear modulus after 1000 min of constant confining stress, and N_G is the rate of increase of shear modulus per log cycle of time.

Wu and Woods (1987) performed resonant column tests on sands and silts with different degree of saturation and concluded that the time effects on shear modulus for partially saturated soils are more than those of dry soils.

Mesri et al. (1990), Schmertmann (1991) and Jamiolkowski and Manassero (1995) suggested to change the reference value shear modulus from the value measured at 1000 min to the end of primary consolidation to account for the different primary consolidation times for various soils. Values of N_G obtained by Jamiolkowski and Manassero (1995) for various soils are shown in Table 2.1. It is interesting to note that for sands containing predominantly silica, the N_G value increases with particle size which contradicts the observation of Afifi and Woods (1971). This suggests that other factors apart from particle size might be contributing to the increase in shear modulus. The grain mineral might be a probable factor affecting sand aging.

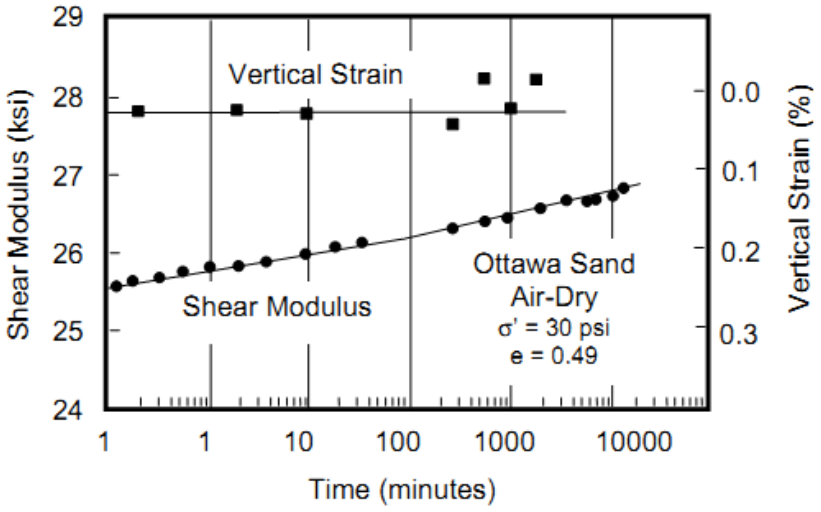

Figure 2.8. Increase in shear modulus of Ottawa 20-30 sand with time (from Afifi and Woods, 1971).

Daramola (1980) observed changes in modulus of aged sands during triaxial compression tests. Four samples of Ham river sand were prepared at void ratio of approximately 0.6 and loaded with a confining pressure of 400 kPa and aged over different times. While one sample was tested immediately, the other three were tested after 10, 30 and 152 days. The sand appeared to gain in stiffness, but not in strength as shown in Fig. 2.9.

Thomann and Hryciw (1992) indicated that the initial loss of stiffness in sand depends on the extent of disturbance (measured by shear strain). Tests on Agsco and Ottawa sands were performed using a quasi-static torsional shear resonant column device. A significant increase in stiffness occurred in the first few hours after disturbance, and this increase slowed down considerably afterward. They found out that the amount of sample disturbance governed both the initial decrease and subsequent increase in the shear modulus.

Jovicic and Coop (1997) performed bender element tests on isotropically confined Dogs Bay sand. The Dogs Bay sand is poorly-graded angular biogenic carbonate sand containing mainly unbroken foraminifera and mollusc shells. They tested the sand at confining pressures of 500 kPa, 1900 kPa and 2900 kPa, and noted that the rate of increase in shear modulus was higher at lower confining pressures. They noticed a 15% increase in shear modulus over a 3 days. They suggest that the increase in stiffness cannot be attributed only to volumetric creep.

Table 2.1. N_G values for sands and clays (from Jamiolkowski and Mannasero, 1995).

Soil	**d_{50} (mm)**	**PI (%)**	**N_G (%)**	**Mineral Composition**
Ticino sand	0.54		1.2	Silica
Hokksund sand	0.45		1.1	Silica
Messina sand and gravel	2.1		2.2 to 3.5	Silica
Messina sandy gravel	4		2.2 to 3.5	Silica
Glauconite sand	0.22		3.9	50% Quartz, 50% Glauconite
Quiou sand	0.71		5.3	Carbonatic
Kenya sand	0.13		12	Carbonatic
Pisa clay		23~46	13 to 19	
Avezzano silty sand		10~30	7 to 11	
Taranto clay		35~40	16	

Howie et al., (2002) performed triaxial tests on loose samples of Fraiser River sand, to study time effects on soil stiffness. Samples of sand were confined at different vertical-to-horizontal stress ratios (1, 2, and 2.8) with a lateral pressure of 100 kPa. The researchers calculated the shear modulus (G), from the secant modulus (E) and Poisson's ratio was obtained from triaxial testing by assuming linear elastic behavior. They noticed a linear increase of shear modulus with time. They noticed that isotropically confined sands have a higher initial modulus than anisotropically loaded samples. The rate of increase of modulus was dependent on the stress ratio during the aging process and axial strain at which the measurement was taken. At higher stress ratios, and on looser samples, they observed a greater increase in G. They also noticed that the rate of increase of G diminishes at large strains.

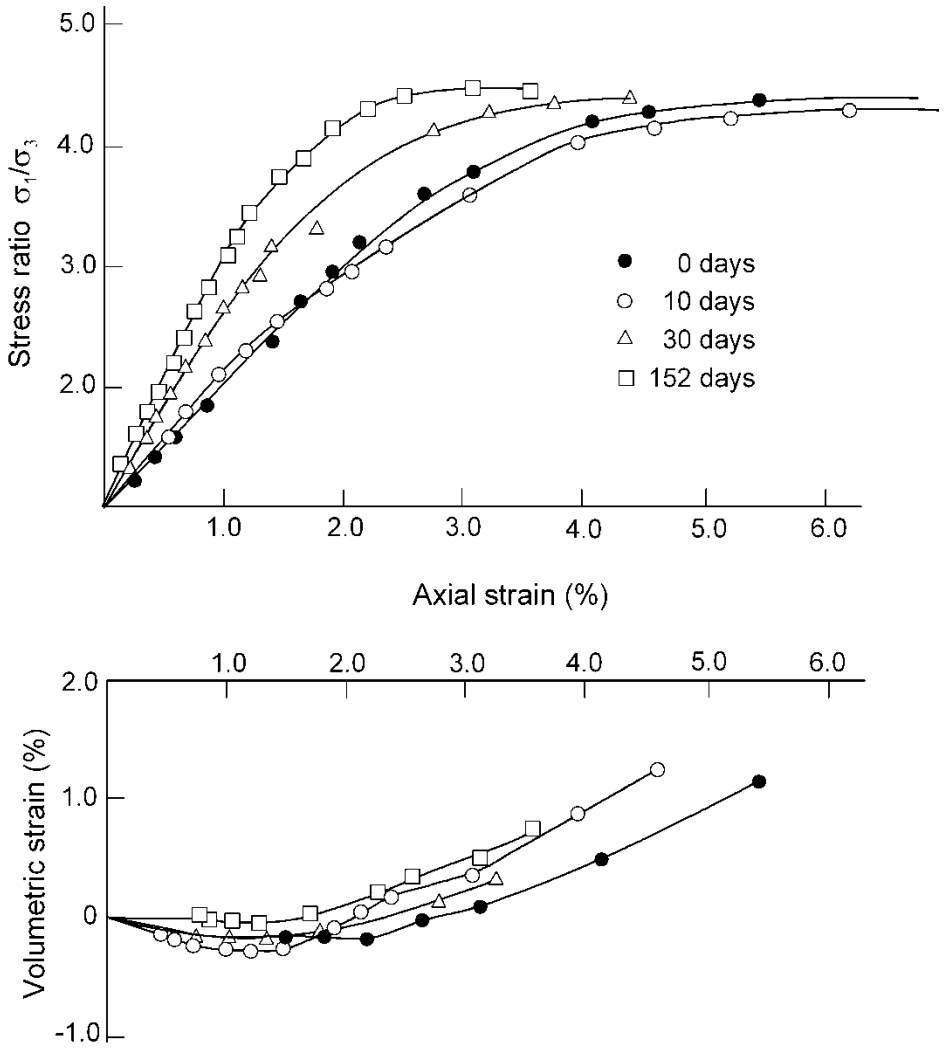

Figure 2.9. The effect of time on drained triaxial compression of sand (redrawn from Daramola, 1980).

Wang and Tsui (2009) studied the time effects on small-strain shear modulus and damping ratio of Ottawa 20-30 sand and Toyoura sand by performing resonant column tests. They found that the increase of small strain shear modulus (G) with time for loose samples is larger than that for dense samples when the confining pressure is 35 kPa. However, at a confining pressure of 100 kPa, the dense samples have a larger increase of G with time. They also noticed that the damping of sands drops during the aging period. They noticed that the rate of increase in shear modulus is higher for samples containing fines (dry kalonite powder). Figures 2.10 and 2.11 show the results for Toyoura and Ottawa 20-30 sand obtained by the researchers.

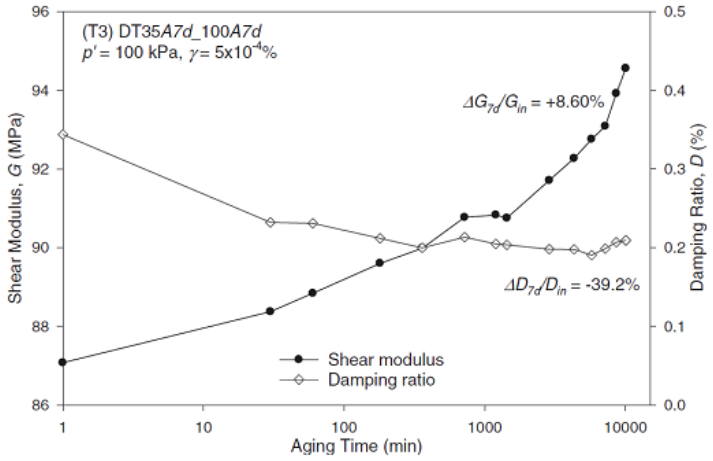

Figure 2.10. Effect of time in small strain shear modulus and damping ratio in dense Toyoura sand at a confining stress of 100 kPa (from Wang and Tsui, 2009).

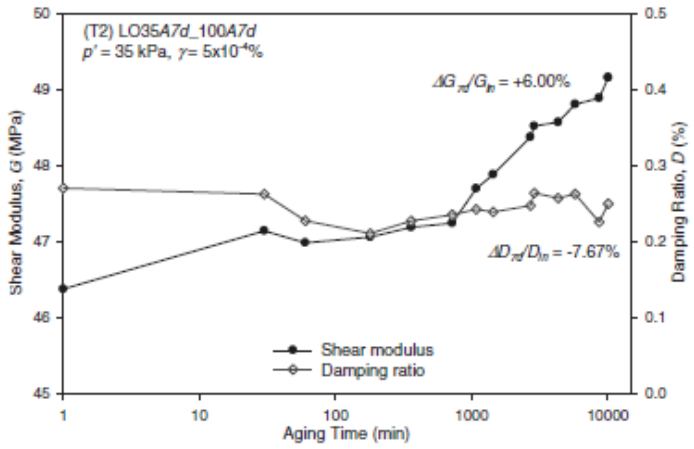

Figure 2.11. Effect of time in small strain shear modulus and damping ratio in loose Ottawa sand at a confining stress of 35 kPa (from Wang and Tsui 2009).

2.3.3 Liquefaction Resistance

The capacity of soil to resist liquefaction is measured by the cyclic resistance ratio (CRR). Several investigators in the past have noted that the liquefaction resistance of soils increases with age of the soil deposit.

Seed (1979) carried out laboratory tests on identical specimens of Moneterey No. 0 sand, 0.1, 1, 10 and 100 days following sample preparation. After 10 days, there was a 12% increase in liquefaction resistance and a 25% increase after 100 days of aging. Seed compared the laboratory data with tests conducted on undisturbed natural deposits and concluded that liquefaction

resistance of natural deposits could be 75% greater than that of freshly deposited laboratory specimens.

Troncoso et al. (1988) performed cyclic triaxial tests on undisturbed and reconstituted samples from two tailings dams in El Cobre, Chile. The samples consisted of sands with 25% fines. The cyclic strength of the reconstituted sample was about 60% of the strength of the 1-year old deposit. The results showed that 5 and 30 year old deposits were 25% and 35% stronger than the 1 year deposit. Figure 2.12. shows the increase in cyclic strength of the sample with deposition age.

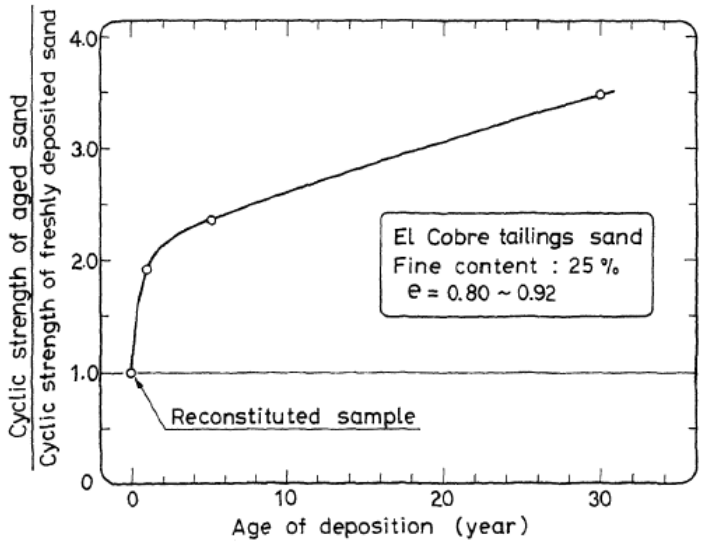

Figure 2.12. Increase in cyclic strength of tailings sand (from Troncoso et al. 1988).

Recently, Saftner (2010) performed cyclic triaxial tests on reconstituted sands with 50% relative density from a test site in Griffin, Indiana. The author reports an increased number of cycles to failure with time at a given cyclic stress ratio following sample consolidation.

2.3.4 Friction Angle

Daramola (1980) observed no changes to friction angle of Ham river sand confined to 100 kPa aged to different times (Fig. 2.9) despite measuring a significant increase in soil stiffness. Al-Sanad and Ismael (1996) reported an increase in friction angle obtained from direct shear tests of previously cemented sands that contain appreciable amounts of fines (17.5% passing the No. 200 sieve), carbonates and sulfates. Identical specimens were prepared at a relative density of 60%. While some samples were tested immediately, other samples were placed in a room at 100%

relative humidity, 20°C temperature and under a vertical pressure of 2 kPa. The shear tests were performed at vertical loads of 40 to 120 kPa. After testing, the researchers noticed that the internal friction angle increased from 36° to 38.7° over a period of 6 months.

2. 4 Proposed Mechanisms of Time Effects in Sand

As discussed in the previous sections, time effects in sand affect the cone penetration resistance, pile capacity, small strain shear stiffness and liquefaction resistance. There is a significant variability in the magnitude and rate of change of these properties observed by researchers in the past. Both dry and wet sands were affected by aging, with larger changes observed in saturated sands. The pH of the water also seems to affect the change in properties. It was also noticed that time effects are significantly diminished under large strains. Many researchers proposed various hypotheses behind sand aging. The hypotheses can be broadly classified as chemical and mechanical processes. The present section summarizes the main hypothesis put forth by researchers.

2.4.1 Chemical Mechanisms

Bonding at grain contacts was thought to be the primary reason behind sand aging for a long time. Cementation between grains due to pressure solution and precipitation was thought to be the reason behind the observed changes. The cementation would produce cohesion in sand without affecting friction angle.

Denisov and Reltov (1961) found out that a quartz sand grain would adhere to a quartz plate on which it rests. The researchers observed that the force required to displace the grain increases with time of contact between the grain and plate. Performing the test under water caused a greater increase in dislodging force than that necessary in the air-dry test. They hypothesized that formation of a cementing agent, most likely silica acid gel precipitated at particle contacts due to pressure solution to be the reason behind the increased adhesion. They suggested that bonds between sand grains may arise due to gradual joining of the silicic acid gel films at grain surfaces. However, no explanation was given to why the required shear force needed to debond the grain in air increased with resting time. Mitchell (2008) suggested that this hypothesis is unlikely as laboratory and field studies on sand ageing occur at temperatures of 0 ~ 30° C and effective stresses less than 200 kPa and pressure solution cannot occur under these

conditions. Mesri et al., (1990) argue against a chemical mechanism being responsible for time effects in sand. Using the data obtained by Daramola (1980), Mesri argues that failure of soil samples at large strains should destroy any cementation and so the increase in stiffness could not be caused by cementation. Mesri, et al., (1990) suggest a different mechanism that does not involve brittle cementation should be responsible for the observed time effects.

Lee (1977) presented evidence of adhesion bonds in Sacramento River sands at pressures greater than 6 MPa at room temperature. Particle size of the sand varied from 0.149 mm to 0.297 mm and contained quartz, feldspar and amphibole or pyroxene minerals. Before triaxial testing on saturated specimens, the sand was washed. After triaxial testing, when the sample was being removed the author found that the samples were "hard to the touch", and, had the appearance and texture of soft sandstone. The samples retained their shape even after drying to remove possible capillary effects. Submerging the samples under water for about 4 hours made the specimens to break down and revert back into free flowing sands. The tests performed by Lee (1977) do not show any form of adhesion at pressures less than 6 MPa. Most of the observed changes in mechanical properties of sand are at depths, where pressures are much less than 6 MPa. Hence adhesion bonds between sands could not be the reason behind time effects in sand at lower vertical stresses.

Joshi et al., (1995) reported the formation of silica precipitates on and in between sand grains to be the reason behind time effects in sand. Their laboratory tests described in section 2.3.1 showed that over time, the cone penetration resistance was greater for sands submerged in simulated sea water than for samples submerged in distilled water or dry samples. Scanning electron micrographs of sand specimens at the end of the test (2 years) showed precipitates linking sand grains. X-ray Diffraction (XRD) analysis on river sand before the test showed the presence of Quartz along with Calcite and Norsethite. XRD on Beaufort Sea sand showed presence quartz and albite. Energy Dispersive X-ray Analysis (EDXA) of river sand in distilled water after the test showed the precipitates were made of calcium and possibly silica. EDXA of river sand submerged in sea water after the test showed presence of sodium, silica, calcium and chlorine in the precipitates. While the tests reported by Joshi, et al. show cementation as a likely hypothesis for time effects, there are several reported cases where changes to sand properties were found in dry sands (Afifi and Woods 1971, Human, 1992). Cementation in these dry sands is unlikely as moisture is required to drive the pressure solution and precipitation reactions.

Baxter and Mitchell (2004) performed laboratory tests to study the chemical mechanism reported by researchers in greater detail. The details of the test are described in section 2.3.1. Although a chemical and mineralogical study of the sand following the test showed the precipitation of carbonates and silica, no visible evidence of precipitation was observed in scanning electron micrographs of the sand. Also, no increase in penetration resistance was observed in any of the test. Inductively Coupled Plasma analysis of the pore fluid after the test indicated significant dissolution of silica and calcium. The pore fluid concentration after testing was slightly super saturated with respect to SiO_2 making precipitation of silica a likely scenario. However, Mitchell (2008) used dissolution of quartz data from Dove and Elston (1992) and estimated that the maximum dissolution of quartz per kg of sand would be $5 \cdot 10^{-5}$ kg per year and concluded that even if this dissolved quartz precipitated at the grain contacts instantaneously forming a cementing bond, it was highly improbable that it could produce sufficient bonding between grains that results in the observed significant changes to mechanical properties of sand over time. Hryciw (1986) performed solubility and precipitation tests of silica sand pretreated with lime in carbonated water. Hryciw found out that adding lime to silica sand in water increases silica solubility due to an increased pH. Carbonation of water, as caused during blast densification, increases silica solubility. This showed that the silica was not precipitated, although the solution was highly supersaturated with respect to crystalline silica solubility. These results show the precipitation of silica at grain contacts to be an unlikely cause behind sand aging.

2.4.2 Mechanical Processes

Schmertmann (1987) proposed two alternative mechanisms that could result in changes to cone penetration resistance of sand over time following ground improvement. He suggested that blasting or vibroflotation during ground improvement could produce temporary zones of low lateral effective stresses in the soil. He hypothesized that this could be the reason behind the drop in cone penetration resistance immediately after ground improvement. Increase in effective lateral stress over time could then be responsible for the time-dependent increase in cone penetration resistance. The second alternative mechanism hypothesized by Schmertmann was a purely frictional gain in strength and modulus over time due to dispersive particle reorientations during secondary compression. Mesri et al. (1990) and Schmertmann (1991) suggested creep

involving grain slippage and increased particle interlocking as the dominant mechanisms responsible for time effects in sand.

Mesri et al., (1990) suggested that aging of clean sands develops increased frictional resistance through macrointerlocking of grains and micro-interlocking of grain asperities. They hypothesized that a continued rearrangement of sand grains occurs during aging, leading to an increase in stiffness and an increase in effective horizontal stress, and giving rise to time effects in sand. They also argued against a cementing bond hypothesis (chemical mechanism) behind sand aging. Based on the adsorption rates of SiO_2 obtained from Henderson et al. (1970) who suggested that precipitation of quartz from amorphous silica would take millions of years, Mesri et al. (1990) argued that cementation is not the reason behind the observed changes in sand over a period of weeks to months. However, Mesri et al. (1990) do not provide any explanation behind the drop in CPT resistance following ground improvement.

From results demonstrated in Schmertmann (1981, 1983, 1987) and other researchers in the past, in his Terzaghi lecture, Schmertmann (1991) postulated that aging in sand is a result of increased soil friction and not cohesion. He suggested that in situ effective stresses drive the mechanisms involved in aging. The mechanisms hypothesized by Schmertmann (1991) were thixotropy, secondary compression, dispersive particle movements, internal stress arching and increased interlocking. He argued that during aging, all these mechanisms should lead to a more stable soil structure resulting in an increased soil stiffness and strength. Schmertmann (1964) (cited in Schmertmann 1991) used a modified triaxial test and showed that the mechanisms behind sand aging are due to an increase in soil friction over time and not a change in cohesion. He thus deduced that a mechanical process must be behind aging and not a chemical process. It should be noted that all of the modified triaxial tests were performed on clays and no tests on sands were performed.

Axelsson (2000) summarizes the observations obtained from various researchers during pile set up. After pile driving, very low horizontal effective stresses (stress ratios of 0.07 ~ 0.30) were recorded by earth pressure cells on the pile shaft. Axelsson performed field tests on 235 mm square piles and observed a large increase in horizontal effective stress after pile driving. At the toe of the pile, no increase in set up was observed. Axelsson suggests the presence of a strong soil arch around the pile during pile driving. He concluded that the arch formed during pile driving deteriorates with time due to stress relaxation, leading to an increase in lateral stress on

the pile shaft. This explanation based on formation and breaking down of a soil arch around the pile shaft is owed to Chow et al. (1998).

Bowmann and Soga (2003) performed uniaxial compression tests on Leighton Buzzard sand at relative densities of about 75%. The clean sand had a d_{10} of 0.120 mm and a d_{50} of 0.148 mm. Different samples of the sand were loaded to 500 kPa for different durations. At the end of each test, a resin was impregnated into the specimens. Changes to soil fabric were studied by analyzing cut cross sections of the sample. They found that over time, the sand grains rotated in space making the soil fabric more isotropic. They also noticed that although the particles were evenly spaced at the starting of the test, over time they clustered together changing the local void ratio distribution. Based on their experiments, they suggest that creep in granular material occurs in the weak force chain network which prop the strong force chains. As particles slip, the strong force chain network buckles, producing greater interlocking regions and also changing the force chain pattern. In time, this leads to areas of large voids neighboring tightly packed areas, which are more resistant to load application.

Jirathanathaworn (2009) performed plane strain laboratory compression tests on glass cylinders. Lateral stresses were measured by photo-elastic sensors developed by the author. Jirathanathaworn measured time-dependent increase in lateral stress and surface settlement. When subjected to a constant load, bending of force chains in the glass cylinders was observed. The observations from this research support the hypothesis of Bowmann and Soga (2003).

Lade et al. (2010) and Lade and Karimpour (2010) suggested delayed crushing of grains after loading to be responsible for time effects in sand. These researchers proposed that the strength of sand grains is a function of the loading time akin to the strength of glass, ceramics and rocks. They suggest static fatigue of individual particles to be the main reason responsible for time effects in sand. According to the researchers, the delayed fracturing of the grains causes stress redistribution in the soil. This redistribution is responsible for the observed changes to mechanical properties of sand over time. While the suggested hypothesis might explain why time effects are observed at high stresses (> 1 MPa), it does not explain why larger changes are observed at lower confining stresses (Afifi and Woods 1971, Hryciw 1986, Joshi et al. 1995).

Recently, Suarez (2012) suggested that mechanical processes at the particle level were responsible for changes to soil properties over time. By performing X-Ray CT scans during sand creep, Suarez observed small particle movements and rotations of grains. He noticed that during

creep, grains rotate, resulting in a homogenous distribution of long-axis orientation. He suggested that this should result in a more uniform and stable soil structure.

2.4.3 Other Processes

Hryciw (1986) postulated that gradual dissipation of gases after explosions (used for compaction) could be responsible for the delayed increase in cone penetration resistance. It was suggested that during blast densification of loose sands, when the sand is being liquefied, the large volume of gases produced due to blasting could cause arching in the soil preventing the grains to be deposited into a denser configuration. It was proposed that soil arching due to gases would cause a high local void ratio due to which the cone penetration resistance decreases following the blast. Over time, the trapped gases dissolve and/or escape to the surface resulting in an increased penetration resistance. Figure 2.13 shows the gas bubbles causing arching in the soil. Following the blast, Hryciw (1986) observed larger decreases in CPT resistance closer to the blast. Decrease in penetration resistance was also observed below the charges.

Microbial activity occurring in the soils could result in changes to mechanical properties of sands (Mitchell and Santamarina, 2005). Stocks-Fischer at al., (1999) studied $CaCO_3$ precipitation induced by *Bacillus pasteurii*, a common soil microorganism. This microorganism uses urea as energy to produce ammonia which increases the pH of the solution, causing calcium and carbonate ions to precipitate as $CaCO_3$ (Kroll, 1990). DeJong et al. (2006) used this microorganism (*Bacillus pasteurii)* to induce calcite cementation in Ottawa 50-70 sand. Undrained Triaxial tests performed on these sands show an increase in the axial capacity. The bacteria treated sands showed an increase in the initial stiffness and elastic capacity over the untreated specimens. It should be noted that for the bacteria to thrive, very specific parameters such as water pH, oxygen supply, metabolic status, concentration of bacteria, flush timings etc., are needed. These conditions might not be found in the field. Also, these findings do not explain why time-delayed changes to properties are seen in dry sands.

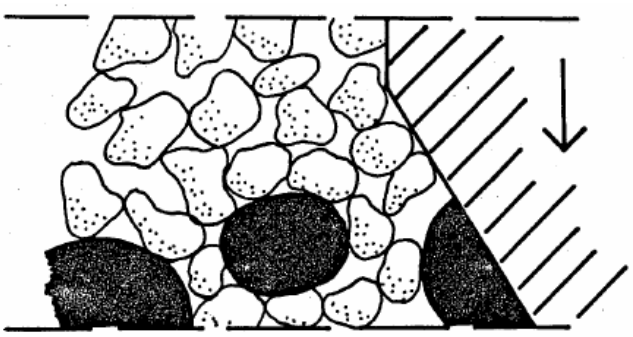

Figure 2.13. Gases released during explosive densification causing arching in the soil (from Hryciw, 1986).

2.5 Conclusions

There exists a considerable body of literature on sand aging with information reported by various researchers. Every study on sand aging reported changes follows a deposition or disturbance. Aging in sand causes a change in its engineering properties. Some of the changes to sand properties due to aging include small strain stiffness, liquefaction resistance, pile set-up, standard penetration test blow count and cone penetration resistance. The changes occur with little or no measurable variation in void ratio. Aging effects are diminished if the soil is subjected to large strains. The energy imparted to the soil during densification seems to affect the magnitude of aging. The increase in CPT tip resistance continues at a decreasing rate after substantial initial increase. It is worthwhile to note that while aging affects the stiffness of sand, the friction angle at critical volume is not affected.

While changes to engineering properties of sand over time are widely recognized by all researchers, a difference in opinion exists within the geotechnical community on the mechanisms behind these peculiar changes. Early explanation of this phenomenon included bonding of particles, which would be damaged during dynamic disturbance, but would form again in time after the disturbance. Since then, the explanation of the phenomenon shifted toward phenomena occurring during secondary compression or creep-like process. Such conclusion, however, does not provide any physical explanation: creep itself is a phenomenological concept, and is a result of an underlying physical process, i.e., creep is not the cause of aging. Creep is a term used to classify an observed behavior of the material at the macroscopic scale, but it does not provide any insight into mechanisms by which time effects come about. In this thesis, a hypothesis will be presented capable of explaining the time effects in sands.

Chapter 3

RESEARCH OBJECTIVES

3.1 The Hypothesis

Two Scanning Electron Microscope images of sand surfaces are presented in Fig. 3.1. When grains with such surface micromorphology come into contact during load transfer, it is the asperities and small crystalline fragments that are loaded to a considerable degree as the areas of surfaces in contact are relatively small. The small features of the contact morphology are prone to develop cracks in time, a process called *static fatigue*. It is this delayed fracturing that is hypothesized to be the primary cause of time effects: the predominant mechanism contributing to time effects in sand is the delayed fracturing of the micro-morphological features on surfaces of grains in contact (asperities, crystalline fragments, or mineral debris).

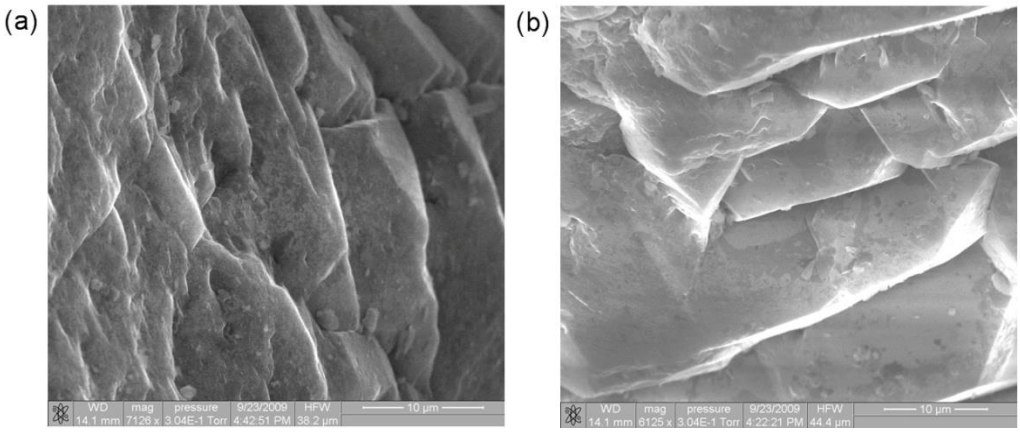

Figure 3.1. Scanning Electron Microscope image of Flint Shot.

Static fatigue has been considered in material science for decades (Charles 1958) as a time-dependent micro-fracturing process in brittle materials. Scholz (1968a, 1972) reviewed experimental work on creep of rocks, and concluded that, at low temperatures and pressure, the primary mechanism of creep of brittle rocks is delayed micro-fracturing. Materials such as glass and ceramics, subjected to stress, have a tendency to develop cracks in time (Wiederhorn & Bolz 1970), even though at some time after initiation of loading they may have been intact. This process is also referred to as *stress corrosion cracking*, as it is affected by environmental factors such as moisture (Cuallar et al. 1987). Scholz (1968b) examined experimental results from investigations on deformation of rocks, and he pointed out that deformation is accompanied by micro-fracturing, which releases elastic energy analogous to earthquakes. The delayed micro-fracturing (static fatigue) is then analogous to aftershocks. Recently, McLaskey and Glaser (2011) showed that asperities on rock fail by brittle fracture during stick slip motion of rock. Untill now, however, *static fatigue* of the micro-morphological features at grain contacts has not been considered as the predominant mechanism behind time effects in sand.

3.2 Objectives

This research focuses on the development of a better understanding of the behavior of sands, and, in particular, on collecting experimental evidence for the hypothesis outlined in the previous subsection, and numerical simulations indicating plausibility of the hypothesis. The secondary topic relates to structural health monitoring and damage detection in underground concrete pipelines, it is limited to one chapter, with the focus on finite element simulations. The specific objectives are:

- Exploring *static fatigue* at the microscopic scale as a possible mechanism responsible for time effects in sand; collect experimental evidence supporting or disproving the hypothesis suggested.
- Exploring the possible consequences of static fatigue on the macroscopic stress state of confined sand, and conduct macro-scale experiments to validate the outcome.
- Development of quantitative measurements for interaction process between two sand grains. Indicate possible consequences of static fatigue (or stress corrosion cracking) on the cone penetration resistance after dynamic compaction of sand.

- Identify the level of modeling complexity required for 3D finite element modeling of segmented concrete pipelines buried in sand and subjected to ground rupture.

Chapter 4

EXPERIMENTAL INVESTIGATION

4.1 Introduction

To test the suggested hypothesis, sand is considered at three scales; *micro*, *meso* and *macro*. The *micro* scale relates to interactions between individual grains. What is considered a contact between two sand grains in the description of the soil fabric is a small region where asperities at the surfaces of the two grains interact through multiple contact "points". A contact of two grains is illustrated in Fig. 4.1. The *meso* scale includes assemblies of grains, load transfer through formation of force chains (Fig. 4.2), and relative motion of grains. The *macro* scale is the level at which the response of the assemblies or clusters of grains is averaged. The notions of an average stress σ_{ij} and average strain ε_{ij} are introduced at the macro scale. Relations between the increments of the two give rise to constitutive equations. This is the scale at which engineering problems are solved. At the *micro* and *macro* scales, laboratory experiments are carried out. At the *meso* scale, numerical simulations are carried out. In this chapter, laboratory experiments performed at the micro and macro scales are discussed.

At the *micro* scale, surfaces of sand grains have a rich surface morphology. Surface morphology of grain surfaces plays an important role in the behavior of a contact. Atomic Force Microscope (AFM) and Scanning Electron Microscope (SEM) are used to characterize the surface morphology of quartz grains (Ottawa 20-30 sand). Nano-indentation tests are performed to obtain mechanical properties of individual sand grains. Micro scale laboratory experiments are performed with two custom-made devices to study changes occurring on sand grain surfaces when subjected to a constant load.

At the *macro* scale, tests are performed using a consolidometer with lateral stress measurement capability. Tests are performed with both dry and wet specimens of Ottawa 20-30

sand under different loads. Changes to stress state of sand in time under a constant load are studied.

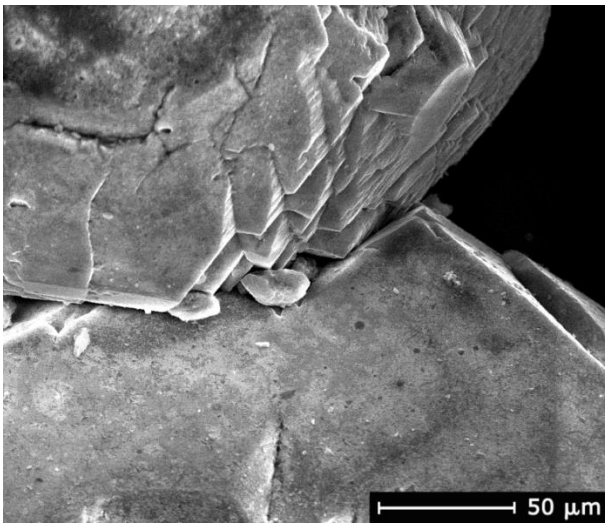

Figure 4.1 SEM image of a contact between two quartz grains (Micro scale).

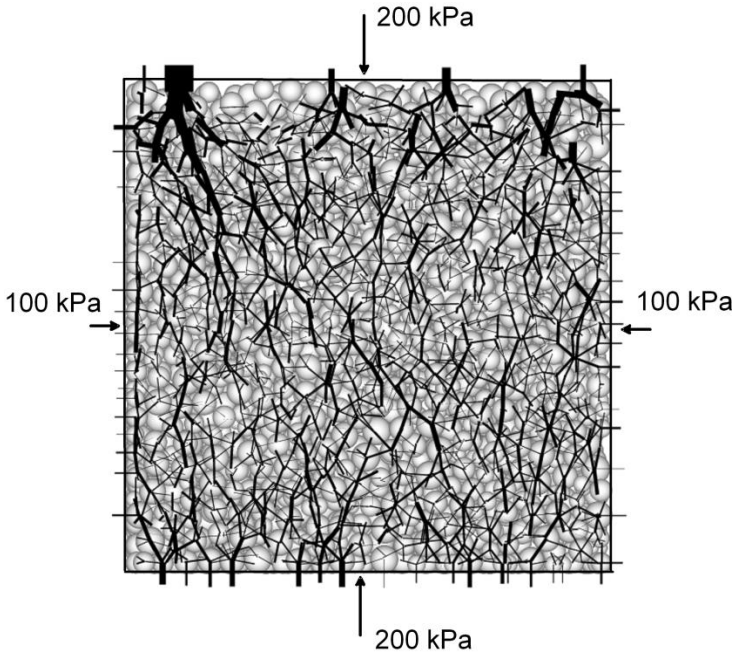

Figure 4.2 Force chains formed in an assembly of grains confined to a particular state of stress; Discrete Element Simulation (Meso scale).

4.2 Surface morphology of sand grains

At a millimeter scale, grain surfaces might appear flat and smooth. But at a micrometer scale, the surface has many asperities giving the surface its roughness. When two grains come in contact, it

is these asperities that come in contact with one another. Hence, the true area in contact is many times smaller than the apparent area. This important concept should be taken into account while studying time effects in sand as the load in a granular material is carried through these asperities and any changes occurring on these contacts could influence the mechanical properties of sand at a *macro* scale. Due to this, knowledge about the size and shape of asperities along with the true contact area on grain surfaces is important. Morphological characterization of sand grain surfaces is performed using the Atomic Force Microscope (AFM) and Scanning Electron Microscope (SEM).

4.2.1 Atomic Force Microscope (AFM) characterization

AFM has an advantage of quantitative assessment of the surface roughness. The resolution of an AFM could be as small as a few picometers allowing the researchers to resolve features as small as an atomic lattice. The AFM belongs to the family of scanning probe microscopes and was invented by Binning et al. (1986). Scanning probe microscopy refers to a group of imaging techniques where a probe is moved over a substrate in a raster pattern to collect details of the surface. The AFM consists of a cantilever with a sharp tip (radius in the order of a few nanometers) at its end that is used to scan the specimen surface. When the tip is brought in proximity of the sample surface, forces between the tip and sample lead to a deflection of the cantilever governed by the Hooke's law. This deflection is measured using a laser spot reflected by the top of the cantilever onto a photodetector. The sensitivity of cantilever movement is derived from the large distance between the cantilever and photodetector. To avoid the damage to the cantilever tip caused by the sample surface, a feedback mechanism is employed to maintain a constant force between the tip and the sample surface by adjusting the distance between them through a piezo crystal (the tip of the tool and the surface are not in the actual contact). By moving across the sample surface in a rectangular pattern, information regarding the surface morphology of the sample is collected. Figure 4.3 shows a schematic of the major components in an AFM.

Veeco Dimension Icon® AFM by Bruker was used for imaging sand grain surfaces. The maximum vertical height measured by this AFM is about 5 microns. Maximum scan size is about 50 x 50 μm. Due to the curvature and roughness of grain surfaces, the maximum scan area was

limited to about 5 x 5 μm or less. A silicon nitride tip with a tip radius of 1 nm was used in the study. Figure 4.4 shows geometry of the AFM tip used in the analysis.

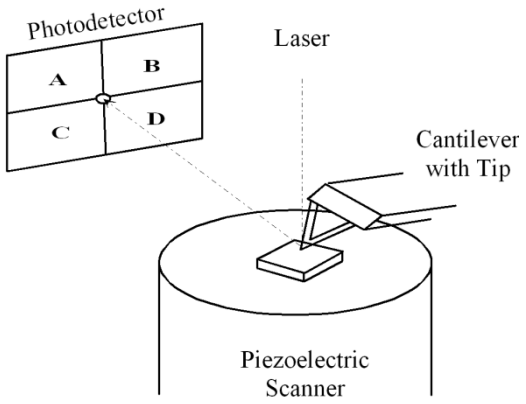

Figure 4.3. Schematic of an AFM.

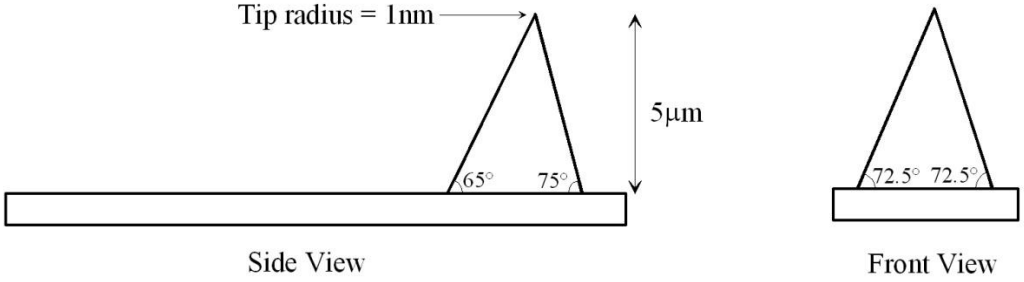

Figure 4.4. AFM tip specifications used in the analysis.

Ottawa 20-30 sand obtained from US Silica and Lake Michigan Dune sand were used in AFM analysis. Energy Dispersive X-Ray Analysis (EDX) of Ottawa 20-30 sand grains showed the presence of Silicon and Oxygen (which was expected). EDX analysis of Lake Michigan Dune sand showed primarily Silicon and Oxygen with trace amounts of Carbon and Aluminum. Surfaces of four Ottawa 20-30 sand grains, and one dune sand grain are scanned using the AFM. Each grain was glued on top of a magnetic stainless steel (alloy 430) disc using a double sided copper tape. The disc was then placed in the AFM for scanning.

AFM scanning is performed at a resolution of 512 x 512 pixels resulting in 262,144 data points, irrespective of scan area size. Figures 4.5 to 4.11 show results from AFM analysis. It is seen that the grain surface is made up of hills and valleys of varied vertical and lateral sizes often referred to as *surface asperities*. After AFM analysis, the elevations of hills and valleys are subtracted from a mean height line, which is an arithmetic mean of all feature elevations. The

randomness in asperity sizes suggests that statistical methods of surface characterization must be adopted to study surface profiles. Statistical distributions of asperity elevation and slopes are also presented in Figs. 4.5 to 4.11. In these plots, the quantity on the abscissa is either the asperity elevation or asperity slope in degrees. On the ordinate, the density of the corresponding abscissa parameter is shown. The density is obtained by normalizing the number of asperities of a particular height/slope with the total number of measurements. While, asperity elevations and slopes of both Ottawa sand and Lake Michigan Dune sand seem to follow simple statistical distributions (Gaussian or Lorentzian), the shape of asperities present a stark contrast. Asperities on Ottawa sand, Figs. 4.5(a), 4.6(a), 4.7(a), 4.8(a), 4.9(a) and 4.10(a) are more jagged and random compared to Dune sand asperities, Fig. 4.11(a), which are more rounded. This shows that erosion processes affect the surface morphology of grains at sub-micro scales.

Various standard parameters can be used to describe the surface profile of the sand grains. ASME B46.1 (2009) defines a number of amplitude parameters to describe the surface based on the vertical deviations of the profile from the mean line. Table 4.1 shows calculated values of commonly used roughness parameters for the seven AFM scans. Average surface roughness (S_a), is the average of individual asperity elevations (z_{ij}) measured from the mean elevation (μ) of the profile.

$$S_a = \frac{1}{MN}\sum_{i=1}^{M}\sum_{j=1}^{N}\left|z_{ij} - \mu\right| \tag{4.1}$$

where,

$$\mu = \frac{1}{MN}\sum_{i=1}^{M}\sum_{j=1}^{N} z_{ij} \tag{4.2}$$

and z_{ij} is the vertical elevation at point (i, j), and M and N are the number of points (resolution) along the scan directions.

Root Mean Square (RMS) surface roughness (S_q) is the average of height deviations from a mean line over the evaluation length, defined in the following formula

$$S_q = \sqrt{\frac{1}{MN}\sum_{i=1}^{M}\sum_{j=1}^{N}\left(z_{ij} - \mu\right)^2} \tag{4.3}$$

Surface Skewness (S_{sk}) is a measure of surface symmetry, or, more precisely, surface asymmetry, and it is defined as

$$S_{sk} = \frac{1}{MNS_q^3} \sum_{i=1}^{M} \sum_{j=1}^{N} \left(z_{ij} - \mu \right)^3 \tag{4.4}$$

It can be either positive or negative. It shows the extent to which a distribution inclines to one side of the mean. Zero skewness suggests a symmetric height distribution (Gaussian distribution). A negative skewness suggests that the distribution is skewed to the left, i.e., the distribution is concentrated to the right (more valleys than peaks). Positive skew is when the distribution skews to the right, i.e., distribution is concentrated to the left (more peaks than valleys).

Surface Kurtosis (S_{ku}) is a measure of sharpness of the profile heights, and it indicates whether the distribution is peaked or flat, relative to the normal distribution; it is defined as

$$S_{ku} = \frac{1}{MNS_q^4} \sum_{i=1}^{M} \sum_{j=1}^{N} \left(z_{ij} - \mu \right)^4 \tag{4.5}$$

The Kurtosis for a standard normal distribution is three. Kurtosis values smaller than three indicate a distribution having a flat peak near the mean. Values larger than three indicate a distribution with a sharp peak near the mean.

Observations of grain surfaces at various scales point towards a self-similar notion of asperity height and slope distribution. Figure 4.7 shows the analysis of a 2 x 2 μm area on grain #3. Figures 4.8 & 4.9 show AFM analyses of two sub regions numbered (i) and (ii) on Fig. 4.7(a). It is interesting to note that even at larger magnifications, asperity heights and slopes continue to follow similar statistical distributions as that of smaller magnifications. It is argued that since the grains for AFM are chosen at random and statistical distributions at various magnifications follow a normal distribution, any processes such as weathering or static fatigue should also produce asperities whose heights and slopes follow a normal distribution. The self-similarity concept in asperity distribution also suggests that even at larger scales, surface asperities could potentially follow a normal distribution.

The topography of the grain surfaces reveals a rich surface texture and roughness. ASME B46.1 (2009) defines *roughness* as the finer scale in the geometry. The larger scales are the *form* and the intermediate scales are termed *waviness*. *Texture* is defined as the combination of waviness and roughness. For a sand grain, the form is the overall shape of the grain (round, angular, etc.). Using AFM, the texture of grain surfaces is obtained. By performing a Fast Fourier decomposition of the texture data using a low-pass and high-pass filter the waviness and roughness of the profile can be calculated. Figure 4.12 shows the texture, waviness and roughness along a diagonal line shown on Fig. 4.5(a). Figure 4.13 shows the analysis applied to a small area on the surface of a quartz grain (rather than along one cross section). Figure 4.14 shows a similar analysis performed on Lake Michigan Dune sand grain. A comparison of Fig. 4.13(c) and 4.14(c) shows that wind erosion on dune sand produced roughness features that are more systematic, less random and denser packed compared to Ottawa 20-30 sand. It should be noted that if the cut off wavelength for the Fourier decomposition is changed, we get different set of asperities with different sizes; however the spatial distribution of the asperities are similar. Comparison of Fig. 4.13(a) and 4.14(a) shows that although the dune sand grain might appear smooth when compared to the 20-30 sand grain, at larger magnifications (also scanned at 512 x 512 pixel resolution), dune sand is, in fact, quite rough. A profile of the surface of an Ottawa 20-30 grain in Fig. 4.15, suggests existence of multiple scales in surface roughness. Repeated magnifications of the same surface reveal different levels of roughness. In fact, this multi-scale roughness keeps appearing till the atomic scale is reached, where roughness occurs in the form of atomic steps (Williams and Bartlet 1991). The randomness of the surface texture, along with multi-scale roughness, contributes to the complexity of sand grain surfaces. This complexity in grain surface topography prevents us in using conventional Euclidian mathematics (geometry) to describe the grain surfaces. Any characterization technique to describe grain surfaces must be independent of length scales. This imposes limitations on using statistical distributions.

Fractal techniques have the potential of exploiting this self-repeating nature of surface roughness and texture to develop mathematical tools and equations that can describe grain surfaces. The word fractal comes from the Latin word *fractus*, meaning irregular segments and was coined by Mandelbrot (1967). The repeating nature of roughness observed on grain surfaces is also found in nature in general. Mandelbrot (1967 & 1982) discusses the fractal geometry of nature. The cornerstone in fractal geometry is the idea of *self-similarity*. An object is *self-similar*

if it can be described as rescaled copies of itself or decomposed into smaller copies of itself with the rescaling or decomposition performed isotropically in all directions. If the rescaling or decomposition is dependent on the direction and is anisotropic, the geometric object is said to be *self-affine*. Surfaces in general are self-affine and can be described by a parameter called *Fractal Dimension* (Mandelbrot 1982, Mandelbrot 1985, Hastings and Sugihara, 1993). Fractal dimension is an index of the complexity of a surface and can be measured as the ratio of change in detail to the change in scale (Mandelbrot 1982). While the topological dimension of any object is an integer (1D, 2D or 3D), the fractal dimension can take non-integer values. The fractal dimension is a number that describes the ability of an object or shape to fill a particular area or volume. For regular objects such as a square, circle, triangle, cube etc., the fractal dimension approaches the topological dimension. There are several methods to calculate the fractal dimension (Hastings and Sugihara 1993, Vicsek 1999), and each method can give a different fractal dimension. This is due to the fundamental difference associated with each technique. However using the same method to compute the fractal dimension for different grain surfaces should provide valuable information regarding the surface morphology. The fractal dimension (D_f) of a surface is defined as

$$D_f = \lim_{\delta \to 0} \frac{\log(N_\delta)}{\log(1/\delta)} \tag{4.6}$$

where, N_δ is the least number of non-overlapping copies of the surface in the scale δ. All of the distinct N_δ copies must cover surface completely. For the present analysis the fractal dimension is calculated by using a box counting method (Hastings and Sugihara 1993, Sarkar and Chaudhuri 1994). In this method, a cubical box with an initial edge length δ is kept on the AFM scan surface. The initial edge length of the box is chosen as half the edge length of the surface scan. This results in 8 boxes to fill the entire surface. The number of boxes, N_δ that contain at least one pixel of the image are then counted. The box edge length is now halved and the process is repeated until δ equals the distance between two adjacent pixels. The fractal dimension (D_f) of the surface can now be calculated according to Equation. (4.6). Table 4.2 shows fractal dimensions of seven AFM scans.

(a)

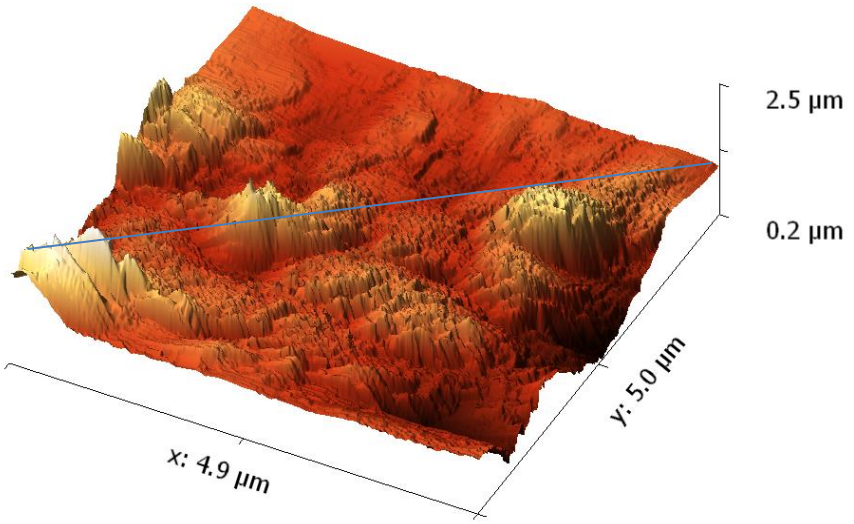

(b)

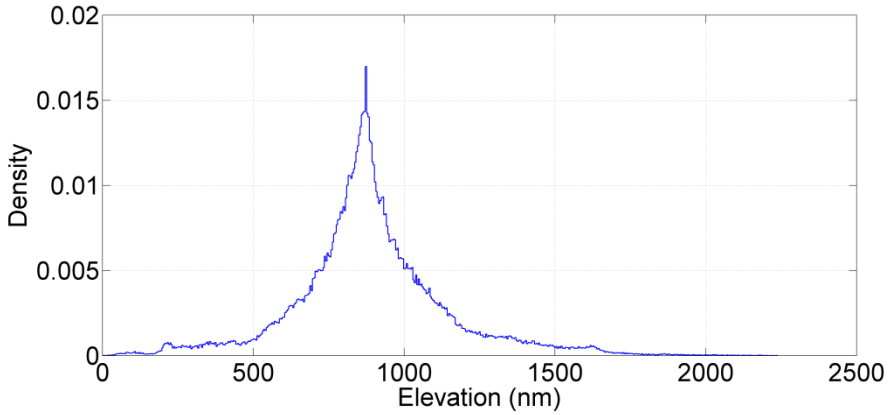

(c)

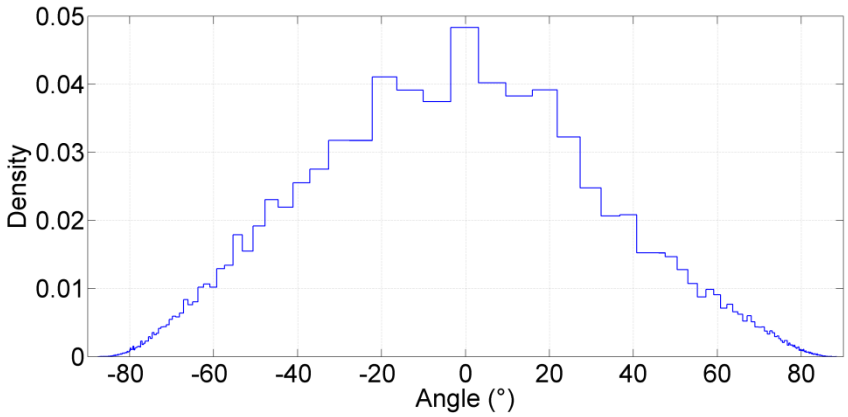

Figure 4.5. AFM analysis on Grain 1, (a) 3D AFM image of a 5 x 5 µm area on grain surface, (b) statistical distribution of asperity heights for the entire scan surface (elevations not subtracted from the mean value), and (c) statistical distribution of slopes of asperities for the entire scan surface.

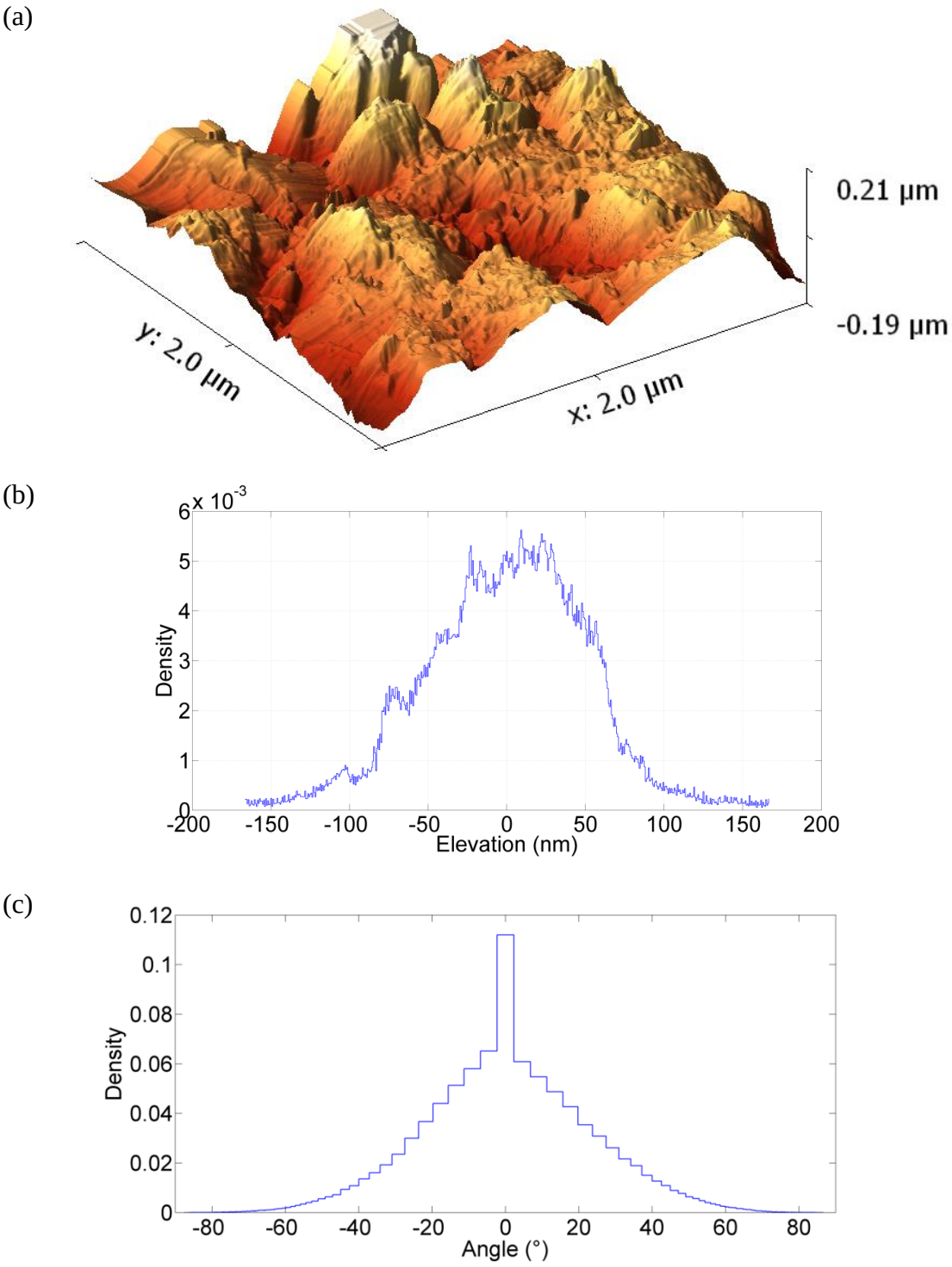

Figure 4.6. AFM analysis on Grain 2, (a) 3D AFM image of a 2 x 2 µm area on grain surface, (b) statistical distribution of asperity heights for the entire scan surface, and (c) statistical distribution of slopes of asperities for the entire scan surface.

(a)

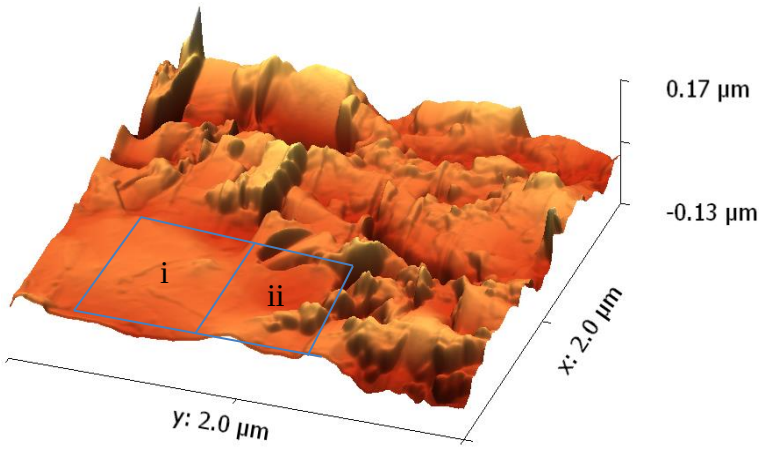

(b)

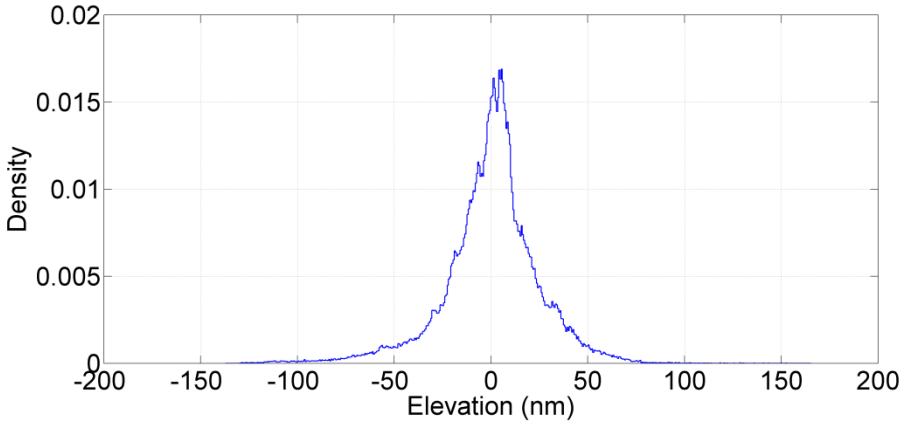

(c)

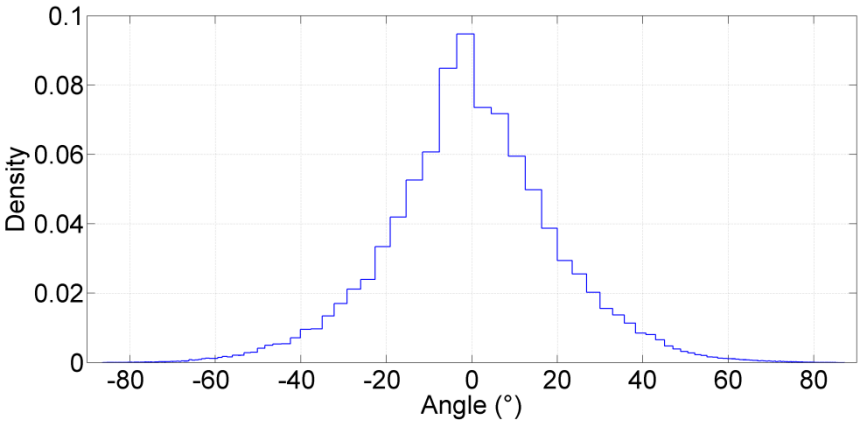

Figure 4.7. AFM analysis on Grain 3, (a) 3D AFM image of a 2 x 2 µm area on grain surface, (b) statistical distribution of asperity heights for the entire scan surface, and (c) statistical distribution of slopes of asperities for the entire scan surface.

(a)

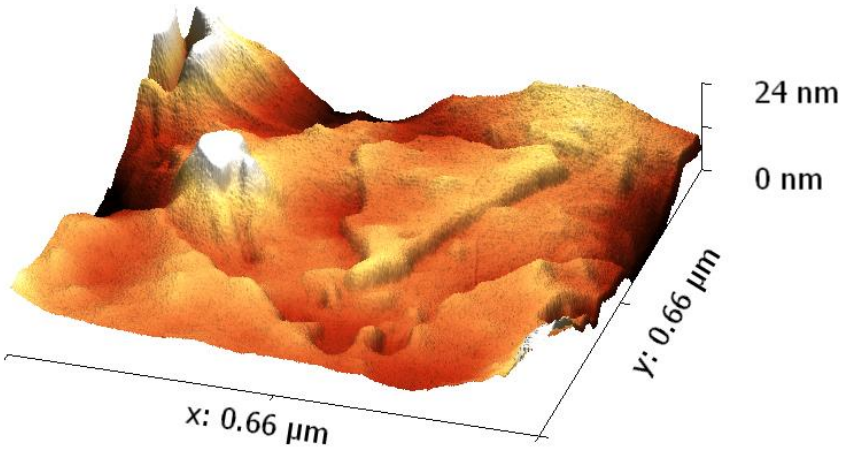

(b)

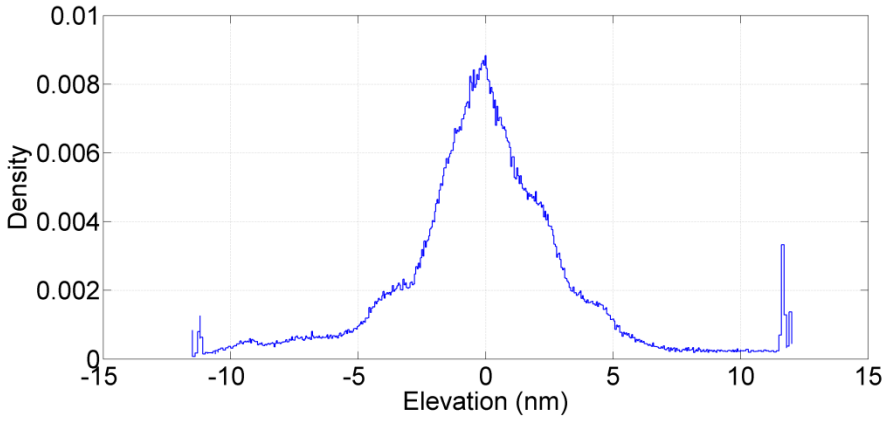

(c)

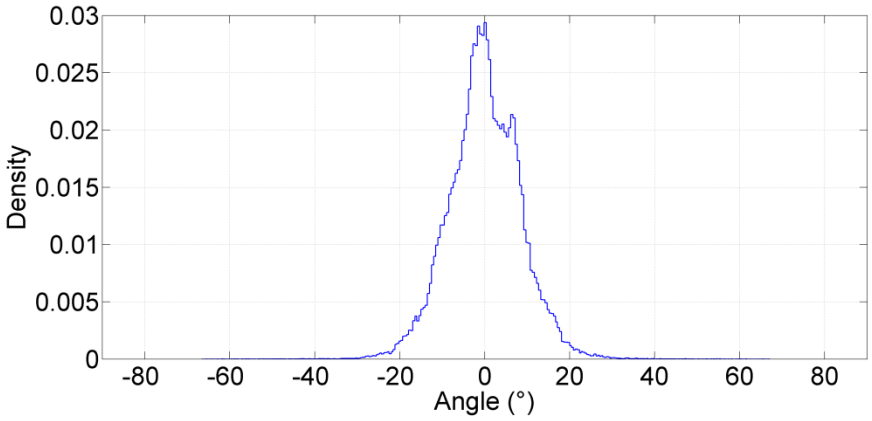

Figure 4.8. AFM analysis of region (i) in Fig. 4.7(a), (a) 3D AFM image of 0.66 x 0.66 µm area of surface, (b) statistical distribution of asperity heights, and (c) statistical distribution of slopes of asperities.

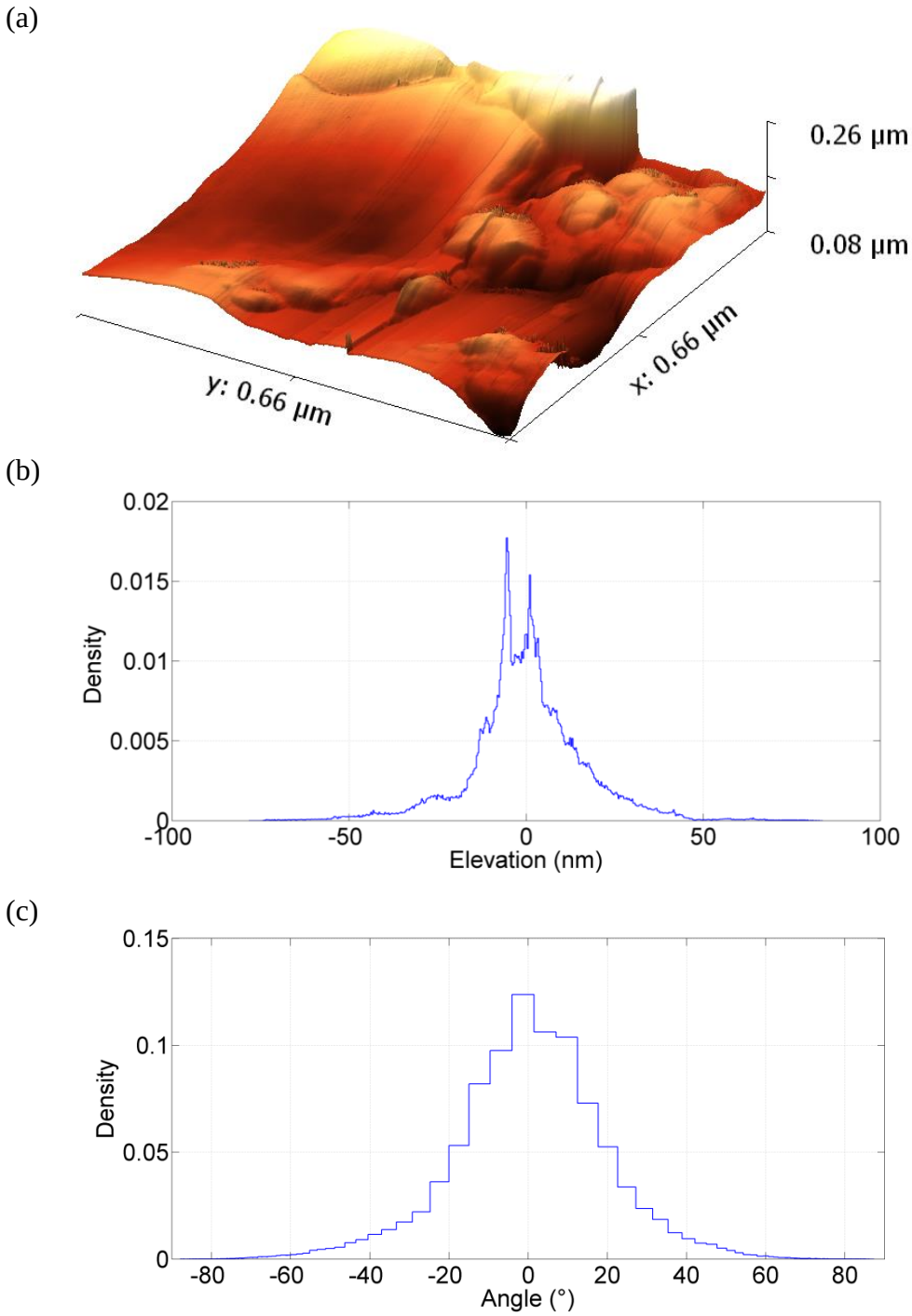

Figure 4.9. AFM analysis of region (ii) in Fig. 4.7(a), (a) 3D AFM image of 0.66 x 0.66 µm area of surface, (b) statistical distribution of asperity heights, and (c) statistical distribution of slopes of asperities.

(a)

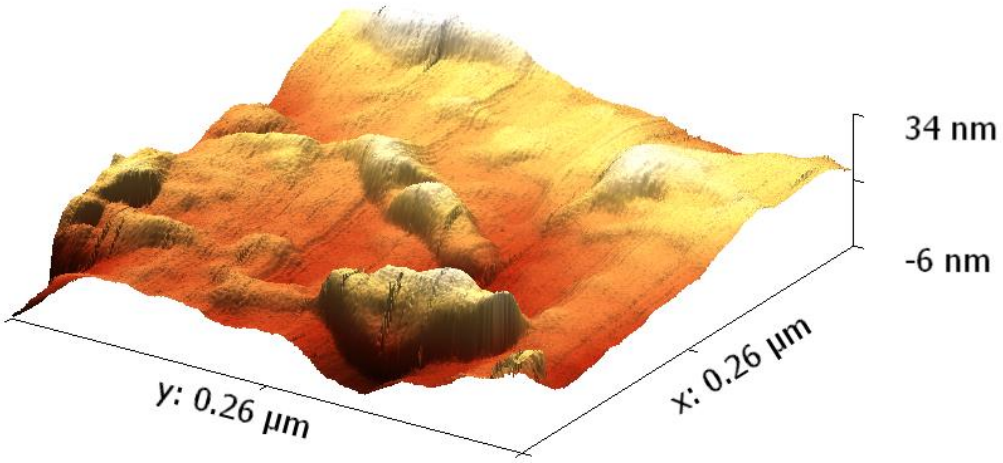

(b)

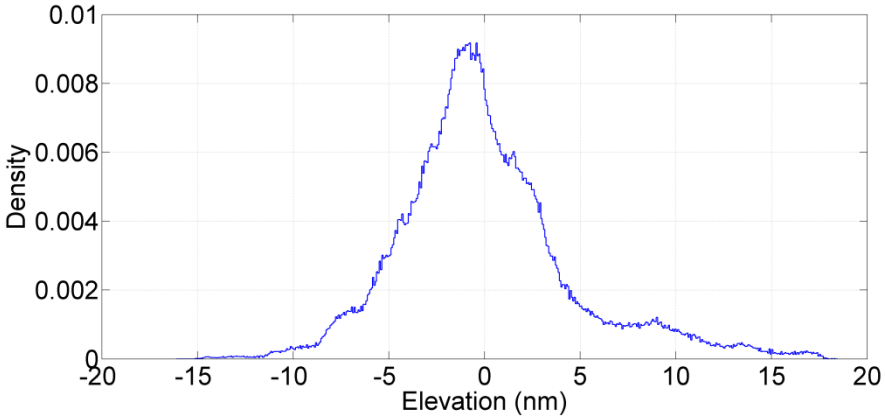

(c)

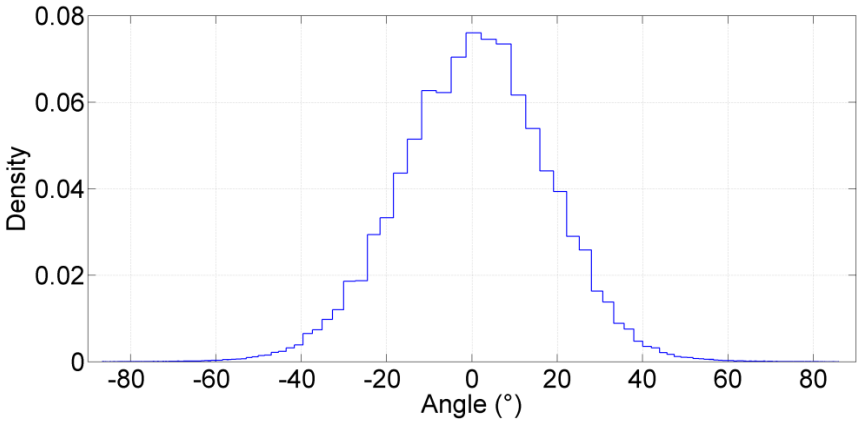

Figure 4.10. AFM analysis on Grain 4, (a) 3D AFM image of a 0.26 x 0.26 µm area on grain surface, (b) statistical distribution of asperity heights for the scanned surface, and (c) statistical distribution of slopes of asperities for the scanned surface.

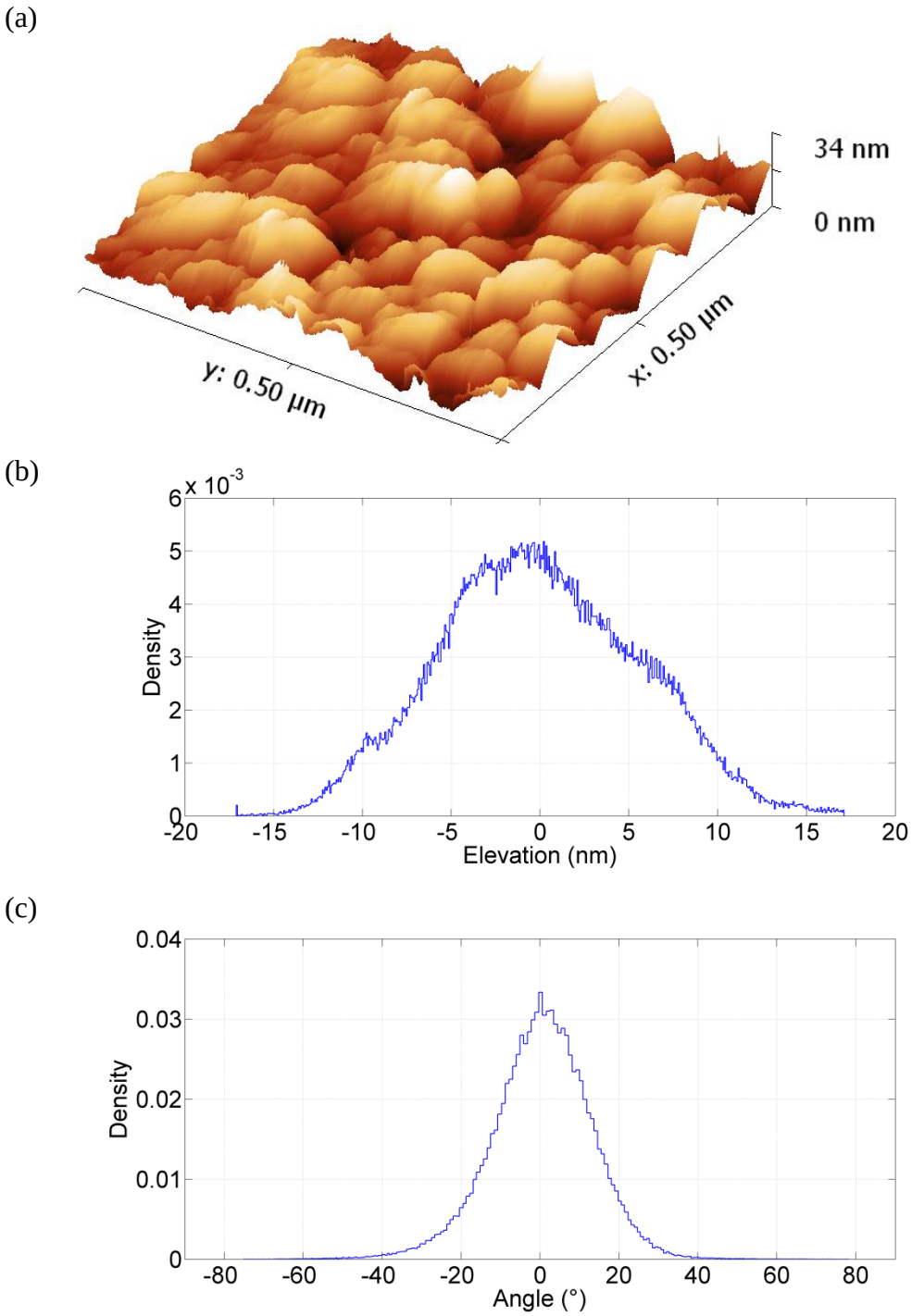

Figure 4.11. AFM analysis on Grain 5 (Lake Michigan Dune sand), (a) 3D AFM image of a 0.26 x 0.26 µm area on grain surface, (b) statistical distribution of asperity heights for the entire scan surface, and (c) statistical distribution of slopes of asperities for the entire scan surface.

Table 4.1. Sand grain surface roughness parameters.

Grain Number	Source	Projected area (μm^2)	Surface area (μm^2)	Surface area/Projected area (%)	S_a (nm)	S_q(nm)	S_{sk}	S_{ku}
Grain #1	Ottawa 20-30 sand	25	70.1520	281	174	250	0.453	2.21
Grain #2	Ottawa 20-30 sand	4	5.6594	141	42.9	55.7	-0.017	0.966
Grain #3	Ottawa 20-30 sand	4	4.6420	116	17.4	24.5	-0.585	2.81
Grain #3 (i)	Ottawa 20-30 sand	0.4356	0.4490	103	2.57	3.69	0.178	1.99
Grain #3 (ii)	Ottawa 20-30 sand	0.4356	0.5250	121	11.4	16.1	-0.011	2.52
Grain #4	Ottawa 20-30 sand	0.0676	0.0898	133	3.33	4.53	0.801	1.5
Grain #5	Michigan Dune sand	0.25	0.3137	125	4.56	5.66	0.18	-0.19

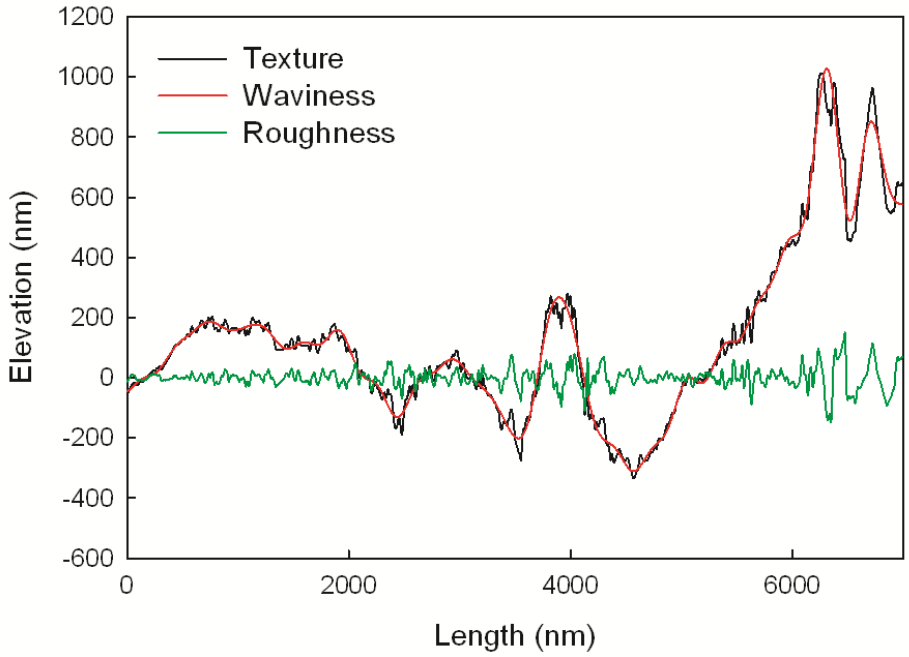

Figure 4.12. Surface characteristics along the diagonal line shown in Fig. 4.5(a).

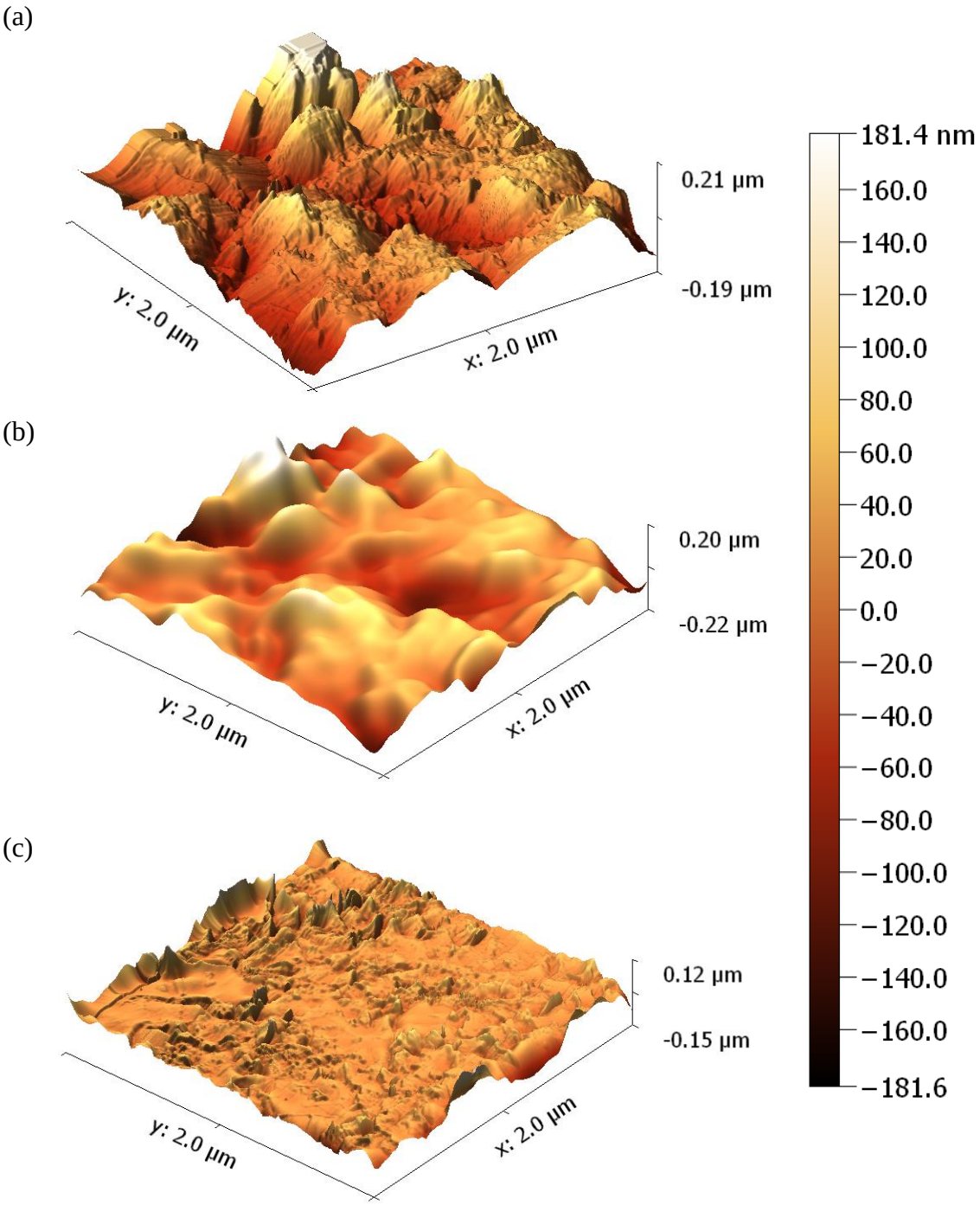

Figure 4.13. 2D Fourier decomposition of Ottawa 20-30 grain surface, (a) texture of grain surface, (b) waviness of the surface (low frequency components), and (c) roughness of the surface (high frequency components).

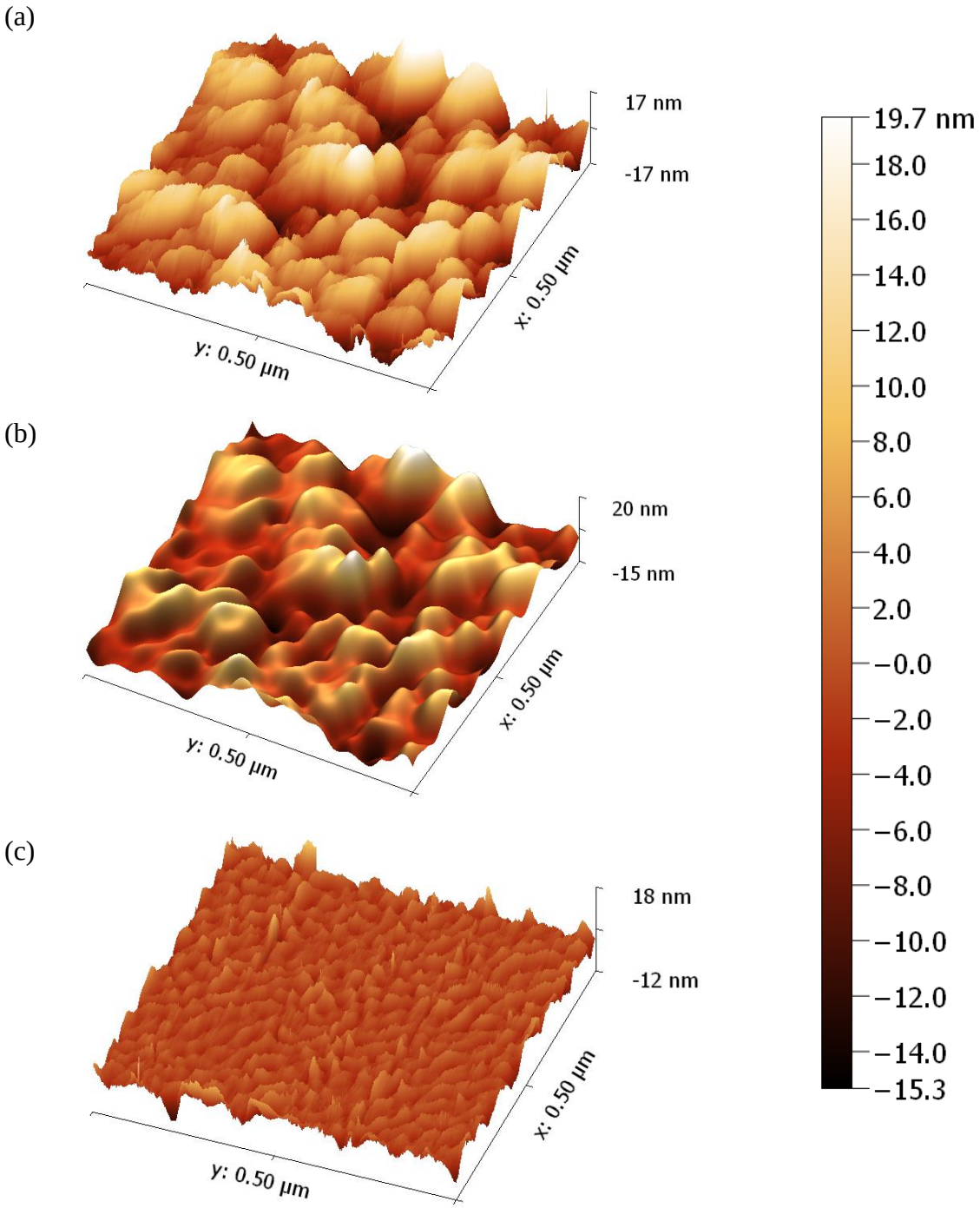

Figure 4.14. 2D Fourier decomposition of Lake Michigan dune sand grain surface, (a) texture of grain surface, (b) waviness of the surface (low frequency components), and (c) roughness of the surface (high frequency components).

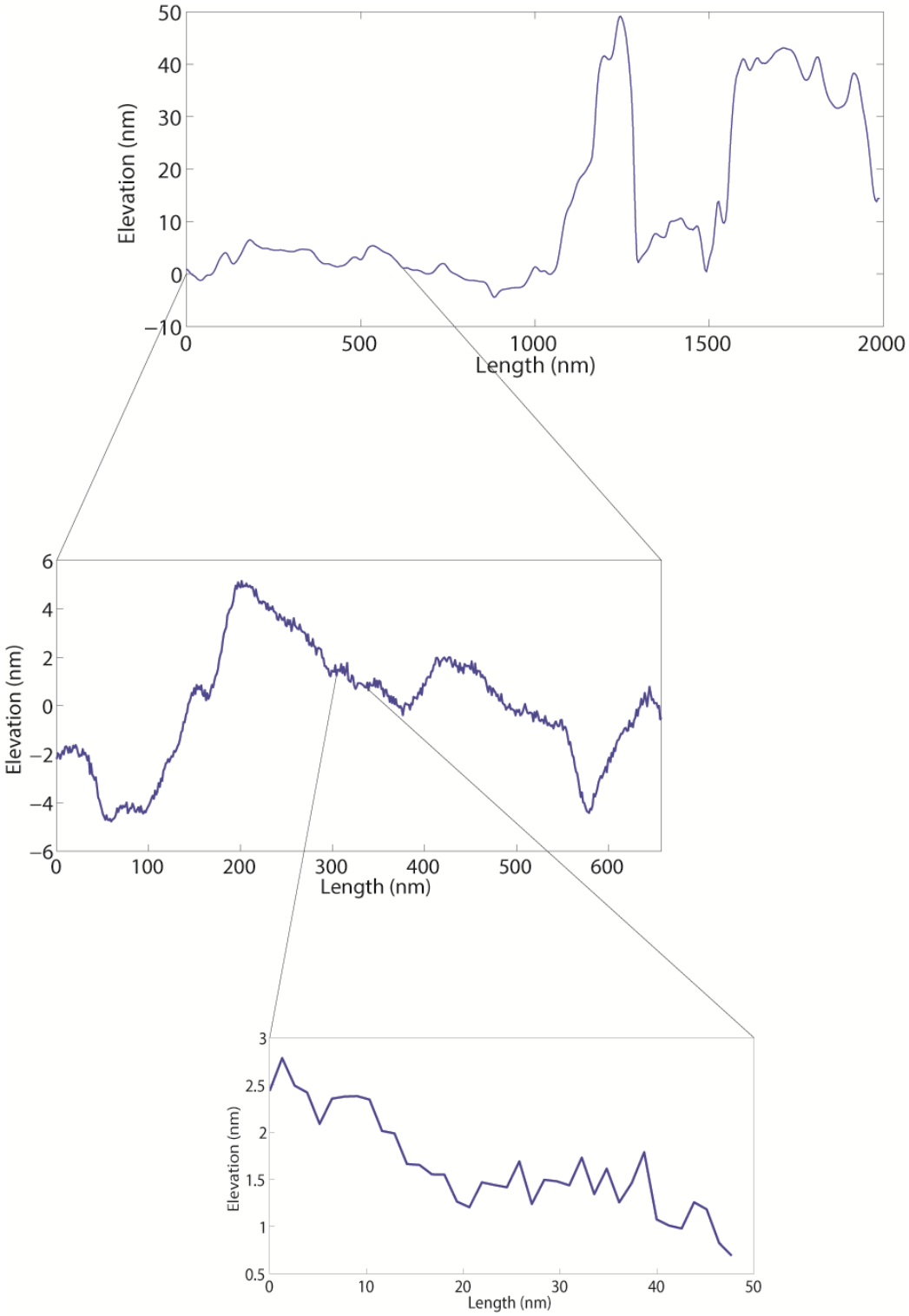

Figure 4.15. Sand grain surface roughness at different levels (data from grain #3).

Table 4.2. Fractal dimension of sand grain surfaces.

Grain Number	Grain Origin	Fractal Dimension
Grain #1	Ottawa 20-30 sand	2.23
Grain #2		2.19
Grain #3		2.15
Grain #3 (i)		2.19
Grain #3 (ii)		2.09
Grain #4		2.17
Grain #5	Michigan dune sand	2.28

4.2.2 Scanning Electron Microscope (SEM)

Although the AFM can be a great tool for characterizing surface morphology of grain surfaces, it is limited by its scan area and maximum vertical height measurement. These two parameters limit the maximum scan area to about 5 x 5 μm or less. Scanning Electron Microscope (SEM) is used to obtain morphological information about larger surface areas on the grain surface as well as to study changes in the micro-morphology of grain surfaces at contacts subjected to loads.

Scanning Electron Microscopes (SEM) use a high energy electron beam under vacuum to scan the sample surface in a repeating rectangular pattern. The high energy electrons (or primary electrons) interact with the atoms that make up the sample surface ejecting secondary electrons. These electrons are collected by a secondary electron detector. This is shown in Fig. 4.16. The analog signal produced by the detector is converted into a digital signal by an analog to digital convertor (ADC) and is synchronized with the position of the primary electron beam as it moves in a rectangular array on the sample surface. The digitized analog signal is then converted into pixels with varying grey level in concert with the movement of the primary electron beam. Thus instead of getting an instantaneous snapshot of the sample as with a camera, the image is built pixel by pixel as the primary electron beam traverses the surface of the sample in a rectangular pattern. If from a certain spot on the sample more secondary electrons are ejected, a bright spot is recorded. Many secondary electrons are generally produced along raised areas of the sample. In the case of a “valley” only a few electrons are produced. This produces a dark spot on the image.

Thus the image obtained from secondary electrons can be regarded as an elevation model with intensity of the image as the elevation.

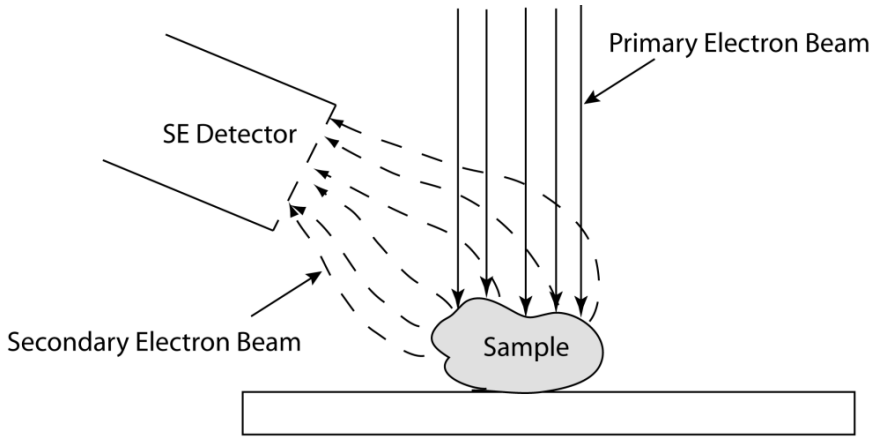

Figure 4.16. Working of a Scanning Electron Microscope.

SEM imaging of sand grains is performed using FEI Quanta 3D. The grains are fastened to a specimen stub using a double sided copper tape, and are placed in the SEM chamber. Typically for nonconducting surfaces (such as sand grain surfaces), a thin coating of gold or silver is applied to make the sample conductive and prevent surface charging the sample. Surface charging of the sample causes problems in imaging. Since the goal of this study is to investigate the morphology of grain surfaces, no coating was applied to the grains to prevent surface contamination. Hence, SEM imaging of the grain surfaces was carried out in the Low Vacuum mode of the device. In order to study the effects of weathering processes on grain asperities and to get morphological information for different types of grains, sands from four different sources subjected to different weathering processes were used for imaging; Fig. 4.17 shows SEM images of Lake Michigan Empire Beach sand surfaces, Fig. 4.18 shows Lake Michigan Dune sand surfaces, Fig. 4.19 shows Huron River sand surfaces, and Fig. 4.20 shows Ottawa 20-30 sand grain surfaces. Although these figures represent only a limited range of features on grain surfaces, they are representative of the morphology commonly occurring in many types of sand. The difference in micromorphology of various grain surfaces can be due to mineralogy or due to the process of weathering. For instance, it is evident from comparison of Figs. 4.18 and 4.20 that the Aeolic weathering process leaves microscopic features (asperities) more rounded than the grains that come from crushing of rock (Ottawa-type). More detailed SEM images of asperities present on sand grain surfaces are discussed in Krinsley and Doornkamp (1973).

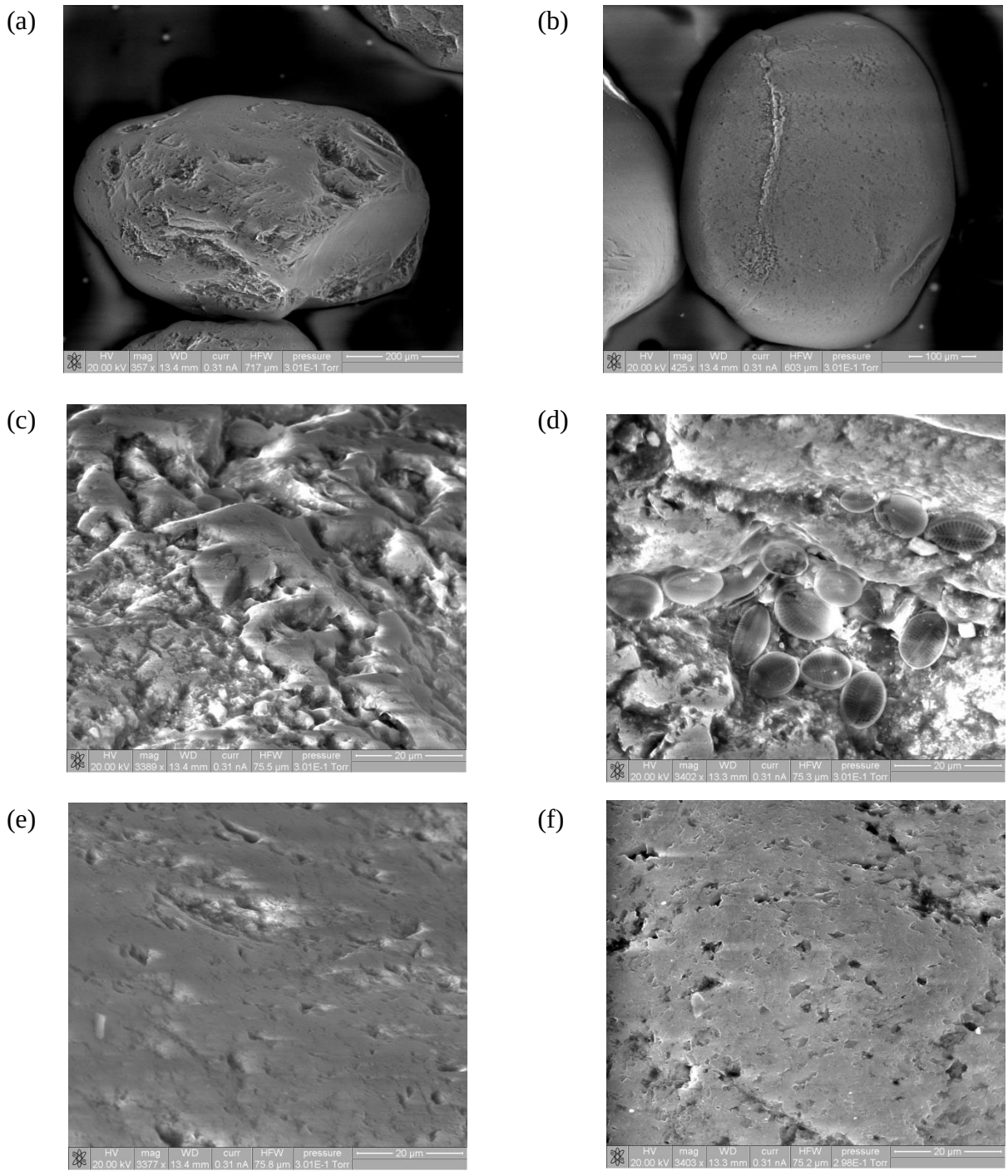

Figure 4.17. SEM images of Lake Michigan Empire Beach sand, (a) angular grain with a broken face (image width = 717 μm), (b) rounded grain (image width = 603 μm), (c) surface asperities (image width = 75.5 μm), (d) microorganisms living on the grain (image width = 75.3 μm), (e) & (f) regions with smooth surface morphology (image width ~ 75 μm).

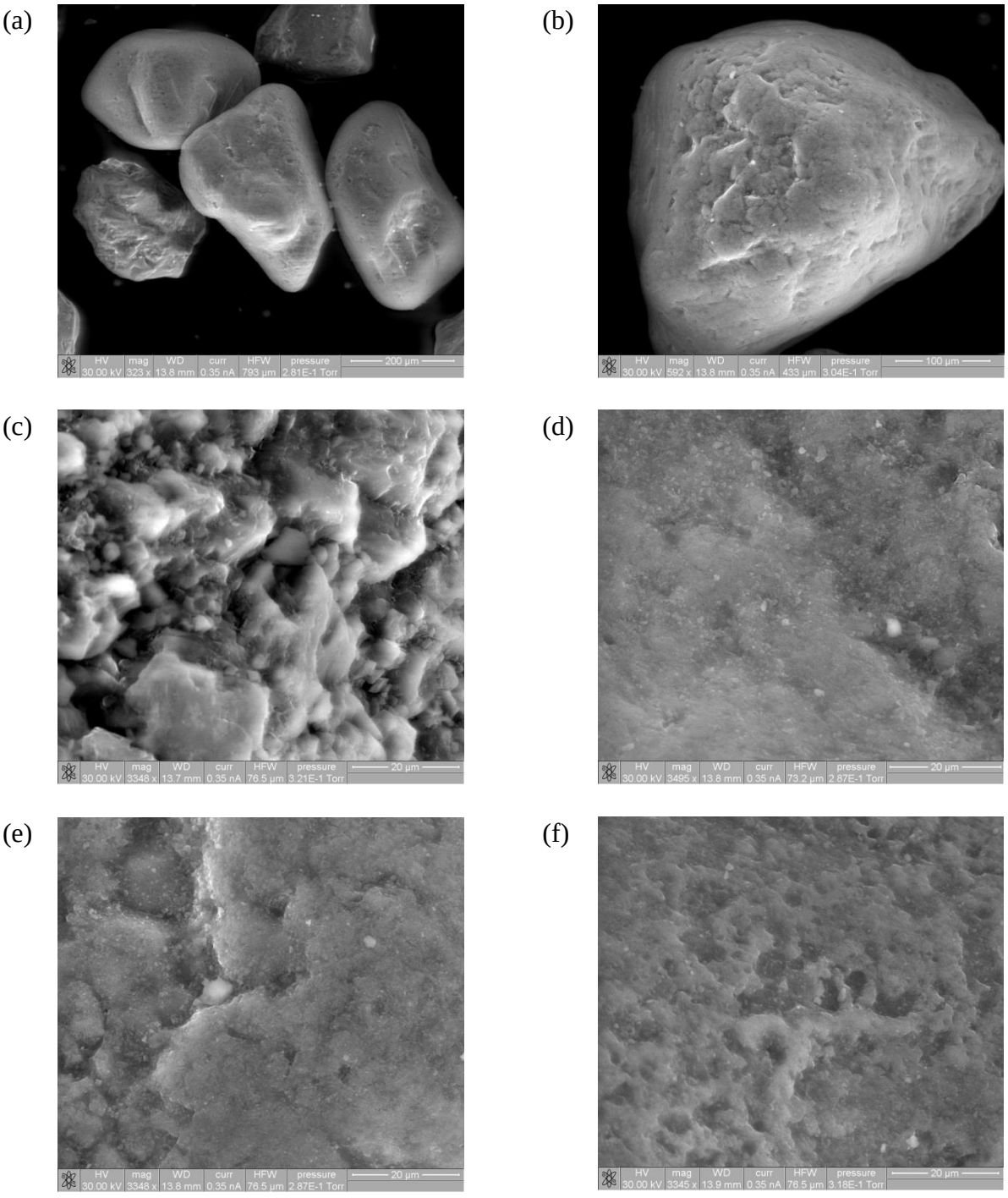

Figure 4.18. SEM images of Lake Michigan Dune sand, (a) typical grains (image width = 793 μm), (b) weathered grain displaying a smooth surface texture (image width = 433 μm), (c), (d), (e) & (f) surface asperities (image width ~ 75 μm).

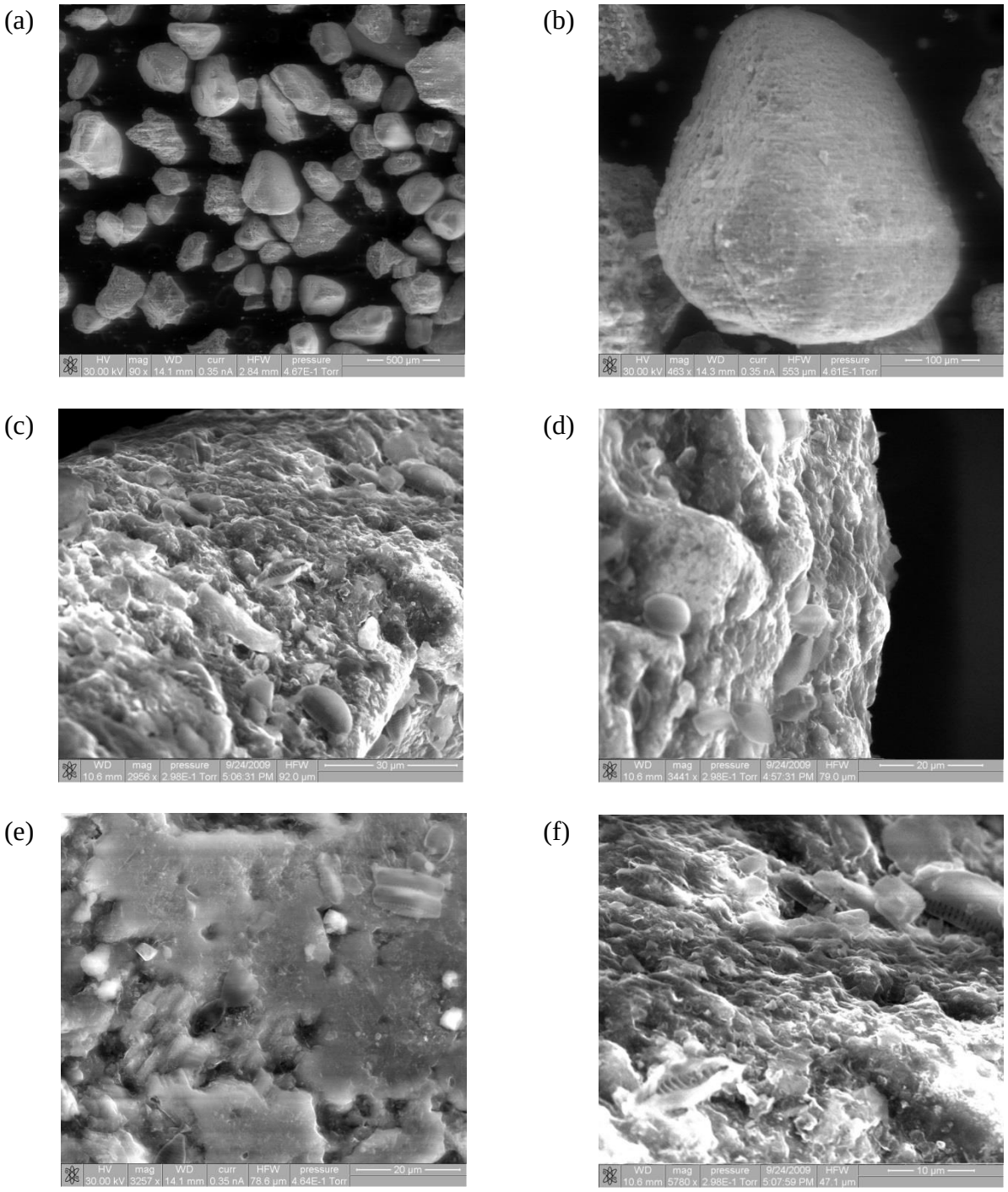

Figure 4.19. SEM images of Huron River sand, (a) sand grains of various sizes and shapes (image width = 2.84 mm), (b) a typical sand grain (image width = 553 μm), (c), (d), (e) & (f) surface asperities and microorganisms on grain surfaces (image width = 92, 79, 78.6 and 47.1 μm).

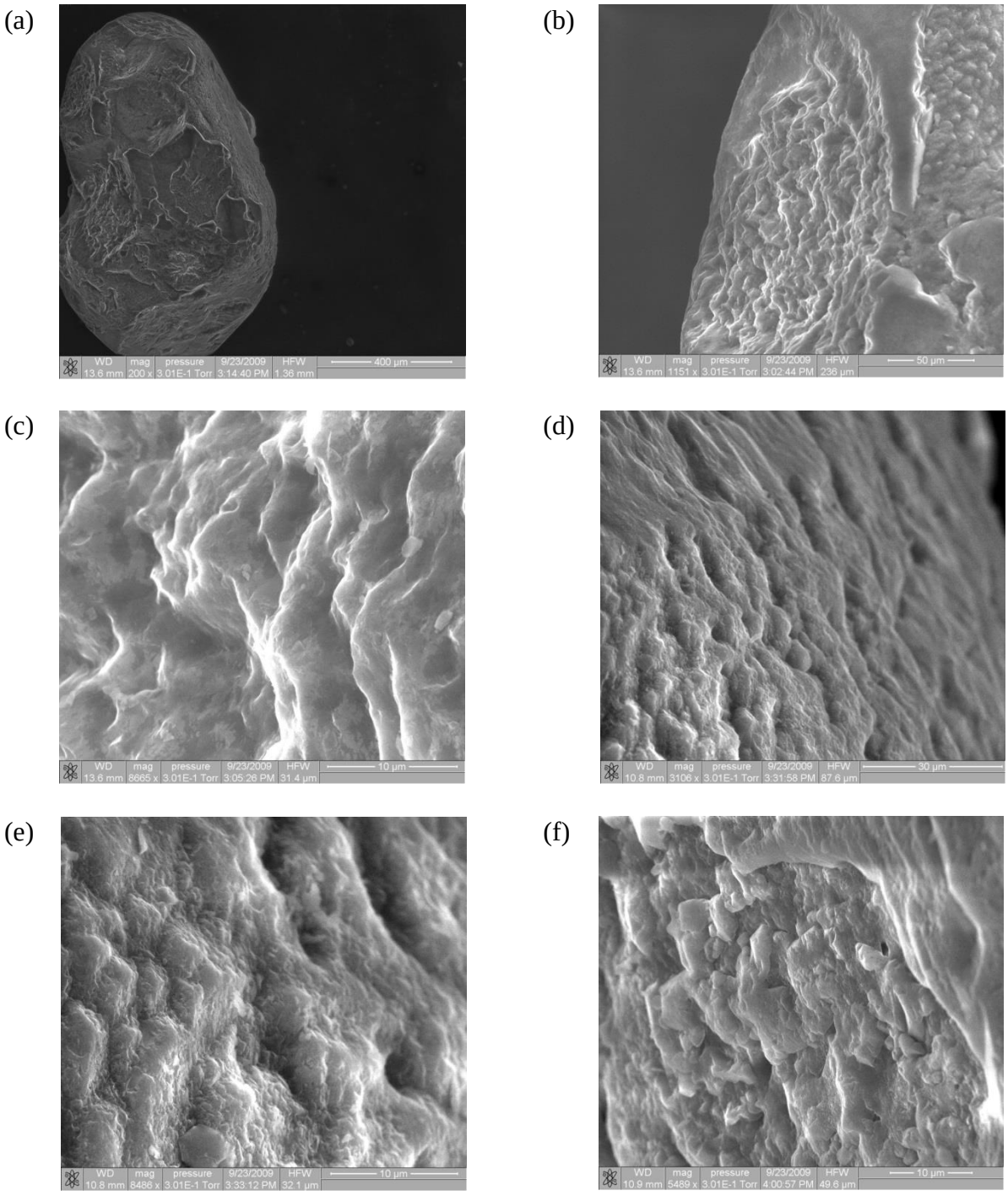

Figure 4.20. SEM images of Ottawa 20-30 sand, (a) sand grain with a fractured corner (image width = 1.36 mm), (b) close-up view of the fractured surface (image width = 236 μm), (c) close-up view of the asperities present on the fractured surface (image width = 31.4 μm), (d), (e) & (f) close-up views of surface asperities on the sand grains (image width = 87.6, 32.1, and 49.6 μm).

Among the grains from four different sources used in the analyses, Ottawa 20-30 sand has the largest size asperities and appears to be the roughest. On the other grains, due to weathering action of wind and water, grain surfaces appear smoother and this can be seen in Figs. 4.17 to 4.20. Even though other grains used in this study have a smoother appearance when compared to Ottawa 20-30 sand grains at the same magnifications, they could have a rich surface texture at smaller magnifications. This was discussed in section 4.2.2. Microorganisms, most likely diatoms, were seen in surface groves on both Huron River and Empire beach sand. Diatoms are unicellular photosynthetic algae whose cell walls are made of silica. These organisms have the ability to take dissolved silica (silicilic acid or $Si(OH)_4$) from its environment, transport it into their cells, and repolymerize silica to form their cell walls during the process of photosynthesis – a process called bio-silicification. Qualitative examination of many sand grain surfaces revealed a greater number of diatoms (algea or phytoplankton, typically unicellular) on Huron River sand grains than on the Lake Michigan Empire Beach sand. Lake Michigan Dune sand did not show presence of any microorganisms.

4.3 Mechanical properties of sand grains (Nanoindentation)

In Sections 4.1 and 4.2, the sizes and shapes of surface asperities were discussed. When these asperities are subjected to loads, they first deform elastically until yield point is reached in some regions, after which plastic deformation and/or brittle failure is observed. Nanoindentation tests are performed on sand grains to measure the deformation modulus and hardness of the grain mineral, as these parameters affect the performance of grain asperities. It should be noted that while the modulus (Young's modulus) is an elastic model parameter, hardness is not. The hardness property value depends on the measurement procedure. In this thesis the nano-indentation hardness is computed. Creep tests during the indentation process are also carried out to understand the creep behavior of the grain mineral.

Nano-indentation is a well-accepted technique for measuring local material response, and it provides load-displacement curves at the micro and nano scales (Pethica et al. 1983, Pharr 1998, Bushan 1999). Figure 4.21 shows a typical load-displacement curve. By using a dynamic Nanoindentation technique called the Continuous Stiffness Measurement (CSM) method, it is possible to measure the modulus and hardness of the sample as a function of penetration depth (Oliver and Pethica 1989, Pethica and Oliver 1989). In Nanoindentation, an indenter (the

Berkovich indenter is used here) with a known geometry is indented onto a sample while continuously measuring the penetration depth and applied load. The load is controlled by changing direct current (DC), which controls the position of the indentation head. Indentation tests were performed using the "Nanoinstruments Nanoindenter" device. The load measurement system had a resolution of 75 nN. The displacement sensing system is made up of a three plate capacitive displacement sensor which has a resolution of 0.1 nm. Obtaining stresses and strains from a Nanoindetation test is not straight forward as contact area under the indenter changes with penetration depth. In the indentation test, a load-displacement curve is first obtained. By measuring the slope of the unloading curve on the load-displacement plot, stiffness of the material can be obtained. This stiffness is then used to calculate the Young's modulus of the material. There are two assumptions in using the Nanoindentation procedure to obtain the sample stiffness and hardness:

- initial deformation upon unloading is purely elastic, and
- the contact between the indenter and sample can be modeled using an analytical model for contact between a rigid indenter and a homogenous isotropic half space.

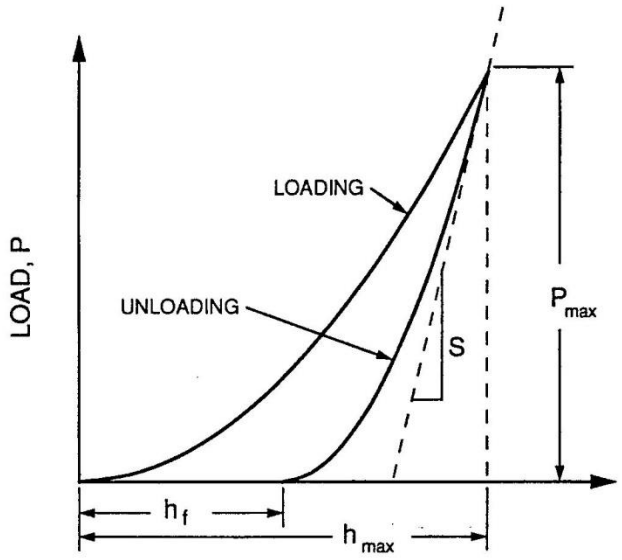

Figure 4.21. Load vs. displacement curve during a nanoindentation test (from Oliver and Pharr, 1992).

Oliver and Pharr (1992), used the results of Sneddon (1948 & 1965) to calculate the modulus of the sample (E_s) and sample Hardness (H) from Equations (4.7), (4.8) and (4.9).

$$S = \left(\frac{dP}{dh}\right)_{@P_{\max}} = \frac{2}{\sqrt{\pi}} E_r \sqrt{A_c} \tag{4.7}$$

$$\frac{1}{E_r} = \frac{(1-\nu_s^{\,2})}{E_s} + \frac{(1-\nu_i^{\,2})}{E_i} \tag{4.8}$$

$$H = \frac{P_{\max}}{A_c} \tag{4.9}$$

where, $S = (dP/dh)_{@P_{\max}}$ is the experimentally measured slope of the initial unloading segment of the load-displacement curve (Fig. 4.21),

A_c is the projected area of the contact (a function of contact depth h_c),

E_r is the reduced modulus considering the modulus of the indenter (E_i) and specimen (E_s),

ν_i and ν_s are the Poisson's ratio values of the indenter and specimen,

H is the hardness of the sample defined as the load divided by the projected contact area,

P_{max} is the peak indentation load.

The contact depth h_c (Fig. 4.22) and the projected depth A_c can be calculated (Oliver and Pharr 1992) from Equations (4.10) and (4.11).

$$h_c = h_{\max} - \varepsilon \frac{P_{\max}}{S} \tag{4.10}$$

$$A_c = F(h_c) = C_0 h_c^2 + C_1 h_c + C_2 h_c^{1/2} + \ldots + C_8 h_c^{1/128} \tag{4.11}$$

where, ε and C_0 to C_8 are geometric constants which vary with the geometry of the indenter. For a Berkovich indenter, $\varepsilon = 0.72$, C_0 = 25.5 and terms C_1 to C_8 describe deviations of the tip due to blunting. By performing a calibration test with the indenter on a standard material whose material constants are known (typically fused quartz), terms C_1 to C_8 are estimated.

The indenter used for Nanoindentation tests should have a high elastic modulus, no plastic deformation, low friction ("smooth" surface), and a well-defined geometry (Bhushan 1999). For this reason, a diamond indenter is used for the indentation tests. To get a sharp tip with a well-defined geometry, a Berkovich tip, which is a thee-sided pyramidal diamond ($E_i = 1440$ GPa and $\nu_i = 0.17$) is used (Fig. 4.23).

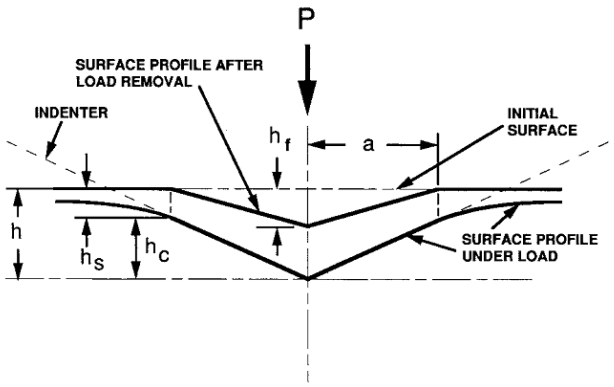

Figure 4.22. A typical indentation test (from Oliver and Pharr, 1992).

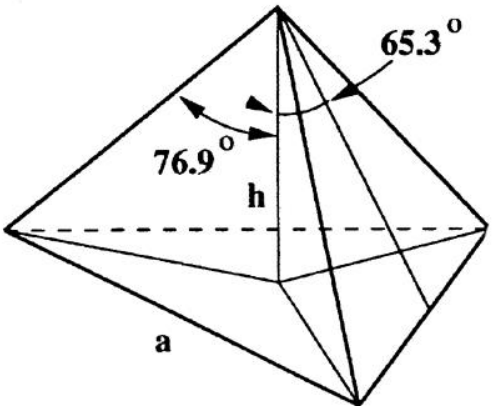

Figure 4.23. Schematic of a Berkovich Indenter (a = 7.407 h).

In the CSM method of nanoindentation, a very small alternate current (AC) at known frequency (69 Hz) is applied on top of the direct current controlling the nominal load on the indenter, causing the indenter to vibrate at a frequency which is a function of the sample stiffness. The ratio of the imposed AC signal to the indenter vibration allows the stiffness at a particular depth to be calculated (Pethica and Oliver 1989). The hardness at a particular depth can also be

calculated in the same way using equation (4.9) during the indentation process. The CSM method of nanoindentation is used in the thesis.

Nanoindentation requires the sample to be flat and smooth, absent of any surface asperities. This however presents a problem as sand grains are neither flat nor smooth. For this reason, sand grains were ground down and polished prior to indentation tests. The sand used for the indentation tests was Ottawa 20-30 sand. Sand grains were placed on a sample holder and embedded in an epoxy matrix. After the epoxy had cured, the grains were ground on a Silicon Carbide grinding base rotating at 250 rpm to remove the epoxy covering the grains. The grain sample was then ground and polished using alumina abrasive powder followed by 0.25 μm Buehler Diamond suspension in water slurry for 30 minutes to provide a flat mineral surface for nano-indentation tests. Fig. 4.24 shows the grain surfaces following the polishing operation. A total of 33 load controlled indentation tests on 11 different sand grains (3 indentation tests per grain) were performed. Each of the indentation tests on a single grain is at a distance of 15 μm from the previous indentation. Table 4.3 summarizes the 33 indentation tests. The load displacement plots for all the tests are shown in Fig 4.25 and 4.26.

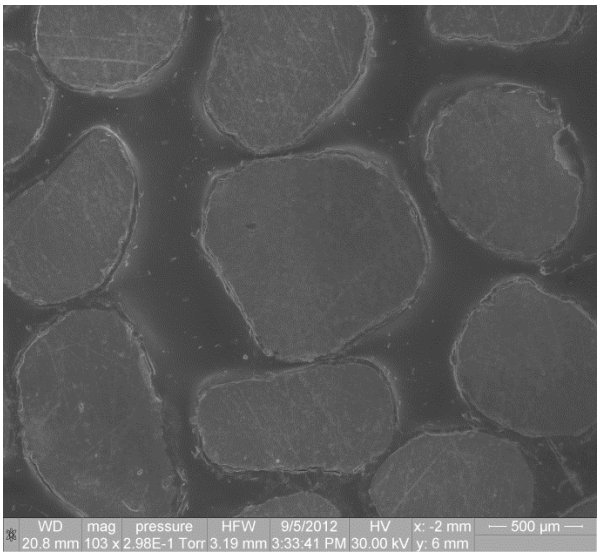

Figure 4.24. Polished sand grains embedded in an epoxy matrix.

Thirty indentation tests were performed at a loading rate of 1.5 mN/sec and three indentation tests were performed at a loading rate of 1 mN/sec. In general, the three indentation tests performed on a single sand grain gave consistent load-displacement results with fairly small

scatter. Comparing the load displacement curves for different grains however, shows a larger scatter in the results. Although in tests #1 to 30, a peak load of 300 mN was desired, the Nanoindentation device applied nearly 310 mN in all of the experiments.

During the first test on grain #1, after keeping the load constant at 310 mN for 23 min, the Nanoindentation instrument stopped recording data. Hence data for the unloading segment of this test is not available. The data for the other two indentation tests on grain #1 was recorded in its entirety (Fig. 4.25(a)). In tests 4 to 30, after loading the grain to 310 mN, the load was held constant for 1 min, after which it was unloaded to 31 mN and held constant for 50 seconds, and finally unloaded to 0 N. Indentation tests on grain #5 (Fig. 4.25(e)) shows two instances in two tests where a discontinuity in the data in the form of a sudden slip (at loads of about 260 mN and 100 mN) or "pop-in" in the loading curve is observed. A similar pop-in mechanism is also observed in a test on grain #9 (Fig. 4.25(i) at 100 mN). The exact reason for this pop-in is not known, and it is an active research area in the material science community. It is thought that this may be due to the inception of plasticity in the material response (Tromas et al. 1999). Since the pop-ins are observed in only 3 out of 33 tests, onset of plasticity is, probably, not the reason. Other possible reasons for this are near-surface dislocation nucleation, crack formation in the material, phase transformation, encountering surface roughness and surface defects (Schuh 2006). Focused Ion Beam (FIB) milling of sand grains showed the presence of voids in the bulk of sand grains at depths of about 10 μm. FIB microscopy works similar to a SEM except that an ion beam is used instead of an electron beam. As the ion has a large momentum when it hits the sample, it can sputter the material from the sample. FIB is normally used to prepare thin sections of materials for Transmission Electron Microscopic studies of the material or to etch patterns on substrates. In the present case, FIB is used to make a depression or cut in the sand grain to observe cross sectional features in the bulk of the grain. Figure. 4.27 shows SEM images of the voids after FIB milling. It could be possible that during some of the nano-indentation tests, the indenter could have encountered similar voids in the core of the grain causing a sudden increase in penetration or a "pop-in" in the load-displacement plot.

Table 4.3. Summary of nanoindentation experiments.

Test No.	Grain No.	Loading Pattern	Figure No.
1	1	Load to 310 mN; hold 310 mN for 25 min; unload to 30 mN; hold 30 mN for 50 sec; unload to 0 N	4.25(a)
2 & 3	1	Load to 310 mN; hold 310 mN for 1 min; unload to 30 mN; Hold 30 mN for 50 sec; unload to 0 N	4.25(a)
4 to 30	2 to 10	Load to 310 mN; hold 310 mN for 1 min; unload to 30 mN; hold 30 mN for 50 sec; unload to 0 N	4.25(b) to (j)
31 to 33	11	Load to 100 mN; hold 100 mN for 1 min; load to 200 mN; hold 200 mN for 1 min; load to 300 mN; hold 300 mN for 1 min; unload to 0 N	4.25(k)

(a)

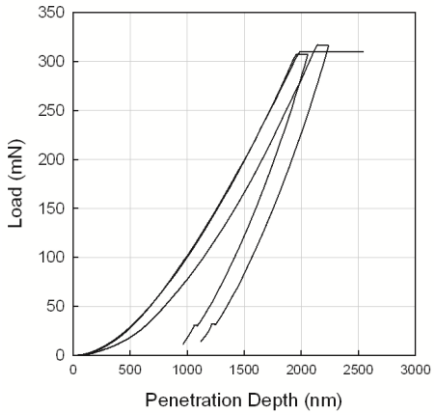

(b)

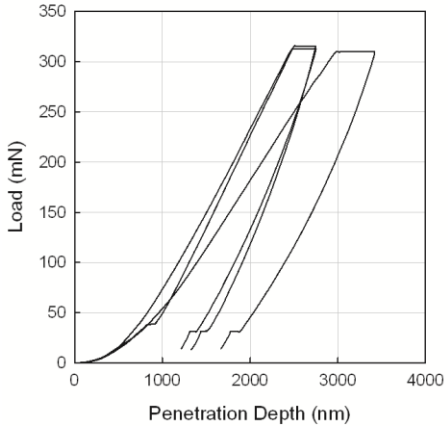

(c)

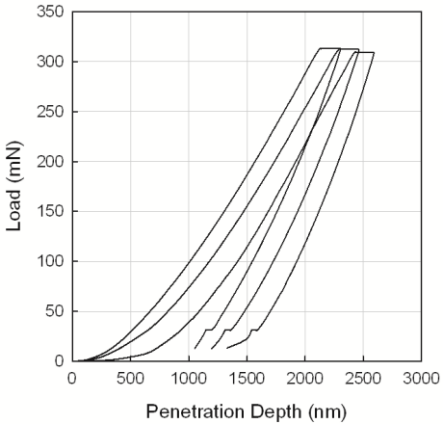

(d)

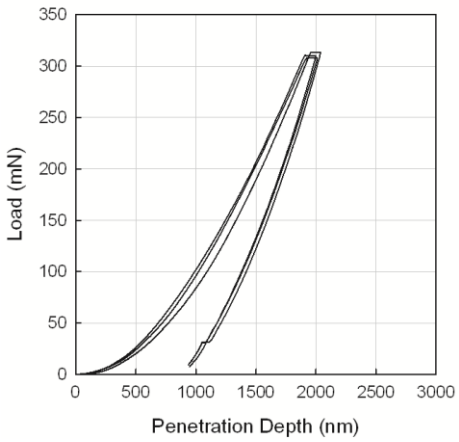

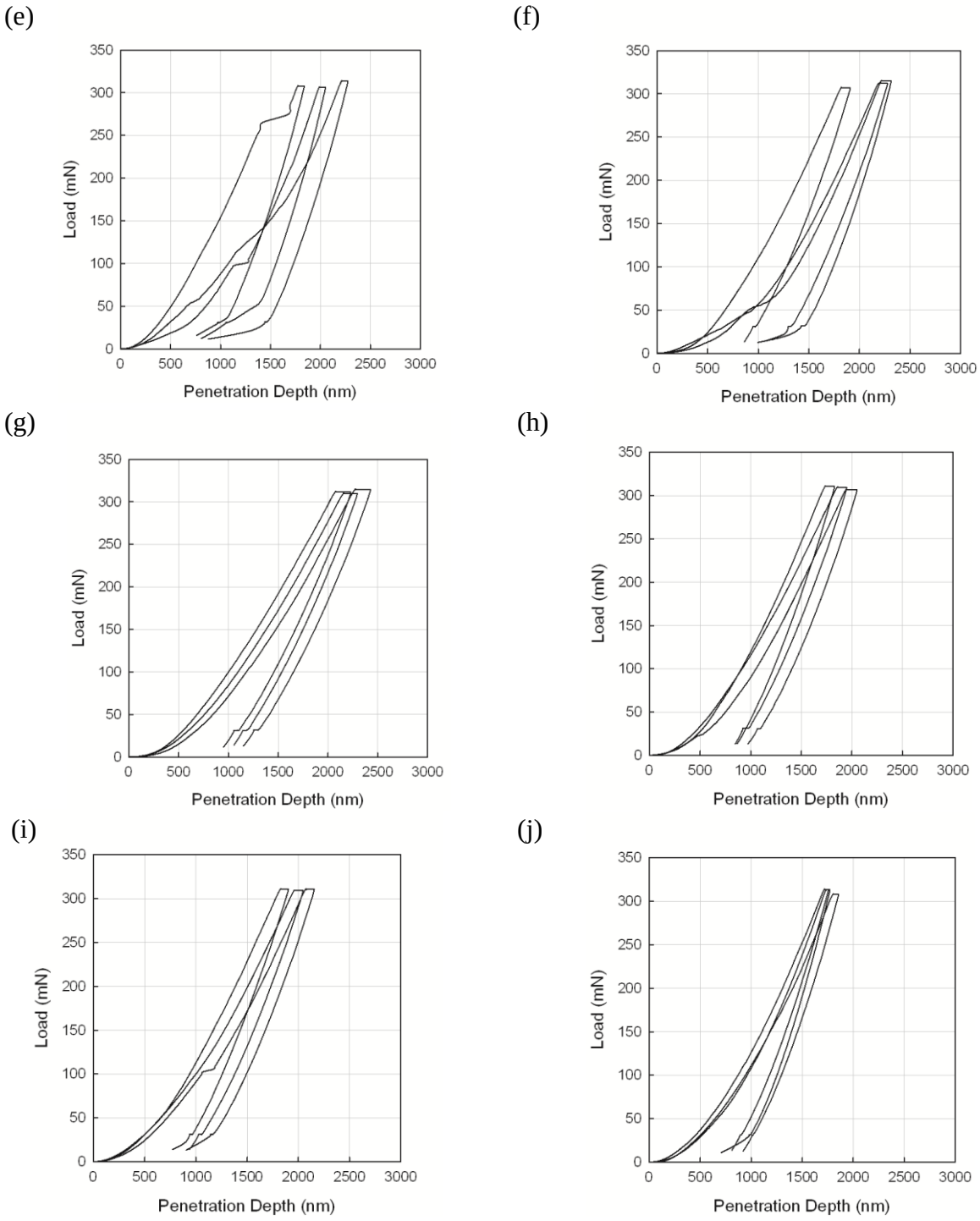

Figure 4.25. Nanoindentation load-displacement plots on Ottawa 20-30 sand (loading/ unloading rate = 1.5 mN/sec), (a) results from 3 tests on grain #1; load is kept constant at 310 mN for 1 min in two tests and 25 min in the third one (the unloading part is not available for this test), (b) to (d) results from tests on grain #2 to 4; load is kept constant at 310 mN for 1 min, (e) results from grain #5 showing pop-in mechanism at 100 mN and 260 mN in two tests; load is kept constant at 310 mN for 1 min, (f) to (h) result from tests on grain #6 to 8, (i) results from grain #9 showing

pop-in mechanism at 100 mN in one of the tests; load is kept constant at 310 mN for 1 min, and (j) results from grain #10; load is kept constant at 310 mN for 1 min.

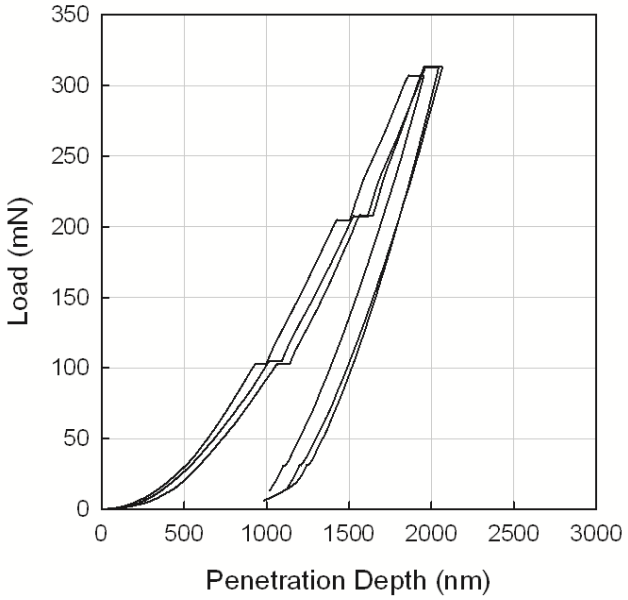

Figure 4.26. Load-displacement plots for three tests on Grain #11; loading rate is 1 mN/sec (the load is kept constant for 5 min at 100, 200, and 300 mN).

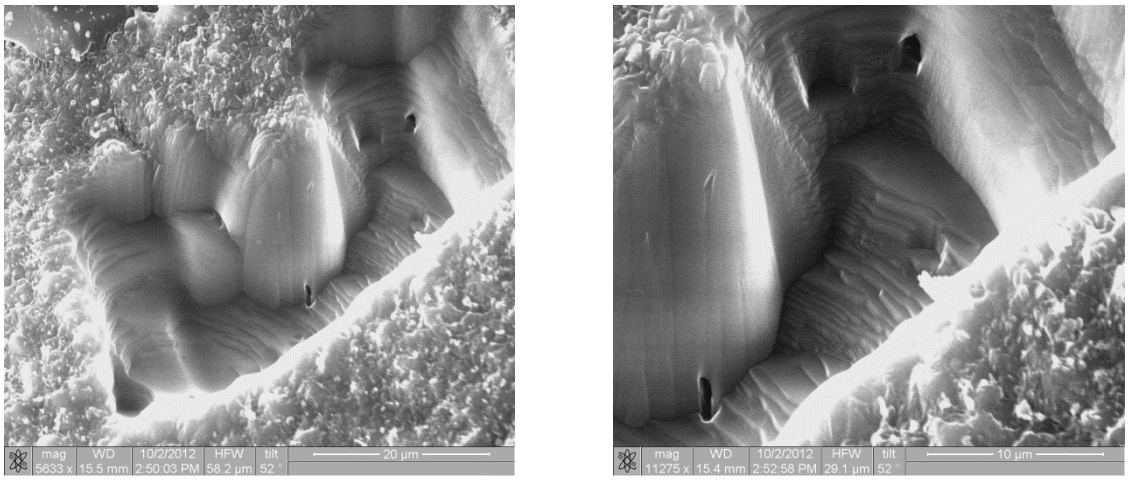

Figure 4.27. SEM image of FIB sputtering of Ottawa 20-30 sand grain, (a) the entire sputtered area showing the presence of two voids, and (b) a magnified image of the voids.

During the 30 indentation tests (Fig. 4.25) the loading rate was 1.5 mN/sec, and the load was kept constant at 310 mN for 25 minutes in one test and for 1 min in all other tests. Time-

dependent deformation in sand grains occurred during this time and it is manifested as a change in indentation depth under a constant applied load. Figure 4.28 shows the creep data for the 30 tests in Fig. 4.25.

(a)

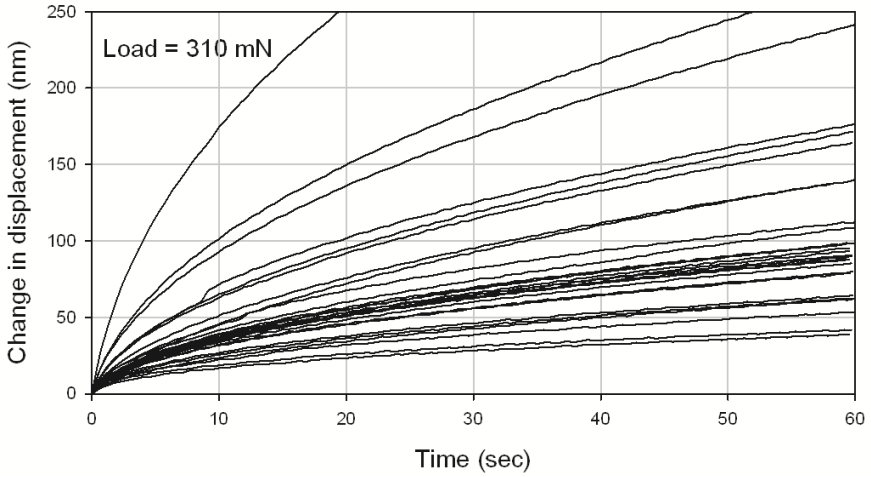

(b)

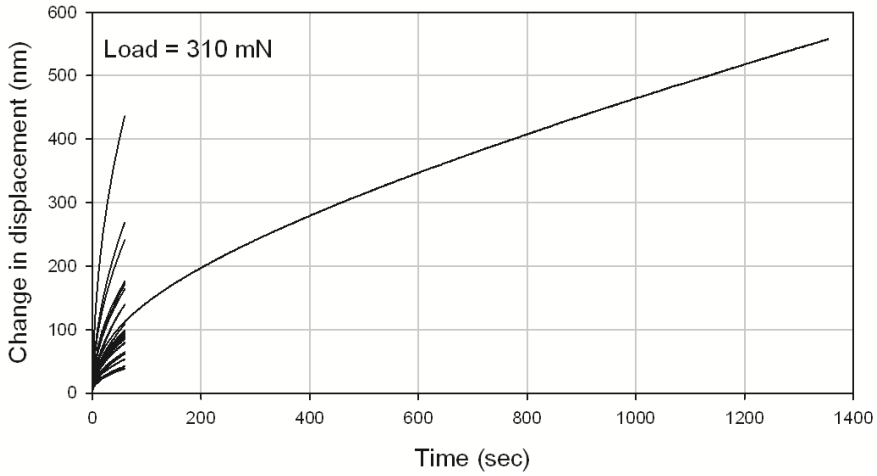

Figure 4.28. Creep data obtained from 30 different indentation tests on 10 sand grains, (a) creep curves at a load of 310 mN showing substantial scatter in results, and (b) creep curve for the test on grain #1 performed at 310 mN for 23 min; data from other 29 tests is also shown.

The creep curves suggest that sand grain mineral (quartz) is viscoelastic. A lot of variability in creep test results is observed even when all the indentation tests are performed at a constant force of 310 mN. However, creep tests performed on a single grain showed consistent results with little scatter in results (Fig. 4.29). This shows that even though sand from the same source is used in all tests, different grains have widely different creep properties. Li and Warren (1993) proposed that creep is due to the high indentation stress fields in the specimen material below an

indenter, leading to a chemical potential gradient that leads to a thermally activated diffusional flux of atoms that flow from beneath the indenter to the specimen surface, even under an elastic contact. Based on this hypothesis of creep, the wide variability in creep results could be explained due to the presence discontinuities in the quartz atomic lattice structure or the presence of flaws/voids in the sand grain as shown in Fig. 4.27.

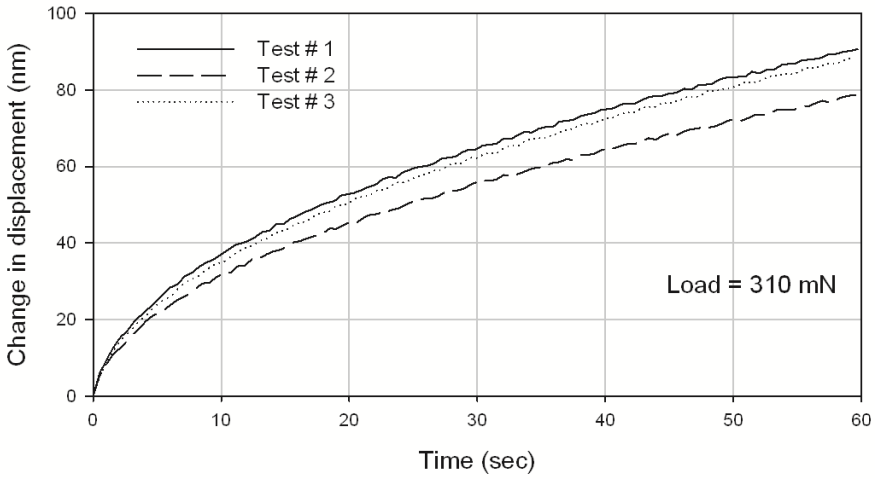

Figure 4.29. Creep curves from three tests on grain #4 showing little variability in data.

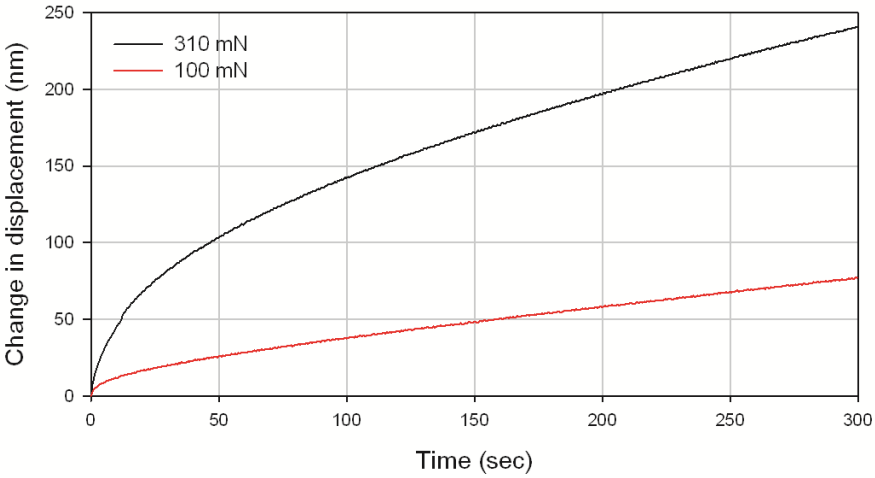

Figure 4.30. Creep curves at different loads performed on grain #1.

Figure 4.30 shows a comparison of creep curves at different loads performed on grain #1. The results show that the magnitude of load influences the creep curves. The creep behavior at given constant load was found to be sensitive to the rate at which this load was reached. The faster the loading rate (prior to creep), the higher is the creep rate once the load is kept constant (Fig. 4.31).

However, since these tests were performed on different grains (grain #1 and #11), the results from the loading rate tests could also be influenced by variability of material properties from one sand grain to the other.

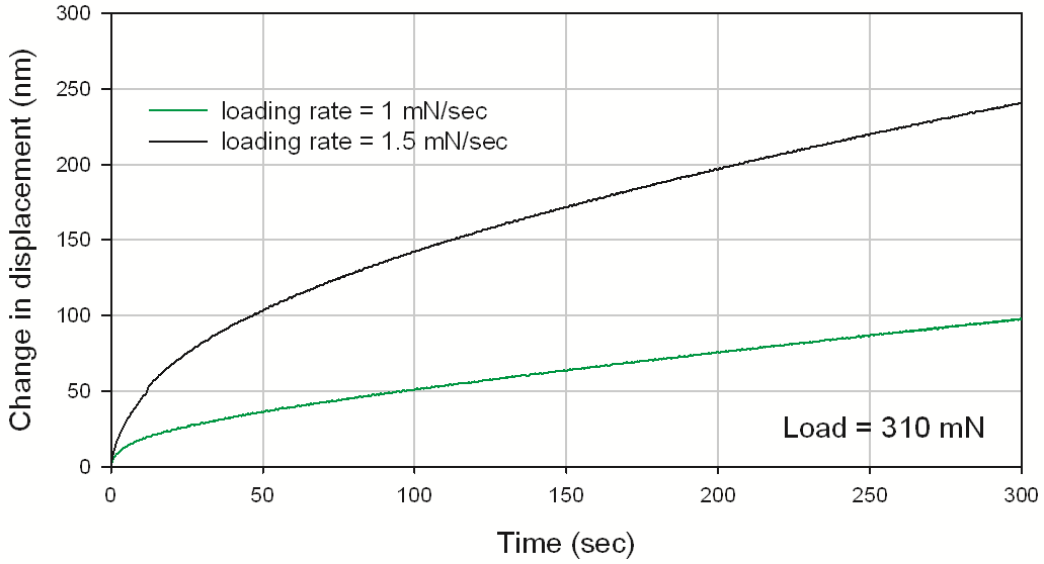

Figure 4.31. Influence of the indentation loading rate prior to creep on the creep rate; tests performed on grain #1 (1.5 mN/sec) and grain 11 (1 mN/sec).

Using Equations (4.7), (4.8), (4.10) and (4.11), the Young's Modulus E_s and Hardness H of the grains, as a function of the penetration depth was calculated. Figure 4.32 shows the results from all 33 tests. Figure 4.32 shows a wide scatter in results at low indentation depths (< 400 nm). At greater indentation depths (> 400 nm), the scatter is fairly consistent throughout the rest of the depth. The surface roughness of the polished grain surface might be responsible for this. Since the polishing compound used had particles that were 250 nm, we can expect surface roughness of grain surfaces to be of the same order. This suggests that the data for indentation depths less than 250 nm in Fig. 4.32 is not representative of the true material properties of the quartz mineral. The hardness of the grains as a function of penetration depth is shown in Fig. 4.33.

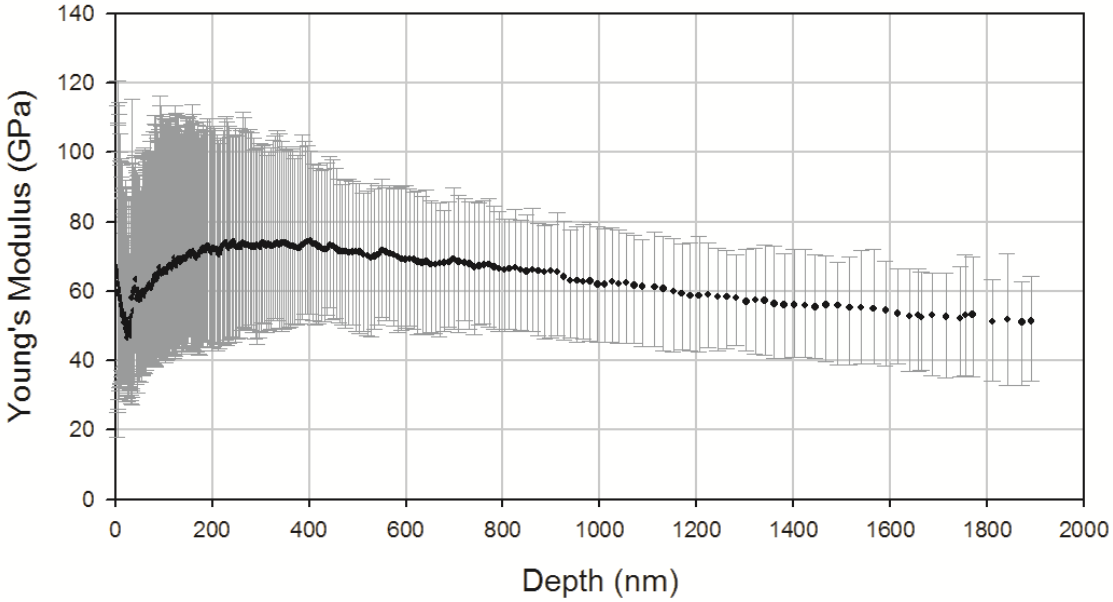

Figure 4.32. Young's Modulus of sand grains as a function of depth obtained from 33 indentation tests.

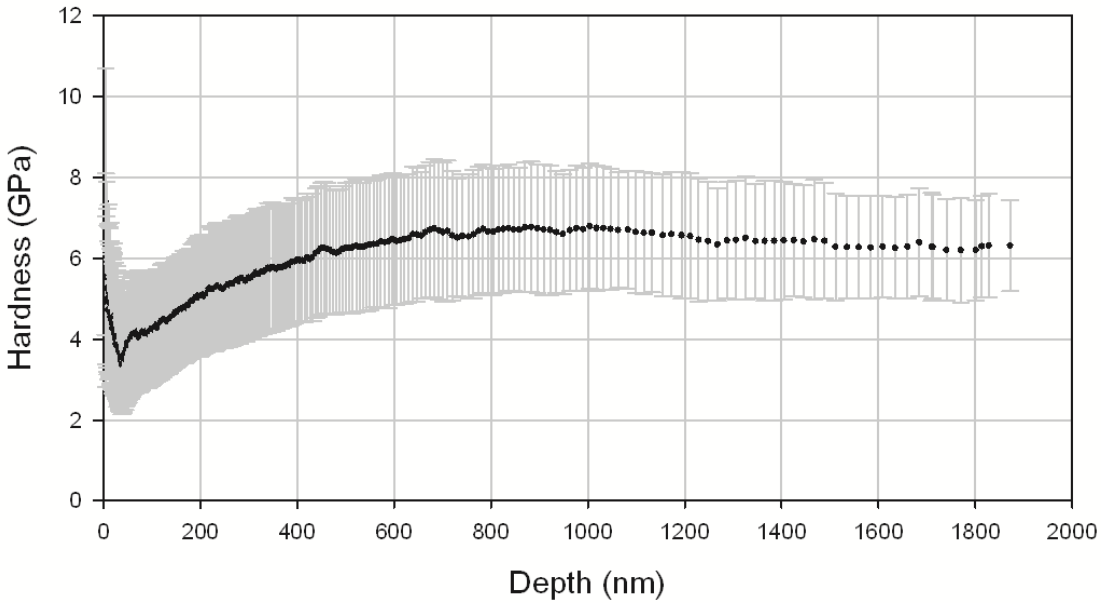

Figure 4.33. Indentation hardness of sand grains as a function of penetration depth obtained from 33 tests on 11 sand grains.

The Young's modulus and hardness values obtained in this thesis are in line with results obtained by other researchers. Daphalapurkar et al. (2011) performed Nanoindentation tests on Stillwater Lake sand in Oklahoma in an attempt to obtain the mechanical properties of these grains. After

performing many indentation tests on a number of grains (500 indentations on 250 sand grains), the researchers obtained a mean Young's modulus of 91.1 GPa, Hardness of 10.7 GPa and a fracture toughness of 1.77 MPa-$m^{0.5}$. In this thesis the fracture toughness of Ottawa 20-30 sand grains is not obtained as the Nanoindentation device available did not have a diamond cube tip with which the fracture toughness is obtained. However, as the Young's modulus and hardness value of Ottawa 20-30 sand is in line with the values obtained by Daphalapurkar et al. (2011), we could assume that the fracture toughness of Ottawa 20-30 sand would be close to 1.77 MPa-$m^{0.5}$. Fracture toughness is the ability of a material with a crack to resist fracture. The low fracture toughness value for sand grains suggests that the grains are very susceptible to cracks and undergo brittle fracture rather than a ductile failure. For comparison, the fracture toughness of steel is 50 MPa-$m^{0.5}$ and that of concrete is 0.2 ~ 1.4 MPa-$m^{0.5}$.

The results from nanoindentation tests present a complicated picture of sand grain material properties. While mechanical properties, such as elastic modulus and hardness vary from grain to grain, within a single grain the properties are consistent. The low fracture toughness of sand grains suggests that the grains subjected to load tend to dissipate energy by cracking or fracturing, rather than undergo plastic deformation. Acoustic emission from such events can be captured with data acquisition system capable of recording large amounts of data in the MHz to GHz range (McLaskey and Glaser, 2011).

4.4 Micro-scale tests

The behavior of a contact between two grains is central to the proposed hypothesis of time effects in sand in this thesis. The variability in sand grain mineral (quartz) mechanical properties discussed in section 4.3, combined with the complexity of the surface morphology discussed in section 4.2, presents challenges in micro-scale testing of grain surfaces. This section discuses tests performed on grain surfaces using two different devices developed by the author. The first test was an attempt to demonstrate qualitatively the changes to the surface morphology after contact loading. This test is performed to understand if the asperities on grain surfaces are prone to plastic deformation or brittle failure. In the second type of test, two grains are loaded with a constant force and the relative displacement of the grains over time is continuously monitored. If the grain asperities exhibit static fatigue, then time-dependent displacement of the grains should be observed.

4.4.1 Three Grain Tests

These tests were performed to qualitatively assess the damage, if any, on a sand grain surface when subjected to constant load with different durations. Tests were performed on dry sand grains as well as sand grains in an acidic environment. In the dry test, three Ottawa 20-30 sand grains were glued to a SEM sample stub using a colloidal silver liquid with good adhesion properties, to form three corners of an equilateral triangle (see schematic in Fig. 4.34). The colloidal silver serves two functions: (1) it keeps the sand particles glued firmly to the stub, and (2) it behaves as a conductor and it disperses accumulated charge on the specimen, giving a better SEM image. After the surface morphology of the grains was recorded using SEM, a glass plate (mass of 15 g) was used to cover the grains, forming a platform for a load. The grains were then loaded with 2 N of dead weight (mass of 200 g), and they were scanned after 15 min, and after 1 week of loading. The forces on grains can be assumed equal due to symmetries in the equilateral triangle; however, only the vertical component can be found ($2.15/3 \approx 0.72$ N). The test was performed at room temperature (about 23°C). Figures 4.35 and 4.36 show SEM images of grain surfaces on two grains before and after the loading process. From these figures, crushing of the micro-morphological features on grain surfaces can be clearly seen in the figures. The failure of asperities seems to be brittle rather than plastic. SEM imaging did not reveal a clear region with damage on the third grain (could be at a different spatial scale). The damage to the asperity in Fig. 4.35 is especially revealing. In addition to asperity crushing, surface cracks can be identified (Fig. 4.35 (b)). Upon continuous loading, damage appears to propagate (Fig. 4.35(c)), along with formation of new surface cracks. On the second grain, the damage occurred on the kidney-bean shaped feature, Fig. 4.36(a), and little or no clear damage took place after the initial 15 min of loading.

In the wet test, 0.5 ml of 2N Hydrochloric acid was diluted with sufficient amount of distilled water to make a pH 5.5 solution. This solution was used in the wet three grain test. The entire test set up (Fig. 4.34) was immersed in the solution in such a way so that the solution was just touching the loading plate. The same mass of 200 g was used to load the grains. Grain surfaces were scanned before loading and then after 1 day and 5 days of continuous loading. For SEM imaging, the sample stub was dried at 50° C in an oven for five minutes to remove the water present on the grain surfaces, as it would interfere with the imaging process. SEM imaging revealed clear damage to grain surfaces on two of the three grains. Figures 4.37 & 4.38 show the

damaged areas on the grains. A close up SEM image of the grain surfaces after the test revealed several rod-shaped features, most likely bacteria on the grain surfaces (Fig. 4.39). EDX analysis of the grains after loading showed the presence of Silicon, Oxygen, Carbon and Fluorine.

The three-grain tests on dry and wet grains suggest that when sand grains are loaded with about 0.7 N, damage to the asperities in the form of brittle failure (crushing and fracture) occurs. The three-grain tests support the hypothesis of asperity crushing. However, weather asperity crushing is a time-delayed effect still needs to be investigated.

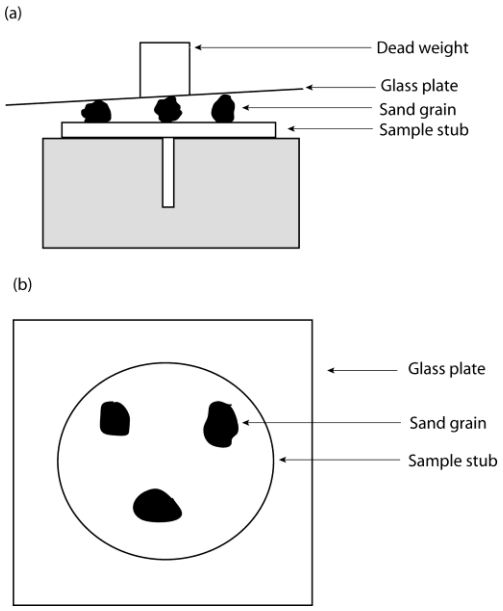

Figure 4.34. Schematic of the three-grain test: (a) side view, and (b) plan view.

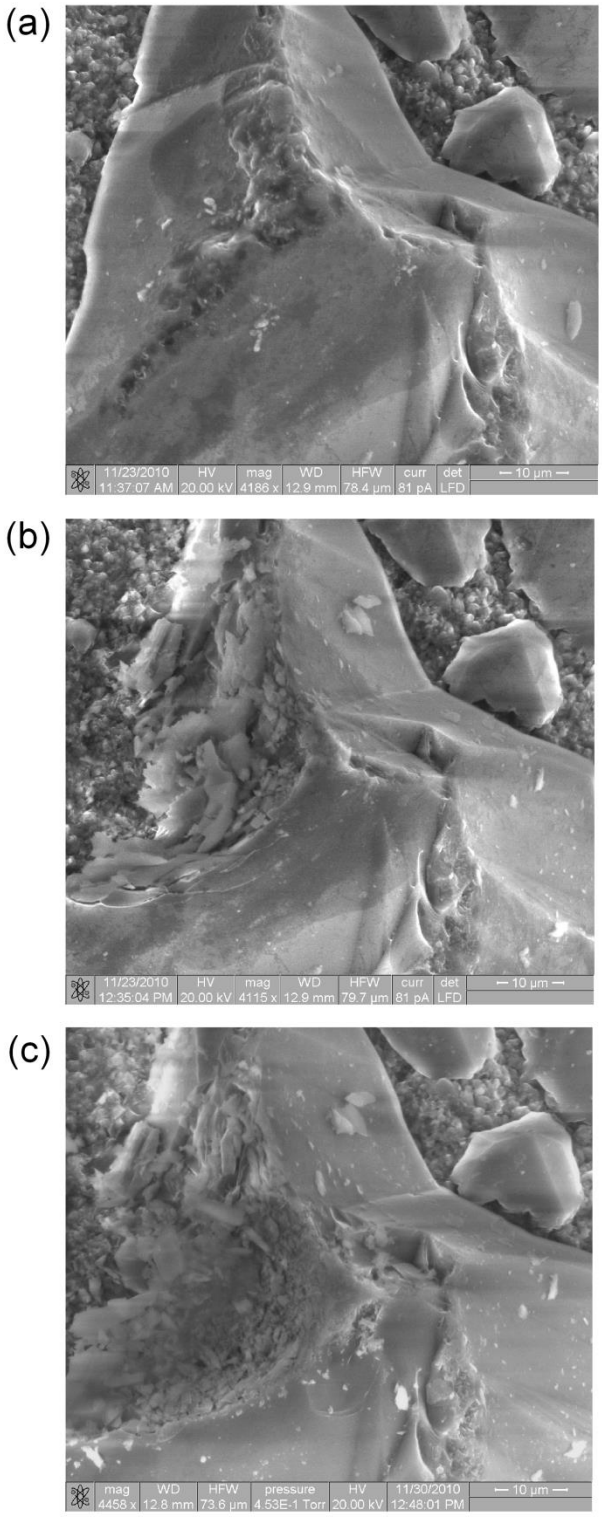

Figure 4.35. SEM image of a silica grain asperity on grain #1 (dry grain test): (a) before loading, (b) after 15 min of loading with a force of about 0.72 N, and (c) after 1 week of loading; total image width is about 80 µm.

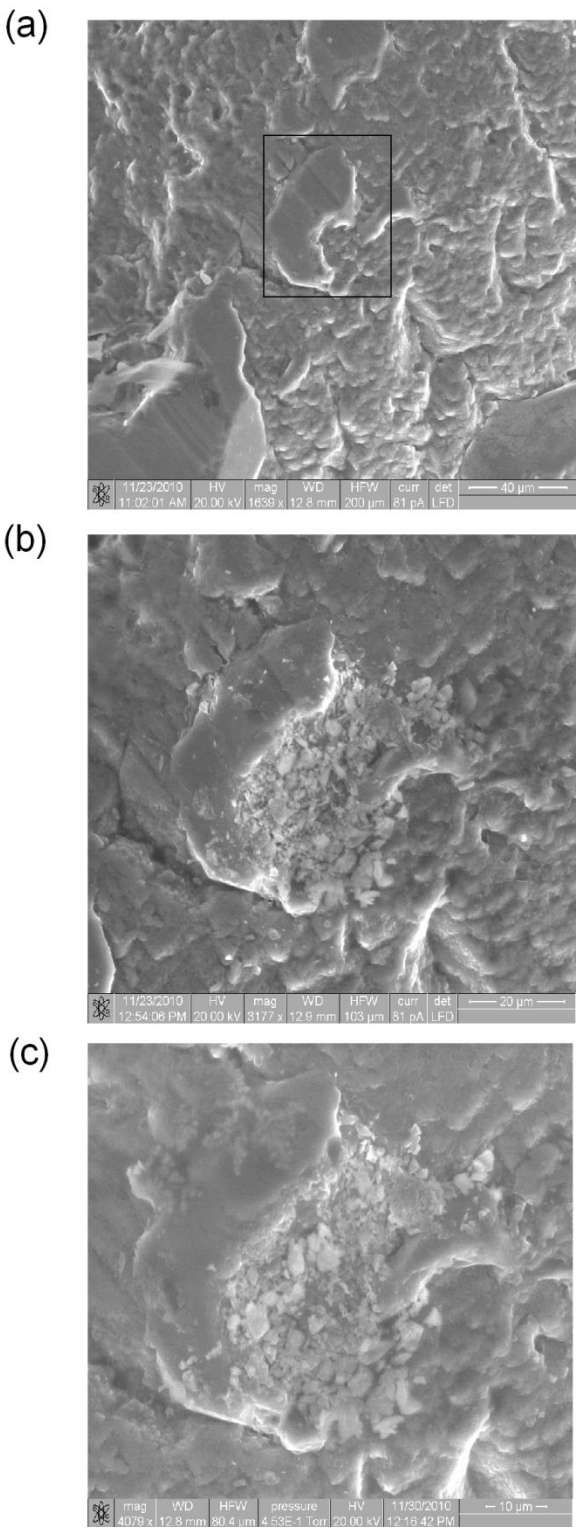

Figure 4.36. SEM image of a silica grain asperity on grain #2 (dry grain test): (a) before loading (total image width is 200 μm); the rectangular box shows the region of interest, (b) after 15 min of loading with a force of about 0.72 N (total image width is 103 μm), and (c) after 1 week of loading (total image width is about 80 μm).

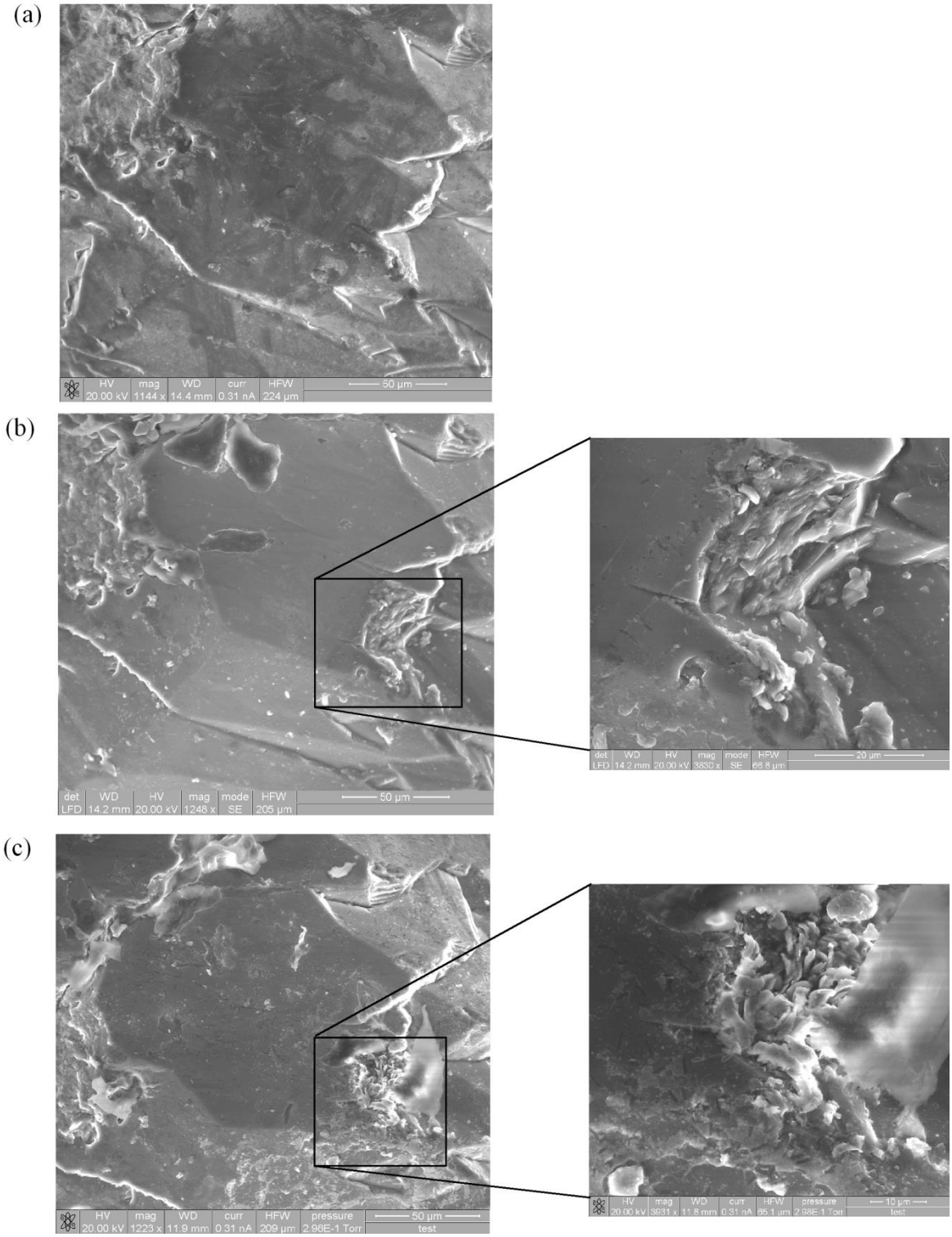

Figure 4.37. SEM image of a grain surface before and after loading with 0.7 N in an acidic (pH 5.5) environment (grain #1); boxed areas in each figure show the area of interest, (a) before loading (image width = 224 μm), (b) after 1day of loading (image width = 205 μm) and, (c) after 5 days of loading (image width = 230 μm).

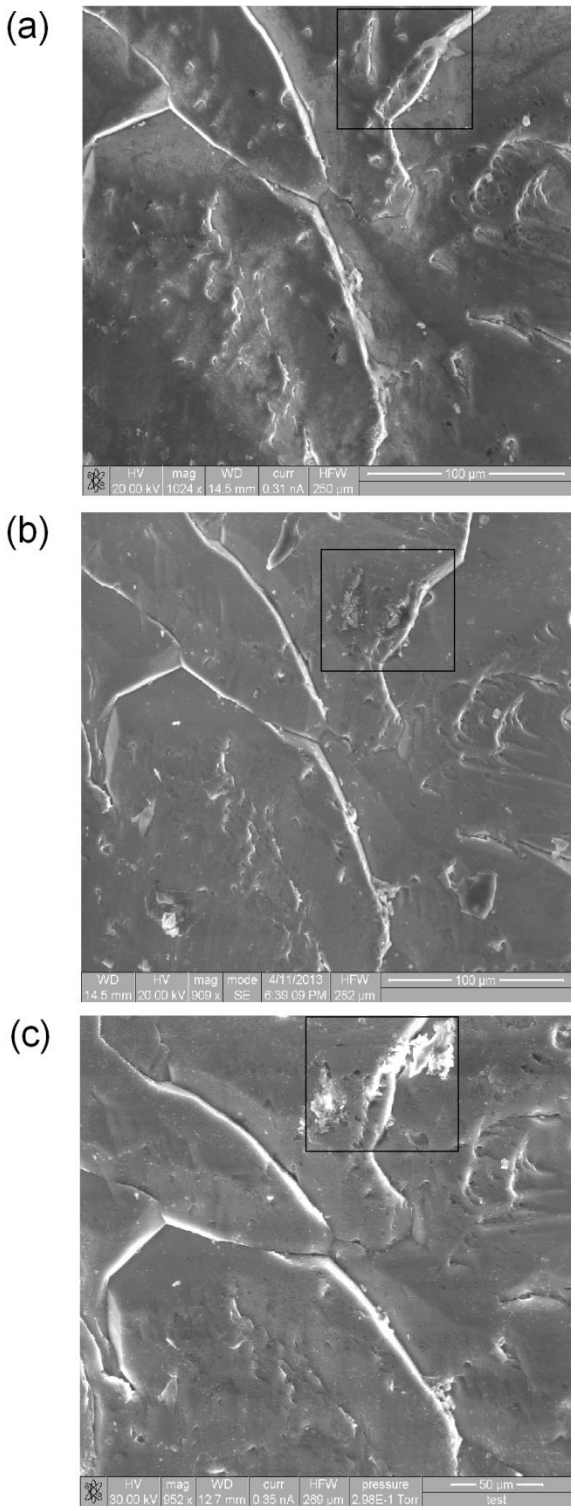

Figure 4.38. SEM image of a grain surface before and after loading with 0.7 N in an acidic (pH 5.5) environment (grain #2); boxed areas in each figure show the area of interest: (a) before loading (image width = 250 μm), (b) after 1day of loading (image width = 282 μm) and, (c) after 5 days of loading (image width = 269 μm).

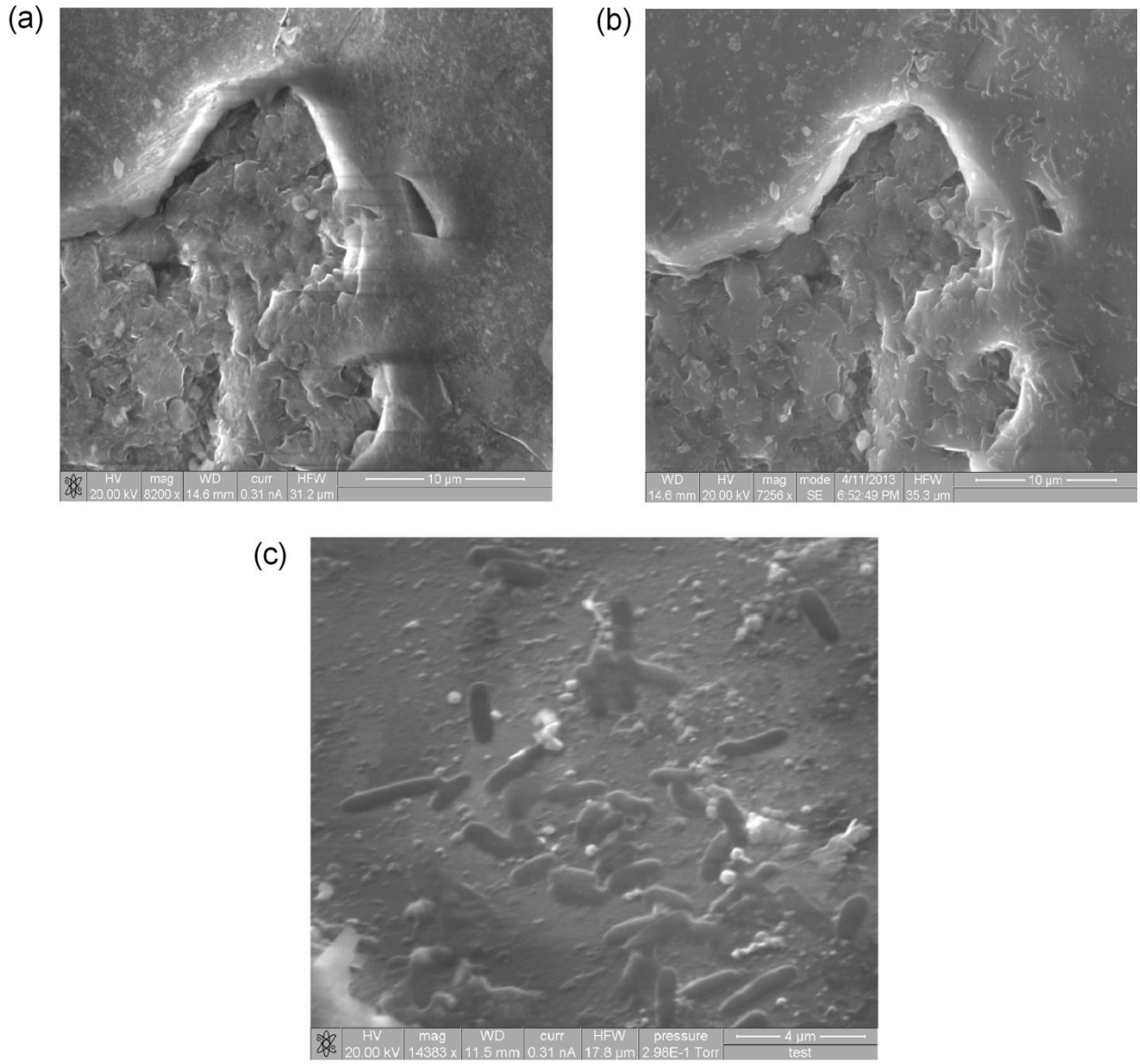

Figure 4.39. SEM images showing the presence of bacteria (most likely) on grain surfaces after the wet three grain test: (a) before the test (image width = 31.2 µm), (b) 1 day after submerging the grain in an acidic environment (pH 5.5) and applying 0.7 N load; observe the rod shaped features and, (c) a close up view of the rod shaped features (bacteria).

4.4.2 Grain-grain contact tests

The three grain tests support the hypothesis of asperity fracturing and crushing. The contact between the two surfaces in the three grain test is between the rough surface of the sand grain and the glass plate with a smooth surface (relative to the sand grain). However, a contact between two sand grains is different, with two rough surfaces in contact with one another, leading to a complex interaction between asperities on both surfaces and debris fragments. In

order to document the asperity fracturing (and crushing) in the three grain test, one needs to unload the grains. It is then difficult to determine whether fracturing occurs immediately after loading and reloading, or is a time-delayed process. Therefore, to confirm that the process of fracturing of asperities is time-dependent, and the fracturing occurs on surfaces of two grains in contact the same way as it does on a contact of one grain with a smoother surface (glass plate), grain-to-grain contact tests were performed. Cole and Peters (2007 & 2008) obtained load-deformation responses of two grains in contact in an attempt to obtain the contact stiffness of grains of different geologic origin. However, the contact behavior under sustained loading was not investigated by these researchers. Hence, grain-to-grain experiments are vital in understanding the long-term behavior of contacts under sustained load.

Two devices were constructed for performing grain-to-grain contact tests. Ottawa 20-30 sand grains (0.6 ~ 0.85 mm in diameter) were used in all tests. The first device, illustrated in Fig. 4.40, can be placed in a SEM chamber, and visual inspection of relative displacements of grains subjected to a constant force can be made after particular loading durations, giving discrete measurements in time. Vibrations caused due to user handling are unavoidable in this device, as a user must handle the device by placing it in a SEM every time an observation needs to be made. These vibrations affect the grain movements. To reduce the vibrations, and also to obtain quantitative data, a second device was constructed (shown later in Fig. 4.49). In the second device, two grains are brought in contact and the displacement of one grain over the other is continuously monitored. However, this device cannot be used in a SEM. Results from the two devices will assist in supporting or disproving the hypothesis of delayed fracture of grain asperities during sustained loading.

The first device, Fig. 4.40, is essentially a vice, capable of applying a force between two grains through a loading spring (Fig. 4.40(b)). The spring rests on a reaction plate, whose movement can be controlled by a loading screw (Fig. 4.40 (a)). The two sand grains were glued to a movable and a stationary base using multipurpose glue (Duco® cement), Fig. 4.40(b). Pelco® Colloidal Silver was applied on top of the glue to make it conductive and avoid charge accumulation during SEM imaging. During the application of glue and silver paint, care was taken to ensure that the grain surface remained clean, void of any foreign debris. The relative position of the grains was controlled by vertical and lateral movement screws located on the movable and stationary grain bases (Fig. 4.40(a)). Calibration of the device was performed by

applying a known force on the movable grain base and measuring the displacement of the loading spring by a vernier caliper. Figure 4.41 shows the calibration curve. The stiffness of the spring assembly obtained by drawing the best fit line through the loading and unloading curve is 0.3417 N/mm. By using the loading screw to control the movement of the loading spring, Fig. 4.40(b), the grains are loaded with a known force. A total of five tests were performed with this apparatus.

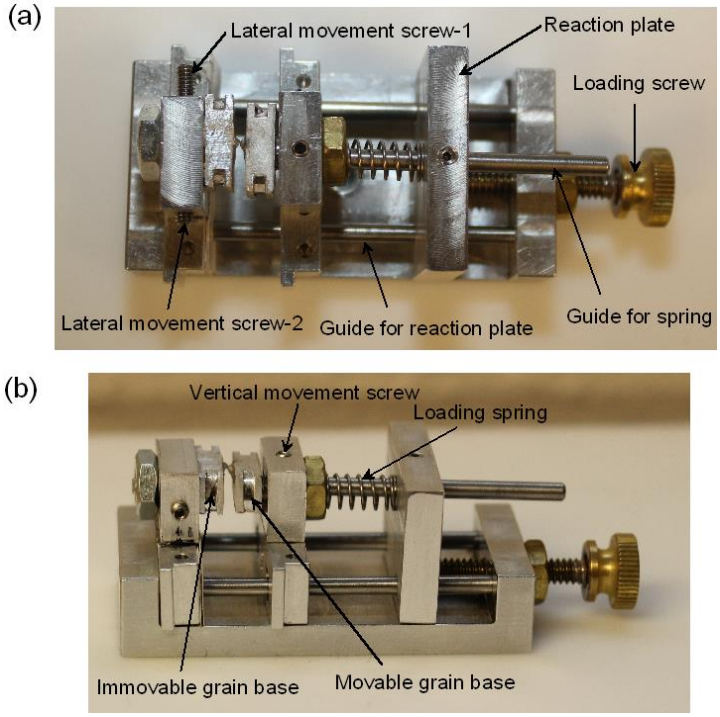

Figure 4.40. Set-up of the grain-to-grain contact vice, (a) top view, and (b) side view.

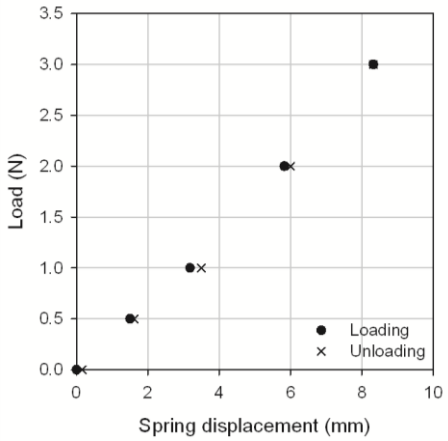

Figure 4.41. Calibration curve for the grain-grain contact vice.

In the first test, after two sand grains were glued to the two grain bases of the grain-to-grain contact vice, grain surfaces were recorded at different magnifications using SEM. The grains were then brought close together and loaded to 2 N using the loading spring, Fig. 4.40. After 3 days, the grains were unloaded and grain surfaces were again scanned under the SEM. Figure 4.42 shows the SEM images of two grain surfaces before and after loading of 2N for 3 days. The asperity in Fig. 4.42(b) is on the grain that was glued to the immovable grain base. The surface shown in Fig. 4.42(d) is a small area on the grain glued to the movable grain base. Figure 4.42(c) and (e) show the damaged areas corresponding to Fig. 4.42(b) and (d). Asperity crushing can be clearly seen in the SEM images.

To measure grain relative displacements after loading, reference points were chosen on SEM images of the two grains at the start of the loading process, and these reference points were tracked in subsequent SEM images after different loading durations. Grain displacement immediately upon loading cannot be measured. Two grains in contact can have a normal or an oblique contact, depending on their relative positions. Grain positions were controlled by adjusting lateral and vertical movement screws in the vice before the grains came in contact. Accurate positioning of grains in the vertical direction to obtain a normal contact was difficult to achieve due to the irregular shape and size of grains. Figure 4.43 shows SEM images of two grains that were misaligned in the vertical direction (into the paper) resulting in a shear contact. The major problem with misalignment is due to the limited depth of SEM view; points on the two grains will not be in focus at the same time, making the reference point identification a cumbersome process. Also, due to vertical misalignment, a shear contact is formed, and the movement of grains is three–dimensional; consequently, measuring distances between reference points using two-dimensional SEM images yields projected displacements and not the true grain displacements.

In the second test, two grains were loaded to 0.51 N in the grain-to-grain contact vice, and then placed in the SEM chamber for 1 hour. SEM images of the contact were obtained after every one minute. Since the vice was in the SEM chamber, no vibrations would have occurred as the SEM rests on a vibration isolation table. Analysis of the SEM images revealed no measurable grain movement for the one hour loading period. However, SEM imaging of the grain surface after loading revealed broken asperities on grain surface. This suggests that asperity crushing in this test might have been caused immediately after loading. Figure 4.44 shows the SEM images

of grain contact in this test. In the second test, grain surfaces were not scanned with the SEM before the loading process. However, damage to the grain surface in Fig. 4.44(d) in the form of crystalline debris is clearly visible.

The third test was performed using two new grains loaded again to 0.51 N. The grain-grain contact vice was then placed in the SEM for 3 hours and SEM images were recorded every minute. Analyzing the SEM images showed no grain movement in the 3-hour duration. After the 3-hour duration, the grain-grain contact vice was removed from the SEM and placed in an isolated location free from human interference for 100 days. SEM imaging of the contact after 100 days showed grain movement. Figure 4.45 shows the SEM images from the third test. In Fig. 4.45(a), two reference points are chosen on the two different grains and a dotted line is drawn connecting them. The same points are identified on Fig. 4.45(b) (after 3 hours) and Fig. 4.45(c) (after 100 days). After 100 days, change in the inclination and length of the dotted line joining the reference points indicates relative grain displacement. SEM imaging of grain surfaces after the test showed damage of asperities.

In the fourth test, two grains were loaded with 2.5 N force and relative grain positions were observed under the SEM after 10 min, 2 days, 3 days, 4 days and 9 days. Figure 4.46 shows the SEM images. Taking the 10 min SEM image (Fig. 4.46(a)) as a reference, grain movement was observed after 2 days (Fig. 4.46(b)), 3 days (Fig. 4.46(c)), 4 days (Fig. 4.46(d)) and 9 days (Fig. 4.46(e)). By identifying reference points on each grain and tracking their movement in intervals between each consecutive pair of images, the distance travelled by the grain is estimated. The purpose of this exercise was to detect the time-dependent movement, and not the entire motion represented by translation and rotation. Figure 4.47 shows the distance travelled by the grains relative to one another during the 9 days of sustained loading. It should be noted that this distance travelled is the two-dimensional projection of the true three-dimensional grain displacement. At the end of the test, SEM imaging of the surfaces of both grains showed asperity crushing.

In the fifth test, two grains were loaded with 0.2N force for 30 days. SEM imaging of the contact on day one, day twelve and day thirty showed no grain displacement. No identifiable surface damage was observed in the SEM images after the 30 day loading period.

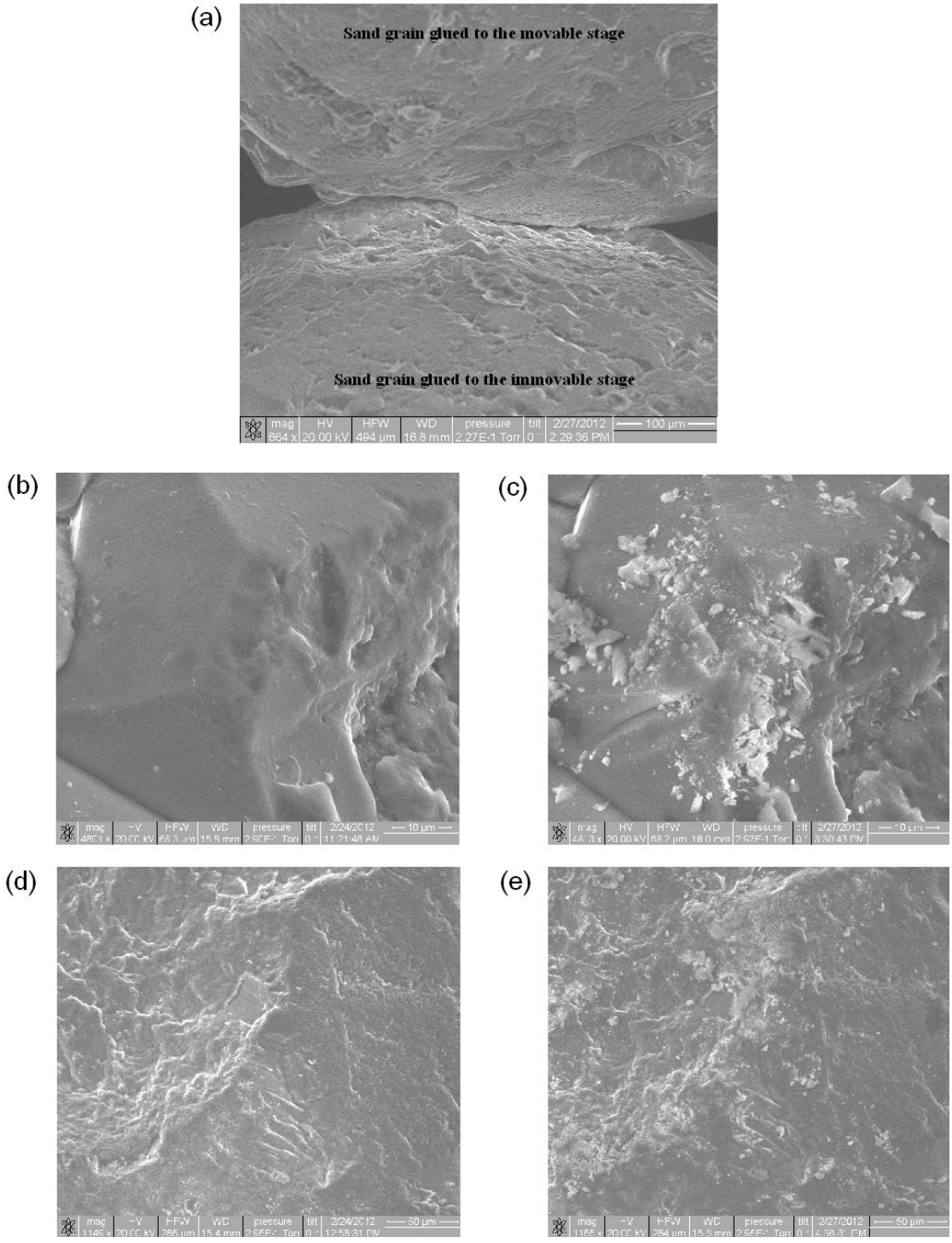

Figure 4.42. SEM images of grain surfaces used in the grain-grain contact vice, (a) contact between two grains (image width = 494 μm), (b) asperity on immovable grain before loading (image width = 68.3 μm), (c) the same asperity shown after sustained load of 2N for 3 days (image width = 68.3 μm), (d) surface of movable grain before loading (image width = 285 μm), and (e) surface in (d) after sustained load of 2N for 3 days (image width = 284 μm).

(a)

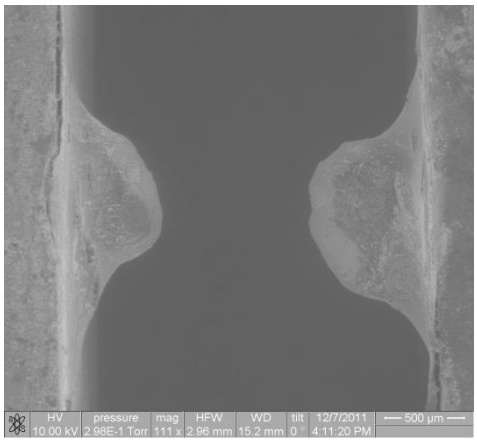

(b)

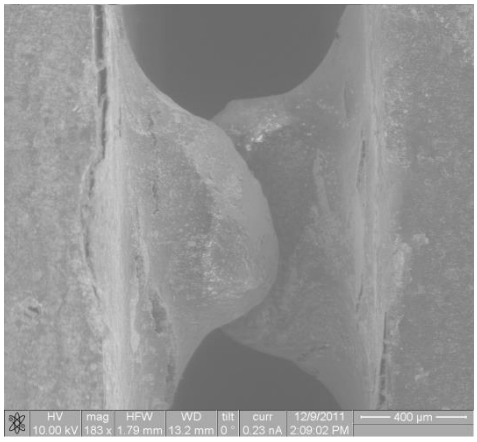

Figure 4.43. Alignment problems with the grain-to-grain testing vice; top view of the grains, (a) good alignment in the lateral direction (image width = 2.96 mm) and, (b) misalignment in vertical direction (image width = 1.79 mm).

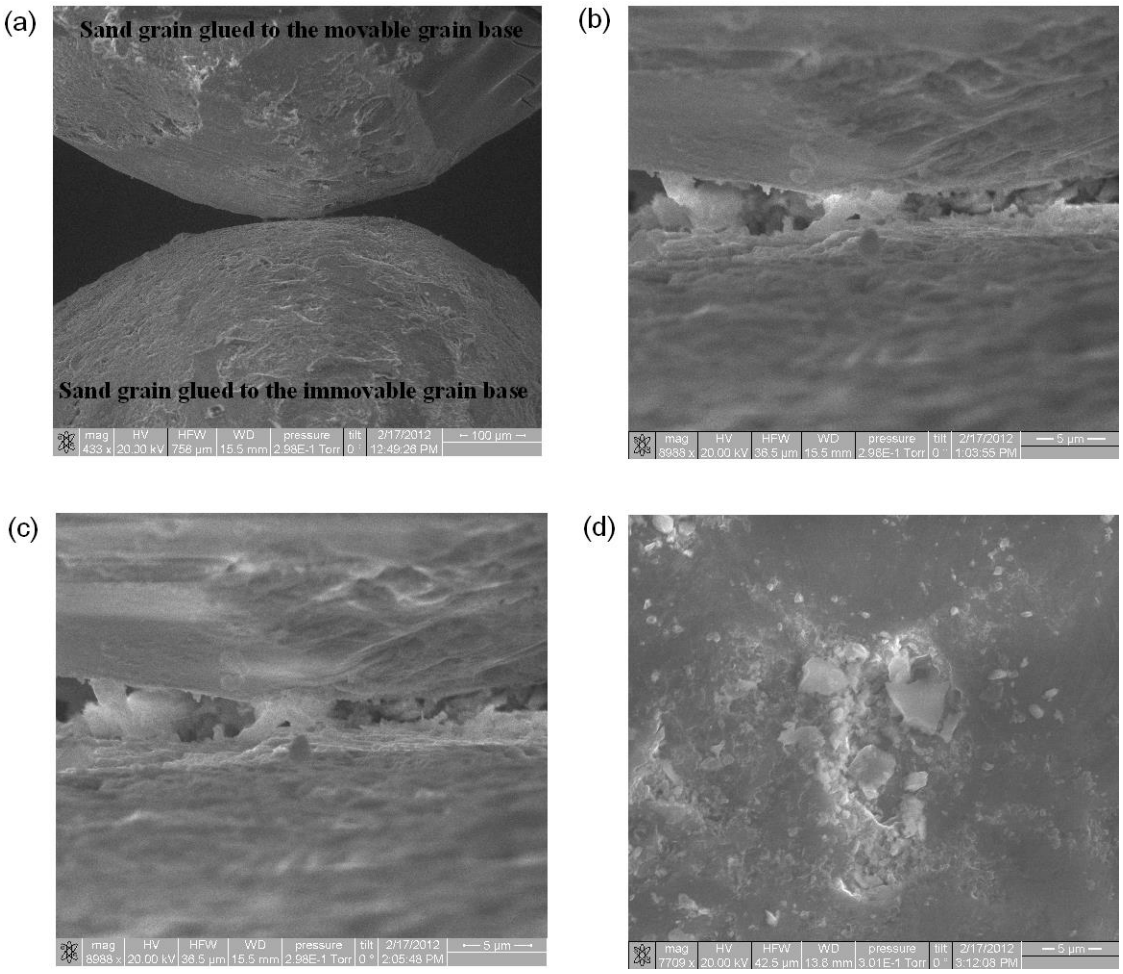

Figure 4.44. SEM image of a grain-to-grain contact: (a) contact between two grains, (b) a close up view of the contact between two grains after 10 minutes of loading with 0.51 N (image width = 36.5 μm), (c) the same contact after 1 hour of loading with 0.51 N, and (d) damage to the movable grain surface upon loading (image width = 42.5 μm).

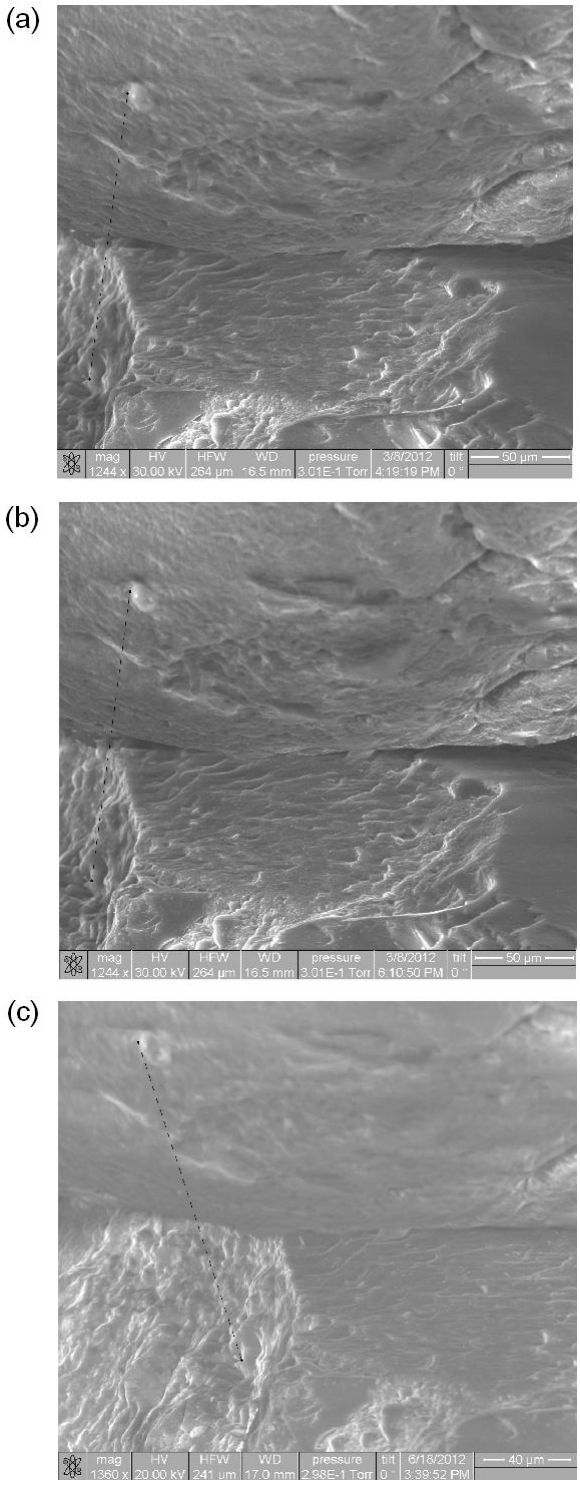

Figure 4.45. SEM images of two grains in contact loaded with 0.51N, (a) after 10 minutes of loading (image width = 264 μm), (b) after 3 hours of loading (image width = 264 μm), and (c) after 100 days of loading (image width = 241 μm).

(a)

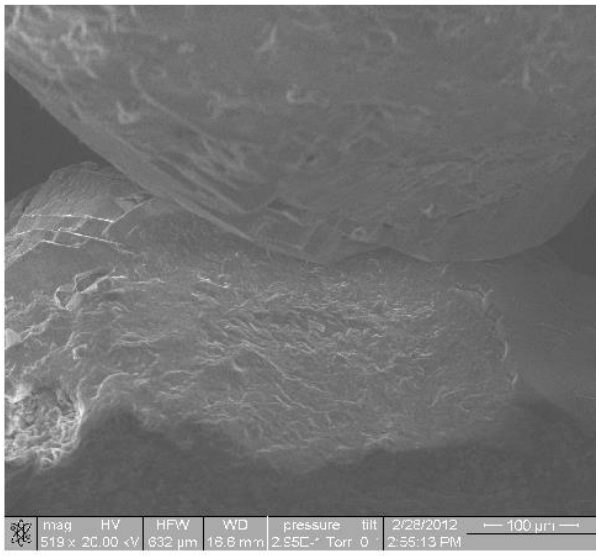
mag HV HFW WD pressure tilt 2/28/2012
518 x 20.00 kV 632 µm 16.6 mm 2.95E-4 Torr 0 ° 2:55:13 PM
100 µm

(b)

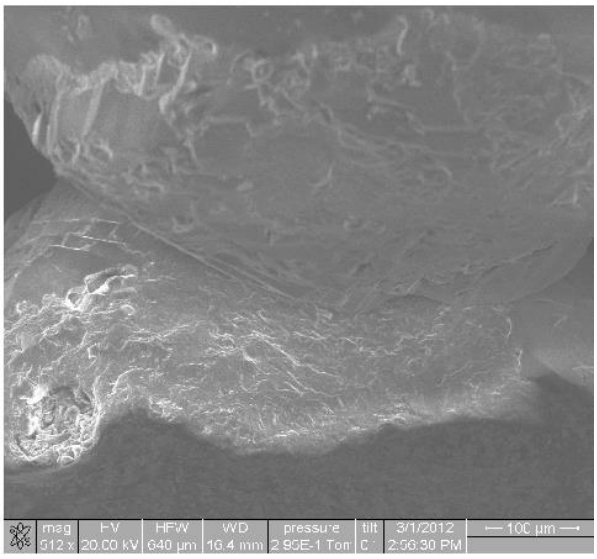
mag HV HFW WD pressure tilt 3/1/2012
512 x 20.00 kV 640 µm 16.4 mm 2.95E-1 Torr 0 ° 2:50:30 PM
100 µm

(c)

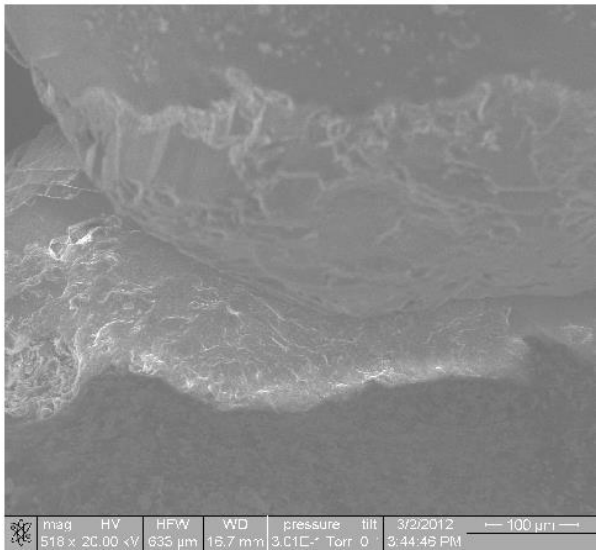
mag HV HFW WD pressure tilt 3/2/2012
518 x 20.00 kV 633 µm 16.7 mm 3.01E-4 Torr 0 ° 3:44:45 PM
100 µm

(d)

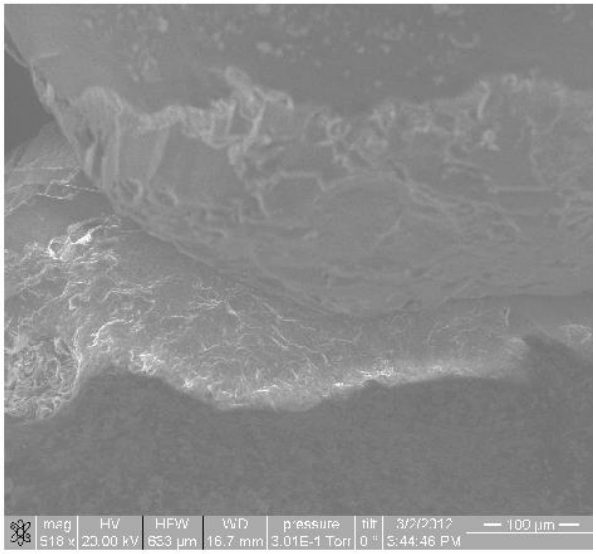

(e)

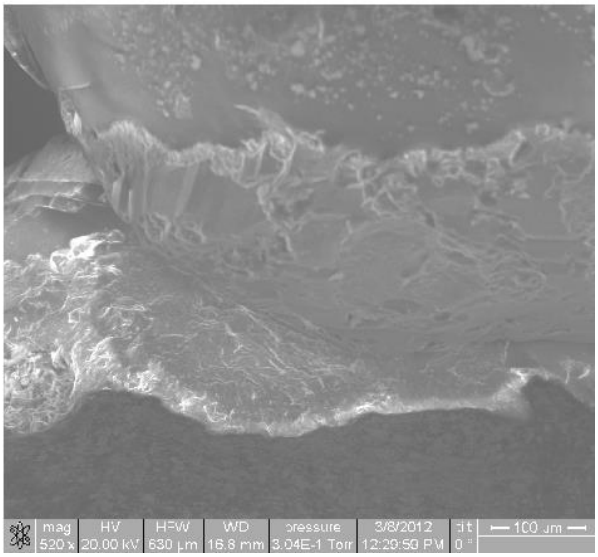

Figure 4.46. SEM images of two grains in contact subjected to 2.5N force, (a) after 10 min (image width = 632 μm), (b) after 2 days (image width = 640 μm), (c) after 3 days (image width = 635 μm), (d) after 4 days (image width = 653 μm), and (e) after 9 days (image width = 630 μm).

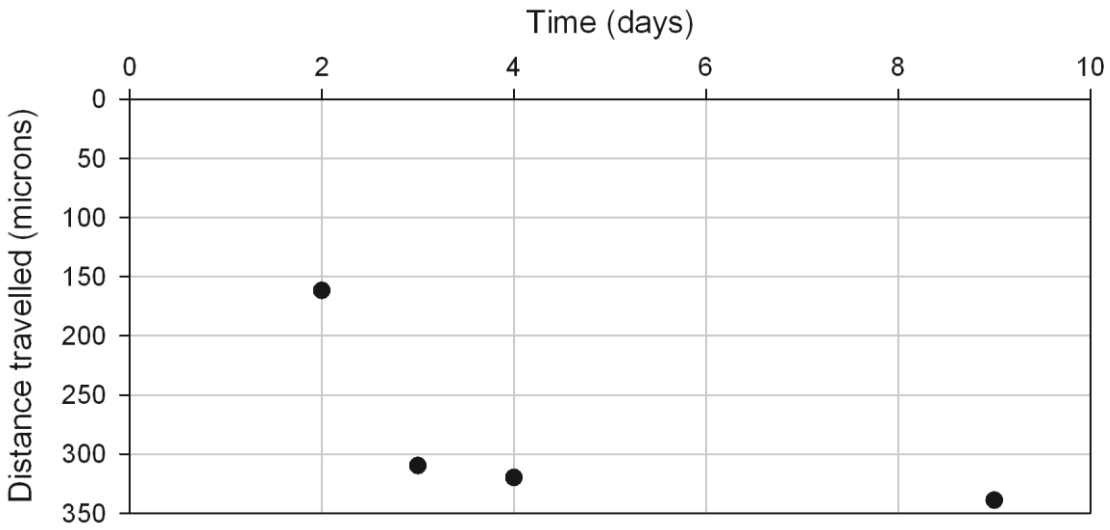

Figure 4.47. Distance travelled by one grain over the other (result from test # 4).

It was suggested earlier that grains in contact could be subjected to dynamic effects (such as vibrations) during handling of the grain-to-grain contact vice. These vibrations could affect the interaction between the grains and their relative movement. To reduce the effect of external disturbances another device was constructed. This device was capable of measuring the relative distance travelled by two grains in contact (grain convergence). The device was kept in an environmental chamber, free from temperature fluctuations (temp. maintained at 20°C and relative humidity of 20%), and, to some extent, free of human interference. Figure 4.48 shows a schematic of this device. The device is made up of two potentiometers measuring displacements (Novotechnik TR 10) and two staging devices (C and D) allowing required alignment of the grains.

Two potentiometers were needed because the spring in one of the potentiometers (Potentiometer A) was used as the loading mechanism. Consequently, during the loading process, the displacement indicated by Potentiometer A had two components: one associated with the force in the spring being increased to the required level, and the second component related to the grain convergence. In order to isolate the relative grain displacement during the loading process (convergence), the total displacement measured by Potentiometer A was reduced by the displacement of the potentiometer's sleeve. Potentiometer A was mounted on Stage D, and its displacement during the loading process (using the x-direction screw in stage D) was measured by Potentiometer B. Once the required force was reached at the contact, Potentiometer

A became stationary, and the relative displacement of the two grains (convergence) was measured entirely by Potentiometer A. In principle, the displacement of the sleeve of Potentiometer A during the contact loading process could be read from the staging micrometer screw, but the precision of such readings was found insufficient, and Potentiometer B was used instead.

Figure 4.49 shows the grain-to-grain contact apparatus. When the sand grains are in contact, and the base of Potentiometer A is moved in x-direction by amount x in order to generate the force in the potentiometer spring, the displacement measured by the potentiometer is $x-\Delta x$, where, Δx is the displacement due to grain convergence. Once the target force is reached, Potentiometer A becomes stationary, and its subsequent reading, increasing over time, is equal to Δx. The influence of changing Δx on the contact force was ignored, as Δx is of the order one micron. Figure 4.50 shows the calibration curve for Potentiometer A. In this plot, on the X-axis, the potentiometer displacement is shown, and on the Y-axis is the corresponding force. The calibration curve for the Potentiometer A (grain potentiometer) is given by Equation. (4.12)

$$F = (8.3\times10^{-5})x + 2.65 \tag{4.12}$$

where F is the force in Newtons and x is the grain potentiometer reading in microns. A non-zero value of the force intercept in Equation. (4.12) suggests that, even for an infinitesimally small displacement of the potentiometer there exists a force equal to 2.65 N. This was found to be rather limiting, as no forces less than 2.65 N could be applied to the contact. To overcome this issue, the stiffness of the Potentiometer A was reduced by placing an additional spring between the front and the mid reaction bases, Fig. 4.51. The stiffness of the Potentiometer A after placing the additional spring is shown in Fig. 4.52.

The calibration curve for the Potentiometer A after changing its stiffness is given by

$$F = (7\times10^{-4})x + 0.15 \tag{4.13}$$

where F is the force in Newtons and x is the potentiometer reading in microns.

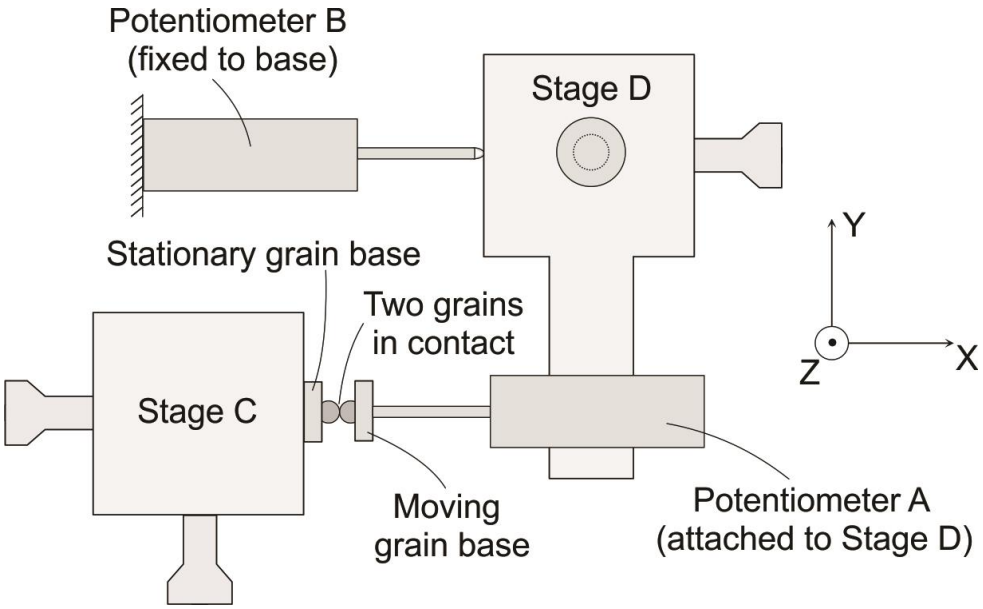

Figure 4.48. Schematic of the grain to grain contact device.

Potentiometers A and B in the device were connected to the National Instruments (NI) cDAQ 9178 Chassis having a NI 9219 24 bit Analog Input module. The potentiometers were powered using a NI 9263 16 bit output module. The cDAQ was connected to a computer and data was acquired continuously at 1 Hz. By taking a ratiometric of the applied voltage to the measured voltage from the potentiometer at every time step, a very high degree of resolution in displacement measurement was achieved. The noise level in the measured displacements was less than 0.1 μm. Fast Fourier Transform (FFT) filtering by using a low pass filter to remove the higher frequency components reduced the noise level to less than 0.05 μm. To check the long term stability and drift in the potentiometers and the NI cDAQ system, the potentiometer was displaced to about 764 μm and the signal was measured by the cDAQ continuously for 8 days at 1 Hz. Figure 4.53 shows the result. The figure also shows the FFT filtered signal (in red). The result from this test suggests almost no drift in the potentiometer reading.

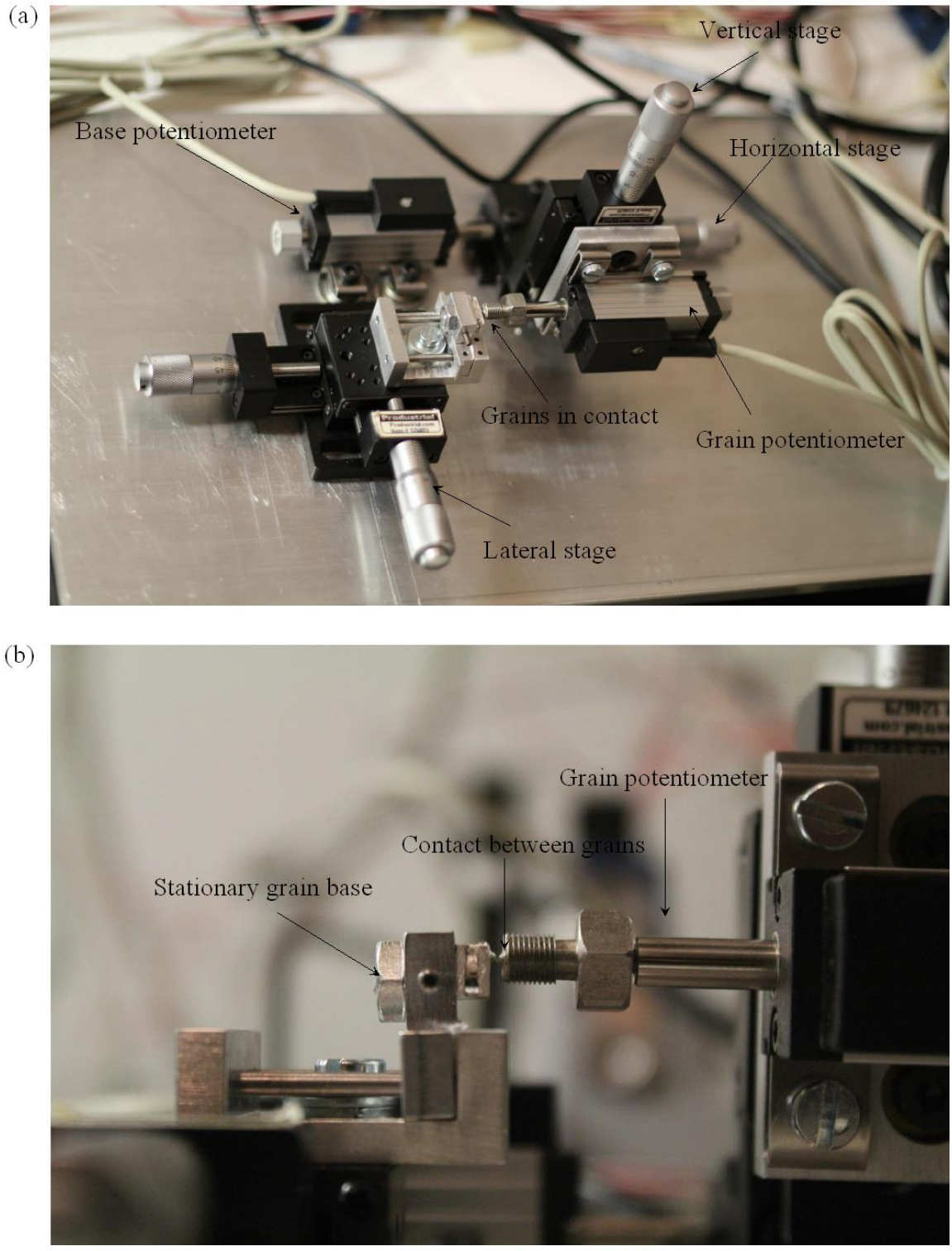

Figure 4.49. Photograph of the grain-to-grain contact apparatus for measuring time-dependent behavior of contacts between two grains, (a) a general view of the apparatus, and (b) a close up view showing two grains in contact.

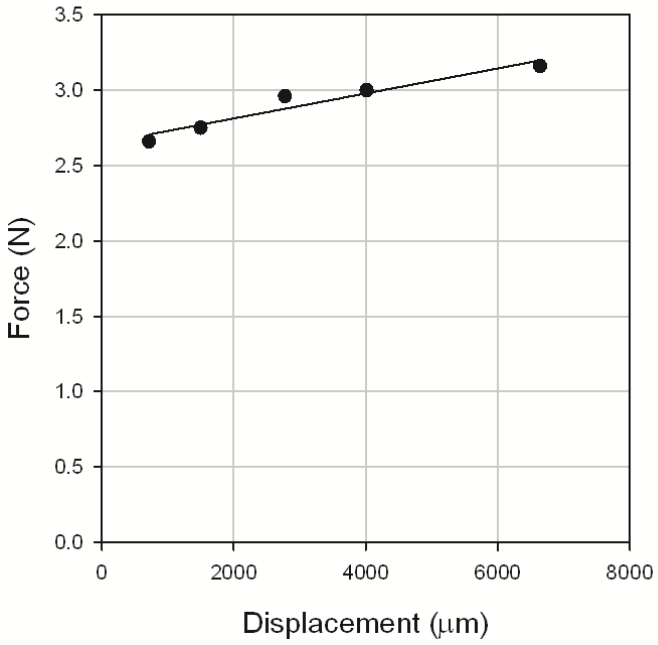

Figure 4.50. Force-displacement calibration function of the spring in the potentiometer (one spring as in Fig. 4.51).

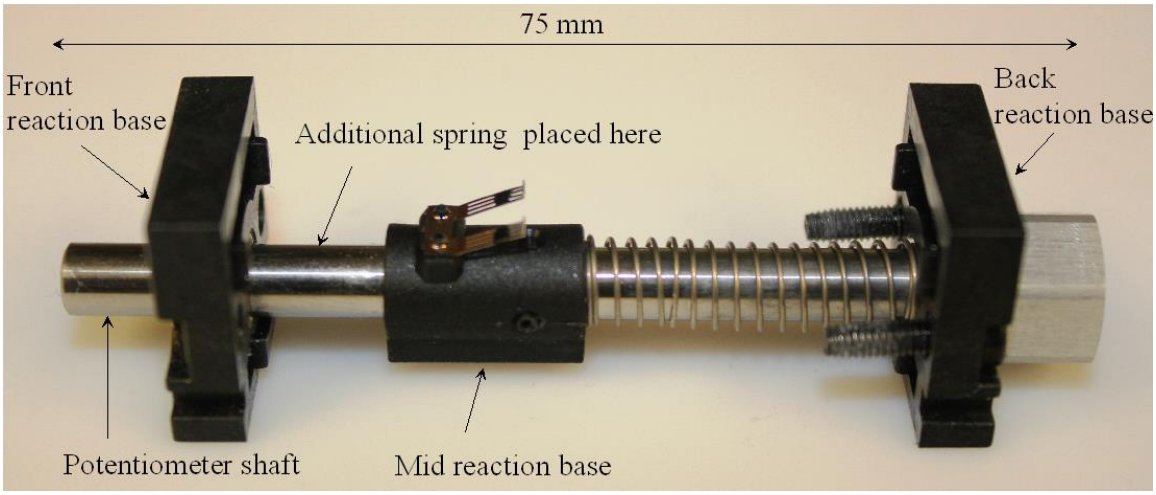

Figure 4.51. Stiffness modification of the grain potentiometer; potentiometer housing (not shown) encloses the area in-between the front and back reaction base).

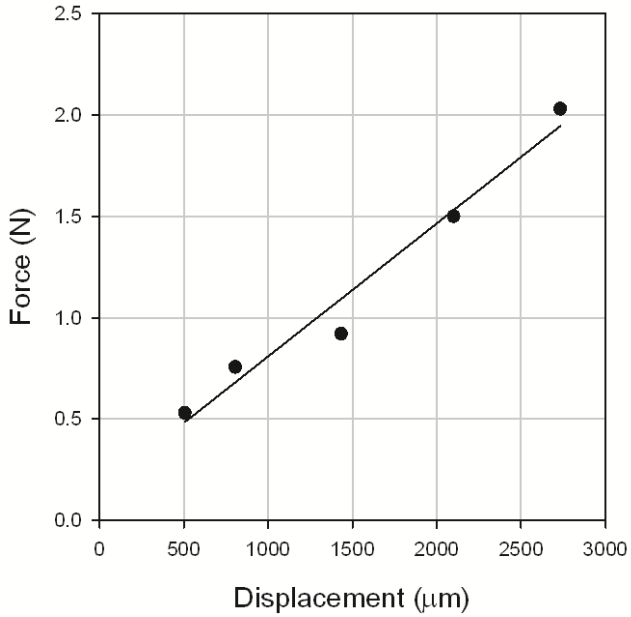

Figure 4.52. Displacement-force calibration curve of the modified potentiometer (two springs).

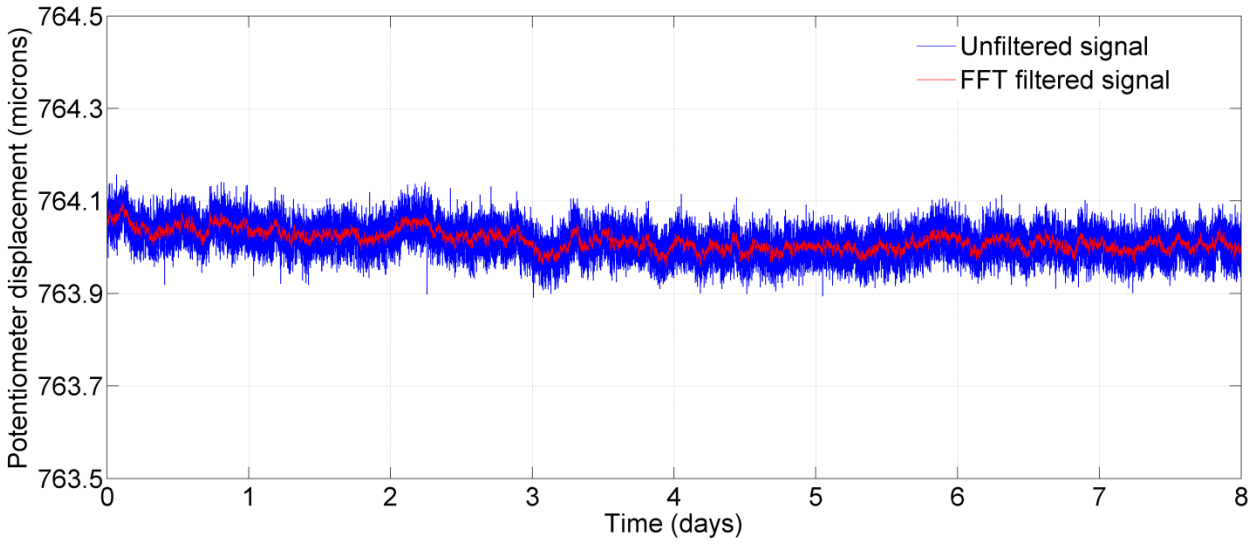

Figure 4.53. Test showing very small drift in the potentiometer reading for a period of 8 days; FFT filtered signal shows a significant reduction in noise level.

A total of four tests were performed using the grain-to-grain contact apparatus. Table 4.4 summarizes the tests. The first two tests were performed using the unmodified grain potentiometer while tests 3 and 4 were performed with the modified grain potentiometer.

Table 4.4. Summary of grain-to-grain contact tests.

Test #	**Test particles**	**Contact force (N)**	**Contact load**	**Test duration (days)**	**Displacement after 1.8 days (μm)**	**Final displacement (μm)**	**Fig. No.**
1	Stainless steel (R = 3.175 mm)	3.1	Nearly normal	1.67	0	0	4.54
2	Ottawa 20-30	2.9	Oblique	1.8	0.66	0.8	4.55
3	Ottawa 20-30	1.9	Oblique	2.4	0.61	0.7	4.56
4	Ottawa 20-30	0.8	Oblique	21	0.47	1.9	4.57

The first test was performed with two steel shots. This test was performed to study the long term stability in the test apparatus. Figure 4.54 shows the result from this test. In this test, the Potentiometer A was moved by 5408.35 μm (this reading is from Potentiometer B). The reading from Potentiometer A was 5408.34 μm. Using the Potentiometer A reading and Equation. (4.12), the force acting on the steel shot contact was calculated as 3.1 N. The test was continued for 40 hours under a constant load of 3.1 N. The difference in Potentiometer B and Potentiometer A reading which is indicative of relative grain displacement or grain convergence is shown in Fig. 4.54. This result shows no grain convergence for steel shot during the entire period of testing.

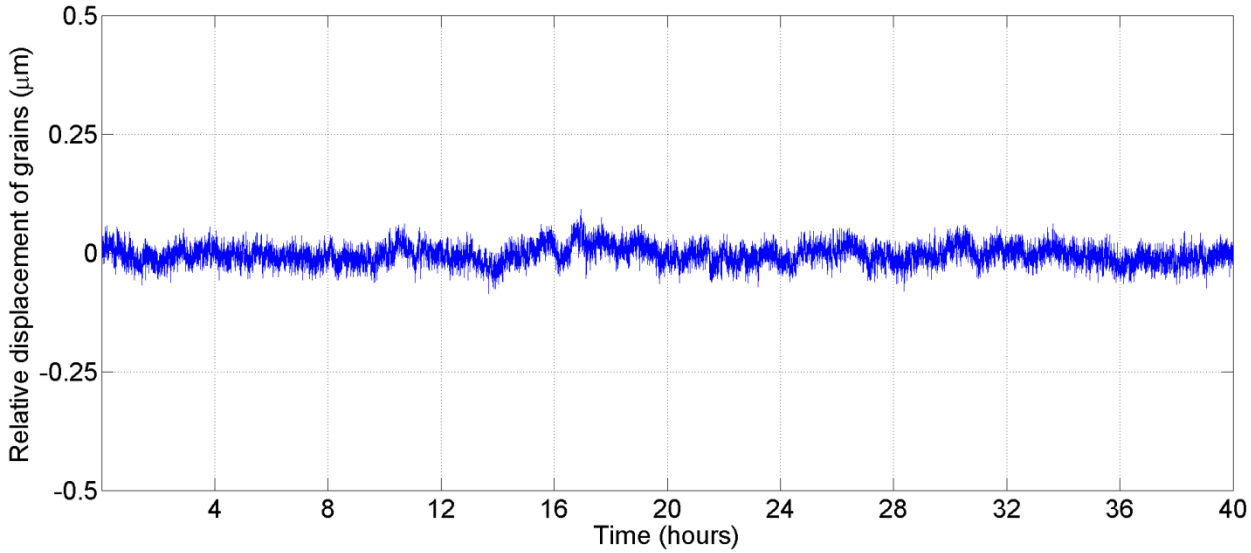

Figure 4.54. Relative displacement of two stainless steel shots in contact under a force of 3.1 N.

In the second test, two Ottawa 20-30 sand grains were brought in contact and subjected to 2.9 N force, Fig. 4.55. It is seen in Fig. 4.55(a) that the two grains were loaded at some oblique angle. Thus, the contact is loaded with both the normal and tangential force components. A force of 2.9 N was applied on the contact in two load increments. The force was kept constant for about 43 hours before the grains were unloaded. Fig. 4.55(b) shows the load vs. grain displacement plot during the entire test. Upon application of the 2.9 N force, there was a large initial relative grain displacement (over 200 μm). Fig. 4.55(c) shows an increase in relative displacement of the grains during 43 hours at the constant load, which amounts to about 0.8 μm. Figures 4.55(e) to (g) show the damage on one of the grains after 43 hours. Figure 4.55(a) shows the SEM image of the grain surface before loading. Figure 4.55(b) shows the damaged grain surface at the end of the 43-hour loading period. Figures 4.55(c) & (d) show a close up view of the damaged area.

In the third test, the sand grains were loaded to 1.9 N in three load increments. Figs. 4.56(a) and (b) show the side and the top view of the grains in contact, respectively. The grains in this case too are loaded in shear. Application of the 1.9 N force caused the grains to move by about 152 μm. The load of 1.9 N was kept constant for the next 54 hours. The grain convergence during this time was 0.7 μm, Fig. 4.56(d).

(a)

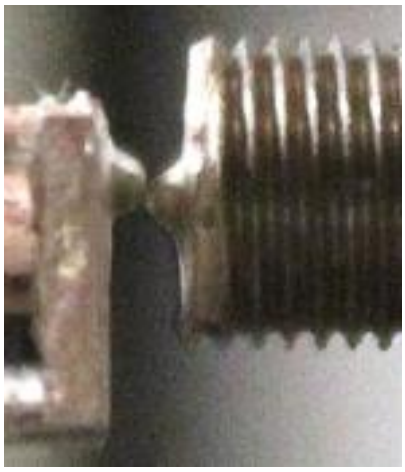

(b)

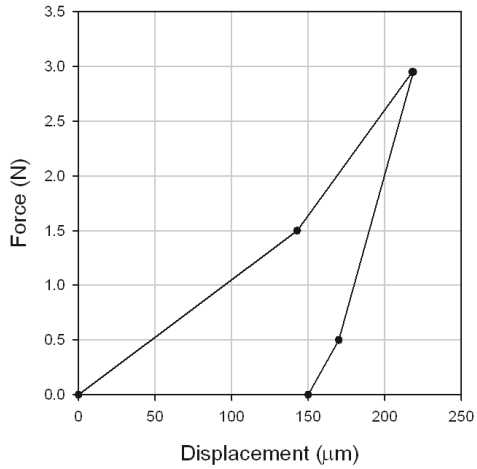
Force (N)
Displacement (μm)
0.0
0.5
1.0
1.5
2.0
2.5
3.0
3.5
0
50
100
150
200
250

(c)

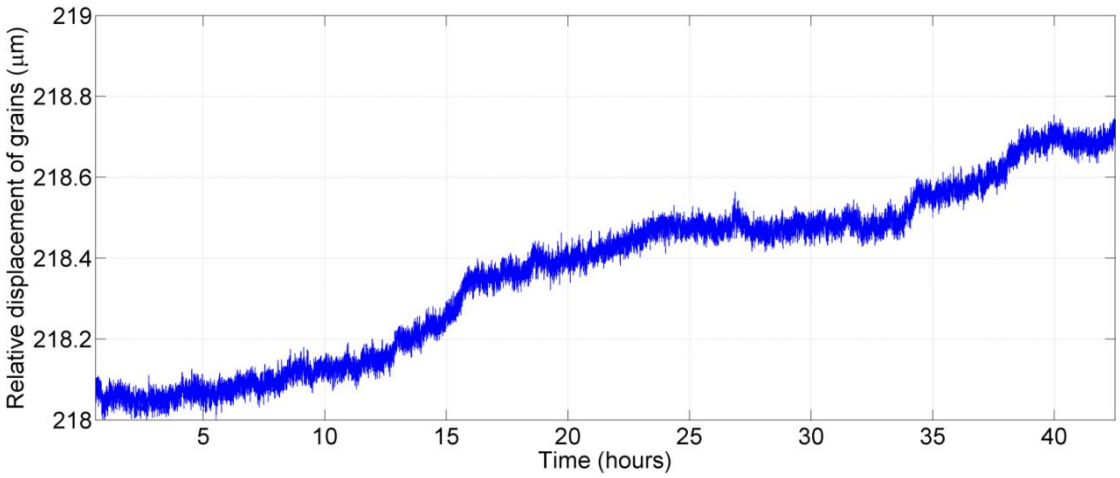
Relative displacement of grains (μm)
Time (hours)
218
218.2
218.4
218.6
218.8
219
5
10
15
20
25
30
35
40

(d)

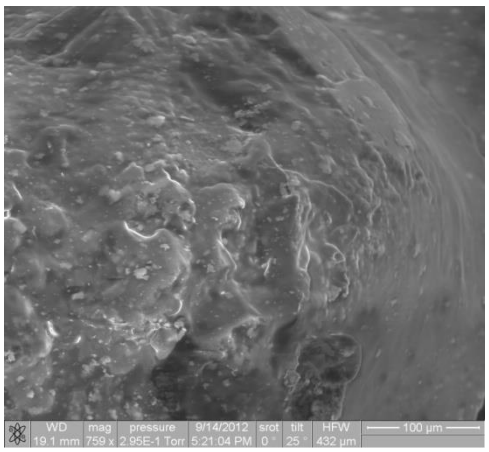

(e)

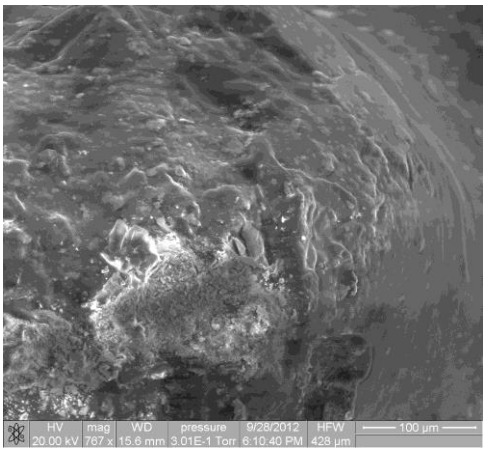

(f)

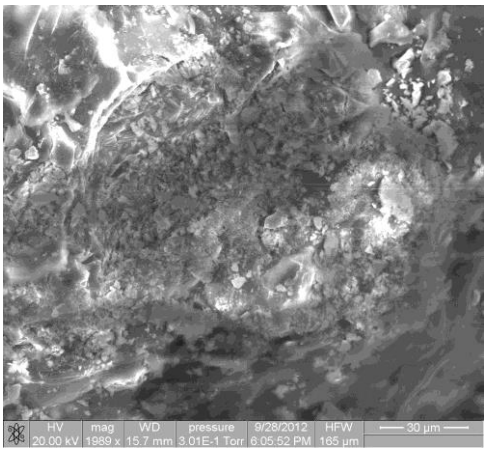

(g)

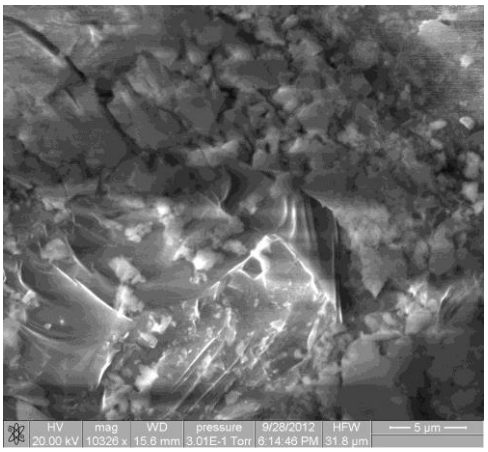

Figure 4.55. Results from test #2 using the grain-grain-contact apparatus, (a) side view of grains in contact (image width = 8.42 mm), (b) applied force versus grain relative displacement curve, (c) time-dependent convergence of the two sand grains under 2.9 N force, (d) SEM image of one of the grains before the test (image width = 412 μm), (e) SEM image of the grain after test (image width = 428 μm), (f) a close up view of the damaged surface (image width = 165 μm), and (g) close-up view of the broken debris (image width = 31.8 μm).

In the fourth and final test, the sand grains were loaded with 0.8 N force for 21 days. As the other sand grain contacts tested in the apparatus, the grains were loaded at some oblique angle, Fig. 4.57(a) & (b). The load of 0.8 N was applied in five load increments. Fig 4.57(c) shows the force vs. grain relative displacement plot. The relative grain displacement results from this test seemed to have a larger noise level than other tests, Fig. 4.57(d). This could be due to powering the cDAQ through an Uninterrupted Power Supply (UPS). As the test was planned to run for a long period of time, the UPS was used to avoid any potential data loss during power outages. The grains converged by 1.9 μm during the 21 days of constant load. The rate of grain convergence

decreased with increasing time. SEM imaging of grain surfaces after loading showed asperity damage.

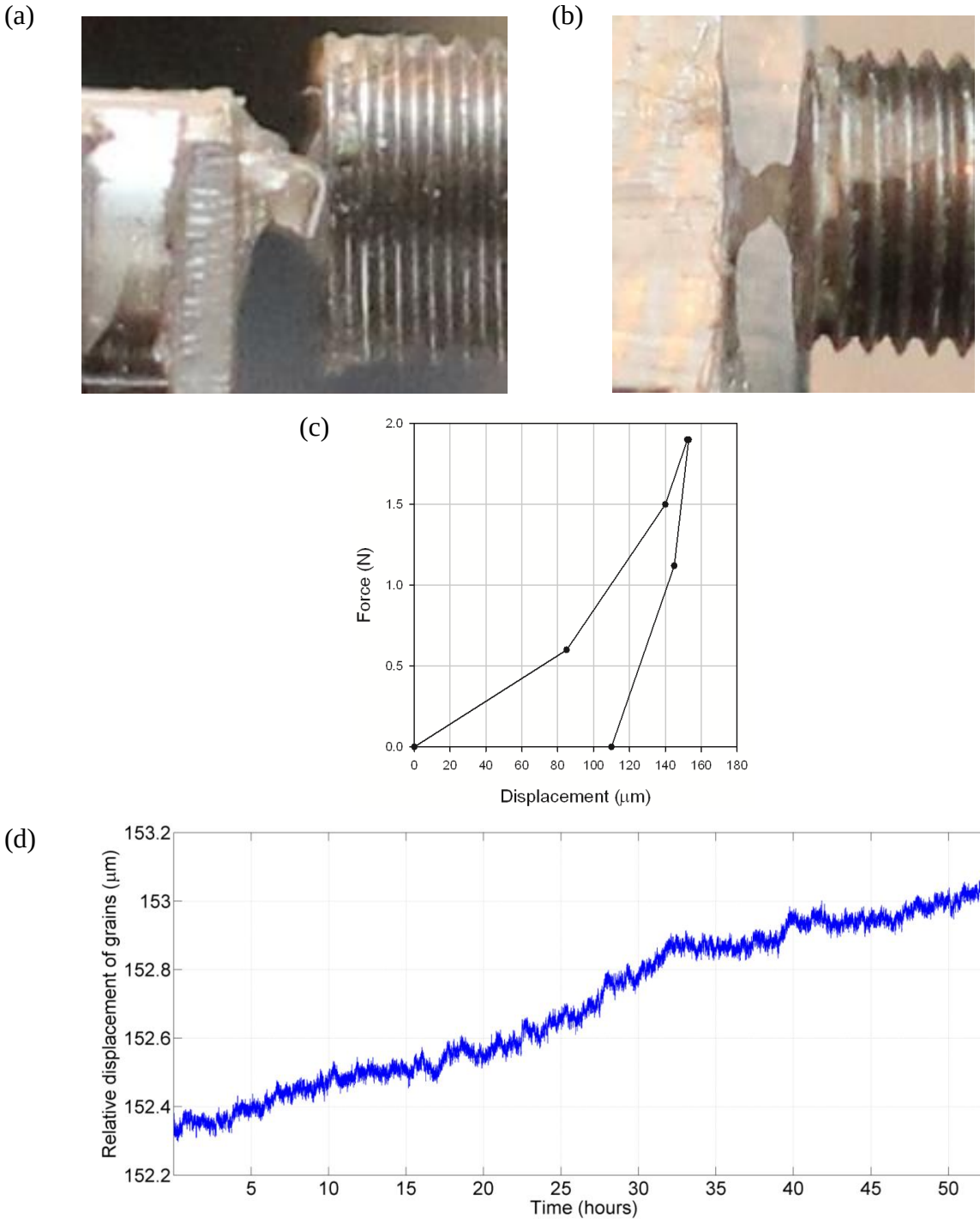

Figure 4.56. Test #3 in the grain-grain-contact apparatus, (a) side view of the grains (image width = 7.07 mm), (b) top view of the grain contact (image width = 5.65 mm), (c) applied force versus grain relative displacement curve, and (d) time-dependent convergence of the two sand grains under 1.9 N force.

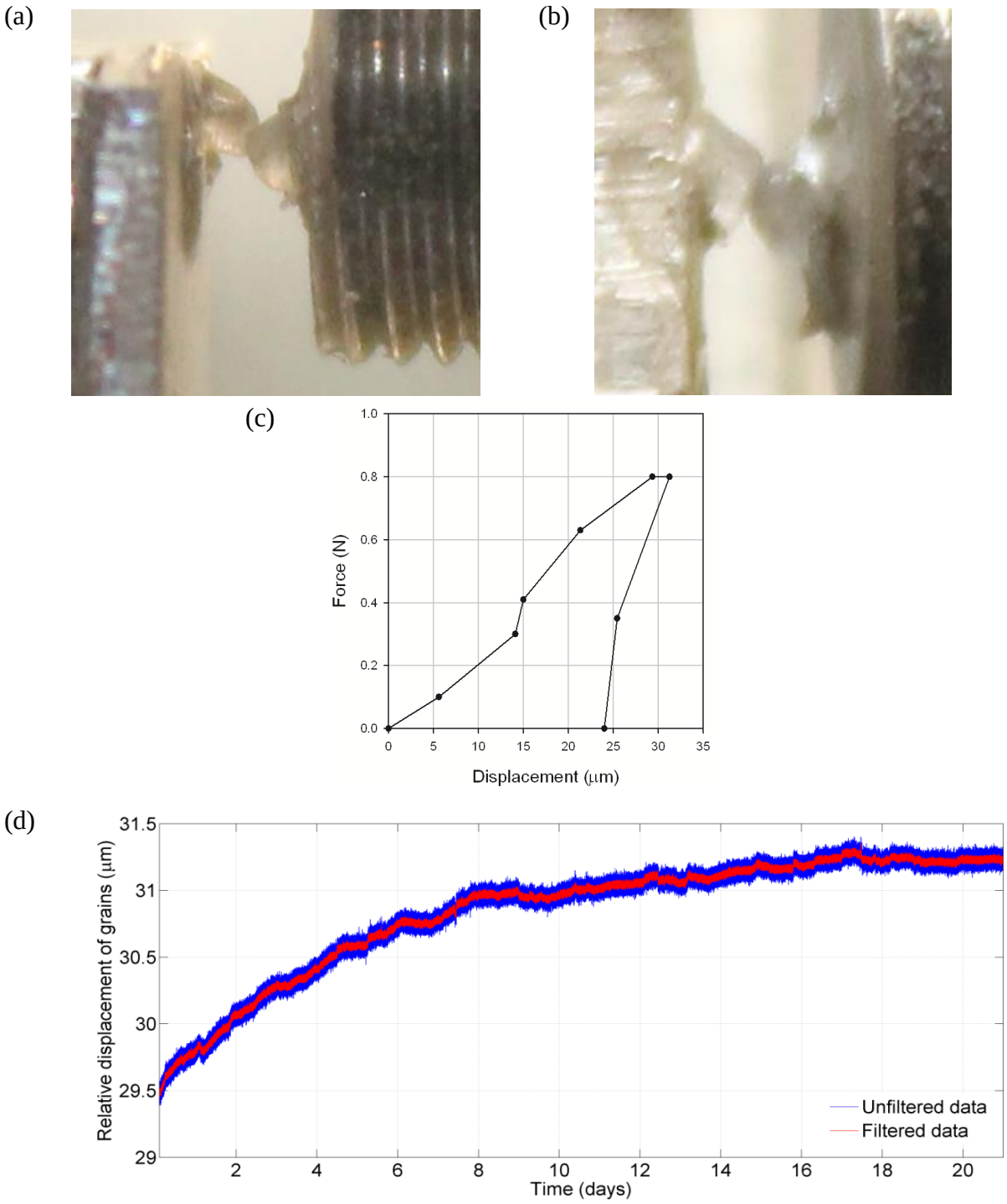

Figure 4.57. Test #4 using the grain-grain-contact apparatus, (a) side view of the grains (image width = 9.39 mm) , (b) top view of the grain contact (image width = 6.91 mm), (c) applied force versus grain relative displacement curve, and (d) time-dependent convergence of the two sand grains under 0.8 N force.

Results from micro-scale testing of sand grains support the hypothesis of time-dependent asperity crushing. The three-grain tests performed in dry and acidic environments showed asperity damage. Grain-to-grain contact tests were performed at loads of 0.2 N, 0.51 N, 0.8 N, 1.9 N, 2 N, 2.5 N, and 2.9 N using the two custom-made devices. Except in the test performed at 0.2 N, asperity damage was observed in all other tests. Grain convergence occurred at a decreasing rate during test with duration more than 2 days.

4.5 Macro-scale tests

In section 4.4, it was shown that grain convergence occurs due to fracturing of asperities. The hypothesis advocated in this thesis asserts that grain convergence leads to firmer contacts, causing an increase in contact stiffness. If this is true, then the increase in contact stiffness will then propagate through the spatial scales and will be manifested at the macroscopic scale as an increase in elastic moduli. This was noticed in the tests of Afifi and Woods (1971), who demonstrated that the shear wave velocity (and therefore the shear modulus) increases in time under sustained load. Consequently, one would expect a change in horizontal stress in a confined sand specimen that is loaded with a constant vertical stress. This conjecture comes from consideration of the elastic energy. The elastic energy stored in a unit volume of sand can be expressed in terms of the average (macroscopic) stresses and strains as

$$W_e = \frac{1}{2}\bar{\sigma}_{ij}\bar{\varepsilon}^e_{ij}\ ; \qquad i, j = 1,2,3 \tag{4.14}$$

where, $\bar{\sigma}_{ij}$ and $\bar{\varepsilon}^e_{ij}$ are the average stress and average elastic strain tensors, respectively. For simplicity, an assumption is made that the sand is isotropic at the macroscopic scale, with strains described by the Hooke's law

$$\bar{\varepsilon}^e_{ij} = C_{ijkl}\bar{\sigma}_{kl} \tag{4.15}$$

where C_{ijkl} is the elastic constitutive tensor

$$C_{ijkl} = \frac{1}{E}\left[(1+\nu)\delta_{ij}\delta_{jl} - \nu\delta_{kl}\delta_{ij}\right] \tag{4.16}$$

E and ν are the Young's modulus and Poisson's ratio, respectively. Specifying directions *1, 2, 3* to coincide with the principal directions, and using the Hooke's law in Equation (4.15), the strain energy in Equation (4.14) can be expressed as

$$W_e = \frac{1}{2E}(\bar{\sigma}_1^2 + \bar{\sigma}_2^2 + \bar{\sigma}_3^2) - \frac{\nu}{E}(\bar{\sigma}_1\bar{\sigma}_2 + \bar{\sigma}_2\bar{\sigma}_3 + \bar{\sigma}_3\bar{\sigma}_1) \tag{4.17}$$

It is clear from Equation (4.17) that if the elastic modulus increases, preservation of the elastic energy will require an increase in the mean stress; for instance, in a natural deposit with the vertical load governed by gravity, the horizontal stresses need to increase to preserve the strain energy.

The increase in elastic modulus at the macroscopic scale is associated with changing stiffness at the contacts. The latter is due to grain convergence, producing larger contact areas and firmer (stiffer) interactions between grains. The process of fracturing requires expenditure of energy to overcome energy barriers to crack propagation. Part of that energy may come from the strain energy, thus reducing it by some amount. It is likely, however, that the horizontal stresses will still increase. Hence a radial stress in a cylindrical sand specimen subjected to constant (time-independent) vertical load should be increasing in time. To test this conjecture, compression tests were performed on sand specimens under different environmental conditions. Two types of tests were performed. The first type was performed using a plexiglass cylinder. In the second type, a standard consolidometer was adapted to test specimens in a "soft" aluminum ring.

4.5.1. Large cylinder test

Air-dry Ottawa 20-30 sand was placed in a Plexiglas cylinder of 30 cm in diameter and 60 cm in height (6.35 mm in thickness). The sand was deposited in the cylinder using a 2-inch diameter tube. Deposition of the specimen took about 30 min. The average porosity in the specimen was 0.41. The cylinder was placed on a Teflon base to allow circumferential (and radial) deformation of the cylinder. A strain gauge was installed at the bottom of the cylinder (Fig. 4.58) to record the changes in circumferential strain in time after the cylinder was filled (TML GFLA-6-50-1L 120Ω metal foil gauge was used; a dummy strain gauge was placed on

another Plexiglas cylinder to record any changes of strain caused due to accidental changes in temperature or instrument drift). Circumferential strain in the cylinder is indicative of changes in radial stresses in sand. If the process of *static fatigue* is indeed a time-delayed phenomenon, the resulting increase in sand stiffness should cause an increase in radial (and circumferential) stresses both in the sand and in the cylinder. To eliminate the influence of thermal changes on the experimental set-up and on the sand, the cylinder was placed in an environmental chamber, with constant temperature of 25°C, and relative humidity of 25%. The settlement of the specimen was measured using a linear potentiometer installed at the top cover of the specimen. The strain gages and the linear potentiometer were interfaced to wireless sensor nodes (Narada), developed at the University of Michigan (Swartz et al., 2005). The increase in the circumferential strain of the cylinder is illustrated in Fig. 4.59(a), as a function of elapsed time.

The strain in the cylinder (and, therefore, the radial stress in the sand) was increasing gradually in the first 24 hours, and, after this period, the strain (and, therefore, the stress) remained approximately constant. Most of the sample settlement occurred during the first 24 hours, Fig. 4.59(b). The sampling rate was 1Hz, and the wirelessly transmitted signal to the data acquisition system was occasionally dropped as shown in Fig. 4.59. The increase in the circumferential strain is indicative of increasing radial stresses in the sand, and it is consistent with the hypothesis of static fatigue being a chief contributor to time effects in sand.

Figure 4.58. Cylinder test set-up for detecting time-dependent behavior of sand (cylinder diameter: 30 cm).

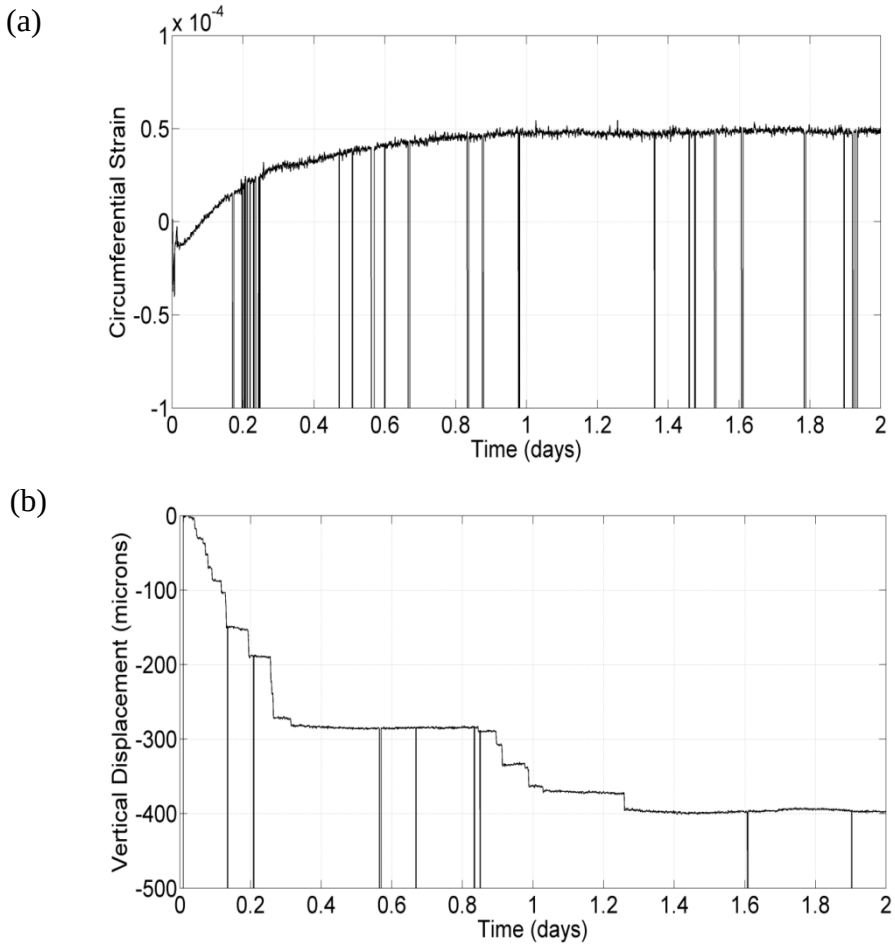

Figure 4.59. Cylinder test: (a) time-dependent circumferential strain of the cylinder, and (b) specimen settlement.

An interesting, step-wise settlement process was found also in consolidometer tests, and will be discussed in the following section.

4.5.2. Modified consolidometer test

The literature published to date on lateral stresses in soils is limited mainly to discrete measurements of lateral stresses in time (whether in the lab or in the field), and does not contain measurements of the variation of lateral pressure with time. In the field, the dilatometer tests (Marchetti, 1980) or Iowa stepped blade tests (Handy et. al, 1982) are often used to find out the lateral stress in soils. It should be noted that in these tests the soil is being disturbed as the blade is pushed into the soil. Hence, the lateral stresses so measured are not accurate. Some

information is available on the subject in the context of variation of coefficient K_o (*in situ* horizontal-to-vertical stress ratio): Mayne and Kulhawy (1982), Jefferies et al. (1987), Mesri and Hayat (1993), Michalowski (2005). Although there may still be some controversy as to whether K_o in soils decreases, increases, or remains constant with time (Schmertmann, 1983), it is often believed it increases with elapse of time (Kavazanjian and Mitchell, 1984). For cohesive soils, Kuhn (1986) and Al-Shamrani and Sture (1994) performed numerical studies, which suggested that the earth pressure at rest increases during secondary consolidation. Consolidometer tests performed by Mesri and Castro (1987) on clays showed an increase in horizontal stress in time. More recently laboratory tests performed by Jirathanathaworn (2009) on glass cylinders showed an increase in lateral stress over time under a constant load during 1D strain conditions. The studies of time-dependent changes in stress state over time are rare (Mesri, 1990; Thomann, 1990 Saftner, 2011). Tests in a modified consolidometer, with measurements of circumferential strain of a thin ring were performed to investigate changes to lateral stresses in sand under different vertical stress levels and environmental conditions.

The measurement of lateral stresses in sand, in laboratory conditions, can be achieved in two ways: using "compensating techniques", or using a "soft ring consolidometer". Both tests can be performed in a modified standard consolidometer. In the compensating method (Ting et al. 1994), a back pressure is applied on thin consolidometer ring to nullify strain in the ring caused as a result of applied axial load to the specimen. By measuring the compensating back pressure, the lateral stress becomes known. Thomann (1990) built a Bender Element Oedometer capable of measuring lateral stresses along with shear wave velocity under zero lateral strain conditions. In the soft consolidometer approach (Kolymbas and Bauer, 1993; Castellanza and Nova, 2004; Slatter, 2005; Shin and Santamarina, 2009), a thin-walled ring is used in place of the standard thick-walled ring in a standard consolidometer. The lateral stress in the soil can be measured by measuring the hoop strain of the ring. This hoop strain can be converted into the lateral stress by using the thin-walled pressure vessel theory. In this thesis, the soft consolidometer approach is followed due to its simplicity of operation.

Earth pressure at rest (K_o) is defined as the ratio of horizontal and vertical effective stresses corresponding to the condition of zero lateral strain (Bishop, 1958). Hence by definition, by using a soft ring in the consolidometer test, K_o is not measured. However, Okochi and Tatsuoka (1984) indicated that the radial strain must be kept smaller than 5×10^{-5} to reduce

errors in K_o to less than 0.01. The soft ring used in this thesis is made of aluminum, 0.1 mm in thickness. Small changes in radial stress produce the circumferential deformation that is measurable by strain gauges installed on the outside surface if the ring. The circumferential strain at an axial load of 230 kPa was about 5×10^{-4}. Hence, the stress ratio determined in this test is not K_o. However, this is not a concern as of interest is the change in radial stress and not the K_o condition. The circumferential strain was measured by two metal foil strain gages (Vishay Instruments, Model No #C2A-13-125LT-350) installed on the exterior of the soft ring at mid height. The gages were coated with polyurethane to prevent contact of moisture with the gage. Each of the sensors has two strain gages arranged in mutually perpendicular directions. In the four active strain gage elements, two are along the direction of circumferential strain and the remaining two are act as Poisson gages and are perpendicular to the circumferential strain direction. The four active strain gage elements were connected to the NI cDAQ through the NI 9219 input module to form the four arms of a Wheatstone bridge. An input voltage of 2.5 V was used for the strain measurements. To convert the voltage readings from the strain gages to strain the following equation was used (National Instruments white paper, 2006):

$$strain\ (\varepsilon) = \frac{-2V_r}{G\left[(\nu+1)-V_r(\nu-1)\right]} \tag{4.18}$$

where V_r is the voltage reading, G is the gage factor (= 2.13 for the gages used) and ν is the poisons ratio of the aluminum ring (assumed to be 0.3).

The radial stress (σ_r) can be calculated from the circumferential strain (ε_θ) using the following equation (theory of thin walled cylinders):

$$\begin{aligned} \sigma_\theta &= E\varepsilon_\theta \\ \sigma_r &= \frac{\sigma_\theta t}{r} \end{aligned} \tag{4.19}$$

where σ_θ is the circumferential stress, ε_θ is the circumferential strain measured by the strain gages, E is the Young's Modulus of Aluminum (69 GPa), t is the wall thickness of the soft ring, and r is the radius of the consolidometer ring.

The soft ring was placed on a mirror-finish stainless steel base plate to reduce the friction between the ring and the base plate. The settlement of the specimen was measured with a potentiometer connected to the cDAQ through the NI 9219 input module. Signals from strain gauges and potentiometer were recorded on a portable computer continuously with frequency of 0.1 Hz and 1 Hz, respectively. A Lab View program was written for the data acquisition process. Figure 4.60 shows the setup of the modified consolidometer. The entire assembly was placed in an environmental chamber with constant temperature of 20°C and constant relative humidity of 20%. To maximize the use of the environmental chamber, two modified consolidometers were developed and placed next to one another in the environmental chamber (Fig. 4.61) to perform simultaneous testing. An accelerometer was placed in-between the consolidometers to measure any accidental disturbances/vibrations. The accelerometer data was recorded at 2000 Hz. Some of the consolidometer tests were performed using a short soft ring (height = 26.4 mm) and some with a tall soft ring (height = 50.8 mm). Test results were unaffected by the height of the soft ring.

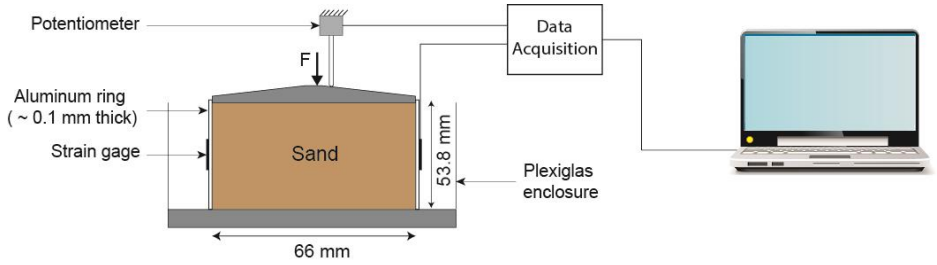

Figure 4.60. Experimental soft ring setup.

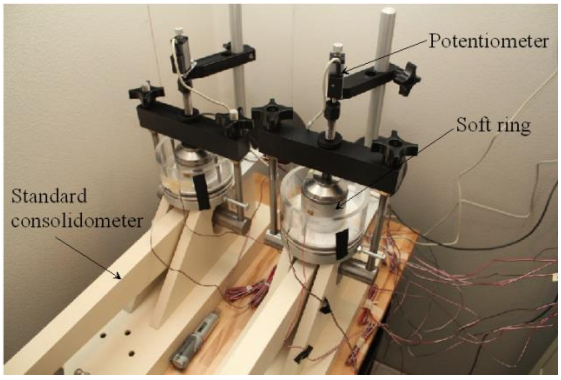

Figure 4.61. Image of the two soft-ring consolidometers in the environmental chamber.

A total of 12 tests were performed using the soft-ring consolidometer. Steel shot was used in two of the tests, and sand specimens were use in the remaining ten tests. Of the two tests on steel shot one was performed on reflective-finish hardened stainless steel ball bearing spheres of 0.125 in in diameter (3.175 mm), and the other was performed with shotgun shot of diameter 0.1 in (2.54 mm, shot #7). Of the 10 tests on sand specimens, 5 were performed on dry sands and 5 on moist/saturated sand. The steel shot and sands were placed in the environmental chamber for 1 ~ 2 days prior to testing to let the material come to ambient temperature. In the "dry tests", specimens were deposited in the ring through a funnel. Removing the specimen from a soft ring is a delicate and cumbersome process; the strain gage connecting wires snapped off in several cases, rendering the gages unusable. Whenever this happened, new rings were manufactured and used in subsequent tests.

The aluminum surface used for the soft ring was smooth compared to sand grain roughness. Figure 4.62(a) shows the SEM image of the aluminum surface (inner side of the soft ring). A scratch was made on this surface to give the image a reference. Figure 4.62(b) shows a SEM image of Ottawa 20-30 sand grain. Figure 4.62(c) shows a SEM image of the reflective-finish hardened steel shot. This surface was smooth with almost no asperities. However, some dust particles adhered to the surface during handling of the shot. Figure 4.62(d) shows a SEM image of the shotgun shot. Although the shotgun shot was relatively smooth compared to sand grains, areas of pitting (due to manufacturing and/or rusting were identified. Figure 4.62(e) shows a close up view of the rusted area. SEM image of a Lake Michigan Empire Beach sand grain is shown in Fig. 4.62(f).

Table 4.5 summarizes all the dry consolidometer tests. The reflective finish stainless ball bearing spheres had a diameter of 0.125 in, and the shot-gun shot had a diameter of 0.1 in. The Ottawa 20-30 sand was sieved to ensure no particles smaller than #30 sieve (0.6 mm) and none larger than #20 sieve (0.85 mm) were present in the test. Figure 4.63 shows the particle size gradation obtained from the sieve analysis of the two sands (Ottawa 20-30 and Lake Michigan Empire Beach sand) used in the consolidometer tests. In all the consolidometer tests (both dry and wet) granulometric analysis before and after the testing showed no changes in particle size gradation curves.

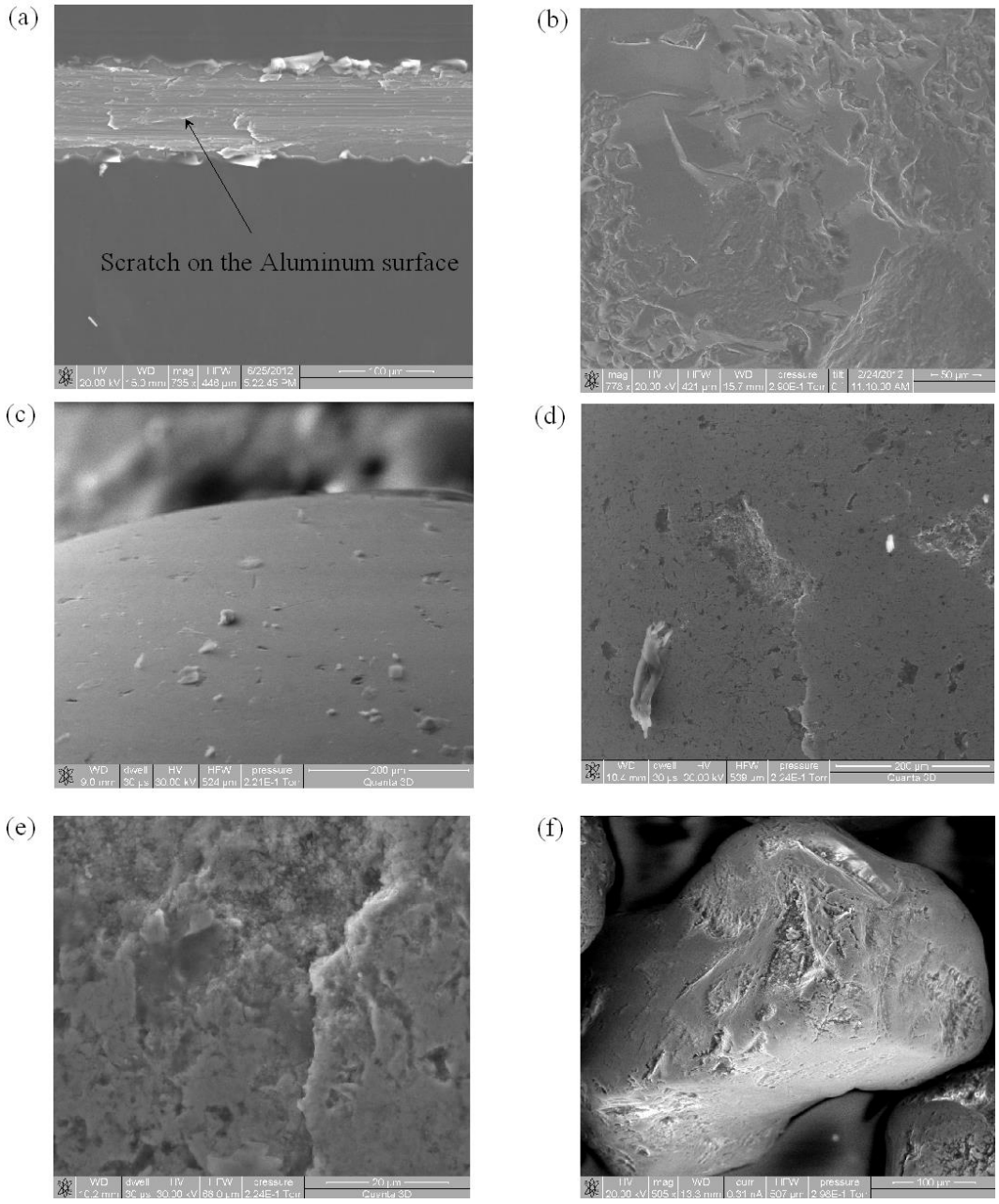

Figure 4.62. SEM images of different surfaces in the modified consolidometer tests: (a) image of the inner side of the aluminum ring (image width = 448 μm); a scratch with a sharp pin is made on the surface to give a reference, (b) image of Ottawa 20-30 sand grain surface (image width = 421μm), (c) image of the stainless steel shot (image width = 524 μm), (d) image of shot gun shot (image width = 539 μm), (e) magnified image of the rusted area in the earlier image (image width = 65 μm), and (f) image of Lake Michigan Empire Beach sand (image width = 507 μm).

Table 4.5. Summary of dry consolidometer tests.

Test #	Specimen	Porosity	Vertical stress (kPa)	Test duration
1	Reflective finish stainless steel	0.41	118.3	~ 7 days
2	Shotgun shot	0.43	229.4 in four load increments	4 days
3	Ottawa 20-30	0.42	229.4 in one load increment	7 days
4	Ottawa 20-30	0.42	229.4 in eight load increments	22 days
5	Ottawa 20-30	0.42	229.4 in four load increments	22 days
6	Ottawa 20-30	0.43	343.8 in six load increments	6 days
7	Lake Michigan Empire Beach sand	0.42	229.4 in four load increments	~ 17 days

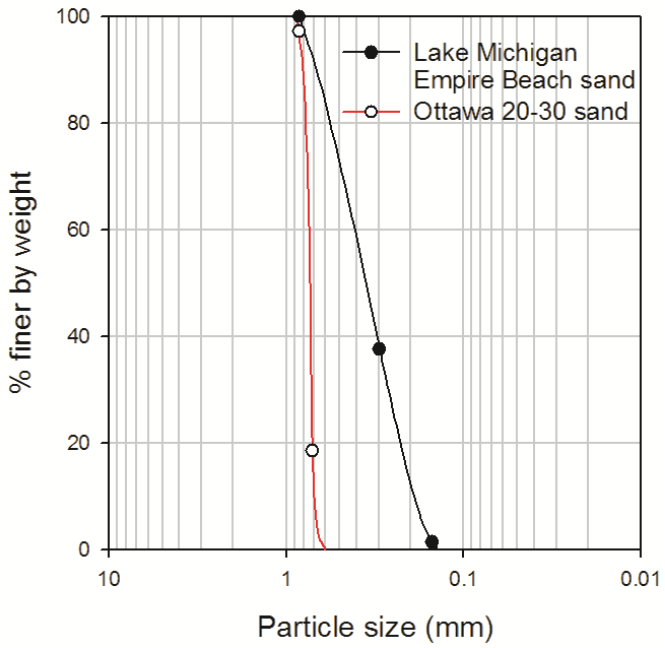

Figure 4.63. Particle size gradation curve of Lake Michigan Empire Beach sand (C_u = 2.39, C_c = 0.87) and Ottawa 20-30 sand (C_u = 1.07, C_c = 0.987).

The first test was performed using reflective finish stainless steel (E52100 Alloy) ball bearing spheres (obtained from McMaster-Carr). The spheres were 3.175 mm in diameter. Figure

4.64 shows the results from this test. After the sphere assembly was deposited into the short soft ring (height = 25.4 mm, wall thickness = 0.099 mm), a vertical load of 118.3 kPa was applied in five load steps (28.7 kPa, 57.4 kPa, 86 kPa, 114.7 kPa, 118.3 kPa). Radial stress and specimen settlement 30 minutes after application of 118.3 kPa was 116.4 kPa and 281.5 μm, respectively (Fig. 4.64). The vertical load of 118.3 kPa was kept constant for the next 7 days. The specimen continued to settle by about 3 μm for nearly a day, after which no further settlement was observed (Fig. 4.64(c)). The radial stress increased by a small amount (~ 0.2 kPa) in the first four hours after which it remained constant at 116.7 kPa for the duration of the test, Fig. 4.64(d). This result was expected as the reflective finish steel shot was smooth and had no surface asperities. Hence no change in radial stress was observed. About 7 days into the test, the data acquisition process encountered a buffer overflow problem and stopped recording the data. The test was stopped at this point. Hence the strain data during specimen unloading was not available (Fig. 4.64(a)). This test also shows the robustness in the measurement system and no drift in sensor data.

In the second test, shotgun shot obtained (Cabelas brand) was used in the specimen. Figure 4.65 shows the results from this test. The shot, 2.54 mm in diameter, was manufactured from mild steel with areas of rust on the shot 4.62(e). After the shot was deposited in the short soft ring (wall thickness = 0.099 mm), a vertical load of 229.4 kPa was applied in four equal load increments. Thirty minutes after application of 229.4 kPa, the radial stress increased to 140.3 kPa (Fig. 4.65(b)) and the specimen settlement increased to 161.6 μm. In the following 24 hours the settlement and radial stresses increased to 164 μm and 142.7 kPa, respectively (Fig. 4.65(c,d)). Geophones placed near the consolidometers picked up disturbances (vibrations) after 1 day and ten after nearly 3 days. A sudden increase in radial stress and vertical displacement can be seen at these instances. Ignoring these jumps due to external disturbances, one would conclude that radial stress and vertical displacement became nearly steady (constant) after one day.

Results from the third test are shown in Fig. 4.66. In this test, Ottawa 20-30 sand was used as the specimen in the tall soft ring (height of 50.8 mm, wall thickness = 0.089 mm). The specimen was vertically loaded to 229.4 kPa in one load increment during which a settlement of 551.2 μm and a radial stress of 112.2 kPa was recorded. Thirty minutes after application of the load these values read 562.8 μm and 113.4 kPa. In the next 7 days, the vertical stress of 230 kPa was kept constant. During this time, the radial stress increased to 117.1 kPa (Fig. 4.66(d)) and

settlement increased to 571.6 μm (Fig. 4.66(c)). Some external vibrations were detected by the geophones after 11 hours, 32.4 hours and 116.8 hours after the start of the test. At the first two instances, vibrations resulted in sudden (though small) jumps in radial stress measurement (Fig. 4.66(d)). It is interesting that the disturbances had lesser effect on vertical displacement.

The fourth test was performed using Ottawa 20-30 sand in a tall soft ring (height = 50.8 mm, wall thickness = 0.089 mm). Figure 4.67 shows the test results. The specimen was loaded to 229.4 kPa in eight equal load increments about every 30 second. The radial stress and vertical settlement immediately after applying the 230 kPa load was 118.5 kPa and 553.3 μm, respectively. Thirty minutes later, the values read 119.2 kPa and 561.3 μm. In the following 22 days, the radial stress and specimen settlement increased to 122.7 kPa (Fig. 4.67(d)) and 583.5 μm (Fig. 4.67(c)), respectively. A distinct sudden increase in radial stress at 6 days was caused by an external excitation, which was registered by geophones installed in the environmental chamber (in subsequent experiments an accelerometer was used to register any external disturbance). It is rather surprising that this disturbance did not cause a comparable anomaly in the settlement function. The time settlement curve has a clear step-wise characteristic.

The fifth test results are shown in Fig. 4.68. Ottawa 20-30 sand was used in a short soft ring (height = 25.4 mm, wall thickness = 0.115 mm). This test was done at the same time as test #4 (samples were in adjoining consolidometers). The specimen was loaded to 229.4 kPa in four load increments, each of 30 second duration. After application of vertical load of 229.4 kPa, the nearly-immediate settlement and radial stress of the specimen were 286.1 μm and 116.7 kPa, respectively. Thirty minutes after loading, they read 289.2 μm and 117.9 kPa. In the subsequent 22 days of testing, the radial stress increased to 122.1 kPa. Six days into the test, a sudden increase in radial stress was measured. This sudden increase was consistent with test #4 (geophones installed near the consolidometer picked up vibrations). During the 22 day constant load process, the settlement curve indicated a rather unusual behavior; later it was identified as faulty potentiometer; long term testing of this potentiometer indicated unexpected drift in readings; consequently, the settlement (vertical displacement) in Fig. 4.68(c) should be discarded.

Results from the sixth test performed on Ottawa 20-30 sand are shown in Fig. 4.69. The specimen was loaded to 344.1 kPa in six equal load increments, each of 30 second duration. The immediate settlement and radial stress after application of 344.1 kPa was 797 μm and 168.6 kPa.

Thirty minutes after loading, the readings were 169.8 kPa and 802.1 μm. Testing was continued for 6 more days at a constant vertical load of 344.1 kPa. During this time the settlement increased to 817.4 μm (Fig. 4.69(c)) and radial stress increased to 176.2 kPa (Fig. 4.69(d)).

The seventh test was performed on Lake Michigan Empire Beach sand. The specimen was loaded to 229.4 kPa in four equal load increments every 30 second. The nearly-immediate settlement and radial stress after application of the final vertical load was 359.7 μm and 112.5 kPa. Thirty minutes after load application, the values read 364.3 μm and 114.6 kPa. The 230 kPa vertical stress was kept for the subsequent 17 days. The specimen settled to 398.3 μm (Fig. 4.70(c)) and radial stress increased to 122.4 kPa (Fig. 4.70(d)) during this time. For the first 7.5 days of this test, the environmental chamber was accessed every day to check the status of another test that was simultaneously running. This caused unwanted vibrations, measured by the accelerometer. This resulted in jumps in radial stress measurement in the first 7.5 days.

In general, comparing all the dry test results, it was observed that at a constant vertical stress, the increase of radial stress continued at a decreasing rate with time. Comparing results from test 1 and 2 (Figs. 4.64, 4.65), it was observed that surface morphology (in this case, rust on the steel shot) produced changes in radial stress in time, at least in the first 24 hours. Results from tests 4 and 5 (Fig. 4.67, 4.68) indicate that the two soft ring height used for testing have negligible influence on radial stress measurement values. Comparing tests 3, 4 and 5 it was seen that the faster the loading rate prior to the period of constant vertical load, the greater the rate of increase in radial stress during ageing in the initial days. When a load of 230 kPa was applied on Ottawa 20-30 sand in one step the radial stress increased by about 3.5 kPa in 6 days; when the same load was applied in four steps (30 seconds for each step) the radial stress increased by 2.5 kPa in 6 days; when applied in eight steps (30 seconds for each step) the radial stress increased by 2.2 kPa in 6 days. This observation follows the nano-indentation test results, where the faster rate of loading prior to creep test caused the larger creep displacement of the nano-indenter. Comparing tests 5 and 6 (Figs. 4.68, 4.69) it was observed that the larger the load, the greater the rate of increase in radial stress. It was interesting to notice that the increase in radial stress of Lake Michigan Empire Beach sand was larger than that for Ottawa 20-30 sand (Figs. 4.68 and 4.70). This observation suggests that the grain surface morphology does influence the aging process, and this is consistent with the hypothesis proposed.

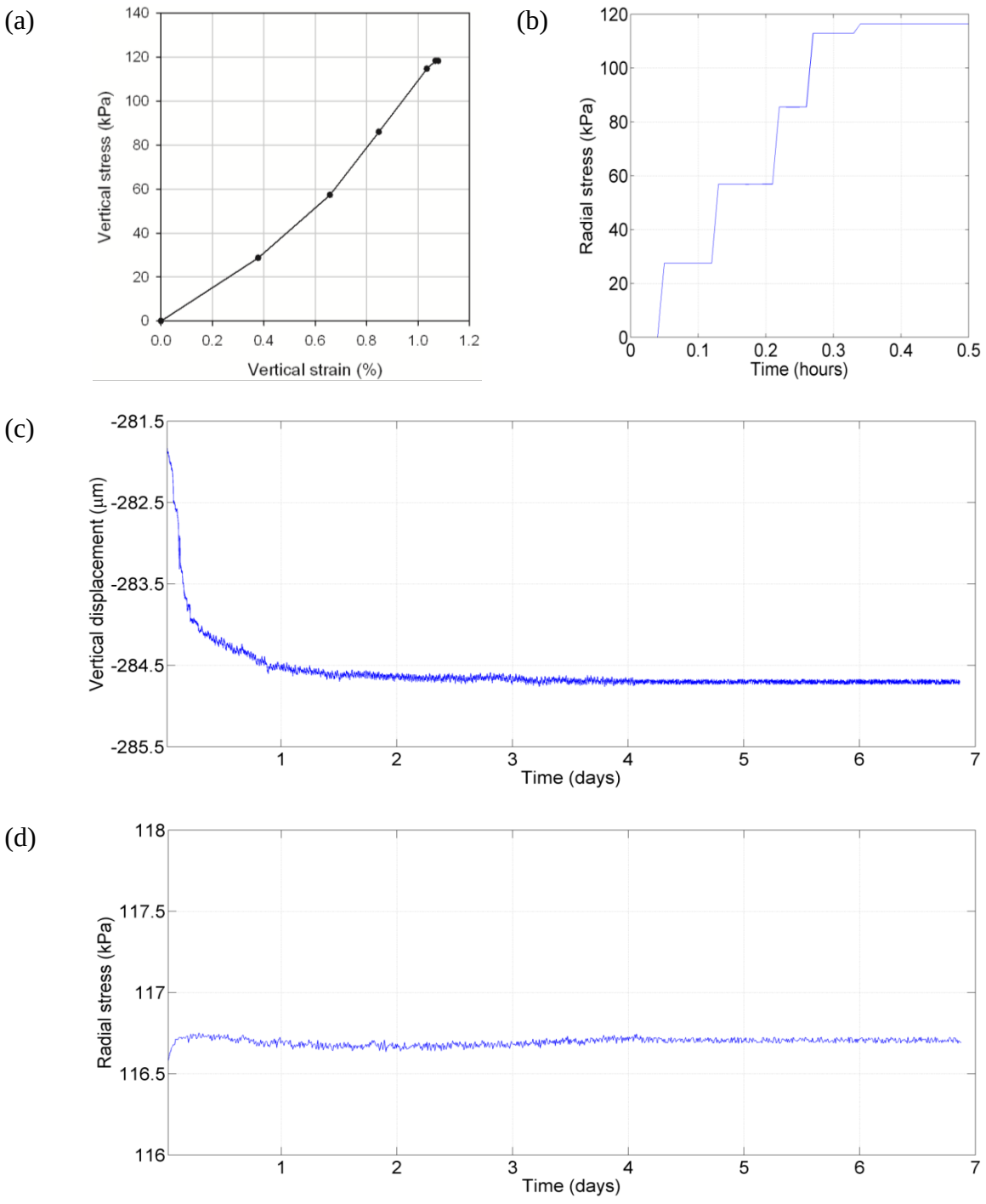

Figure 4.64. Results from consolidometer test #1 (reflective finish steel spheres in soft ring), (a) vertical stress vs. vertical strain during loading and 7 day constant load (unloading portion of the curve is unavailable), (b) increase in radial stress during the loading process (5 load increments), (c) settlement of the specimen after initial 30 min of loading, and (d) radial stress as a function of time (constant vertical stress of 118.3 kPa).

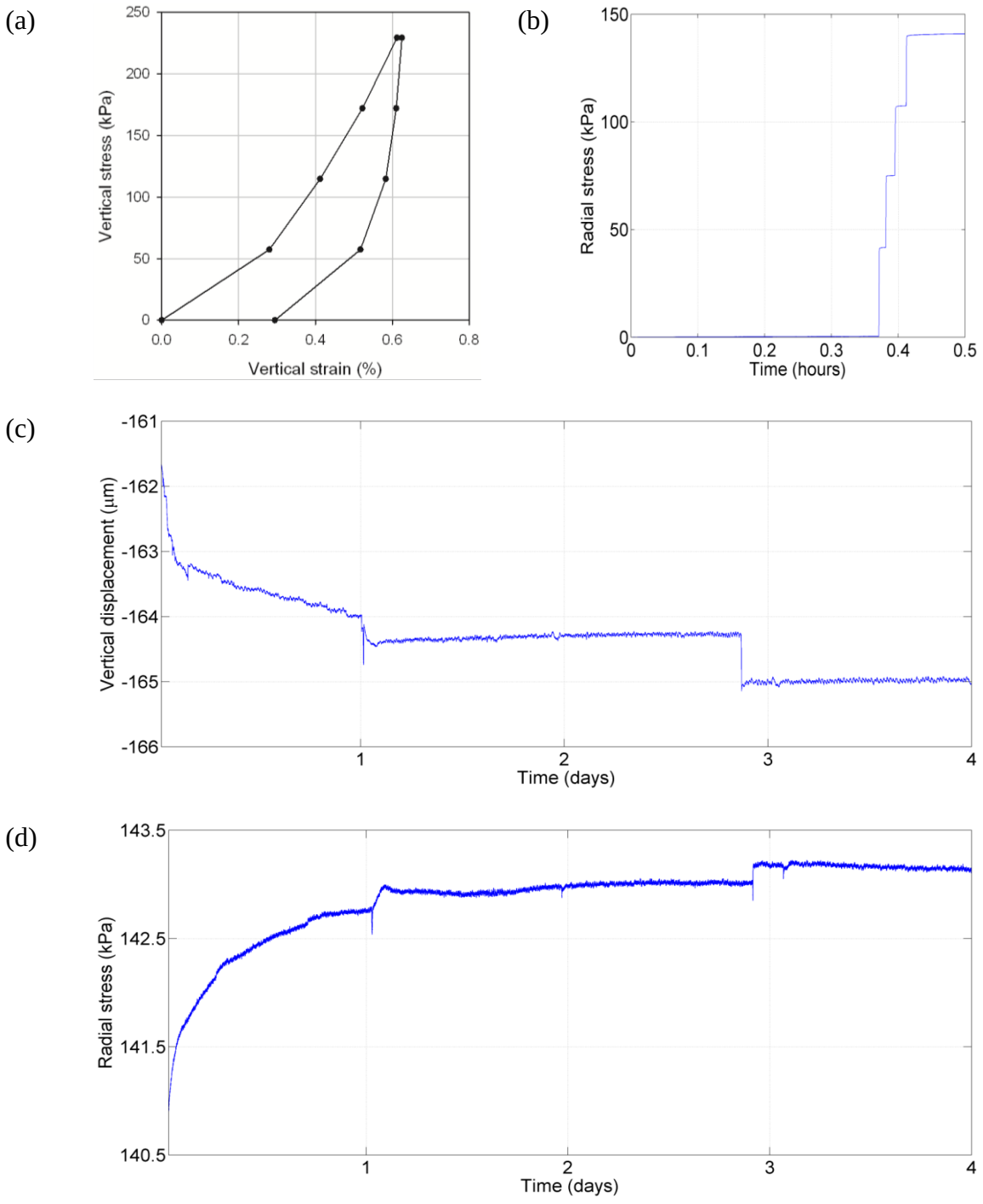

Figure 4.65. Results from consolidometer test #2 (shotgun shot in a short soft ring), (a) vertical stress vs. vertical strain plot during loading, 4 day constant load, and unloading, (b) increase in radial stress during the loading process (four load increments), (c) settlement of the specimen after initial 30 min of loading, and (d) radial stress as a function of time (constant vertical stress of 229.4 kPa).

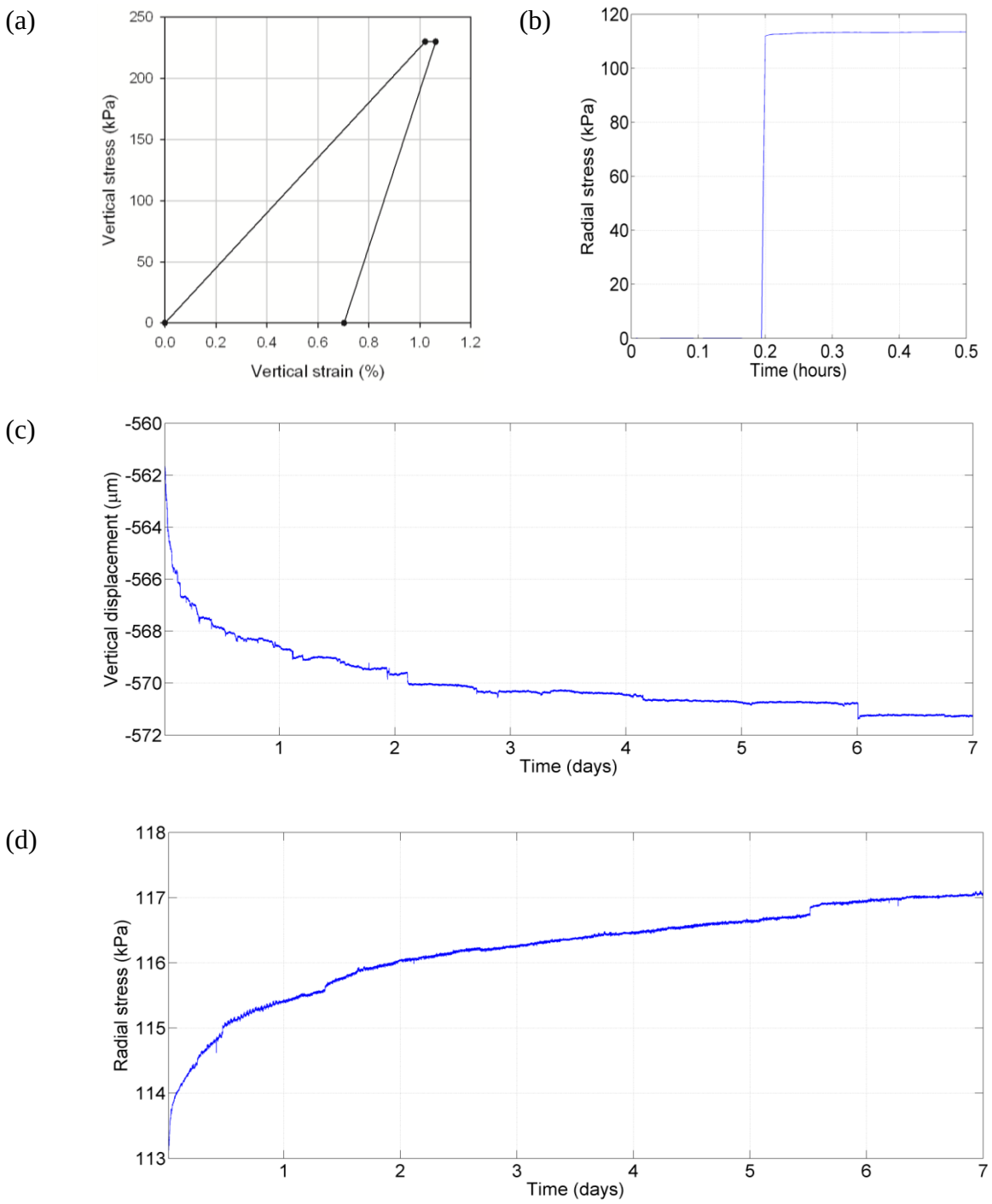

Figure 4.66. Results from consolidometer test #3 (Ottawa 20-30 sand in tall soft ring), (a) vertical stress vs. vertical strain plot during loading, 7 day constant load, and unloading; vertical stress of 229.4 kPa is applied in one step, (b) increase in radial stress during the loading process; application of the vertical stress resulted the radial stress increase of 113.4 kPa, (c) settlement of the specimen after initial 30 min of loading, and (d) increase in radial stress as a function of time (constant vertical stress of 229.4 kPa).

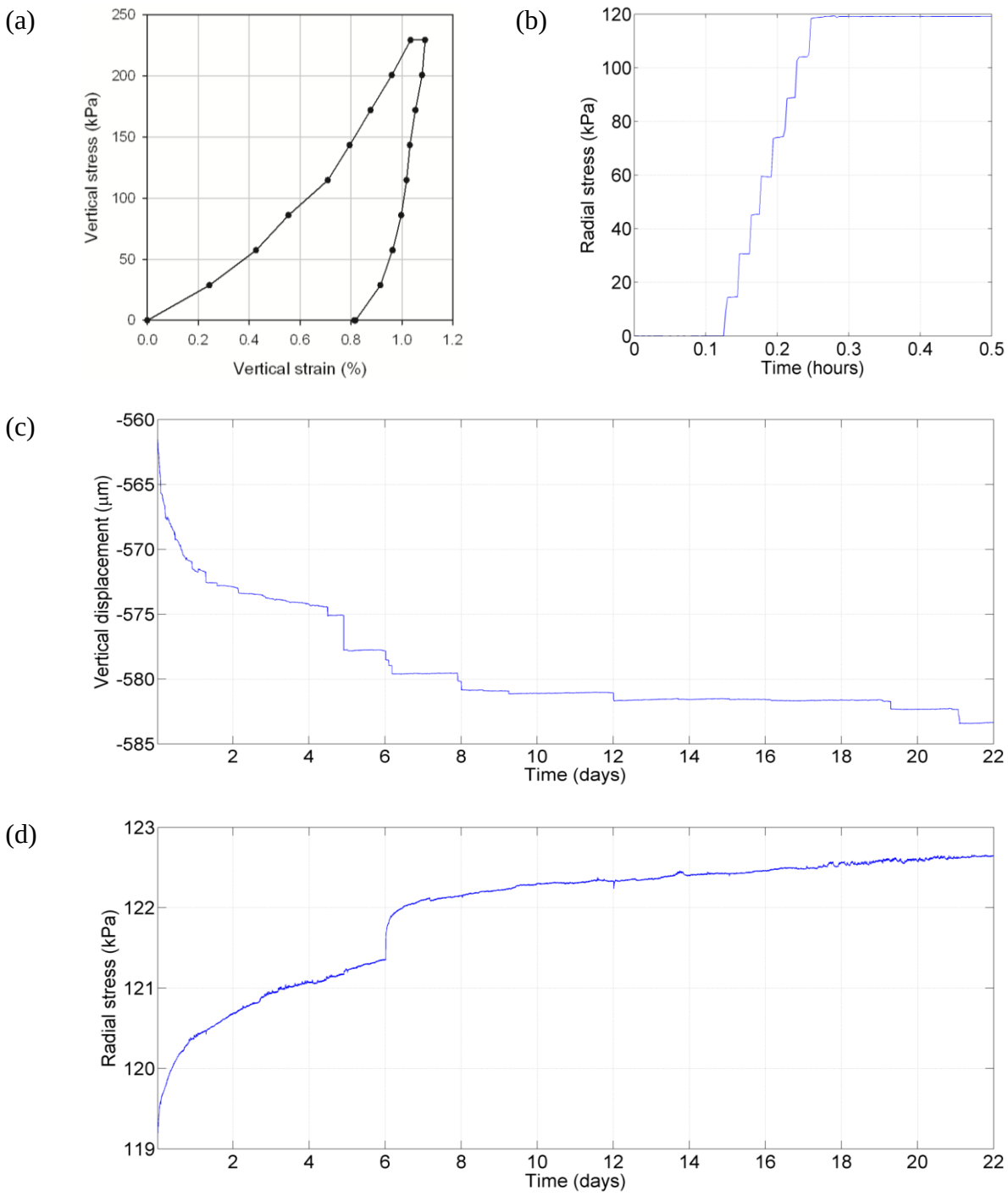

Figure 4.67. Results from consolidometer test #4 (Ottawa 20-30 sand in tall soft ring), (a) vertical stress vs. vertical strain plot during the loading, 22 day constant load and unloading; vertical stress of 229.4 kPa is applied in eight equal load increments, (b) increase in radial stress during the loading process (8 load increments); application of the vertical stress resulted in the radial stress increase of 118.8 kPa, (c) settlement of the specimen after initial 30 min of loading, and (d) increase in radial stress as a function of time (constant vertical stress of 229.4 kPa).

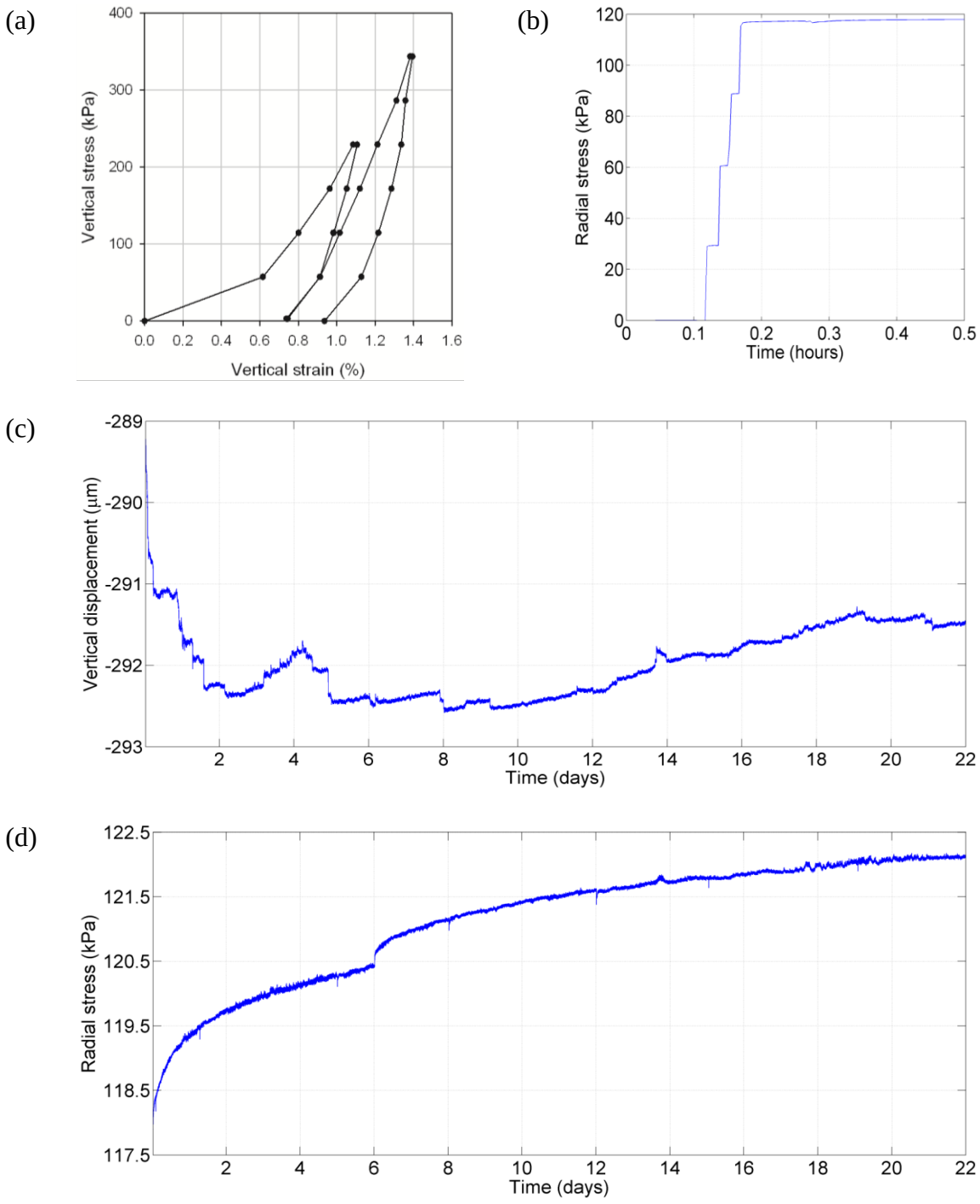

Figure 4.68. Results from consolidometer test #5 (Ottawa 20-30 sand in short soft ring), (a) vertical stress vs. vertical strain plot during loading, 22 day constant load and unloading; vertical stress of 229.4 kPa is applied in four equal load increments, (b) increase in radial stress during the loading process; application of the vertical stress resulted in the radial stress to increase to 117.9 kPa, (c) settlement of the specimen after initial 30 min of loading, and (d) increase in radial stress as a function of time (constant vertical stress of 229.4 kPa).

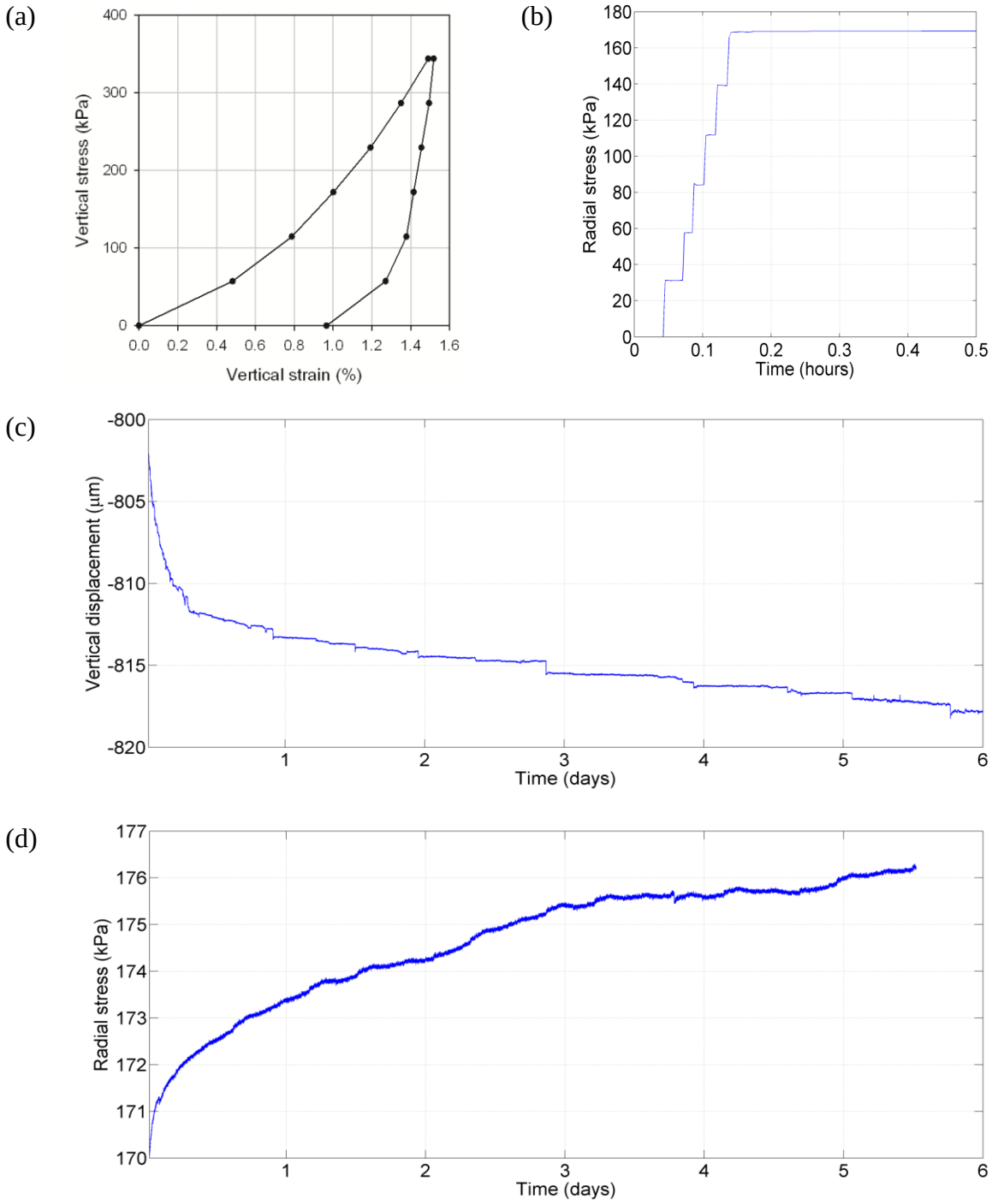

Figure 4.69. Results from consolidometer test #6 (Ottawa 20-30 sand in tall soft ring), (a) vertical stress vs. vertical strain plot during loading, 6 day constant load and unloading process; vertical stress of 344.1 kPa is applied in six equal load increments, (b) increase in radial stress during the loading process; application of the vertical stress resulted in the radial stress to increase to 169.6 kPa, (c) settlement of the specimen after initial 30 min of loading, and (d) increase in radial stress as a function of time (constant vertical stress of 344.1 kPa).

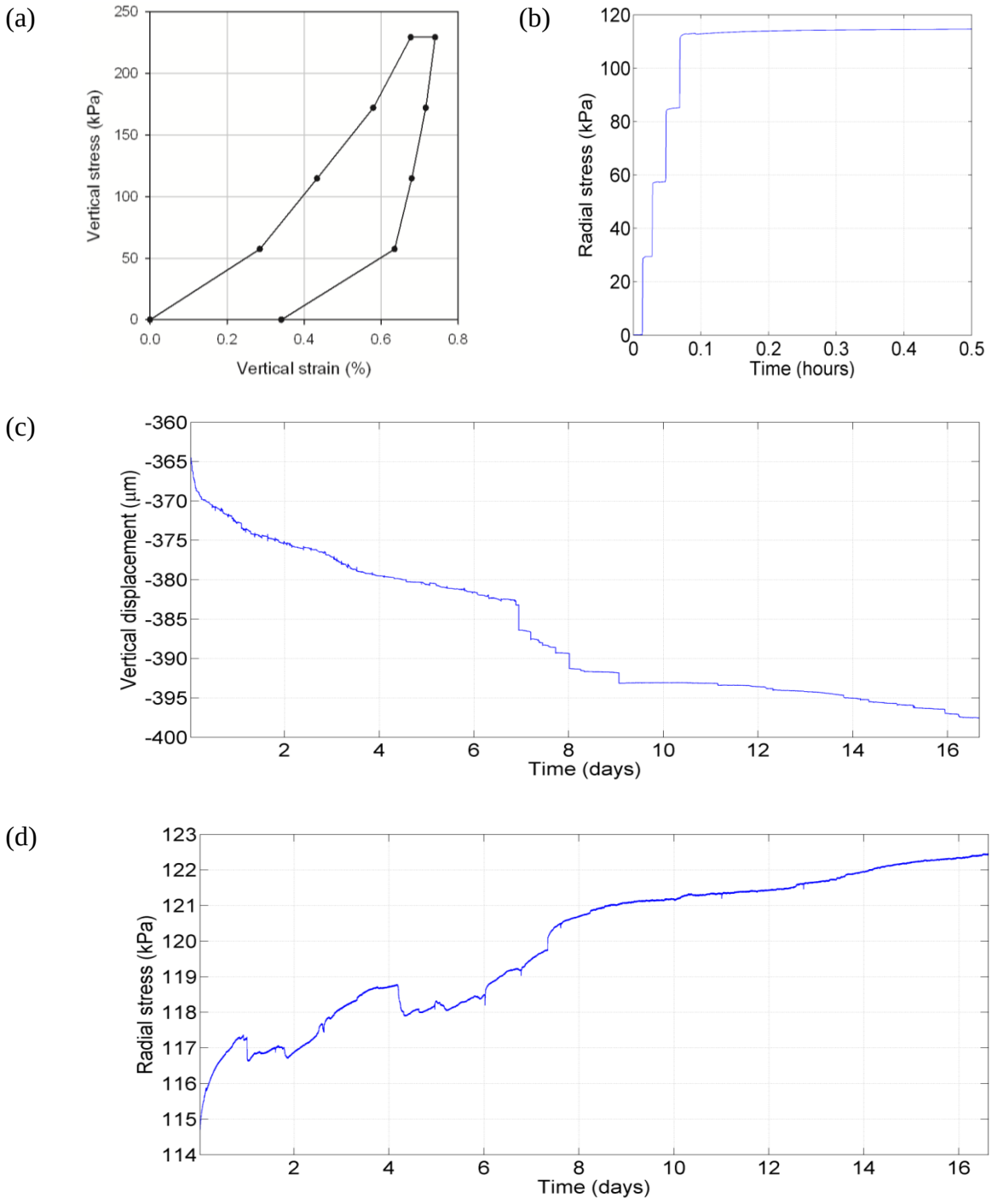

Figure 4.70. Results from consolidometer test #7 (Lake Michigan Empire Beach sand), (a) vertical stress vs. vertical strain plot during the loading, 17 day constant load and unloading process; vertical stress of 229.4 kPa is applied in four equal load increments, (b) increase in radial stress during the loading process; application of the vertical stress resulted in the radial stress to increase to 114.4 kPa, (c) settlement of the specimen after initial 30 min of loading, and (d) increase in radial stress as a function of time (constant vertical stress of 229.4 kPa).

A total of 5 "wet" tests were performed using the soft ring consolidometer. The height of the soft ring seemed to have negligible influence on the radial stress measurement (see tests 4 and 5, Figs. 4.67 and 4.68); for a vertical load of 230 kPa on Ottawa 20-30 sand, the radial stress in the tall (50.8 mm) and short (25.4 mm) soft rings were 119.2 kPa and 117.9 kPa, respectively. The wet tests were performed all using the tall soft ring. The taller soft ring was easier to handle during specimen placement and removal. Initially, wet tests were performed by placing a saran wrap in the soft ring and filling with water. However, because the increase in the ring's circumferential strain (caused by the increase in the radial stress) measured during aging was small (~ 10^{-6}), the influence of creep in the saran wrap had an effect of the measured magnitudes. Consequently, the wet sand tests were performed without saran wrap, by filling the Plexi-glass enclosure surrounding the soft ring with water (Fig. 4.61), such that the water level was just below the strain gage (~ 2.2 cm above the base). As the soft ring was placed on the stainless steel base plate without sealing, water could move freely in and out beneath the ring. The sand was then deposited into the ring using a funnel.

As the bottom part of the ring (~ 2.2 cm) was filled with water, the sand in that part was saturated. The upper portion of the specimen was kept moist due to capillary suction in the sand. The porosity of the specimens so created was 0.40 ~ 0.44. After the ring was filled with the sand, a stainless steel loading cap was placed on the. There was a 1.5 mm gap between the soft ring and loading cap. The entire consolidometer was placed in an environmental chamber with the temperature maintained at 20°C and relative humidity of 20%. Evaporation of water from both the Plexi-glass enclosure (Fig. 4.61) and through the ring-loading platen gap was taking place. Therefore, keeping the water in the Plexi-glass enclosure at the needed level required a small amount of water to be added every 24 hours by physically entering the environmental chamber. As these tests are very sensitive to external disturbances, the undesired vibrations caused by entering the chamber (and measured by the accelerometer), showed up in the radial stress and potentiometer readings.

The five wet tests were performed on Ottawa 20-30 sand under a vertical load of 230 kPa, and water with different pH. Two of the tests were performed with acidic solutions and two were with basic solutions. One test was performed with distilled water. For the acidic solutions, sufficient quantity of distilled water was mixed with 2N Hydrochloric acid (HCl) to make acidic aqueous solutions. For basic solutions, of Sodium Hydroxide (NaOH) was mixed with sufficient

quantity of distilled water to make basic aqueous solutions. All the aqueous solutions used in the tests were placed in the environmental chamber for 2 ~ 3 days before starting the test to ensure the solution comes to ambient temperature.

In addition to measuring the circumferential strain of the ring and vertical settlement during aging, the pH and Total Dissolved Solids (TDS) were also measured at the start and the end of all tests. The pH of water was measured by 'Oakton Eco Tester pH 2' meter (resolution of 0.1). TDS is generally used as a measure of water quality. It is a measure of any mineral, salt, cation or anion dissolved in water. Excluding suspended solids, anything present in water apart from pure water molecules (H_2O) is measured in TDS. Since the electrical conductivity of water is a function of the dissolved ions present in it, the measurement of the conductivity of water can be correlated to TDS. In the present tests, TDS was measured by using 'HM Digital TDS-EZ water quality TDS tester'. Table 4.6 summarizes the wet tests. Tests 8 & 12 were performed at the same time on adjacent consolidometers. This means both were subjected to the same external vibrations. Similarly, tests 9 and 11 were performed at the same time using adjacent consolidometers.

Table 4.6. Summary of wet consolidation tests on Ottawa 20-30 sand at a vertical load of 229.4 kPa (applied in four equal load increments).

Test #	Aqueous solution	Porosity	Test duration	pH		TDS (ppm)	
				Initial	Final	Initial	Final
8*	Acidic (pH 5.5)	0.41	14 days	5.5	6.3	16	88
9**	Acidic (pH 6.5)	0.45	11.5 days	6.5	8.1	216	353
10	Distilled water (pH 6.8)	0.42	10 days	6.8	7.1	0	45
11**	Basic (pH 7.8)	0.45	11.5 days	7.8	7.5	4	63
12*	Basic (pH 9.5)	0.42	14 days	9.5	7.2	77	136

* These two tests were performed on adjacent consolidometers at the same time.
** These two tests were performed on adjacent consolidometers at the same time.

Results from test #8 are shown in Fig. 4.71. This test was performed using a pH 5.5 solution. The initial TDS of the solution was 16 ppm. On applying the load of 230 kPa, the immediate settlement was found to be 454.5 μm and radial stress was measured to be 94.4 kPa. 30 minutes after loading, the specimen settlement and radial stress were 462.3 μm and 93.96 kPa, respectively. In the subsequent 14 days of constant load, the specimen vertical displacement and radial stress increased to 476.4 μm (Fig. 4.71(c)) and 96.73 kPa (Fig. 4.71(d)). The

accelerometer recorded vibrations every time the user walked into the environmental chamber to refill the solution in the Plexiglas enclosure (Fig. 4.61). Vibrations were noticed after 44, 92.7, 139, 183, 210.8, 232.3 and 276.4 hours after the start of the test. These vibrations caused sudden drops in radial stress and settlement measurement. Since test #12 was also performed during the same time in an adjoining consolidometer, results from test #12 were also affected. The pH and TDS of the aqueous solution in contact with the sand (solution inside the soft ring) in test #8 were originally 5.5 and 16, respectively, and after the test, they changed to 6.3 and 88 ppm, respectively.

Results from test #9 are shown in Fig. 4.72. This test was performed using a pH 6.5 solution. The initial TDS of this solution was 216 ppm. This high value of TDS is unusual and could be attributed to some unknown impurity that might have accidentally entered into the aqueous solution. On applying the load of 229.4 kPa, the initial settlement of the specimen was 696 μm and radial stress was 145.8 kPa. Thirty minutes after load application, specimen settlement and radial stress read 703.3 μm and 146.2 kPa respectively. The load of 229.4 kPa was kept constant for the subsequent 11.5 days. The specimen settlement at the end of the test was 721.3 mm (Fig. 4.72(c)). The radial stress at the end of the test read 145.4 kPa. After about 11.5 days, a buffer overflow error caused the data acquisition to stop recording. Hence the unloading part of the vertical stress-strain curve is unavailable (Fig. 4.72(a)). This data acquisition failure also affected results from test #11, which was performed simultaneously. The final measured pH and TDS were 8.1 and 353 ppm, respectively.

Results from the distilled water test (test #10) are shown in Fig. 4.73. The initial pH of the water was 6.8 and there were no dissolved solids (TDS = 0). Immediately after applying the 229.4 kPa vertical load, the vertical settlement and radial stress read 616.8 μm and 104.3 kPa. 30 minutes after loading, the vertical settlement increased to 623.7 μm and radial stress increased to 105.6 kPa. The vertical settlement and radial stress continued to increase for the subsequent duration of the test. 10 days after loading with 229.4 kPa, the vertical settlement was 638.2 μm and 113 kPa.

Figure 4.74 shows results from test #11. This test was performed using a pH 7.8 basic solution. The initial TDS of this solution was 4 ppm. The immediate settlement of the specimen after applying 229.4 kPa vertical stress was 607.8 μm. The radial stress read 140.1 kPa. 30 minutes after loading, specimen settlement and radial stress read 613.9 μm and 140.4 kPa. The

vertical stress of 229.4 kPa was kept constant for the subsequent 11.5 days. The final vertical settlement was 638.7 μm and final radial stress was 144.2 kPa. At the end of the test, pH dropped down to 7.4 and TDS increased to 63 ppm. The pH of the pore water obtained from the sand specimen using a centrifuge was 5.

Results from test #12 are shown in Fig. 4.75. This test was performed using a basic solution (pH = 9.5). The initial TDS of the solution was 77 ppm. On applying the load of 230 kPa, the immediate settlement was found to be 504.6 μm and radial stress was measured to be 117.6 kPa. 30 minutes after loading, the specimen settlement and radial stress were 511.1 μm and 117.9 kPa, respectively. In the subsequent 14 days of constant load, the specimen vertical displacement and radial stress increased to 528.9 μm and 117.2 kPa, respectively. It is interesting to note that while a settlement of 17.8 μm was observed, the radial stress dropped down by 0.7 kPa compared to the 30 min value. The pH and TDS of the aqueous solution in contact with the sand specimen after the test was 7.2 and 136 ppm. The pore water extracted from the specimen at the end of the test had the pH of 5.1.

The solubility of Quartz is 6 ppm (Iler, 1979). Hence the high TDS values observed after the wet consolidometers test (Table 4.6) could not be due to the solubility of Quartz alone. There could be other minerals present in the sand that might be contributing to the high TDS value. To understand better the changes in pH and TDS, solubility tests were performed on Ottawa 20-30 sand. In these tests, 30 grams of Ottawa 20-30 sand was poured in four 75 ml aqueous solution flasks at different pH's. The flasks were covered to prevent evaporation and were kept at room temperature (23°C). pH and TDS measurements were taken from time to time. Two of the aqueous solutions were acidic (pH = 4.4 and 5.7), one was basic (pH = 8.8) and one had distilled water (pH = 6.2). The acidic solutions were prepared by mixing HCl in distilled water. The basic solution was prepared by mixing NaOH with distilled water. Figure 4.76 shows the change in pH and TDS with time. Irrespective of what pH solution was mixed with the silica sand, the pH reached the value of about 5 in less than 2 days. This pH is the same as that of the pore water obtained from centrifuge tests on sands in tests 11 & 12. The TDS on the other hand, kept increasing with time. The TDS in acidic solutions was higher than for basic solutions, and it was the least when the distilled water was used. The solubility of quartz is almost a constant for pH's less than 9 and for pH's greater than 9 the solubility increases dramatically due to the ionization of silicic acid (Krauskopf, 1995). However, the solubility tests performed show a different trend.

Hence, there might had been some other minerals, apart from Quartz, that was dissolving. Also, the high value of TDS observed in Fig. 4.76(b) suggests that some other material, in addition to Quartz, had to be dissolving (the solubility of quartz is about 6 ppm; Iler, 1979). Ottawa 20-30 sand has 99 ~ 99.9% Quartz, < 1% Aluminum Oxide, < 0.1% Iron Oxide and Titanium Oxide (from the MSDS of Ottawa 20-30 sand obtained from US Silica Co.). Therefore, in 30 grams of sand, there is about 0.03 grams of impurities (assuming 0.1% materials other than Quartz). Hence in a 75 ml of solution, assuming all the impurities dissolve, the maximum TDS would be 400 mg/l or 400 ppm. The TDS values observed in the solubility tests were below this value. The observed changes in TDS could be owed to the dissolving of the trace impurities in the sand. The pH of about 5 reached in less than two days in all tests could be due to these impurities dissolving in the aqueous solutions.

In consolidometer tests 11 and 12, while the pH of the pore water was about 5, the pH of the water in the Plexiglas enclosure was 7.5 and 7.2, respectively. This discrepancy is owed to the replenishing the level of water with water of designed pH every 1 to 2 days, and due to limited mixing (and chemical diffusion) of the pore water in the sand specimen and that in the Plexiglas enclosure. The change in TDS values before and after wet consolidometer tests was found to be larger than that obtained from the solubility tests. This suggests that the loading process has an influence on the solubility, i.e., the pressure dissolution at the grain contacts could be occurring.

After the wet consolidometer tests, the specimens were dried in an oven at 50°C for one day (some had the pore fluid extracted in a centrifuge first). SEM imaging of grains from tests #8, 10, 11 and 12 did not reveal any distinct changes on grain surfaces. A few of the grains from test #9, after drying, seemed to have clumped together. SEM images of these grains are shown in Fig. 4.77. The grains appear to have fused together. This is due to dissolved solids (TDS = 353) getting precipitated at contacts during evaporation of water in the oven. It is interesting to note that no clumps were found in the other tests. The TDS values of the other samples (88, 45, 63 and 136) were lower than the TDS value in test #9 (353). Energy dispersive X-Ray analysis of both the areas in-between grains and the actual grains from test #9 indicated the presence of Silicon, Oxygen, Aluminum and Carbon. Joshi et al. (1995) also observed similar precipitation in between sand grains after drying. Based on the SEM images, Joshi et al. (1995) suggested a bonding mechanism to be responsible for aging in sands. However, the bonding seen by Joshi et

al. could be due to the precipitation of the dissolved solids at grain contacts during sample drying, and such bonds may not form in saturated sand.

It has been well established that environmental factors, such as moisture, have crucial effect on the process of subcritical fracturing (Cuallar et al. 1987). The wet consolidometer tests support this observation. It is interesting to note that while in the acidic solution consolidometer tests pH increased at the end of the test, in basic solutions, pH decreased. In consoldiometer test #9, the radial stress (during constant vertical stress) increased for about 1 day, after which it began to decrease. Pressure dissolution causes loss of mass from the contact, which is likely to cause stress relaxation in a confined specimen. Pressure dissolution usually occurs under high confining pressures (MPa range) and at high temperatures (> 100°C) (DeBoer et al., 1977; Robin 1978). Although these conditions were not present in the consolidometer tests performed, the idea of mineral dissolution at contacts is reasonable.

The change in the radial stress (at constant vertical stress) is also consistent with softening of contacts. It is evident from Equation (4.17) that preservation of strain energy requires reduction in radial stress if Young's modulus is reduced. The softening of the sand at the macroscopic scale may be due to pressure dissolution of minerals at contacts (decrease in contact stiffness) in the acidic environment.

Quartz dissolves in water to form silicic acid (a silanol):

$$SiO_2 + 2H_2O \rightarrow H_4SiO_4(aq) \tag{4.20}$$

The solubility of quartz increases with pressure and temperature (Dove and Rimstidt, 1994), though all consolidometer tests were performed at constant temperature. At higher pressures, density of water increases causing an increased interaction between the water molecules and the OH groups of the silicic acid (Chakoumakos and Gibbs, 1986). This results in an increased frequency of the dipolar water molecule coming into contact with silicic acid, resulting in an increased hydrogen bonding, thereby increasing the solubility of Quartz. The rough nature of the sand grains was discussed in section 4.2.1. When the asperities get loaded, some of the water could be trapped in between the asperities and thus might be subjected to high pressures. This could cause a local increase in solubility of the grain surface, thereby resulting in pressure dissolution.

The grain-grain contact tests performed on sand grains in section 4.5.2 showed that the asperities fracture and crack over time. These freshly fractured surfaces and crystalline debris have exposed silicon and oxygen bonds which are unstable and can bond with water forming SiOH or silanol groups (Parks, 1984; Dove and Rimstidt, 1995). This adsorbed film can grow in size over time and can ionize in the presence of water giving it a net surface negative charge which can, in turn, attract cations from the aqueous solution. All this affects the stiffness of the broken crystalline debris.

Using electron diffraction, Alexanian (1956) (from Iler, 1979) found that quartz has a surface layer of amorphous silica about 100 ångströms thick, which is formed under ambient humidity. The solubility of amorphous silica is higher than that of crystalline silica (Quartz) (about 120 ppm; Iler, 1979). The solubility of Quartz is affected by the specific surface area of the particles, temperature, and pH of the solution (Iler, 1955; Krauskopf, 1959; Krauskopf and Bird, 1995). Ganischenko et al. (1960) (from Iler, 1979) found that intense pulverization of quartz in water caused an increase in solubility (from less than 10 ppm to 70 ppm at 25°C). All these factors could assist in pressure dissolution of the silica grain asperities.

The shape of the asperities also affects the dissolution process. Smaller particles of quartz tend to dissolve and small fractures tend to be healed (Dove and Rimstidt, 1994). While the presence of salts accelerates the rate of crack healing, presence of CO_2 decelerates it (Brantley, 1992).

Granulometric analysis before and after consolidometer testing showed no changes in particle size gradation. Hence particle crushing as evidenced by Lade et al. (2010) could not be responsible for the observed time effects. In the dry consolidometer tests, the increase in radial stress and step-wise settlement of the specimen is consistent with static fatigue occurring at grain contacts. While the exact reason for the observed trends in radial stress in the wet consolidometer tests are still not known, it is likely that the grain asperities could be getting softer due to pressure dissolution mechanisms.

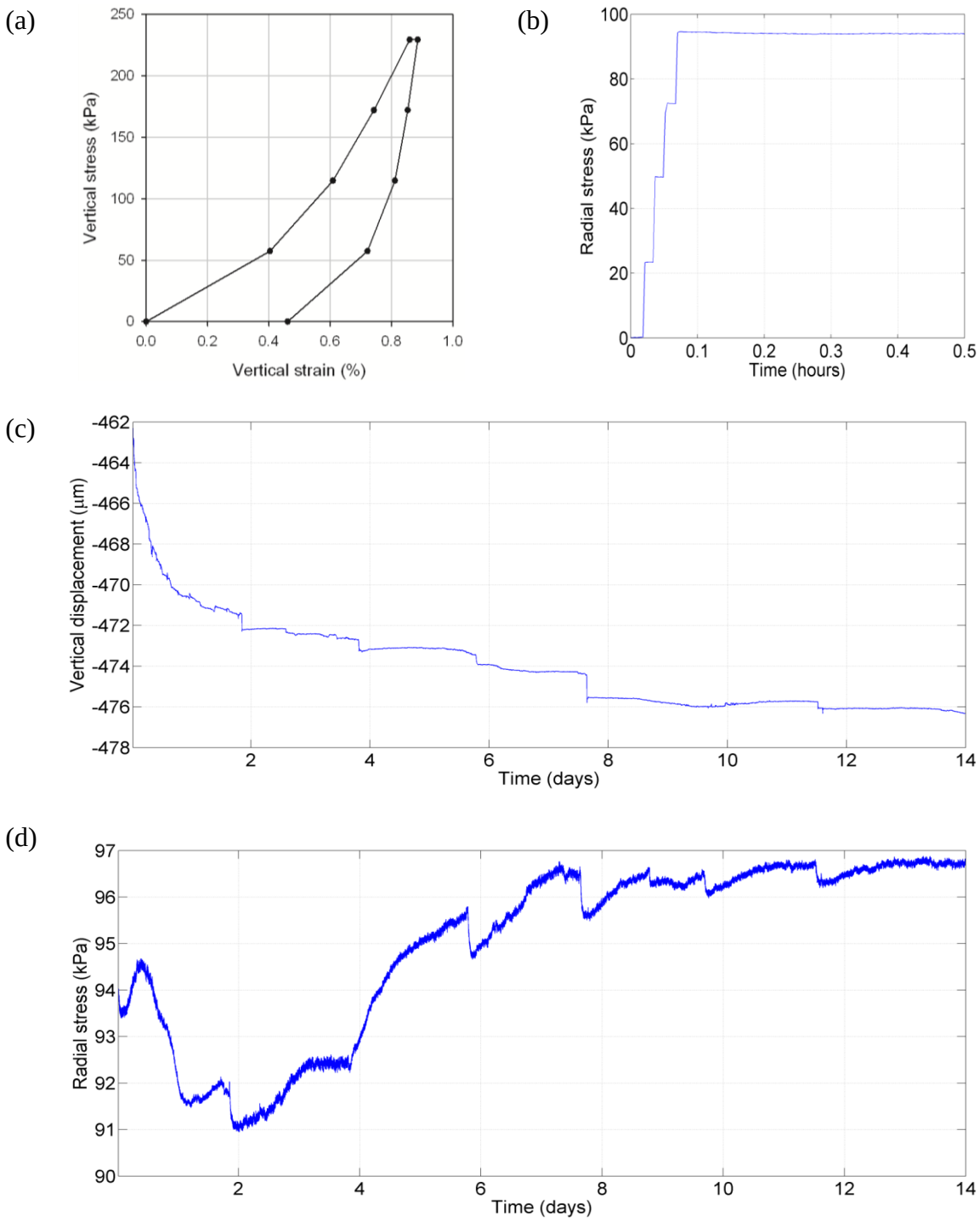

Figure 4.71. Results from consolidometer test #8 (Ottawa 20-30 sand in a pH 5.5 aqueous solution), (a) vertical stress vs. vertical strain plot during loading, 14 day constant load and unloading, (b) increase in radial stress during loading, (c) settlement of the specimen after initial 30 min of loading, and (d) increase in radial stress as a function of time.

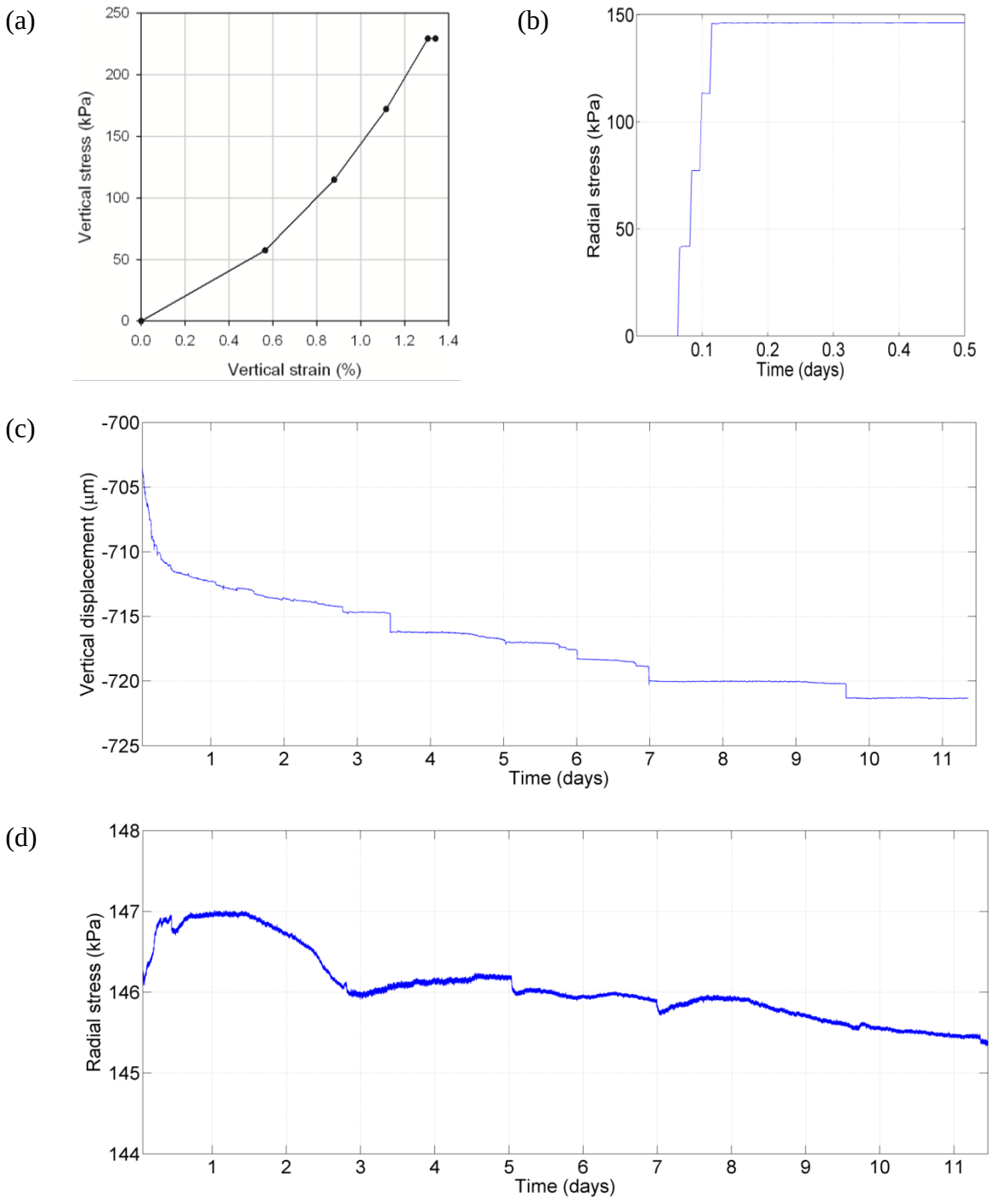

Figure 4.72. Results from consolidometer test #9 (Ottawa 20-30 sand in a pH 6.5 aqueous solution), (a) vertical stress vs. vertical strain plot during loading and 11.5 day constant load, (b) increase in radial stress during the loading process, (c) settlement of the specimen after initial 30 min of loading, and (d) increase in radial stress as a function of time.

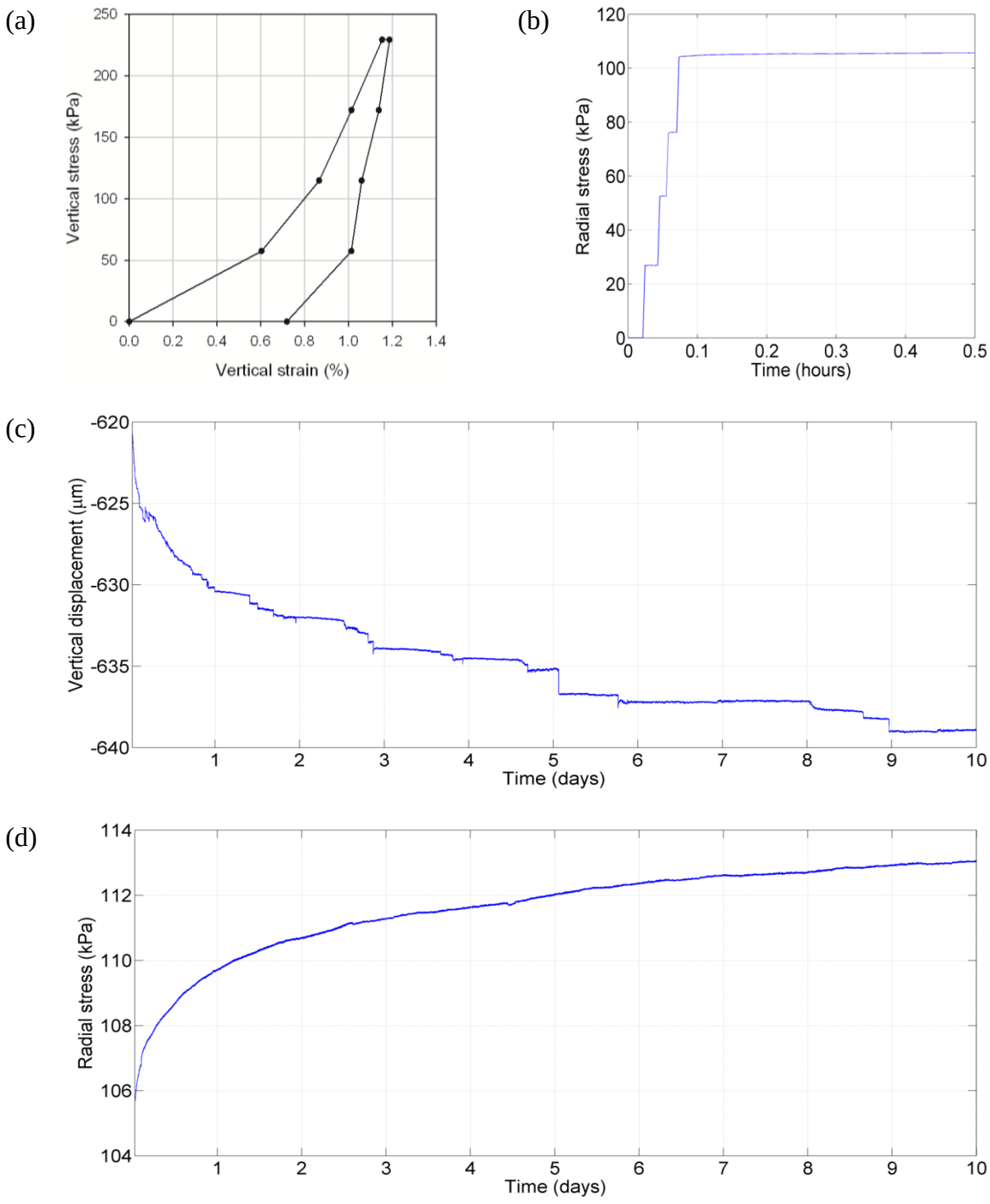

Figure 4.73. Results from consolidometer test #10 (Ottawa 20-30 sand in a pH 6.8 aqueous solution), (a) vertical stress vs. vertical strain plot during loading,10-day constant load, and unloading, (b) increase in radial stress during the loading process, (c) settlement of the specimen after initial 30 min of loading, and (d) increase in radial stress as a function of time.

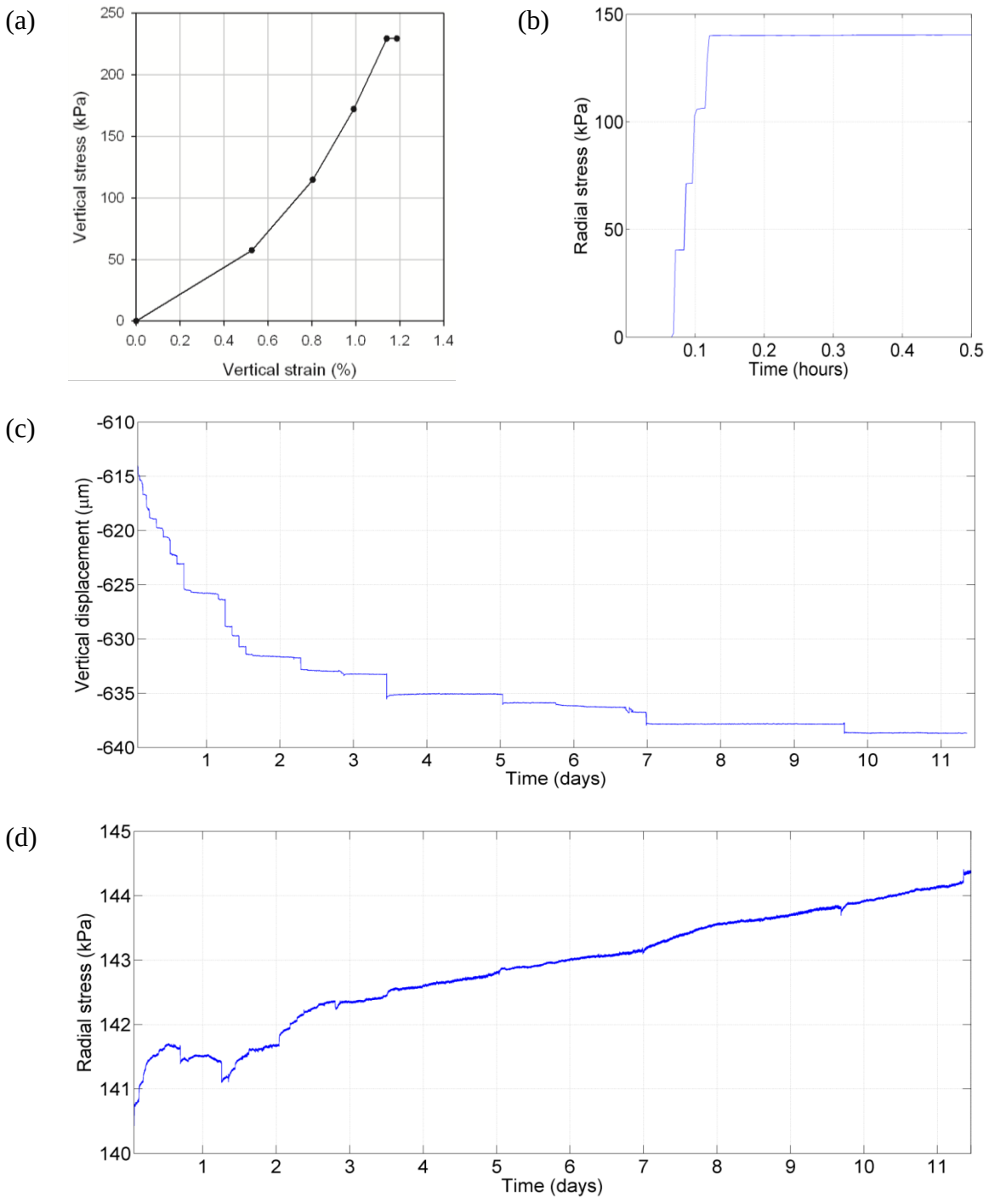

Figure 4.74. Results from consolidometer test #11 (Ottawa 20-30 sand in a pH 7.8 aqueous solution), (a) vertical stress vs. vertical strain plot during loading and 11.5 day constant load, (b) increase in radial stress during the loading process, (c) settlement of the specimen after initial 30 min of loading, and (d) increase in radial stress as a function of time.

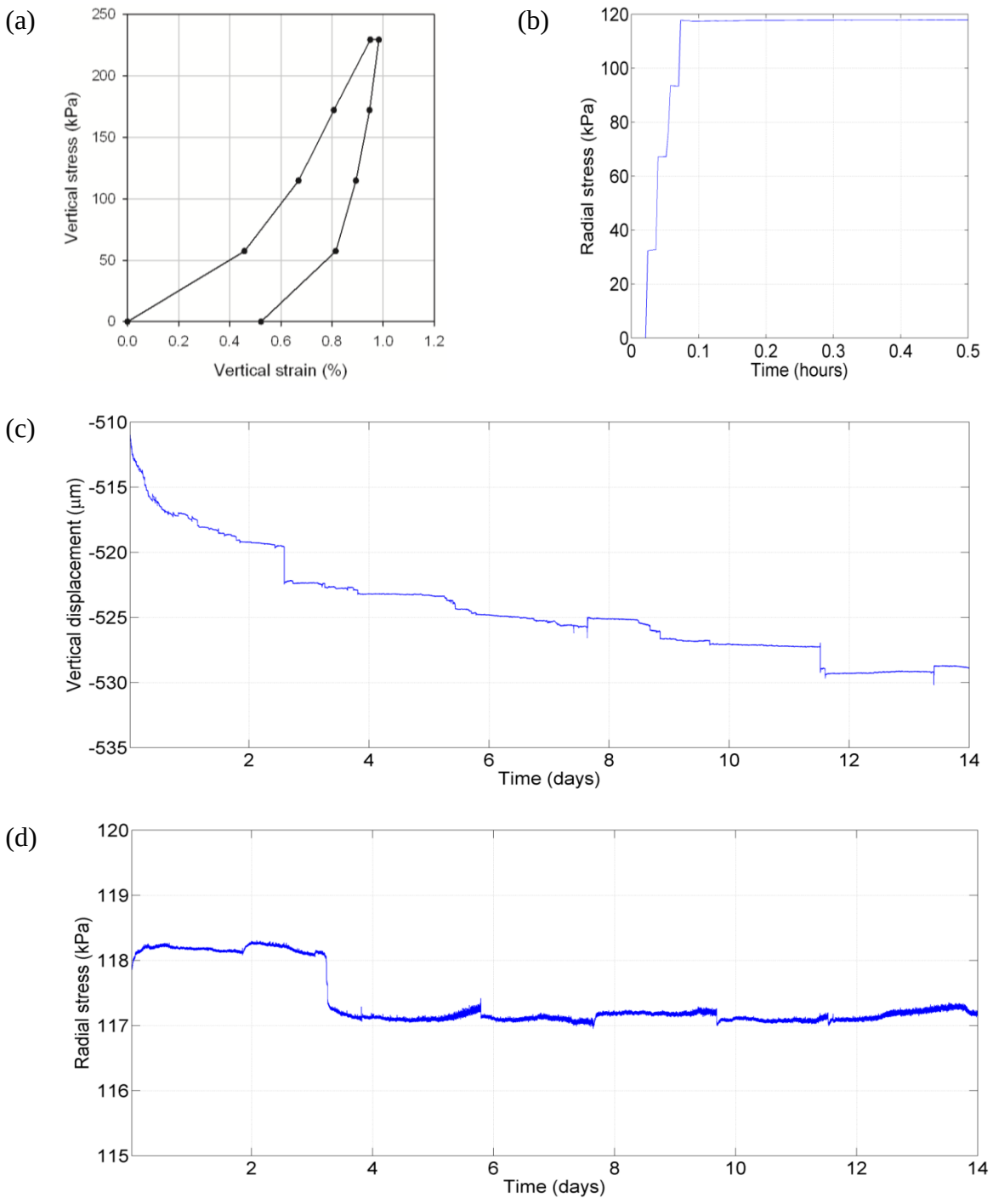

Figure 4.75. Results from consolidometer test #12 (Ottawa 20-30 sand in a pH 9.5 aqueous solution), (a) vertical stress vs. vertical strain plot during loading,14 day constant load, and unloading, (b) increase in radial stress during the loading process, (c) settlement of the specimen after initial 30 min of loading, and (d) increase in radial stress as a function of time.

(a)

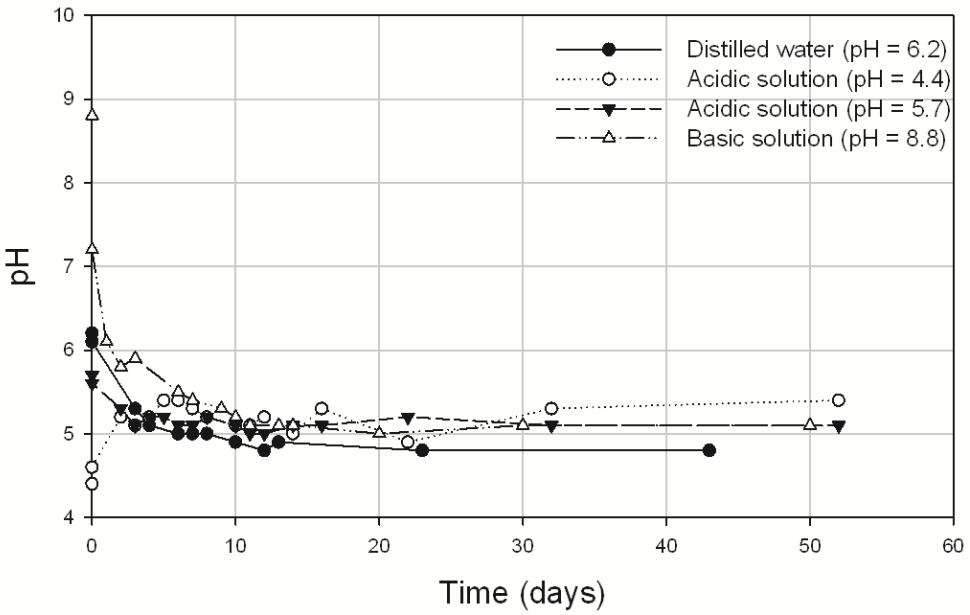

(b)

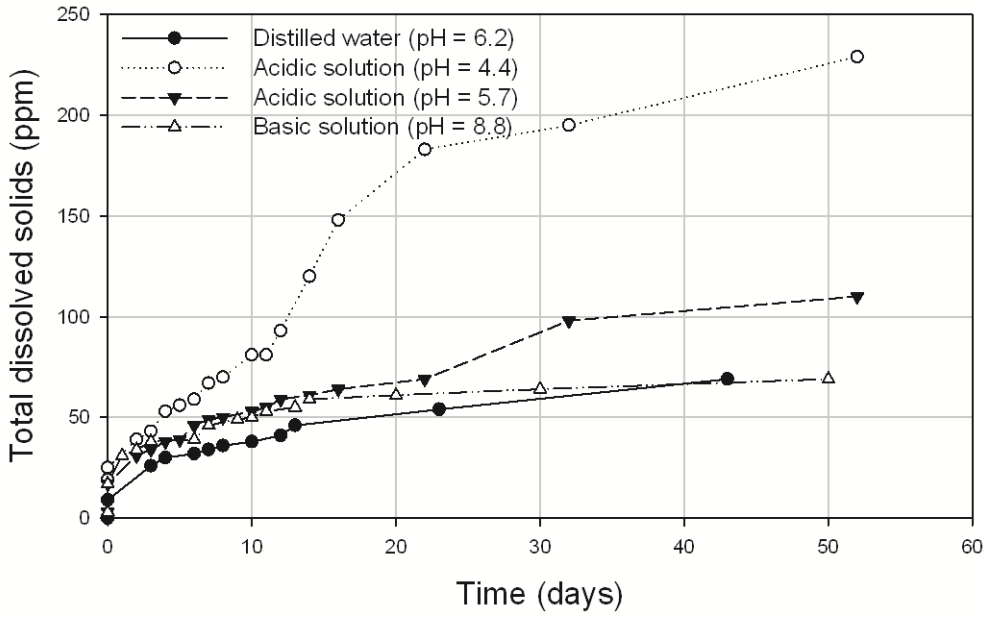

Figure 4.76. Solubility tests of Ottawa 20-30 sand in different aqueous solutions, (a) change of pH with time; irrespective of the starting pH of the aqueous solution, after adding the sand the pH comes to a constant value of about 5, and (b) change of TDS with time; the TDS of the solution increases with time.

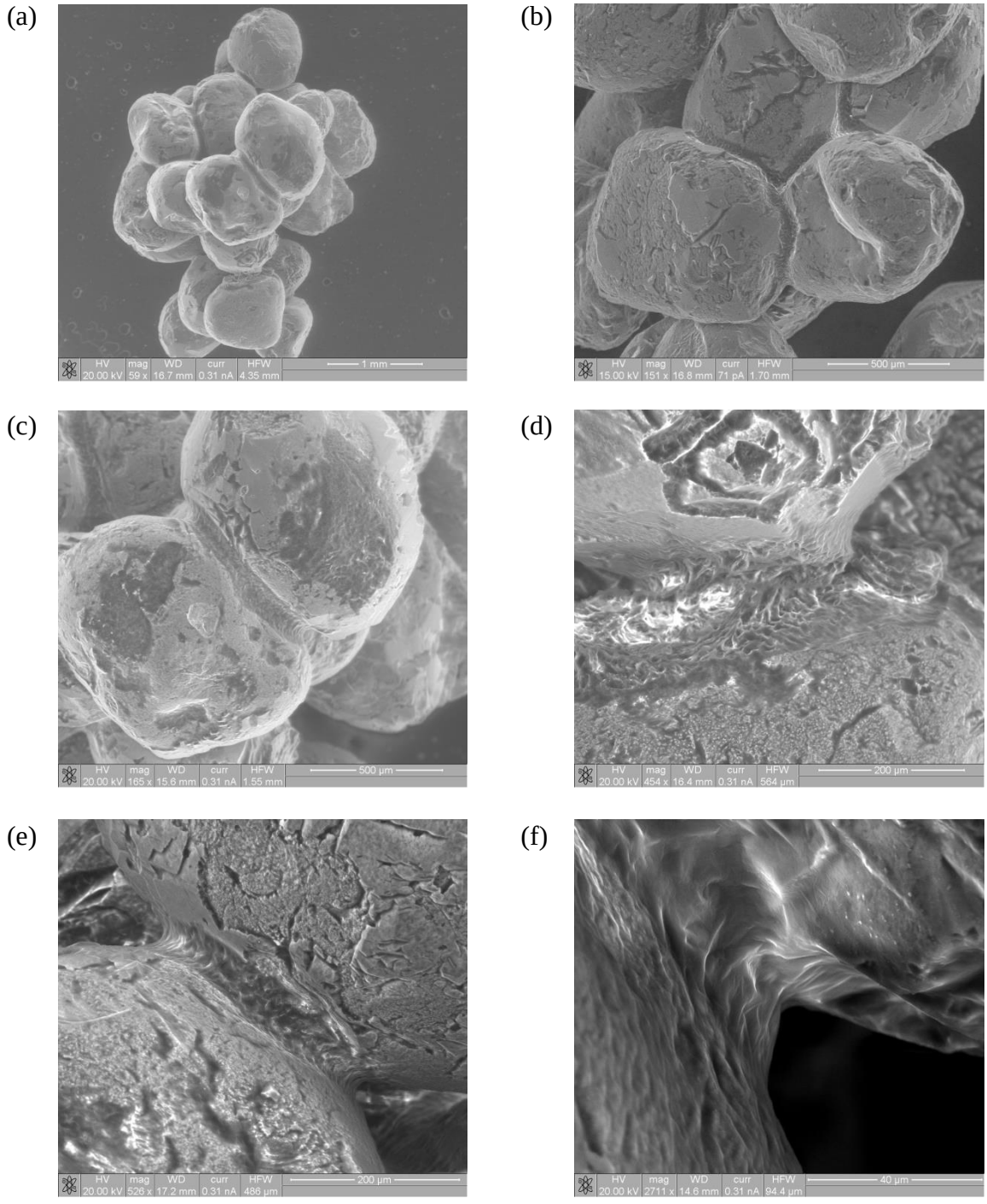

Figure 4.77. Typical SEM images of clumped sand grains found after drying the specimen from test #9, (a) clumped grains (image width = 4.35 mm), (b) close-up view of grains clumped to one another (image width = 1.7 mm), (c) close-up view of two grains clumped together (image width = 1.55 mm), (d) close up view of two grains clumped together (image width = 564 μm), (e) close up view of two grains clumped together (image width = 486 μm), and (f) close up view of the bond region in-between two sand grains (image width = 94.4 μm).

Chapter 5

MODELING AND NUMERICAL INVESTIGATION

5.1 Introduction

The grain-to-grain contact tests performed on sand grains and described in Chapter 4 support the hypothesis of delayed fracturing of sand grain asperities. The modified consolidometer tests on dry sand provide quantitative estimates of increase in lateral stress over time when subjected to a constant vertical load, which is the consequence of the increase in macroscopic stiffness owed to contact fatigue (delayed fracturing of asperities). Consolidometer test results for wet sand, however, were more complicated to interpret, and seemed to be influenced by the pH of the pore water. Nonetheless, the settlement of the specimen in both dry and wet tests during the period of lateral stress increase had a step-wise characteristic. It was argued that the reason behind the observed changes in consolidometer tests was due to static fatigue at grain contacts. This chapter discusses Discrete Element Method (DEM) calculations that support this conjecture. Results from DEM calculations were then used as an input for finite element analysis in solving the boundary value problem focusing on the increase in the cone penetration resistance (or cone penetration test; CPT) after dynamic compaction of sand. Results from DEM and finite element analysis discussed in this chapter provide quantitative estimates for the time-delayed increase in sand penetration resistance.

A DEM model of sand is presented first. While there have been other numerical models in DEM developed in the past to simulate aging (Kuhn and Mitchell, 1992; Kwok and Bolton, 2010), the DEM model presented in this thesis follows a more intuitive approach that draws on the micro-scale test results obtained in Chapter 4. Most of the DEM models focusing on aging available in the literature use a phenomenological description of a contact with some form of dashpot (viscosity) at particle contacts. This allows the model to exhibit creep characteristics at

the macro scale. The phenomenological assumption of viscosity at contacts circumvents all the physical, mechanical, and chemical interactions that are crucial to understanding of the process of aging in sands. While phenomenological assumptions at the micro scale are used in modeling with success, these models can only be useful in quantitative predictions, but not in the explaining the sources of time effects in sand. The DEM model presented in this thesis is only used as a tool in order to indicate that the fatigue of individual contacts, integrated over the volume of sand can indeed result in the behavior that is observed in the laboratory. This effort is centered on providing a piece of evidence supporting the hypothesis of contact static fatigue being responsible for time effects in sands. The latter part of this chapter suggests a plausible explanation behind the observed drop and time-dependent increase in CPT tip resistance following dynamic compaction of sands. The changes in the stress state obtained from the DEM model before and after sand liquefaction were used in finite element analysis to simulate the cone penetration test (CPT).

The Discrete Element Method (DEM) software PFC^{3D} (particle flow code in three dimensions) and the finite element method (FEM) software ABAQUS/CAE ver. 6.10 were used to simulate and study the effects of static fatigue on the behavior of soil masses and on soil-structure interaction. The primary goal was to gain additional evidence supporting the hypothesis, but not to further develop or significantly modify these methods (DEM and FEM).

5.2 Discrete Element Method (DEM)

DEM is a numerical tool suitable to study the mechanical behavior of granular assemblies. The DEM as applied to geomaterials was developed by Cundall (1971) for rock mass problems; Cundall and Strack (1979) later applied it to granular materials. The unique feature of DEM is the explicit consideration of individual particles and their interactions in a granular system. This is a stark contrast from finite element methods which use a continuum mechanics framework to represent the granular material. The term DEM can refer to both Discrete Element Method and Distinct Element Method. The term *discrete* element method is used for a method that allows for finite displacements and rotations of discrete bodies, including detachment, and it automatically recognizes the formation of new contacts as the calculation progresses. The term *distinct* element method is used for methods that use an explicit dynamic solution algorithm. Discrete element methods and distinct element methods also differ in the representation of the

contact and solid material. In the *distinct* element method, the particles are assumed to be rigid and contact is considered compliant, with a finite stiffness. In the *discrete* element method, the solid material is assumed to be deformable, and algorithms are used to prevent penetration of two particles that form the contact.

Modeling in distinct element method involves repeated execution of many time steps. Calculations alternate between a force displacement law (typically governed by the contact stiffness) and Newton's second law. At every step and for each particle, for a given set of contact forces and body forces, Newton's second law (a = F/m) is integrated twice to obtain updated velocity and displacement. Based on the new positions, contact forces are derived from the relative displacement of particles and a force-displacement law at the contacts. A state of equilibrium is reached whenever the internal forces are balanced. The calculation cycle in DEM is shown in Fig. 5.1. At the start of each time step, the contacts get updated from the positions of spheres (grains) and walls. The force-displacement law is then used to update the contact forces. Next, the velocity and position of each particle is updated using the law of motion. PFC^{3D} is a commercial program developed by Itasca Consulting Group, Inc. that implements the distinct element method. This software was used as a numerical tool to test the influence of static fatigue on the response of sands.

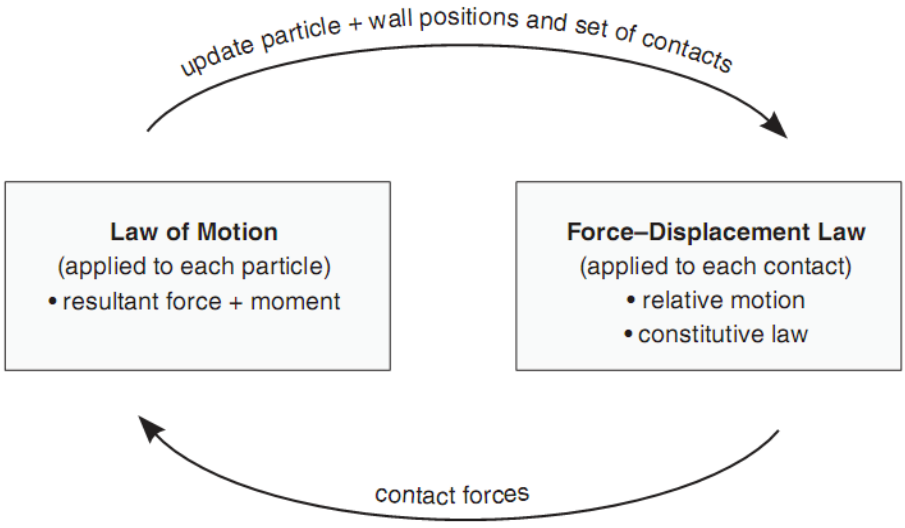

Figure 5.1. Calculation cycle in PFC^{3D} (from Itasca, 2008)

There are two basic entities in PFC^{3D}, viz., walls and spheres. The program provides a framework to model boundary value problems directly using these two entities. To model a

granular material in DEM, a large number of spheres (balls) are needed, thereby increasing the computation cost. To decrease the execution time, the method assumes that the response of particles remains constant during a certain period of time. This allows the particle response to be calculated at discrete time points. The difference between two consecutive time points is called a time step. Although one might be tempted to use a large time step to reduce the time in a DEM simulation, the results obtained could be erroneous due to an occurrence of instability (or non-convergence). Hence there exists a critical time step beyond which the time step should not be increased. Different researchers used different time steps for various DEM models. Generally, the time step in a DEM model is controlled by the mass (m) and particle stiffness (k) of the smallest particle. Different researchers suggest different critical time steps to be used in the simulation. Cundall and Strack (1979) suggest a value of $2\sqrt{m/k}$. Using energy considerations, Tsuji et al. (1993) suggest a value of $\frac{\pi}{5}\sqrt{m/k}$. O'Sullivan and Bray (2004) recommend a value of $0.17\sqrt{m/k}$ for 3D DEM simulations. Ng (2006) recommends a value of $0.05\sqrt{m/k}$. In this thesis the default critical time step ($\sqrt{m/k}$) suggested in Itasca (2008) was used. Since the system of particles in the DEM simulation can be made up of different bodies (spherical particles and 'clumps') of varying size and stiffness, the critical time step is the minimum value of $\sqrt{m/k}$ among all particles.

The Energy supplied to a particle model in PFC^{3D} is dissipated through sliding at contacts. However, this dissipation may not be sufficient to obtain a steady state solution in a reasonable amount of computation time. PFC^{3D} offers two types of damping to dissipate the kinetic energy; namely, local damping and viscous damping. Local damping (non-viscous) is applied on each ball and applies a damping force, whose magnitude is proportional to the unbalanced force acting on the ball. Viscous damping is applied on each contact and adds normal and shear dashpots at each contact, to provide damping forces proportional to the relative velocity difference between the contacting entities. These dashpots act in parallel with a linear contact model. Local damping is used in the PFC^{3D} simulations performed in this thesis. The equilibrium value of force is not affected by damping (Cundall, 1987). However, Cundall found that damping reduces the number of cycles required to reach equilibrium.

In PFC^{3D}, particle interactions are between one another or with walls. During interactions, forces develop at contacts. For unbonded particles, each contact corresponds to a physical interaction and is always in between two entities (ball-ball or ball-wall). The magnitude of force developed depends on the contact model used. A linear contact-stiffness model was used in all the DEM simulations in this thesis. This model provides an elastic relation between contact force and relative displacement. There are three major parameters in this model; namely, particle normal stiffness (k_n), particle shear stiffness (k_s) and friction coefficient (μ). The contact stiffness's of two entities A and B in contact can be calculated as (Itasca, 2008)

$$K_n = \frac{k_n^A k_n^B}{k_n^A + k_n^B}$$
$$K_s = \frac{k_s^A k_s^B}{k_s^A + k_s^B} \qquad (5.1)$$

where K_n and K_s are the contact normal and shear stiffnesses; $k_n{}^A$ and $k_n{}^B$ are normal stiffnesses of entities A and B; $k_s{}^A$ and $k_s{}^B$ are shear stiffnesses of entities A and B.

In the linear contact-stiffness model, the forces and displacements are linearly related to the stiffnesses of the two contacting entities; normal component of force is computed from the contact normal stiffness and shear component is computed from the contact shear stiffness. Slip occurs in between two entities when the shear component of force reaches the maximum allowable shear contact force. This allowable shear contact force is obtained by multiplying the minimum friction coefficient by the compressive normal component of force.

5.2.1 Parameter selection in PFC^{3D}

An important aspect of modeling geomaterials in PFC^{3D} is choosing the appropriate values of micro-parameters (particle stiffness and friction) such that the macro response of the specimen is akin to physical tests. Due to the large computation effort required in a DEM simulations it is not possible to model large number of particles in DEM. Hence, often particle up-scaling is performed, where the actual granular material is represented by larger sized grains. In addition to spherical particles, arbitrary shaped particles termed 'clumps' can also be used. Clumps are formed by joining two or more particles together to form a 'super-particle.' Since the particle

micro-parameters to be used in a PFC model were unknown, inverse modeling approaches were followed. In this approach, particle micro-parameters are varied until the behavior of the numerical sample follows the response of the physical sample. A study was performed to understand the effect of changing particle parameters on macroscopic friction angle (ϕ) and Young's Modulus (E) (obtained from a triaxial test at 100 kPa confining pressure). The parameters studied were

- Effects of clumps
- Particle normal stiffness (k_n)
- Particle size
- Ratio of normal to shear particle stiffness (k_n/k_s)

Clumps can be formed by joining different spheres together. The most basic clump is a peanut-shape particle, where two particles are joined together, Fig. 5.2. Even though different shaped clumps might represent the actual grain shape better, it increases the simulation time and so were avoided in this research. Peanut shaped clumps were used. It should be noted that if there were no clumps in the system, to obtain a friction angle of about 32°, a very high friction coefficient of 2 or 3 would have to be used. This is because the clumps provide rotational 'frustration' to the system arresting the rotation of spheres to some degree. The effect of clumps on the macroscopic behavior was studied by varying three parameters; namely, percentage of clumps, relative size of each sphere in the clump (R_1/R_2), and degree of clump overlap (δ_c). Tables 5.1 shows the changes to the internal friction angle (at critical volume) obtained from a numerical triaxial test (cylindrical specimen) performed with about 8000 particles (clumps + spheres) at a porosity of 0.35. For all tests shown in Table 5.1, radius R_1 was set to 0.5 mm, particle normal stiffness (k_n) was set to 2×10^5 N/m, ratio of normal to shear stiffness (k_n/k_s) was set to 2.5 and the friction coefficient was set to 0.6.

From Table 5.1 it can be seen that the greater the number of clumps in the model, the higher the friction angle. This should not be a surprise, as larger numbers of clumps provide a greater rotational frustration to the system. It was also seen that the larger the size ratio of particles in a clump (R_1/R_2), the greater the friction angle. The friction angle also increased as the overlap distance δ_c of two spheres in the clump increased.

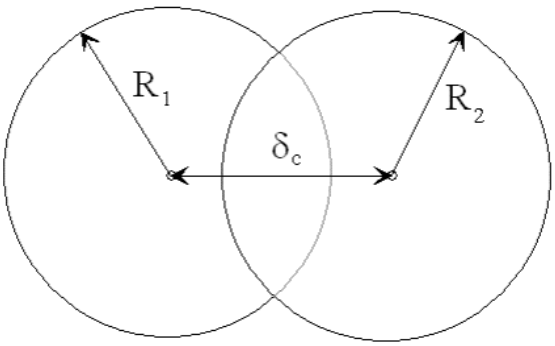

Figure 5.2. Different parameters of a peanut shaped clump.

Table 5.1. Effect of clumps on macroscopic internal friction angle of the granular system.

% clumps	% spheres	R_1/R_2	δ_c	ϕ
75	25	1	R_1	47
25	75	1	R_1	37
20	80	1	R_1	35.5
20	80	1	R_1	35.5
20	80	0.5	R_1	30.65
20	80	1	$0.75R_1$	32
20	80	1	R_1	35.5
20	80	1	$1.75R_1$	36.7

Based on the results in table 5.1, clumps made of two spheres of equal radius ($R_1 = R_2 = R$) with a degree of overlap equal to one radius ($\delta_c = R$) were used in all DEM simulations.

Itasca (2008) suggests parameter E_c, termed the modulus at a single contact, as a scaling parameter of particle stiffness and size. E_c is given by Equation (5.2)

$$E_c = \frac{k_n}{4\tilde{R}} \tag{5.2}$$

where $\tilde{R}$ is the mean radius of two particles having a particle normal stiffness of k_n in contact.

Table 5.2 shows the effect of changes in particle stiffness. For these simulations the particle sizes (diameter) were in-between 1.22 mm to 2.02 mm. It was seen that as the particle

stiffness decreases, the macroscopic Young's Modulus obtained from a triaxial test decreases, while the Poisson's ratio and friction angle remain almost a constant; a hundred fold decrease in particle stiffness caused a sixty-eight fold reduction in Young's Modulus and a 0.4° increase in friction angle.

Table 5.2. Effect of changing particle stiffness on macroscopic properties.

Input parameters					Scaling parameter	PFC^{3D} triaxial test results		
% clumps	Particle size, D_{avg} (mm)	k_n (MN/m)	k_n/k_s	μ	E_c (MPa)	Young's Modulus, E (MPa)	Poisson's ratio (ν)	ϕ
20	1.62	20	2.5	0.6	6700	2800	0.28	34.7°
20	1.62	2	2.5	0.6	670	320	0.27	34.9°
20	1.62	0.2	2.5	0.6	67	41	0.26	35.1°

Table 5.3. shows the effect of particle size. It was seen that as the particle size increased, keeping the particle stiffness a constant, the Young's modulus decreased while the friction angle remained constant. If the particle size was increased and the contact modulus (E_c) was not changed, the Young's Modulus or friction angle remained unchanged. Hence, if the parameter E_c given by Equation (5.2) is kept constant, consistent macro parameters can be obtained even if the particle sizes were up-scaled (increased).

Table 5.4 shows the effect of changing the particle shear stiffness and keeping the particle normal stiffness a constant. It was seen that as k_n/k_s increases, the Poisson's ratio increases while the friction angle does not change. The Young's Modulus on the other hand decreased; a four-fold increase in k_n/k_s caused the Poisson's ratio to increase by about 40% while the Young's Modulus decreased by 40%.

The numerical triaxial tests performed on models with varying parameters showed that the strength of the granular material (represented by the friction angle) was unaffected by changes in particle's stiffness (k_n and k_s). However, as the number of clumps in a granular assembly decrease, the friction angle reduces. Increasing the particle size had no effect on the friction angle, implying that the friction angle is a scale-invariant property (though dependent on fabric/packing).

Table 5.3. Effect of particle size on macroscopic properties.

Input parameters					Scaling parameter	PFC^{3D} triaxial test results		
% clumps	Particle size, D_{avg} (mm)	k_n (MN/m)	k_n/k_s	μ	E_c (MPa)	Young's Modulus, E (MPa)	Poisson's ratio (ν)	ϕ
20	1.62	0.2	2.5	0.6	67	40.41	0.26	35.5
20	8.1	0.2	2.5	0.6	13.4	10.9	0.23	35.6
20	16.2	0.2	2.5	0.6	6.7	6.31	0.3	35.8
20	3.24	0.4	2.5	0.6	67	40.32	0.26	36.6
20	8.1	1	2.5	0.6	67	39.41	0.27	35.6
20	16.2	2	2.5	0.6	67	39.74	0.28	35.7

Table 5.4. Effect of change in shear modulus on macroscopic properties.

Input parameters					Scaling parameter	PFC^{3D} triaxial test results		
% Clumps	Particle size, D_{avg} (mm)	k_n (MN/m)	k_n/k_s	μ	E_c (MPa)	Young's Modulus, E (MPa)	Poisson's ratio (ν)	ϕ
20	1.62	2	2.5	0.6	670	320	0.28	34.9
20	1.62	2	5	0.6	670	220	0.37	35
20	1.62	2	10	0.6	670	190	0.39	35

The quantitative estimates of particle micro-parameters in a DEM model have an effect on the resulting macroscopic modulus and strength of the soil. However, physical phenomena occurring in the granular assembly can still be captured if reasonable estimates of the parameters are used. Figure 5.3 shows such a physical phenomenon, namely, *arching* occurring beneath a sand pile. Approximately 12,000 particles (25% clumps) of particle size 2.3 ~ 3.7 cm were first rained into a box with a base of 4.8 x 0.6 m; subsequently, instability was induced by removing side walls and a prismatic heap was formed during a process of particles' rolling and sliding off under gravity. The particle normal and shear stiffness were 4.0 and 1.6 MN/m respectively. The coefficient of friction was assumed to be 0.65. A triaxial test performed on the same particles as in the heap (porosity 0.36), at a confining pressure of 100 kPa, gave the Young's Modulus of

5.14 MPa and the peak internal friction angle of 39.5° (Fig. 5.4). After the wedge-shaped heap was formed, Fig. 5.3(a), the two halves of the base were rotated about their end edges to produce subsidence Δ at the center equal to 0.67% of the heap's height $(\Delta/H = 0.0067)$. Figure 5.3(b) indicates the force chains characteristic of soil arching. The force chains are indicated by lines joining the centroids of contacting particles and their thickness is indicative of the intensity of forces transferred through the contacts. The distributions of normal macroscopic stress at the base immediately after heap formation and after deflection of the base are shown in Fig. 5.3(c). Not surprisingly, the load on the central portion of the base was reduced in the process of deflection, at the expense of the less compliant portions farther away from the center. Consequently, the stress distribution exhibits a distinct local minimum at the center (a "dip"). This dip was also observed previously by other researchers (Michalowski and Park, 2004). Analogous to the redistribution of the base reaction caused by deflection, the rotation of a retaining structure should be expected to affect the stress distribution and, possibly, induce arching. This was discussed in Nadukuru and Michalowski (2012).

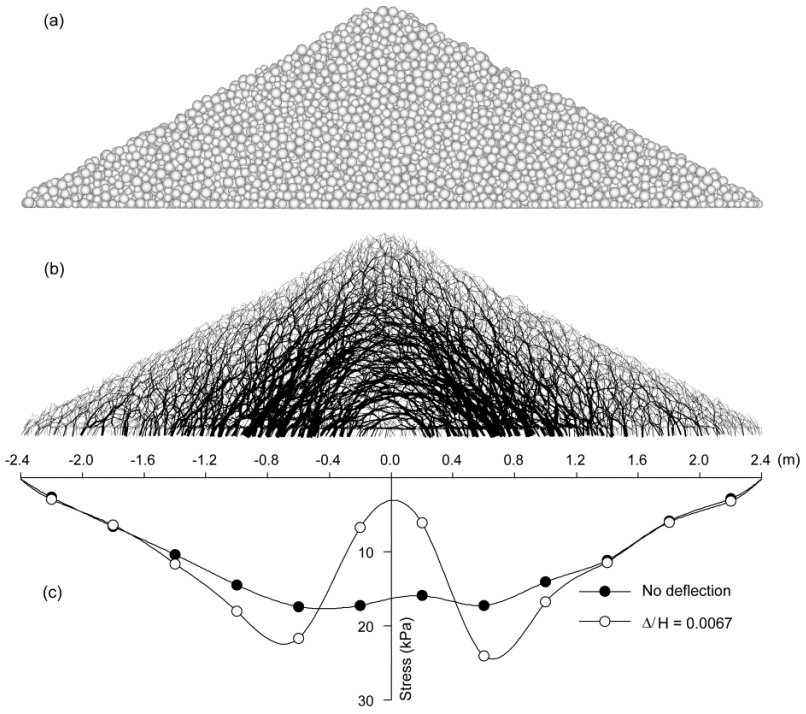

Figure 5.3. Discrete element simulation, (a) prismatic sand heap, (b) force chains, and (c) base stress distribution before and after base deflection (after Nadukuru and Michalowski, 2012).

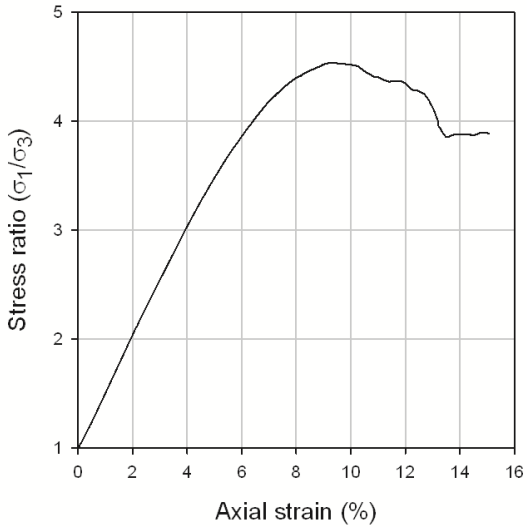

Figure 5.4. Numerical triaxial test result using the sand heap particle parameters.

Results from this section indicate that the microscopic parameters affecting the macroscopic Young's Modulus of a grain assembly are particle stiffness and size (in addition to packing/porosity). The friction coefficient had no influence on the Young's Modulus. The strength of the assembly was dependent on the particle friction coefficient, the fabric of the assembly (void ratio), the amount and size of clumps, and was independent of particle stiffness or size. Further, it was seen that with a reasonable estimate of particle parameters, physical phenomena occurring in the true soil can be captured.

5.2.2 Inhomogeneity in contact forces

The presence of static fatigue at grain contacts was advocated in Chapter 4, where supporting experimental evidence was described. Static fatigue was influenced by many factors of which the applied load is one of them. Unlike in continuum solids, loads are distributed through a granular material, such as sand, in a highly inhomogeneous manner, along the networks comprising of inter-particle forces. These "force chains" support the entire external load. A good understanding of the geometrical structure of grain contacts and associated forces is a necessary basis for a study into static fatigue and time effects of sand. Due to the inhomogeneity of the force chain network, some particles witness higher loads than others. In addition to this, the applied loading also causes anisotropy in the force chain network. This is shown in Fig. 5.5(a). For a specimen confined to a lateral to vertical stress ratio of 0.4, the force

chains are primarily oriented along the vertical direction, Fig. 5.5(a). For a specimen confined isotropically, there is no preferred orientation, Fig. 5.5(b). Understanding the inhomogeneity in the spatial distribution of the force network is important, because static fatigue at an individual contact is dependent on the contact force. DEM simulations can provide information on these "contact force networks" or "force chain skeletons". Cundall and Strack (1978) suggested that the force chain network obtained from DEM simulations can be directly compared to physical experiments on photo elastic disks, such as those used by Drescher and De Jong (1972). More recently, Jirathanathaworn (2010) presented a development in photoelastic method to study aging in sand, and Radjai et al., (1996) and Thronton (1997) analyzed these contact force networks and fitted functions to the probability distributions for normal contact force data.

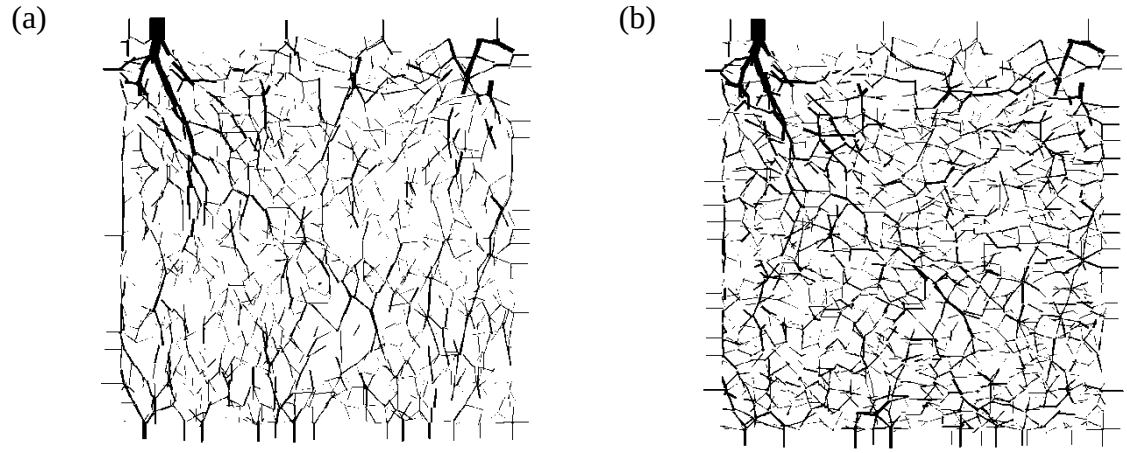

Figure 5.5. Anisotropy in force chain network in a 3D specimen subjected to a vertical stress of 100 kPa, (a) lateral pressure is 40 kPa, (b) lateral stress is 100 kPa; the actual particles are not shown in order not to obscure the force chains.

To understand the variability of contact forces experienced by a granular assembly, a sample was formed by raining about 23,000 particles (25% clumps) of 0.6 ~ 0.85 mm size in a 2 cm cube, Fig. 5.6. The clumps are shaded darker than the spherical particles in Fig. 5.6, which are shaded in a lighter gray. The value of k_n was chosen to be 0.4 MN/m, k_s was chosen to be 0.4 MN/m and μ was 0.65. The sample was then confined to 230 kPa vertical stress and 115 kPa lateral stress. The porosity of the obtained sample was 0.41. The load on the sample was then increased ten-fold, and then a hundred-fold, with the horizontal-to-vertical stress ratio kept at 0.5. The mean contact force at a vertical stress of 0.23 MPa was 0.105 N, at the vertical stress of 2.3 MPa it was 0.856 N, and at the vertical stress of 23 MPa the mean force was 5.82 N. The

inhomogeneity of the magnitude of contact forces can be seen in Fig. 5.7. A large fraction of the contacts hardly participate in the load transmission. This supports earlier observations that large contact forces concentrate along certain paths through the system, often called *strong force chains*. On the other hand, there were a few contacts that carried 10 times the mean contact force in the granular assembly. However, at larger confining stresses, this variability in contact forces decreases. This is shown in Fig. 5.8.

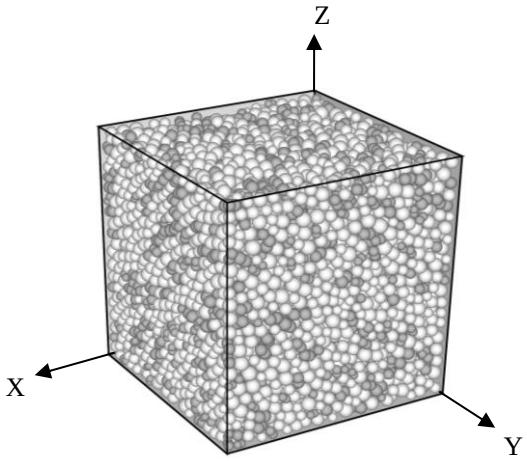

Figure 5.6. A cubical specimen of particles.

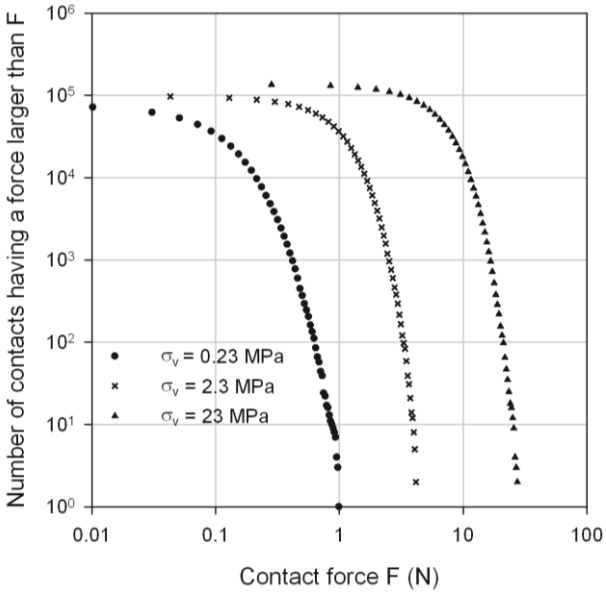

Figure 5.7. Contact force distributions for a sample under different vertical loads (ratio of lateral to vertical stress in each case was 0.5).

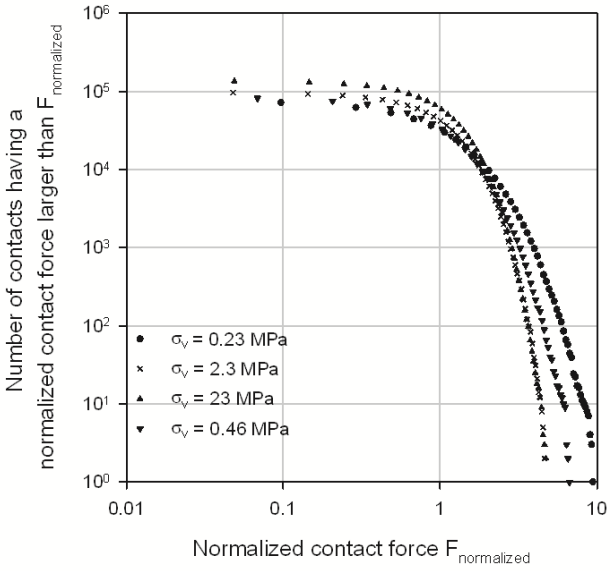

Figure 5.8. Normalized contact force distribution from Fig. 5.7 (contact forces normalized by the mean force magnitude; ratio of lateral to vertical stress kept at 0.5 for all cases).

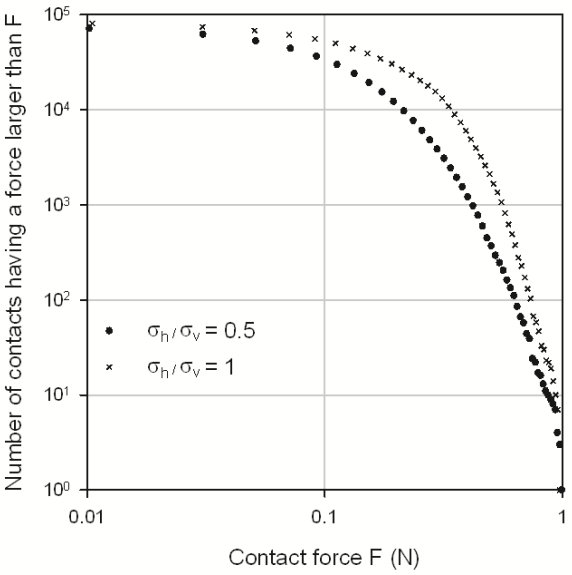

Figure 5.9. Contact force distribution for a sample at different confining stresses (σ_h) ($\sigma_v = 0.23$ MPa).

For the purpose of this study chains carrying a force more than the mean contact force will be referred to as strong force chains and those that carry less as weak force chains. The

DEM simulations performed in this research showed that the strong force chains are made up of less than 40% of all the contacts in the assembly.

Figure 5.10 shows the spatial distribution of contact normal orientation for the specimen in Fig. 5.6 confined at a vertical stress of 0.23 MPa and a horizontal stress of 0.115 MPa. The spatial distribution of the contact normals shows that they are preferentially oriented in the direction of macroscopic major principal stress. Consequently, along a vertical plane, the contact normals were primarily directed along the vertical direction as shown in Fig. 5.10(a). They were more isotropically oriented within the horizontal plane, as shown in Fig. 5.10(b). Along a vertical plane, while the contacts involved in the weak force chain network were more isotropically oriented (Fig. 5.11(a)), the contacts that form the strong force network are oriented with vertical being the preferential direction (Fig. 5.11(b)). This suggests that the strong force chains at the meso scale are responsible for the deviatoric component of the stress state at the macroscopic scale. As static fatigue at a contact is a function of the magnitude of the contact force, contacts along the strong force chains are likely to be affected more by the fatigue than the contacts along the weak force chains.

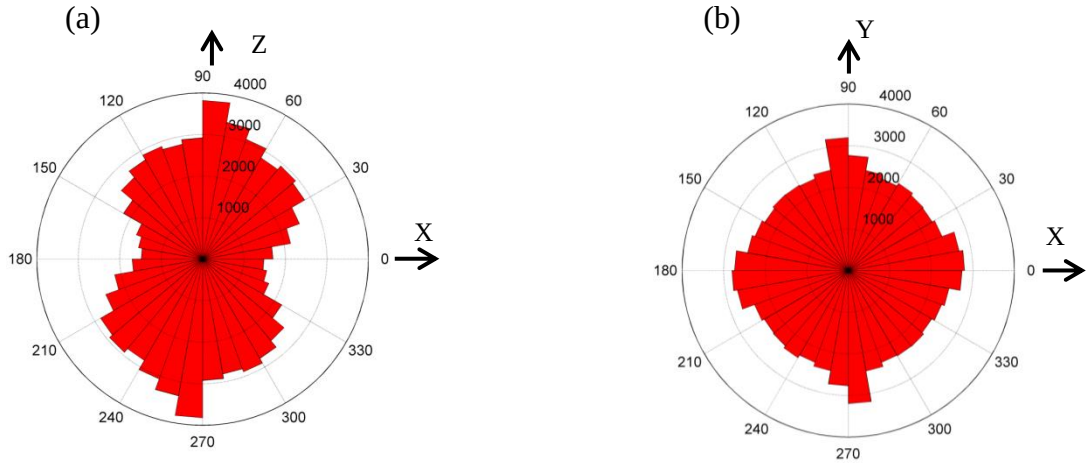

Figure 5.10. Polar plots of contact normal orientations for a specimen confined to 230 kPa vertical stress (σ_{zz} = 230 kPa) and 115 kPa lateral stress ($\sigma_{xx} = \sigma_{yy}$ = 115 kPa) ; the specimen is shown in Fig. 5.6, (a) histogram along a vertical plane, and (b) histogram along a horizontal plane.

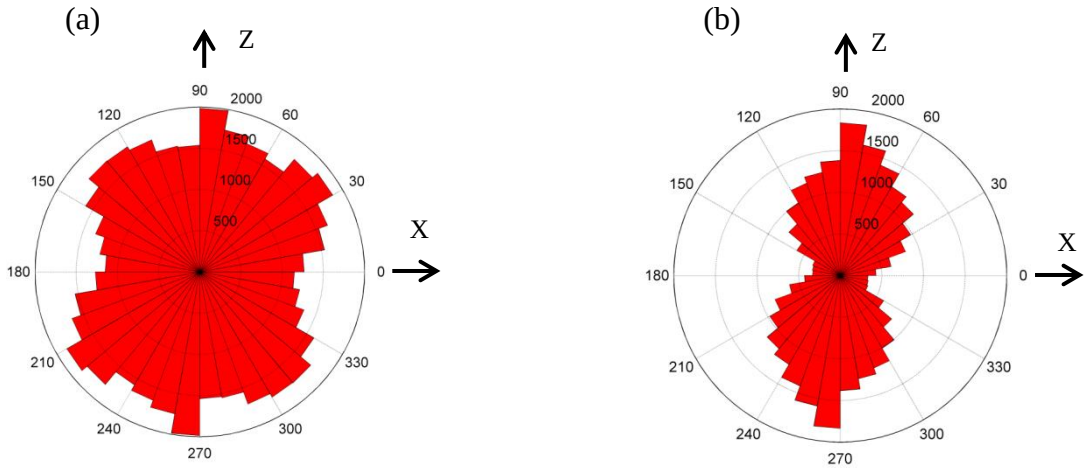

Figure 5.11. Polar plots of contact normal orientations along a vertical plane for a sample subjected to a vertical stress of 230 kPa (σ_{zz} = 230 kPa) and lateral stress of 115 kPa (σ_{xx} = σ_{yy} = 115 kPa), (a) contacts that were part of the weak force chain network, and (b) contacts that were part of the strong force chain network.

Results from this section indicated that contact forces experienced by grains are highly variable and have a wide range of magnitudes. From the consolidometer tests in Chapter 4, it was observed that the lateral stress increases over time for a dry sand subjected to a constant vertical stress. To better understand the effect of static fatigue at a contact on the macroscopic response of a specimen, a DEM model was built. It was shown in Chapter 4 that the vertical settlement of a sand specimen subjected to a constant vertical load was not continuous; rather, it had a step-wise characteristic. Using qualitative observations from the grain-to-grain tests, a DEM model for static fatigue was developed using PFC^{3D}. The objectives of this model was to see if the step wise settlement and increase in lateral stress could be captured at a macro-scale using information from the micro-scale tests.

5.2.3 Model for aging under 1D strain conditions using DEM

In the literature, there are relatively few numerical models that aid in understanding and describing sand aging. It is widely accepted that cause of aging in sand is creep (viscous properties). However, creep is not a physical phenomenon, but rather a term used to classify the type of behavior at the macroscopic scale. Consequently, invoking creep does not shed any light on the nature of the phenomenon. One of the early models to describe creep in sands was that described by Kuhn and Mitchell (1992). These researchers used a rate process model to develop an expression for sliding velocity at grain contact points. This expression was then used as a

contact viscosity parameter between particles in contact. They used this model in 2D DEM calculations. Kwok and Bolton (2010) utilized the model by Mitchell and used it in 3D DEM calculations. The models by these researchers used a linear contact model in the DEM implementation. Suarez (2012) used the rate process theory along with the Hertz-Mindlin contact model to develop creep in soils. Wang et al. (2008) simulated aging in sand by using a Maxwell contact model. Potyondy (2007) developed a model, called parallel-bond stress corrosion model for rock to simulate stress corrosion cracking in granite using DEM. The DEM model presented in this section follows a more intuitive approach that draws on the micro-scale test results obtained in Chapter 4. No dashpots are used here at the contacts between sand grains.

In Chapter 4, from the grain-to-grain contact tests it was observed that the magnitude of the force affects the static fatigue process. Below certain level of the contact force, no damage was observed. SEM imaging of the grains subjected to contact fatigue showed broken asperities and crystalline debris. Due to this process, and the subsequent grain convergence, the applied load on a single contact is now carried by more contact "points". Consequently, the stiffness of the contact should increase. This conjecture is supported by earlier experiments indicating that the speed of the shear wave through sand under sustained loading increases with time (Afifi and Woods 1971). This was also confirmed by increasing horizontal (radial) macroscopic stress in specimens of sand subjected to sustained load (increase in horizontal stress is imperative for preserving strain energy in case of increasing stiffness). The process of aging will be modeled in DEM by introducing increasing (with time) contact stiffness. The purpose of this modeling is to find out whether it is plausible that: (a) increasing stiffness at individual inter-granular contacts can lead to step-wise settlement of aging sand, and (b) to confirm through numerical means that the increasing contact stiffness leads to an increase in horizontal stress in a confined specimen.

Since Ottawa 20-30 sand was used in almost all of the consolidometer tests, the particle size (diameter) in the DEM model was selected to be 0.6 ~ 0.85 mm; 10% clumps were used in the model. The particle micro-parameters used in the model are given in Table 5.5. A triaxial test performed with about 5,000 particles at a confining pressure of 100 kPa using the properties given in Table 5.5 gave a Young's Modulus of 85.4 MPa, Poisson's ratio of 0.27 and a peak friction angle of 31.5°. The result from the triaxial loading test is shown in Fig. 5.12. These parameters to simulate Ottawa 20-30 sand were reasonable. Lambe and Whitman (1969) suggested for hard rounded particles, the Young's Modulus is 55 ~ 105 MPa at 100 kPa

confining pressure. Laboratory direct shear tests performed on Ottawa 20-30 sand gave a friction angle of 31°. Hence the micro parameters chosen for the DEM model were quite reasonable.

Table 5.5. Particle parameters used in the DEM aging model.

Number of particles	23,365 (10% clumps)
Contact normal stiffness (K_n)	0.13×10^6 N/m
Contact shear stiffness (K_s)	0.065×10^6 N/m
Friction coefficient (μ)	0.6

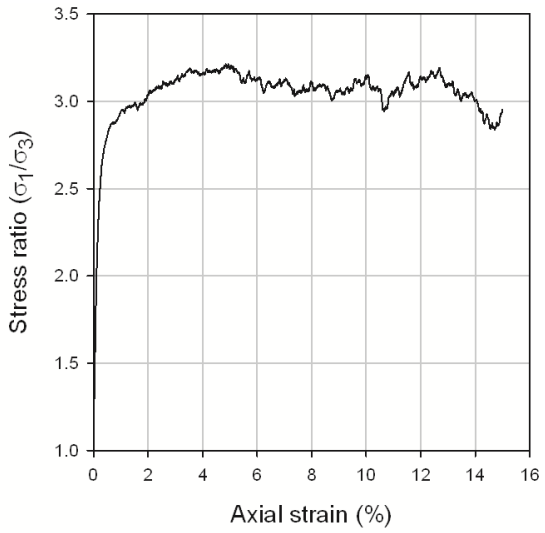

Figure 5.12. Triaxial test result for a specimen having particle parameters in Table 5.5.

23,365 particles (90% spheres + 10% clumps) with properties described above were rained under gravity in a frictionless cubical box of 2 cm side length. The mass density of the grains was set to 2650 kg/m^3. After the system reached equilibrium, the porosity was found to be 0.445. The specimen was then confined to a horizontal stress of 119 kPa and the vertical stress of 230 kPa . These stresses were chosen to mimic the stress state observed in the consolidometer test #2 in Chapter 4. Figure 5.13 shows the confined specimen. It should be noted that due to the confining stress, the initial cubical specimen became a cuboid. The specimen shown in Fig. 5.12 was used as the initial *unaged* specimen.

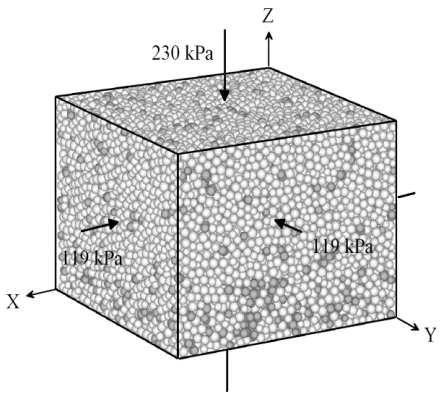

Figure 5.13. Confined specimen used for aging simulation in PFC^{3D}.

Throughout the aging process, the vertical stress for the specimen shown in Fig. 5.13 was maintained at 230 kPa. In the horizontal directions, during aging, zero strain conditions were imposed. These boundary conditions replicate 1D strain conditions as in the consolidometer tests, or in the field. A contact algorithm was written in PFC^{3D} to simulate static fatigue. Whenever the contact force ($F_{contact}$) at a contact exceeds a preselected threshold ($F_{threshold}$), the contact was aged by increasing the contact normal and shear stiffness by a small amount which was a linear function of the contact force, Equation (5.3).

When $F_{contact} > F_{threshold}$, then

$$K_n^{new} = K_n^{old}(1+\beta F_{contact})$$
$$K_s^{new} = K_s^{old}(1+\beta F_{contact}) \qquad (5.3)$$

where K_n^{new} and K_s^{new} are the new contact normal and shear stiffness's and K_n^{old} and K_s^{old} are the old contact normal and shear stiffness's. β is a small number.

While $F_{threshold}$ dictates the contacts at which static fatigue occurs, β controls the amount of increase in contact stiffness. Because contact fatigue occurs through fracturing of the micro-morphological features at grain surfaces, a slip and relaxation of the shear force component is expected to be associated with the phenomenon. Therefore, the change in the contact stiffness in the algorithm, was always associated with an instantaneous drop of the friction coefficient to zero. After changing the stiffness at a single contact and allowing slip, the entire assembly was allowed to reach the state of equilibrium. After equilibrium was attained, friction at the contact

where slip was induced was increased back to its original value (μ = 0.6). This process was continued until the algorithm had run through all the contacts in the assembly. This is referred to as one cycle of the fatigue process. The DEM simulation was made to run through many such cycles.

Figure 5.14 shows the results from aging simulation of the numerical sample. The value of β in this simulation was chosen to be 0.0001 and the $F_{threshold}$ was set to 0.6 N. For a comparative purposes, the results from consolidometer test #4 (refer Chapter 4) are shown in Fig. 5.15. The porosity of the sample in the experiment was 0.42 and the porosity of the numerical sample was 0.41. The qualitative features from the DEM simulation (Fig. 5.14) match the experiment (Fig. 5.15) quite well. Like the vertical strain in the physical test, the vertical strain in the DEM model too had the step-wise characteristic. However, vertical strain in the DEM simulation was about 10 times smaller than that observed in the experiment. This was expected, because in the experiment, static fatigue causes fracture and breaking of asperities leading to grain convergence. Modeling this grain convergence using DEM was not possible. However, the increase in lateral stress in the DEM model and in the experiment was quite similar. It should be noted that the simulation time is measured in computational cycles, which does not have a clear relation to the real time.

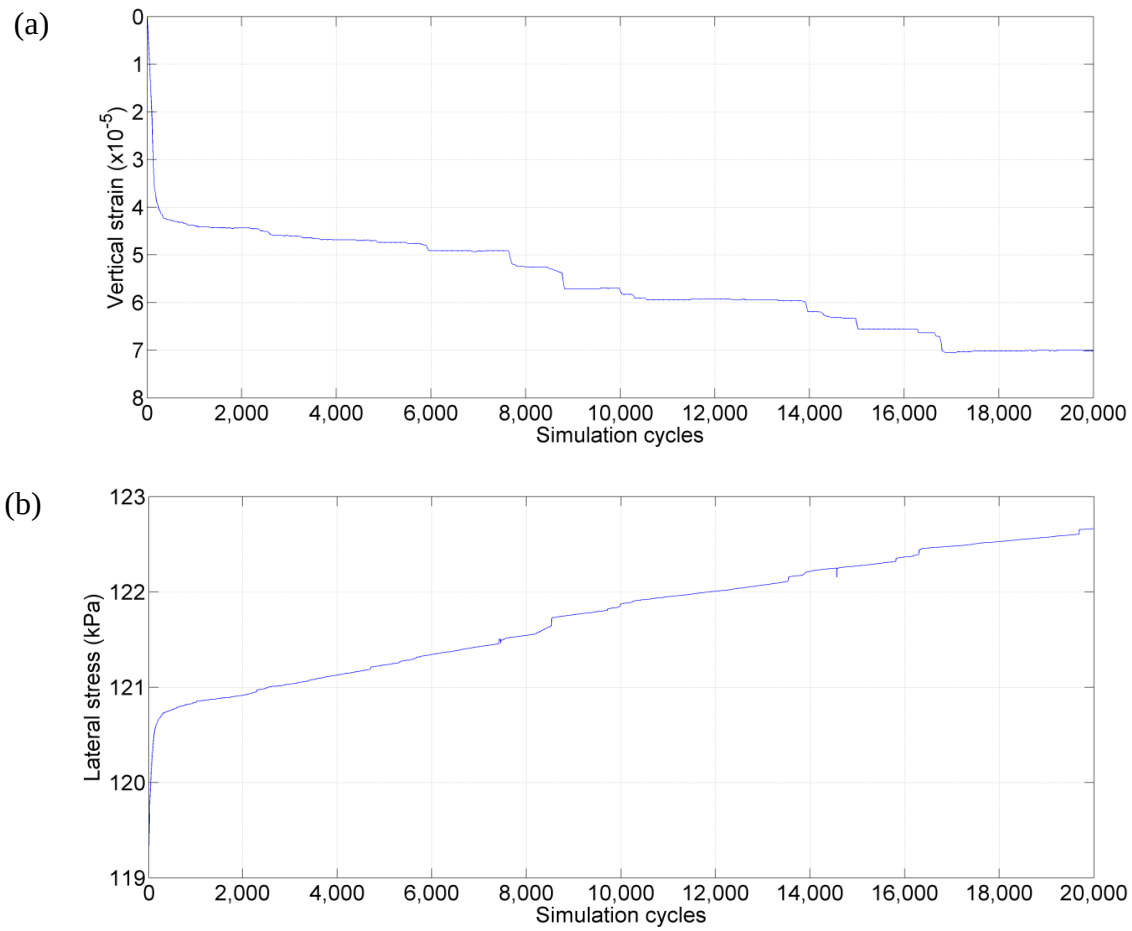

Figure 5.14. DEM simulation of aging; 1D strain conditions, constant vertical load of 230 kPa, (a) specimen vertical settlement during aging, and (b) increase in lateral stress during aging.

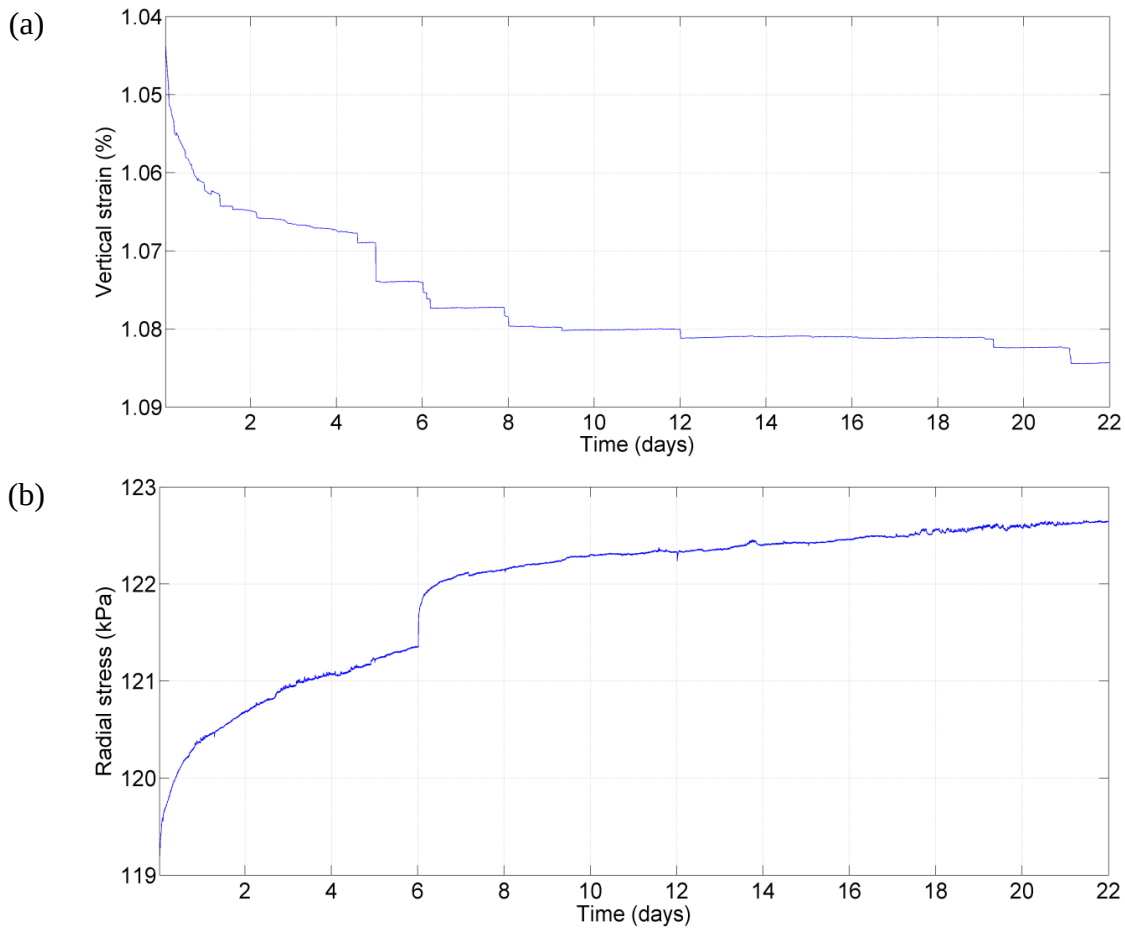

Figure 5.15. Specimen settlement and increase in radial stress under a constant vertical stress of 229.4 kPa (results from consolidometer test #4 in chapter 4), (a) vertical strain in the sample from 30 minutes to 22 days, and (b) increase in radial stress from 30 minutes to 22 days.

Table 5.6 compares some of the DEM model parameters before and after aging. The porosity of the system before and after aging was unchanged. There was almost no change in the total number of contacts and mean contact force in the assembly. The maximum contact force however decreased after aging. The maximum contact normal stiffness in the model after aging increased by a factor of about 10. Figure 5.16 shows a histogram of the change in contact normal stiffness at all contacts during aging; the initial contact normal stiffness for all contacts was 0.13 MN/m. In all, only 145 of almost 97 thousand contacts participated in the aging process. It should be noted that in PFC^{3D}, a contact is defined between two entities (balls or clumps), *A* and *B*. Even if entity *A* slips over *B* or if the two entities rotate to reach a new contact position, it is still regarded as the same contact. However, in reality, if a particle slides or rotates over another

particle to reach a new contact location, a new physical contact between the two particles will be formed.

Table 5.6. Effect of aging on the DEM assembly.

Parameter	Initial model (before aging)	Final model (after aging)
Porosity	0.41	0.41
Total number of contacts	96,804	96,821
Mean contact force	0.099 N	0.101 N
Maximum contact force	1.284 N	1.143 N
Maximum contact stiffness (K_n)	0.13 MPa	1.18 MPa
Lateral-to-vertical stress ratio (K_o)	0.517	0.533

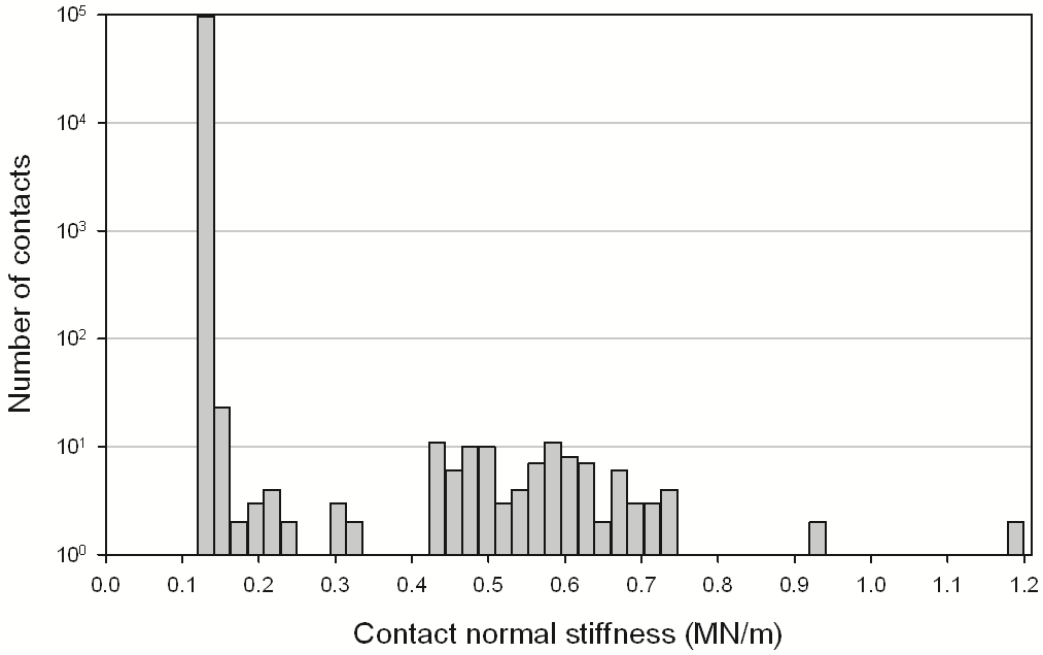

Figure 5.16. Histogram of contact normal stiffness after aging (initial contact normal stiffness was 0.13 MN/m for all the contacts).

Contact force homogenization was observed during aging of the DEM model. Comparing the contact force histogram for the unaged DEM model with the aged DEM model, it was seen that the number of contacts that carry very small and very large forces decreases. This is shown in Fig. 5.17. The contacts carrying a larger load are being loaded less and the contacts carrying a smaller load are being loaded more.

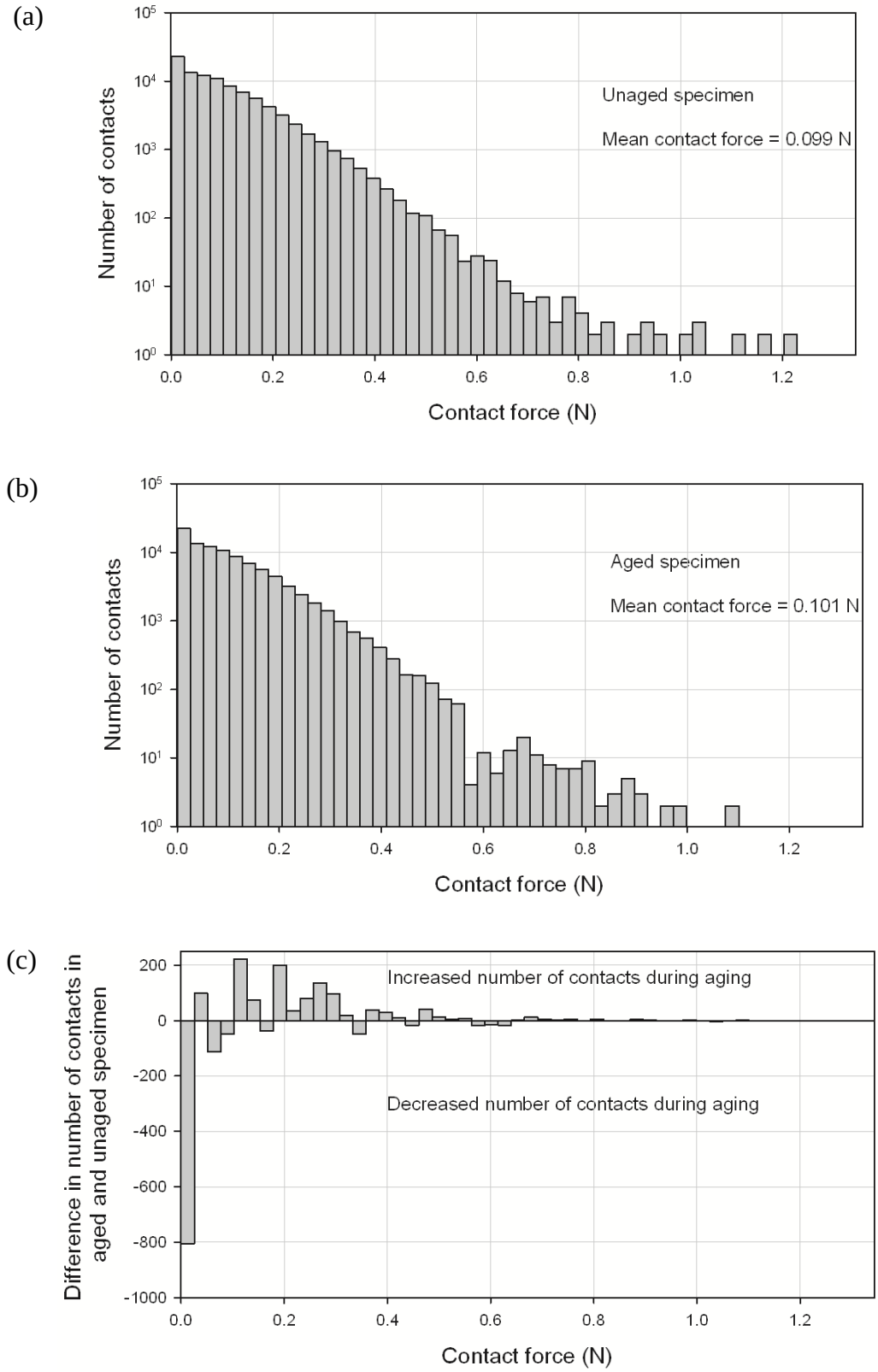

Figure 5.17. Contact force histogram of the specimen, (a) before aging, (b) after aging, and (c) the difference of histograms a and b (histogram in 5.17(b) minus histogram in 5.17(a)).

Figure 5.18 shows the difference in the number of contacts in the aged and unaged model along a vertical plane (XZ plane, Fig. 5.13).

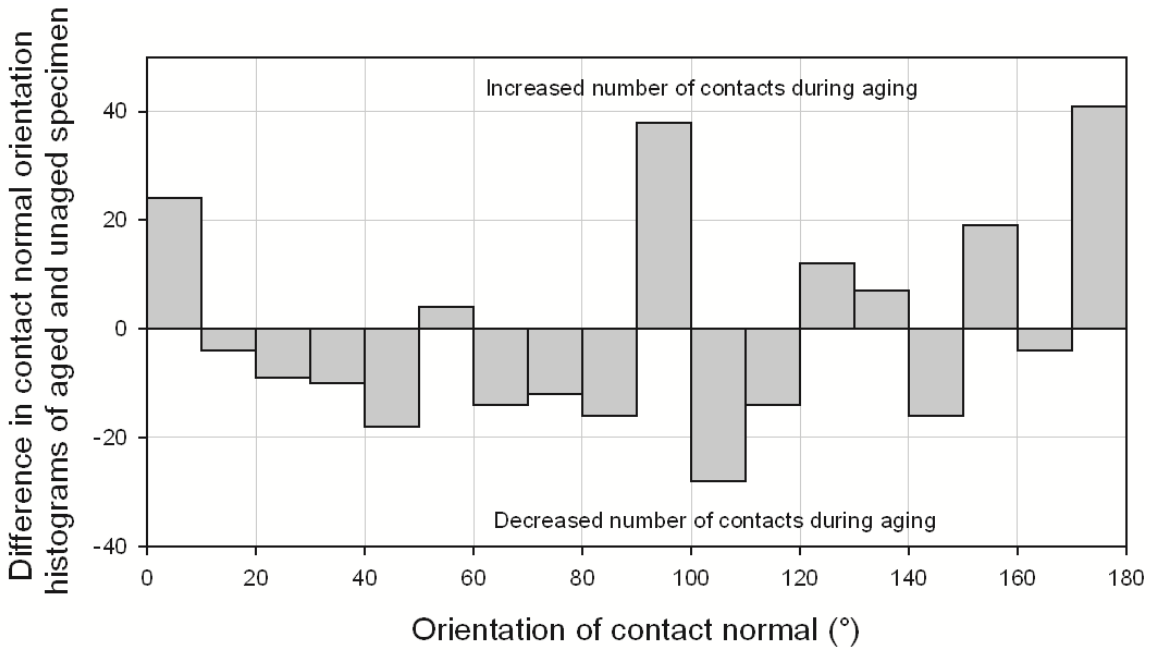

Figure 5.18. Difference in the contact normal orientation of the aged and unaged DEM model along a vertical plane.

Comparing the force chain network before and during aging showed that some of the strong force chains were degraded to weak force chains and vice versa, leading to a change in contact force chain network during aging. This is illustrated in Fig. 5.19. The figure shows all the particles (balls and clumps) touching a plane (XZ plane) at mid distance (y = 1 cm) of the specimen (2 cm cube) shown in Fig. 5.13. The darker shaded particles were part of the strong force chain network and the lighter shaded particles were part of the weak force chain network. Fig. 5.19(a) shows the system before aging. Figs. 5.19(b) and (c) show the system after 10,000 and 20,000 cycles of aging, respectively. The dark-particle chains in Fig. 5.19 are not continuous because this is a 3D simulation; the strong force chains only intersect the mid layer of particles, and they extend out of the plane. Comparing these three figures, it can be seen that the particles that form the strong force chain network keep changing during aging. These changes in force chain network observed in DEM simulation of aging could be interpreted as force chain buckling observed by some researchers in the past (Bowmann and Soga, 2005; Jirathanathaworn, 2009).

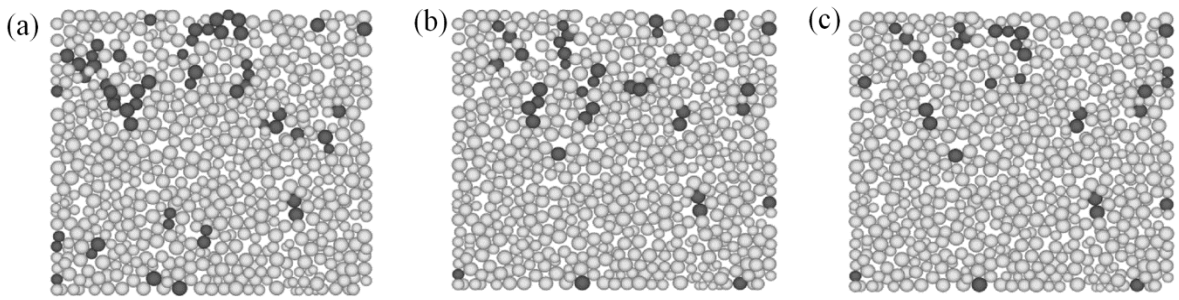

Figure 5.19. Vertical mid layer of grains in the strong force chain network during aging; the dark grains are in the strong force chain network, while the remaining particles are in the weaker force chain network, (a) initial unaged model (0 cycles of aging), (b) 10,000 cycles of aging (see Fig. 5.14), and (c) 20,000 cycles of aging.

The elastic modulus and strength of the specimens before aging and after 250, 10,000, 15,000 and 20,000 cycles of aging was calculated by performing numerical triaxial tests. Table 5.7 summarizes the results. The Young's Modulus in all tests shown in Table 5.7 was calculated at an axial strain of 2×10^{-5}. The small strain macroscopic Young's Modulus (E) increased by nearly 24% after 20,000 cycles of aging. This is not surprising since the stiffness at contacts loaded above the threshold was gradually increasing as aging continued. It is surprising, however, that this was the result of only 145 contacts having fatigued of almost 97 thousand in the entire sample. Figure 5.20. shows the results from triaxial test at a larger axial strain. From Fig. 5.20(a) it can be seen that the stress ratio at failure was about 3 (equivalent to the internal friction angle of 30°). It is seen that the increase in modulus of the aged specimen compared to the unaged specimen becomes smaller as the axial strain increases. This is illustrated in Fig. 5.21. This observation suggests that, as the sample is sheared during the triaxial test, the particles displace and/or rotate causing the loss of already aged contacts while new contacts are formed; consequently, the sample loses its "memory" of aging at larger strains. It was quite interesting to note that the 24% increase in modulus in the DEM model occurred during a very modest increase of about 4 kPa in lateral stress. Howie et al. (2002) observed that the Young's Modulus (calculated as a secant modulus at 0.02% strain) of Fraser River sand increased from 25 MPa after one minute of aging to 95 MPa 10,000 at minutes (7 days) after aging at a horizontal-to-vertical stress ratio of 0.5. Using rate process theory in DEM, Suarez (2012) observed that the constrained modulus increased by about 45%. Thus an increase of 24% in Young's Modulus in the presented DEM model is rather modest by comparison. This may have been caused by setting too high of the contact force threshold for contact aging.

Table 5.7. Modulus and strength of the DEM assembly obtained from triaxial tests before and during aging.

Cycles of aging	Vertical stress (σ_1)[1] (kPa)	Horizontal stress (σ_3)[2] (kPa)	Small strain Young's Modulus[3] (MPa)	Friction angle (°)
0	230	119	138.7	30
250	230	120.7	143.1	30
10,000	230	121.8	155.3	30
15,000	230	122.3	160.1	30
20,000	230	122.7	172.2	30

[1]This was the initial vertical stress before start of the triaxial test.
[2]This was the measured horizontal stress during aging; this stress was kept constant during triaxial testing.
[3]$E = \Delta\sigma_1/\Delta\varepsilon_1$; calculated at a vertical strain of 1.5×10^{-5}.

There were two parameters in the DEM model of static fatigue, namely, $F_{threshold}$ and β (Equation. (5.3)). The effect of changing these two parameters on the lateral stress of the specimen was investigated. For these simulations, the vertical stress was kept constant at 230 kPa and the initial lateral stress was 115 kPa. During aging, the lateral walls of the specimen were not allowed to move (zero strain condition). The effect of changing $F_{threshold}$ is shown in Fig. 5.22. $F_{threshold}$ controls the number of contacts involved in the aging process. The larger number of contacts participating in the aging process, the greater the increase in lateral stress.

Figure 5.23 shows the effect of changing β on the increase in lateral stress. β controls the rate at which the stiffness at a contact increases due to static fatigue. It was interesting and quite surprising to note that β does not significantly influence the magnitude of increase in lateral stress.

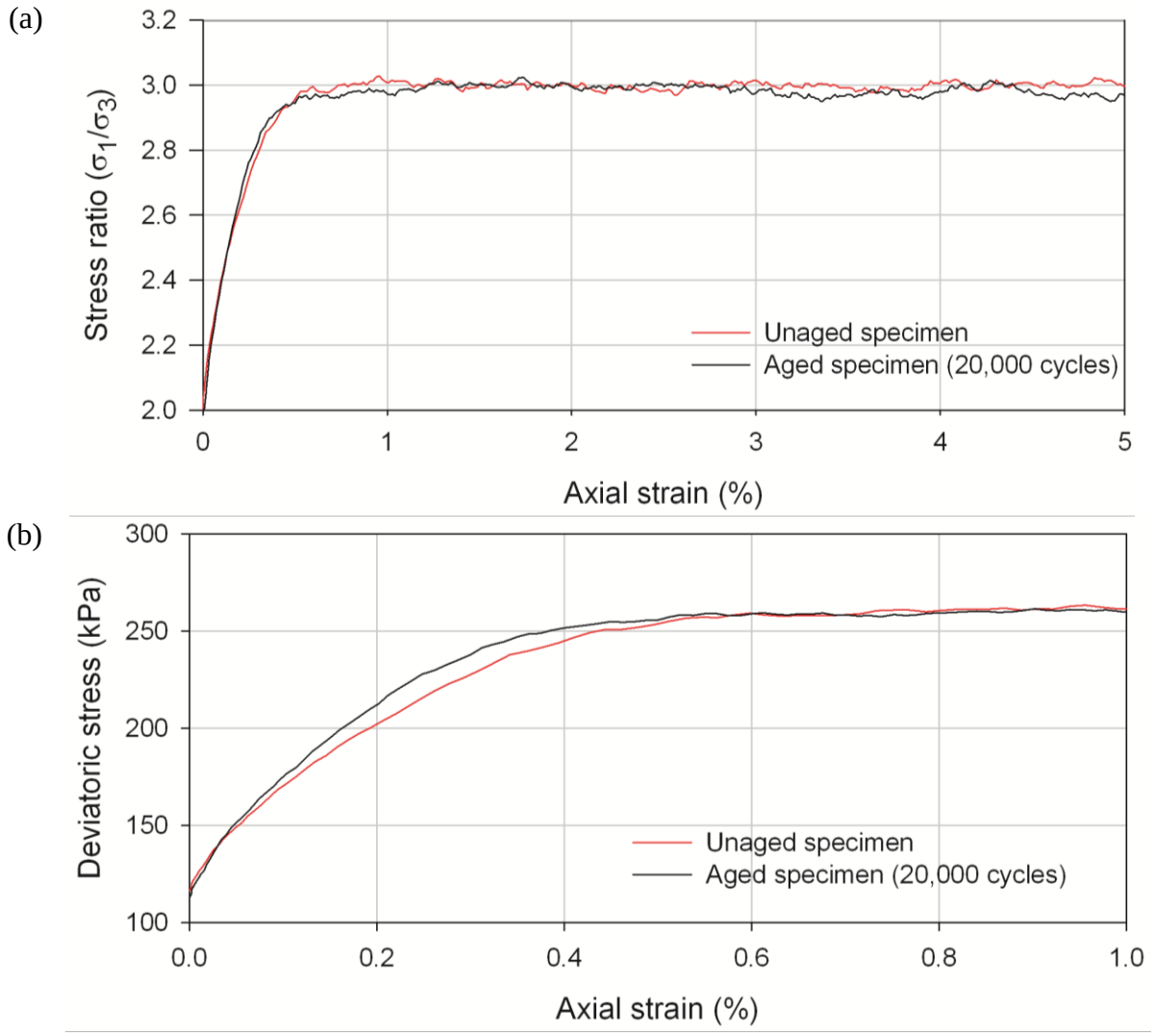

Figure 5.20. Triaxial test result on the aged and unaged DEM specimens, (a) stress ratio vs. axial strain showing no increase in frictional angle, and (b) deviatoric stress vs. axial strain showing an increase in Young's modulus of the assembly during aging; confining stress (σ_3) for the unaged specimen was 119 kPa and for the aged specimen was 122.7 kPa.

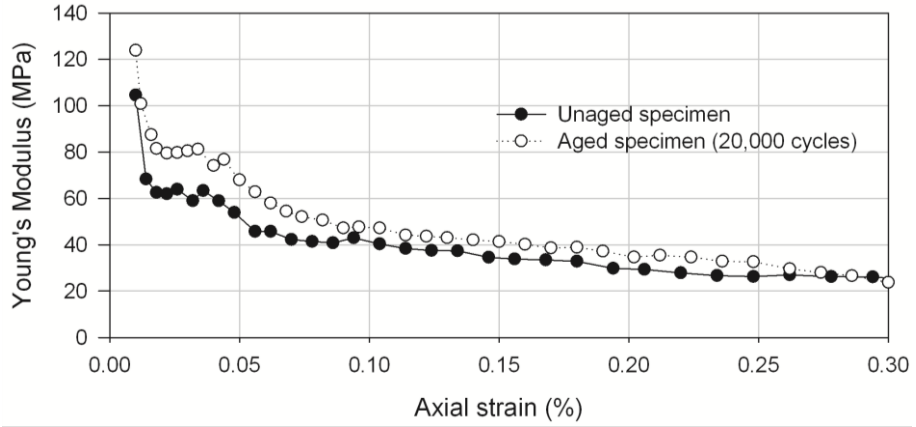

Figure 5.21. Young's Modulus of the aged and unaged DEM specimens as a function of axial strain.

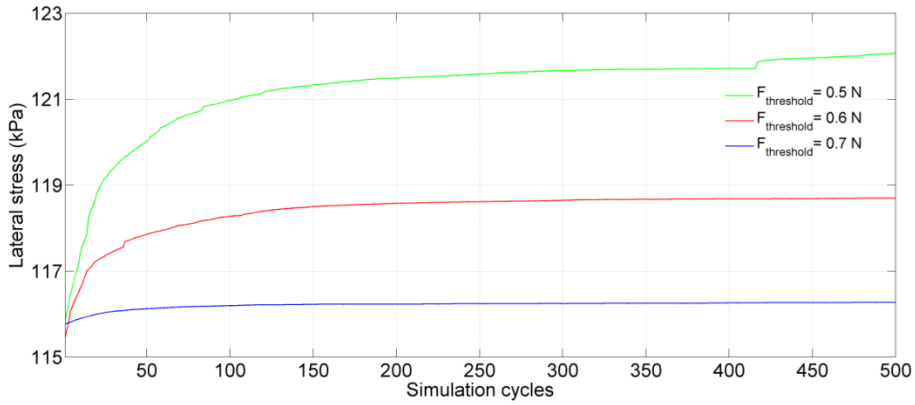

Figure 5.22. Effect of $F_{threshold}$ on the increase in lateral stress increase caused by aging; all tests performed at a constant vertical stress of 230 kPa.

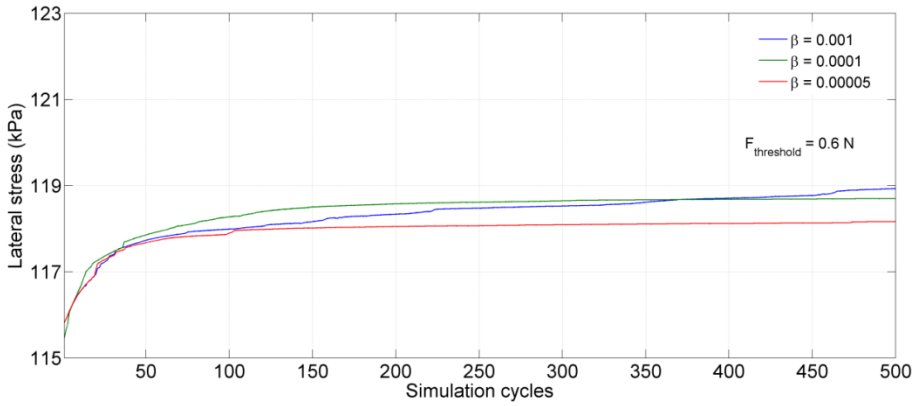

Figure 5.23. Effect of β on the increase in lateral stress during aging; all tests were performed at a constant vertical stress of 230 kPa.

The simple model of static fatigue at grain contacts based on a gradual increase in contact stiffness supports the suggestion that grain convergence and the associated increase in contact stiffness results in an increase of the macroscopic modulus of the assembly, and thereby causing an increase in the lateral stress. Shearing the specimens to large strains, however, seems to eradicate the positive effect of aging (increase in modulus), reducing the modulus to the pre-aging level. The increase in lateral stress of the DEM aging model is comparable to the increase in lateral stress obtained from the consolidometer tests in Chapter 4. The friction angle of the aged DEM specimen was unaffected by aging. To study the effect of increased soil stiffness and lateral stress on the cone penetration resistance of freshly compacted sands, FEA simulations were performed. This is discussed in the next section.

5.3 Finite Element Method (FEM) simulation of CPT resistance

Finite Element Method simulations were performed using Abaqus/CAE ver 6.10 to study the effect of change in stiffness and horizontal-to-vertical stress ratio. The explicit solution scheme was used in the simulations. The modeling approach followed here builds on the modeling scheme suggested by Susila and Hryciw (2003). It is well known that the cone penetration resistance depends on the friction angle of the soil (soil strength), soil compressibility and the in-situ lateral effective stress (Susila, 2005). The tip resistance can also be presented as dependent on the Over Consolidation Ratio (OCR), because the in-situ stress state in soils is affected by OCR. OCR is defined as the ratio of the maximum past effective vertical stress to the current effective stress. Changes to any of these parameters affect the cone penetration resistance. Studies in the literature that looked into combined effect of increase in Young's Modulus and lateral stress on CPT resistance are rare. Susila (2005) studied the changes in CPT resistance due to changes in lateral stress and Young's Modulus (caused by a change in OCR). However, experimental tests and DEM simulations performed showed that the lateral stress and modulus both change in time, and this is not caused by a change in OCR. The effect of the changes in modulus and lateral stress was studied in this section. The objective of the modeling effort was to see by how much the combined increase of stress ratio and Young's Modulus, as measured in the DEM model accounting for aging, affect the cone penetration resistance.

Figure 5.24 shows the model with dimensions and boundary conditions. The soil was modeled by axisymmetric four node elements. The cone was modeled as a rigid indenter to

reduce the fluctuations of tip resistance due to chattering of surfaces. The cone had an apex angle of 60° and was 36 mm in diameter. The conical part of the cone was 3.1 cm in length. Adaptive meshing technique was applied to the entire soil body to minimize mesh distortions. To speed up the simulation time the cone is pushed into soil at a rate of 20 cm/sec. Simulations performed at 2cm/sec and 20cm/sec showed almost no difference in penetration resistance (which is expected, considering rate-independency of the soil model). Computation time decreased by nearly five times due to the increase in penetration velocity. The coefficient of friction between the cone and soil was assumed to be 0.3. The soil was modeled as elastic-perfectly plastic. The elastic part was characterized by the Young's Modulus (E) and poisson's ratio (ν). While E was varied in the simulations, ν was set to 0.2 for all simulations. The yielding of the soil was modeled with the Drucker-Prager criterion with no cohesive component

$$F = t - p \tan\beta = 0 \tag{5.4}$$

and the non-associative flow rule was adopted with the plastic potential in the form

$$G = t - p \tan\psi^* = C \tag{5.5}$$

where

$$t = \frac{1}{2}q\left[1 + \frac{1}{K} - \left(1 - \frac{1}{K}\right)\left(\frac{r}{q}\right)^2\right]; \quad p = -\frac{1}{3}\sigma_{kk}, \quad q = \sqrt{\frac{3}{2}s_{ij}s_{ij}}, \quad r = \sqrt{\frac{9}{2}s_{ij}s_{jk}s_{ki}} \tag{5.6}$$

And s_{ij} is the deviatoric stress tensor. The material properties β and $\psi*$ in Equations (5.4) and (5.5) were related to the internal friction angle ϕ in Mohr-Coulomb yield function and dilatancy angle ψ as (matching compression meridians on the Mohr-Coulomb pyramid)

$$\tan\beta = \frac{6\sin\phi}{3-\sin\phi}, \quad K = \frac{3-\sin\phi}{3+\sin\phi}, \quad \tan\psi^* = \frac{6\sin\psi}{3-\sin\psi} \tag{5.7}$$

A very low dilatancy angle of 2° (nearly incompressible) was used in all of the CPT test simulations. Rather than simulating a continuous process of cone penetration, an analysis was carried out on a block shown schematically in Fig. 5.24. The depth was simulated by the effective stress condition (σ_v) at the top boundary, but the soil in the block was considered

weightless. The CPT simulation was performed to a depth of 300 mm on the soil block and the steady state value was taken as the cone penetration resistance at the depth set by the stress boundary condition. A typical graph of the cone resistance vs. penetration depth is illustrated in Fig. 5.25. For the block shown in Fig. 5.24, a uniform mesh size gradation was used. The ratio of soil element size to cone radius was about 1/10.

Before the combined effect of modulus and increase of lateral stress was studied, the individual (separate) effects of the change in the horizontal-to-vertical stress ratio and the Young's modulus were studied. It should be realized that in reality these changes are not independent. The change in the modulus leads to the change in the stress ratio. Two numerical tests were performed at a vertical stress of 0.25 MPa with a friction angle $\phi = 37°$. Figure 5.26(a) shows the increase in tip resistance as a function of Young's Modulus, and Fig. 5.26(b) shows the increase as a function of the horizontal to vertical stress ratio. The tip resistance increased in both cases. This shows that an increase in cone penetration resistance does not necessarily imply an increase in soil strength (the internal friction angle). However, researchers and engineers often use the chart by Robertson and Campanella (1983) shown in Fig. 5.27 and interpret the increase in CPT resistance as an increase in the internal friction angle. The results obtained in Fig. 5.26 clearly show an increase in CPT resistance could occur without an increase in soil strength.

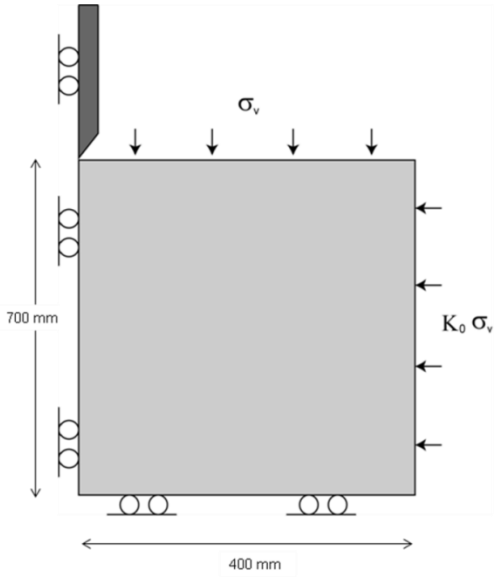

Figure 5.24. Geometry and boundary conditions of the finite element model of the cone penetration process, with depth adjusted by the stress condition on the top boundary.

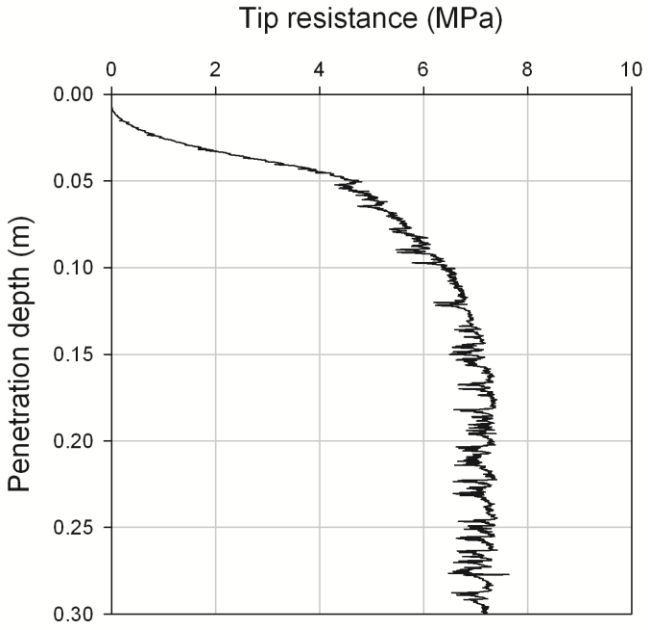

Figure 5.25. Increase in cone penetration resistance with depth; steady-state resistance was taken as the value at the depth related to the stress condition at the top boundary of the simulation block.

(a)

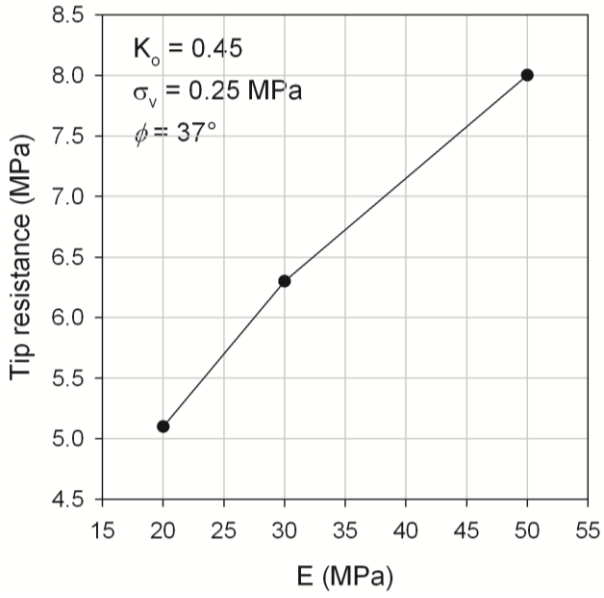

(b)

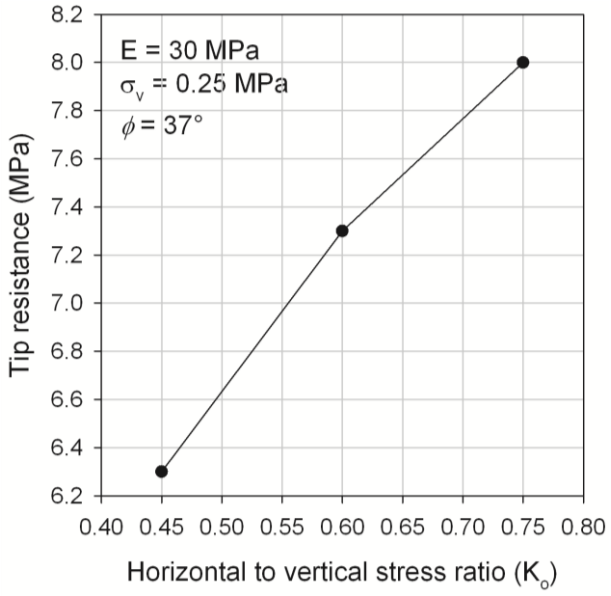

Figure 5.26. Effect of change in soil stiffness and stress ratio on cone penetration tip resistance, (a) increase in tip resistance as a function of Young's Modulus, and (b) increase in tip resistance as a function of stress ratio.

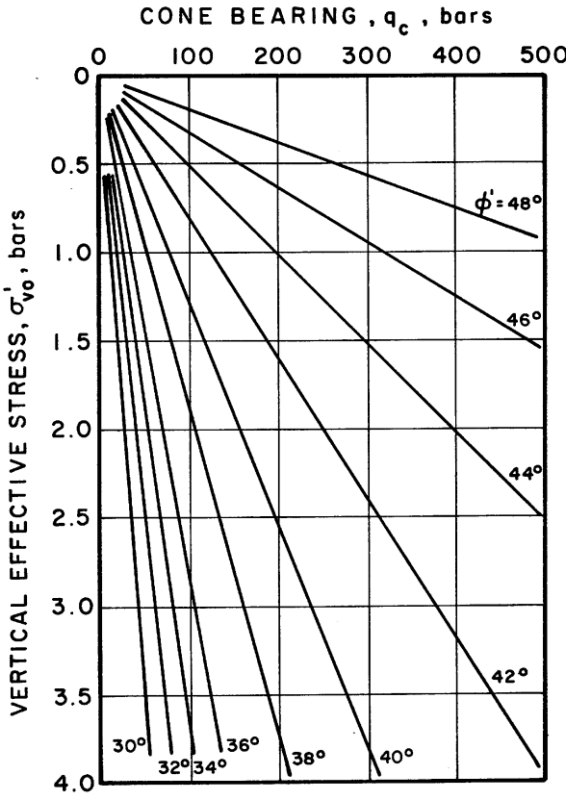

Figure 5.27. Correlation between cone tip resistance (q_c), vertical effective stress (σ_{vo}') and drained internal friction angle (ϕ') (from Robertson and Campanella, 1983).

The model of aging presented in section 5.2.3 showed an increase of 24% in the Young's Modulus (from 138.7 MPa to 172.2 MPa) while the stress ratio *k* increased by 3.1% (from 0.517 to 0.533). Comparing the increase in lateral stress from the DEM model to the dry physical tests (consolidometer tests) from Chapter 4, it was seen that a 3.1% increase in lateral stress could be caused in Ottawa 20-30 sand aged to 21 days at a vertical stress of 230 kPa or aged to 2.5 days at a vertical stress of 345 kPa. The same increase of 3.1% in *k* could also be caused in Michigan Lake Empire Beach sand aged to about 3 days at a vertical stress of 230 kPa. It can be clearly seen that the increase in lateral stress was a function of vertical stress and type of sand. The increase in CPT resistance caused by a 3.1% increase in lateral stress and 24% increase in Young's Modulus was studied by performing FEM simulations.

Figure 5.28 shows the increase in CPT resistance obtained from ABAQUS simulations due to aging. For this simulation, the initial Young's Modulus and stress ratio were 139 MPa and 0.517. The final values were set to 172.2 MPa and 0.533, respectively. The mass density of the soil was set to 1700 kg/m^3, and the Poisson's ratio was chosen as 0.20.

At a depth of 15 m (Fig. 5.28), the CPT resistance increased by nearly 25%. At a depth of 10 m, the increase was 21% and at a depth of 5 m, the increase was 12.5%. Comparing the aging case studies (summarized by Saftner, 2011), it is clear that the increase in CPT resistance in the FEM model is very much in the range of measured increases in the field. After vibrocompaction or blast densification, the drop in porosity produces an increase in internal friction angle. This compaction-induced increase in friction angle was not simulated here. This will be discussed in the next section.

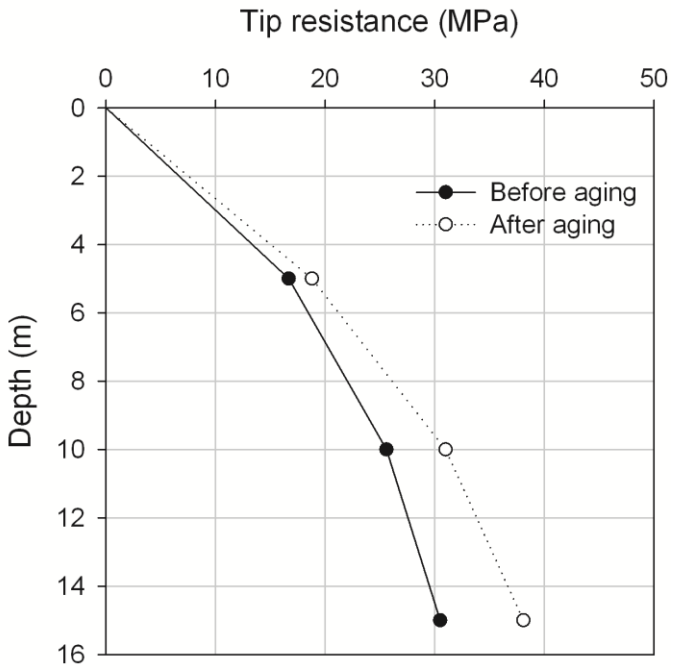

Figure 5.28. FEM simulation of cone penetration resistance; the aged sand bed has 24 % higher Young's Modulus and 3.1% higher stress ratio due to aging, the friction angle was the same (37°) before and after aging.

The increase in CPT resistance following a disturbance was simulated using FEA in this section. It was observed that the time-delayed increase in penetration resistance does not require the strength (ϕ) of the soil to increase, but could be just due to a change in soil stiffness. In fact, the DEM model of aging presented in section 5.2.3 supports the idea that the friction angle does not increase due to aging. It is argued that the strength of sand represented by the friction angle (ϕ) after dynamic compaction increases as soon as the fabric of the compacted sand is formed, whereas the delayed increase in the cone penetration resistance is caused not by an increase in strength, but by a gradual change in the stress state in the compacted soil. Probable causes for a drop in CPT resistance immediately after dynamic compaction, and the development of the stress state in freshly compacted sand, are discussed in the next section.

5.4 Reasons for changes to CPT resistance following a disturbance

Compaction of sand requires a change in its packing, so that the volume of pores can be reduced. In dry deposits the energy imparted to the system leads to an increase in the density of kinetic energy (referred to in physics as the *granular temperature*) leading to vibration of grains. Under

gravity conditions, the granular assembly will compact, with the major force chains aligned in the direction of gravity (however, with a sufficient granular temperature maintained over long intervals a granular bed can be fluidized).

When saturated sands are being dynamically compacted, the contact forces between grains are lost (liquefaction), and the contacts are reconfigured so that a tighter packing can be achieved. The effective stresses are reduced to zero during liquefaction, but the stress state is rebuilt upon dissipation of the excess pore water pressure. The vertical macroscopic stress is governed by gravity, but the horizontal stress does not have a comparable governing rule, and it only needs to be large enough so that the stress state is admissible, i.e., it does not violate the yield condition. When the effective vertical macroscopic stress increases from zero during liquefaction to a value that balances the buoyant weight of the soil at any depth, the horizontal stress will trail with its value such, so that the stress state is just below the yield condition of the newly compacted sand. This horizontal stress is likely to be significantly lower than the stress in the pre-liquefaction sand bed that was subjected to long-term gravity loads. Due to this, the horizontal to vertical stress ratio k decreases after dynamic compaction (and liquefaction). However, in time after compaction, due to static fatigue at grain contacts, the horizontal stress, and therefore the stress ratio k will increase. This initial drop and the subsequent gradual increase in horizontal stress are the reasons why the cone penetration resistance often drops down immediately after compaction, and subsequently increases over time. This explanation was first suggested by Schmertmann (1985), who stressed the importance of stress ratio on CPT/SPT results, was alluded to by Thomann (1990), and many others. For instance, Thomann (1990) and Hryciw (1986) observed no significant changes to the flat plate dilatometer index (and hence lateral stress ratio) following blasting, but laboratory tests by Thomann (1990) showed a decrease in shear modulus of soil following disturbance, and a subsequent increase with time. However, none of the earlier studies provided convincing reasons behind the time-dependent changes in elastic modulus and lateral stress.

The drop and subsequent increase in penetration resistance during aging is illustrated in Fig, 5.29. In Fig. 5.29, the line OA represents the stress ratio before any disturbance to the soil. The disturbance caused to the soil is defined here as any process that causes the grain assembly to reconfigure and create new contacts that have not been subjected to the process of aging before. The disturbance could be in any form, such as placing a hydraulic fill, blast densification,

vibrocompaction etc., and is assumed to occur at point A in Fig. 5.29. If there was no disturbance, the stress ratio would not have changed and would continue along AE. If a disturbance occurred at point A, and caused soil settlement, we can expect an increase in friction angle of soil. In cases where the disturbance caused reduction in stress ratio k and an increase in friction angle ϕ, the cone penetration resistance will drop from point A to point B, Fig. 5.29. Over time static fatigue at grain contacts will cause the stress ratio (under 1D strain conditions) to increase from B to D, producing an increase of the cone penetration resistance beyond that prior to compaction. In a case that the disturbance does not cause the soil to compact, but causes reconfiguration of contacts, the stress ratio will follow along path B'E to reach the pre-disturbance level, Fig. 5.29. In a hypothetical case where very substantial densification has occurred, the stress ratio may not drop down after the disturbance, because of the substantial increase in the internal friction angle (soil strength). The subsequent process will then lead to an increase in the stress ratio along line AC.

The increase in stress ratio due to static fatigue had been showed earlier in Chapter 4 (consolidometer tests). DEM aging simulations suggest that the delayed increase in stress ratio is associated with no increase in internal friction angle of the soil. To demonstrate that the drop in stress ratio (AB in Fig. 5.29) after dynamic compaction can cause the CPT resistance to decrease even though the friction angle increases, discrete element simulations were performed. Some evidence of the drop and subsequent increase in stress ratio k already exists in literature (e.g., Mitchell and Solymar, 1984). During driven pile installation, the stress ratio immediately after pile driving is very low (k ~ 0.1 to 0.2). Over time, k increases significantly (k ~ 0.3 to 0.6). Ng et al. (1988), Karlsrud et al. (1992), and Axelsson (2000) discuss the changes of the stress ratio during pile driving operations in detail.

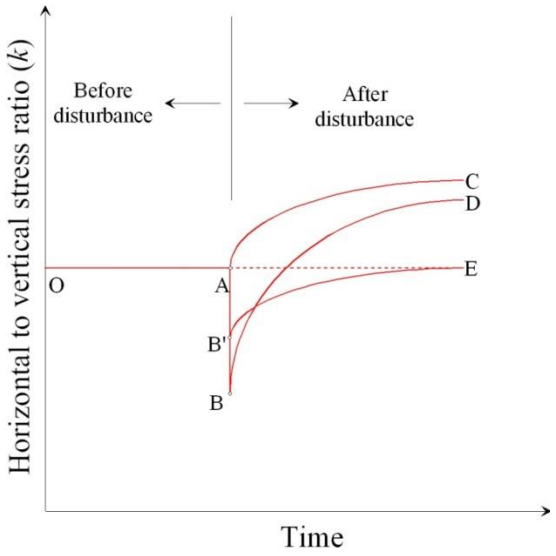

Figure 5.29. Suggested paths of the horizontal to vertical stress ratio before and after a disturbance.

To gain some numerical confirmation that the stress ratio k can indeed decrease immediately after disturbance, and then gradually increase during contact stiffness change (increase), DEM simulations were carried out. An assembly of over 11 thousand grains was generated using the *PFC*^{3D} (2008) computer code. These grains were predominantly spherical with radii between 2.3 and 3.7 cm; 25% of the grains were in the form of "clumps", *i.e.*, particles with a shape of two overlapping spheres with the centers offset by one radius (peanut-shape particles). The assembly was formed by raining particles in a cube of 1.2 m in size; the porosity of the assembly was 0.35. Initial contact normal and tangential stiffness were 4.0 and 1.6 MN/m, respectively, and particles were simulated to be smooth ($\mu = 0$) during deposition. The mass density of the grains was set to 2,650 kg/m^3, and gravity acceleration was taken as 9.81 m/s^2. After the specimens were so constructed, the macroscopic stress state was hydrostatic. Next, the diameter of all particles was reduced by 0.0005, simulating the loss of contacts or breakage of the force chains. At the same time the inter-particle friction coefficient was set to $\mu = 0.65$ (equivalent to a friction angle of 33°). Subsequently, the specimen reache equilibrium, and this concluded the process of preparing the specimen. After the system reached the state of equilibrium, the porosity was practically unchanged, and equal to $n = 0.35$, and the average (macroscopic) horizontal-to-vertical stress ratio was $k = 0.473$. A triaxial compression test of the specimen was then simulated with a confining pressure of 50 kPa. Interpreting the strength of

the granular assembly as frictional with a linear envelope, the peak internal friction angle was found to be 33.5°.

DEM simulations of liquefaction as a hydro-mechanics problem are cumbersome, and they are seldom attempted. Two other methods were considered: (a) inducing liquefaction through a constant-volume cyclic strain process, and (b) a minute reduction in grain size causing an instant loss of inter-granular contacts. Both methods lead to a reduction in the co-ordination number (number of contacts per particle), and loss of shear resistance interpreted as the onset of liquefaction, even though no pore fluid is considered. In the first method, the initial confining (or consolidation) stress is gradually reduced in a kinematically controlled constant-volume cyclic process, and the drop in the pressure associated with this process is interpreted as a build-up of the pore water pressure. Successful simulation of this type can be found, for instance, in Ng and Dobry (1994).

A small reduction in the size of all grains was used in this study to simulate a sudden loss of all contacts during liquefaction (0.001 reduction in grain diameters). This reduction in grain size produced no meaningful reduction in the void ratio (simulation of compaction was not attempted). The purpose of this DEM simulation was to indicate the change in the stress state from the pre-liquefaction to post-liquefaction state. After the instantaneous loss of contacts, the contacts were re-gained in the process driven by gravity under one-dimensional strain conditions. However, the contact stiffness was reduced by half before the new contacts were allowed to form. This was because grains would rotate during liquefaction, so that the newly-formed contacts are shifted with respect to pre-liquefaction contacts. The new contacts have micro-morphological features not previously subjected to stress corrosion cracking (fatigue), hence the expected reduction in contact stiffness. After equilibrium was reached, the average horizontal-to-vertical macroscopic stress ratio was found to be $k = 0.339$, substantially lower than the "pre-liquefaction" value. This state is the stress state of the system immediately after liquefaction. In calculations of this ratio, the horizontal stress was averaged over the vertical boundaries, and the vertical stress was taken as half of the stress at the bottom boundary (average of the stress at the top and bottom). This simulation supports the hypothesis of the reduced horizontal stress (or increased deviatoric stress) in the post liquefaction sand bed, even though it is only numerical evidence. The specimen was then subjected to a (numerical) triaxial test under a confining pressure of 50 kPa. The peak internal friction angle was determined to be 33.6°, which was not

substantially different from the pre-liquefaction value (33.5°). The average stress state in the specimen before and after "liquefaction" is illustrated in Fig. 5.30. It is evident that the stress state after simulated liquefaction has moved closer to failure, whereas the yield condition was not changed (no compaction was simulated).

Once the contacts between particles have been formed after liquefaction, the post-liquefaction stress state developed is characterized by an increased deviatoric stress. This stress state however will not remain constant because of the process of the time-dependent increase in elastic moduli of sand due to static fatigue at grain contacts. The process of aging was simulated by gradually increasing the contact stiffness at all contacts.The normal and tangential stiffness of grain contacts were increased first by 10%, mimicking an increase in stiffness due to static fatigue and convergence of grains. The horizontal-to-vertical stress ratio now increased to the value of 0.365; with another 10% increase in the contact stiffness the horizontal-to-vertical stress ratio increased to 0.378. These increases are reported in Table 5.8. Contact stiffness was then increased in another eight steps up to the double of the post-liquefaction value. After each step, the grain assembly was allowed to reach the state of static equilibrium. Ratio k increased to 0.413 when the contact stiffness reached a 50% increase over the post-liquefaction stiffness, and k = 0.459 when the contact stiffness was doubled. At this stage, the stress reached a state close to the pre-liquefaction level. The numerical triaxial compression test revealed the peak internal friction angle to be ϕ = 33.5°. It is interesting to note that instead of increasing the contact stiffness in an incremental fashion (10% increase), a one-step 100% increase in contact stiffness resulted in k = 0.438, which was lesser than the multi-step increase to k = 0.459. Clearly, the process is not linear. One might expect the process simulated here to occur after any disturbance of sand that will cause the loss of contacts and formation of new contacts that have not been previously subjected to stress corrosion cracking. This could be the reason why in the tests of Dowding and Hryciw (1986), the newly formed bed that was not subjected to blasting also exhibited some delayed increase in penetration resistance.

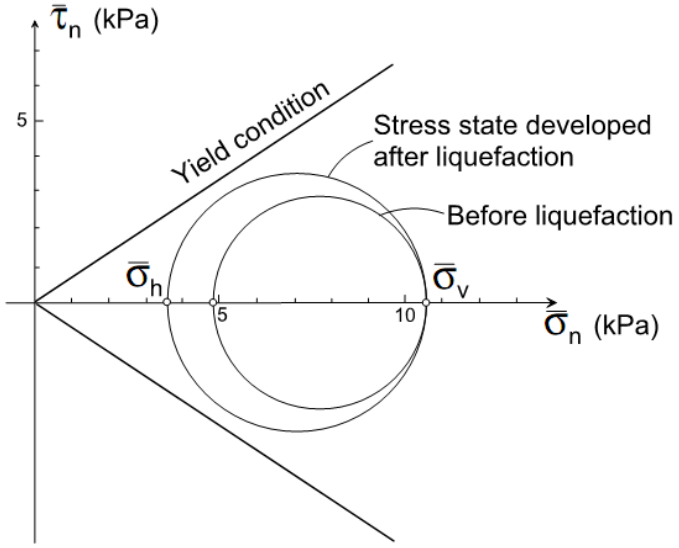

Figure 5.30. Increase in deviatoric stress after liquefaction.

Table 5.8. Increase of horizontal to vertical stress ratio k caused by an increase in inter-granular contact stiffness.

K_n (MN/m)	K_s (MN/m)	k
2.0	0.8	0.339
2.2	0.88	0.365
2.4	0.96	0.378
2.6	1.04	0.391
2.8	1.12	0.399
3.0	1.2	0.413
3.2	1.28	0.424
3.4	1.36	0.433
3.6	1.44	0.442
3.8	1.52	0.451
4.0	1.6	0.459

In order to support the conjecture that the increase in stiffness and the consequent increase in stress ratio are responsible for the gradual increase in cone penetration resistance of sands after dynamic compaction, finite element analysis of the process was carried out. The Young's Modulus associated with states corresponding to k of 0.33, 0.39, 0.43 and 0.45 in Table 5.8 were obtained by performing triaxial tests at 50 kPa confining pressure. Fig. 5.31(b) shows obtained Young's Moduli at each stress state. The solid line with the filled circles in Fig. 5.32 shows the penetration resistance calculated for a soil bed with internal friction angle of $\phi = 32°$ and $k = 0.45$ (state prior to compaction). At the time of dynamic compaction the soil bed is liquefied, and the re-gained effective stress state is characterized with a low k of 0.33. Although the sand was assumed to be compacted with the internal friction angle increasing from 32° to 37°, the penetration resistance decreased to the line marked #0 (dotted line with unfilled circles in Fig. 5.32); such is the impact of the drop in horizontal stress. The decrease in horizontal stress caused an increase in the deviatoric stress, moving the stress state closer to the failure surface (in the stress space). After the first time interval (0 to 1 in Fig. 5.31), the penetration resistance increased to reach the line marked #1 in Fig. 5.32. In the two subsequent intervals the resistance increased as indicated by lines #2 and #3. It is evident that the delayed increase in CPT resistance can be caused by a gradual change in the stress state in the compacted soil and not by an increase in the soil strength. In pressure-dependent soils, the shear strength is, of course, dependent on the first invariant of the stress state.

(a)

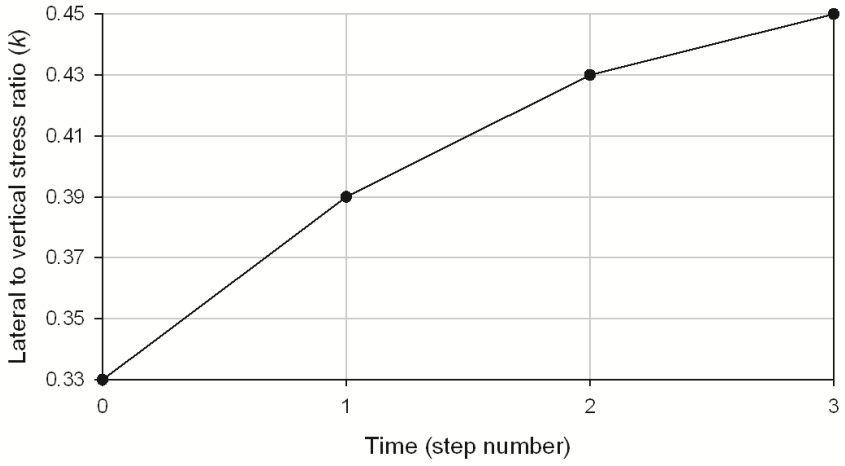

(b)

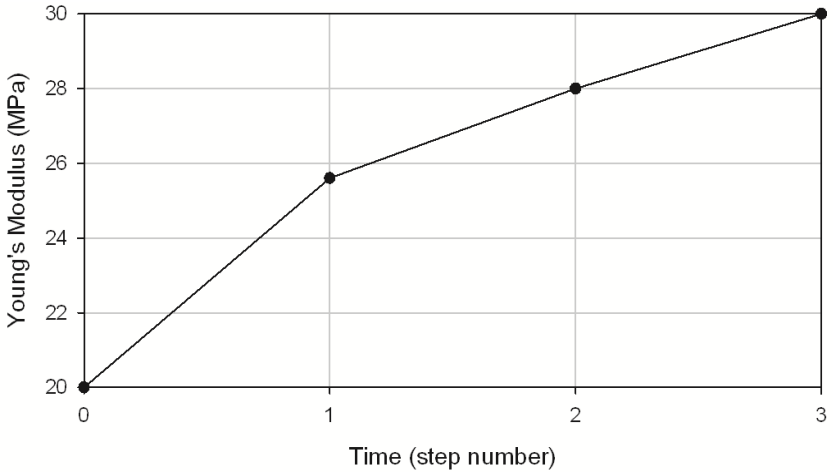

Figure 5.31. Variation of lateral to vertical stress ratio (*k*) and Young's Modulus in the FEA simulation.

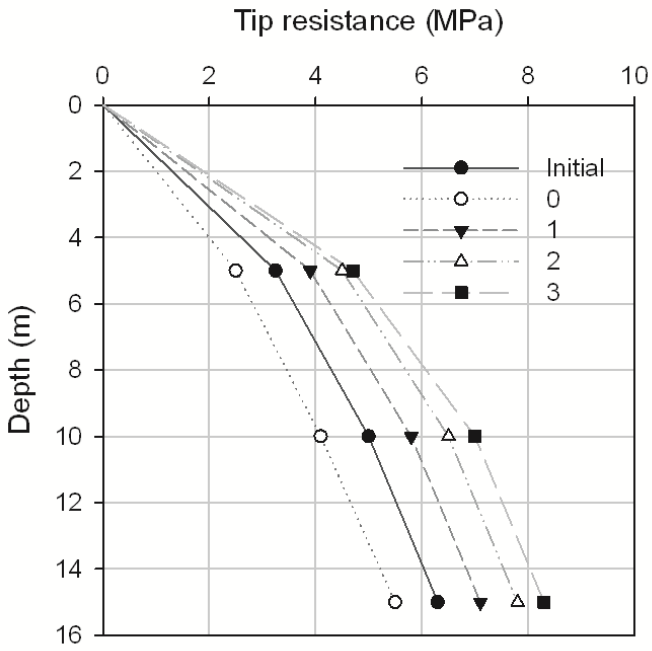

Figure 5.32. Changes in CPT resistance due to changes in stress state (FEM simulation).

The DEM and FEM simulations presented in this section are consistent with the suggested hypothesis that changes to CPT resistance occur due to a change in stress state of the sand bed. The drop in CPT resistance immediately after disturbance can occur even when the soil strength has increased.

Chapter 6

FINITE ELEMENT MODELING OF BURIED CONCRETE PIPELINES SUBJECTED TO GROUND RUPTURE

6.1 Introduction

Simulations reported in this Chapter constitute the author's contribution to a multi-investigator project on structural health monitoring and damage detection of buried concrete pipelines. The interest in the granular backfill used for pipelines was the source of inspiration for the study of time effects in sands described in the previous chapters. While the study started with the focus on pipelines, quickly, the time effects in sand took over the research directions, and the pipeline modeling effort described in this Chapter is the secondary study only loosely related to the primary topic of this thesis.

Damage assessment to lifelines after natural disasters is vital for effective emergency response and recovery efforts. Of particular interest here are water supply systems as water is an essential component for human sustenance. Even minor damages to water pipelines may result in contamination and epidemic outbreaks. Edinger (1996) points out that buried pipelines are one of the most vulnerable systems to damage from ground motions. A report issued 3 days after the 2010 Chile earthquake indicated that more than 1.5 million people were still without access to clean drinking water as a result of the earthquake (TAMC, 2010). 7 days after the 2011 Japan Earthquake and Tsunami, 190,000 households were without water (TAMC, 2011). These numbers indicate the need for rapid restoration of lifelines such as water pipelines as an absolutely essential component of successful response and recovery efforts.

A major damage to pipelines can occur during earthquakes (Wang and O'Rourke, 1978). During an earthquake, propagation of seismic waves through the earth causes ground shaking.

The seismic waves transfer the energy to substructures (buried) and superstructures (above ground). The structures are subject to vibrations that may cause damage, allowing the energy to dissipate. Buried structures, such as pipelines could experience displacements as the seismic waves propagate through the structure. Seismic wave propagation could also cause the ground to permanently displace. Eguchi (1983) classified earthquake-induced damage to pipelines as being caused by wave propagation or by permanent ground deformation. Permanent ground displacement (PGD) is a significant source of damage to water facilities (Heubach 2002, Eidinger and Davis 2012). Types of PGD include fault rupture, settlement, landslide, subsidence/uplift and liquefaction. Damage occurring to water and gas pipelines during PGD has been well documented in the literature (O'Rourke and Lane 1989, O'Rourke and Palmer 1996). Eguchi (1982) evaluated the damage to pipelines caused by the San Fernando earthquake in 1971 and concluded that almost half of the total pipeline damage occurred in specific areas where fault rupture was observed. In this thesis, the effect of a strike slip fault type displacement on buried concrete pipelines was studied.

6.2 Motivation and Research objectives

Pipelines buried in the soil are inaccessible for visual inspection, making damage detection a difficult task. The research performed in this thesis, focuses on the behavior of buried segmented pipelines subjected to a PGD (Fig. 6.1), and better understand the modes and mechanisms of failure of concrete pipes. A pipeline intersecting a fault that undergoes rupture is primarily subjected to bending and shear, but integrated normal stress may result in the overall tensile or compressive force in a given cross-section. This depends on the orientation at which the pipeline crosses a fault plane. Several simplified analytical methods have been developed by Newmark and Hall (1975), Kennedy et al. (1977), Wang and Yeh (1985), with comprehensive summaries of the state-of-the-practice given in O'Rourke and Liu (1999) and O'Rourke (2003). These models can be further categorized depending on whether they apply to continuous or segmented pipes. In addition to simplified models, detailed finite element analyses have been performed on pipelines subjected to PGD, *e.g.* Liu and O'Rourke (1997), Yoshisaki *et al.* (2001). The analytical methods presented in the literature usually work well for small deflections of pipes and cannot be used for large displacements or when material nonlinearities are present.

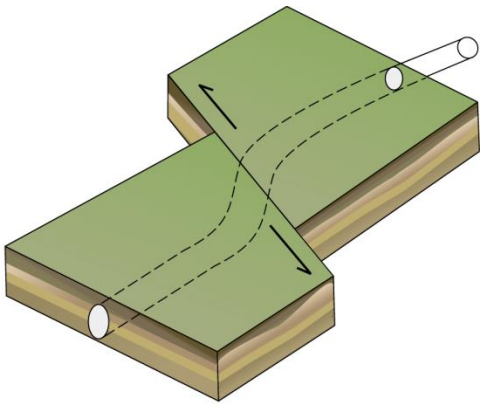

Figure 6.1. Buried pipelines subjected to PGD.

Analytical modeling and field investigation have increased the understanding of continuous and segmented pipeline behavior under PGD. However, experimental testing of buried pipelines in controlled laboratory settings could further accelerate the technological development of durable pipelines that can safely withstand PGD. Large-scale testing of pipelines has been previously conducted with the majority of tests focusing on the behavior of metallic and high density polyethylene pipelines. Less experimental work has been focused on segmented concrete pipelines. To explore the behavior of a segmented concrete pipeline during PGD, 1 scaled-down and 3 full scale tests were performed by a team of researchers from University of Michigan, Purdue University, Virginia Tech, Princeton University and Merrimack College, in the Lifeline Experimental and Testing Facility at Cornell University, Ithaca, NY. The author was a member of the group that carried out the tests from 2008 to 2011.

The tests were designed both to identify the modes of failure of buried segmental pipelines and develop a strategy for monitoring structural health and damage detection that could be used for field deployment. A wide array of sensors was used for structural health monitoring of the pipes. The sensors used for each test included several dozen of strain gages to measure longitudinal and circumferential strain, over a dozen potentiometers to measure the relative displacement and rotation of the pipes, 8 load cells to measure the axial loads at the ends of the pipe, magnetic sensors to measure the closing and opening of joints, acoustic emission sensors to detect the energy released during concrete cracking, conductive grout to measure intensity of microcracking in concrete, tape sensors to monitor surface cracks, fiber optics to measure the deformation of the pipe during the simulated PGD, and LIDAR to obtain the soil deformation after PGD. Sensor placement strategy and a discussion on the data obtained from the various

sensors were presented in Kim et al. (2009, 2010, 2011 & 2012), Pour-Ghaz et al. (2011) and Bradshaw et al. (2009), and will not be discussed here.

The large-scale tests performed at Cornell University were time consuming and involved a large amount of material and man power. Hence, testing of various fault intersections of pipelines would be prohibitively expensive. Therefore, a 3D finite element model of a buried segmented pipeline subjected to a PGD was developed using FE system ABAQUS. The simulation was compared with experimental results to understand the level of complexity required to model pipeline damage with reasonable accuracy. This work would also assist in the sensor deployment strategies by showing the particular areas where damage is concentrated (if there is concentration of damage). The specific objectives of this work were

- To develop a numerical model simulating the response of a buried concrete segmented pipeline subjected to PGD. Also, indicate the extent of the numerical model necessary to make reasonable predictions of pipeline response.
- To understand the response of a buried segmented concrete pipeline subjected to PGD, and to gain insight into damage evolution processes.
- To identify critical components in the numerical model those require major refinement.

6.3 Experimental Investigation

Key features of the large scale testing of pipelines essential for the finite element modeling are discussed in this section. A total of four tests on buried segmented pipelines were performed. The pipeline test basin is shown in Fig. 6.2. The basin was 11.7 m long in the North-South axis, 3.4 m wide and 1.9 m deep. A fault traverses the basin oriented at a fixed angle to the longitudinal axis of the basin. The basin could accommodate a pipeline that was fixed to the end walls and buried under granular back fill. Ground rupture was simulated by moving one-half of the basin (northern part) laterally, parallel to the fault line using four large hydraulic actuators, while the other half of the basin (southern part) remained stationary.

The pipes were assembled on an 0.20 m layer of medium sand, the joints were grouted, and the entire pipeline was backfilled with a 1.22 m layer of sand; more than 100 tons of poorly graded sand was used (D_{50} = 0.67 mm, uniformity coeff. C_u = 3.83, curvature coeff. C_c = 0.94, with moisture content ranging from 3.5 to 5.3%, and dry density 1,668 to 1,703 kg/m^3). The sand was placed in 6 lifts, each compacted with 4 passes of a vibratory plate compactor to reach

relative compaction of about 80% (ratio of dry density to maximum dry density). A 10 cm grid was spray-painted on the surface of the backfill for easier observation of the surface displacements.

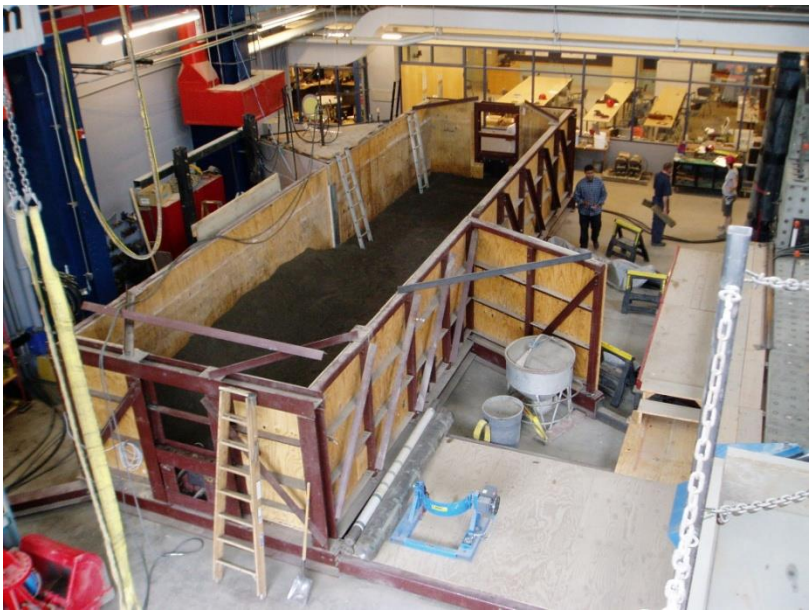

Figure 6.2. The test basin at the Cornell University testing facility.

Fault angle for the first pipe was 65° (measured from the pipe axis) and for the remaining three tests was 50°. In the first test, a scaled (1/5:1) version of a traditional commercial pipe (30 inch inner diameter) was used. For the second test, commercial (Class ¾) 12 inch diameter concrete pipes, manufactured according to ASTM C 76 and ASTM C 655, were used. The pipe segments were 2.44 m long with a wall thickness of 5.1 cm. The segments had a circumferential steel reinforcement ratio of 1.5 cm^2/linear meter length. The compressive strength of the concrete was 27.6 MPa. Each segment weighed about 900 pounds. In the third test, the segment closest to the fault was replaced with a custom-designed and manufactured steel fiber-reinforced pipe. The fourth test was performed using all custom-designed steel fiber-reinforced pipes, with embedded sensors. In all the tests, pipe segments were grouted to one another using the AWWA C300 specification. The pipes had a bell and spigot connections (Fig. 6.4(a)). Traditional pipe installation in the field involves placing a rubber gasket on the spigot portion of a pipe (Fig. 6.4(a)) and jacking it into the bell portion of the other pipe. This was not done in the full scale experiments as such an operation could damage the sensors placed on the pipe. Instead the pipes were joined to one another using grout.

At the two ends (north and south end) of the pipeline, a special steel plate was used to transfer the load to the load cells (Fig. 6.3). The load cells rest on a reaction plates on the test basin wall and were free to move in perpendicular directions to the pipe axis. The entire end assembly was enclosed in a box to prevent soil in coming contact with the load cells. To simulate ground faulting the northern part of the basin was displaced by 12 inches in this test. Figure 6.4 shows a schematic of the pipes arranged in the test basin. The North portion of the box was displaced in 12 equal increments of 2.54 cm, at a speed of 0.5 cm/sec. After every 2.54 cm displacement of the box, the test was paused and resumed after a few minutes.

(a)

(b)

Figure 6.3. End connection of the pipeline, (a) close-up view of load cells resting on the test basin frame, and (b) complete view of the end connection showing the steel plate and the box enclosure.

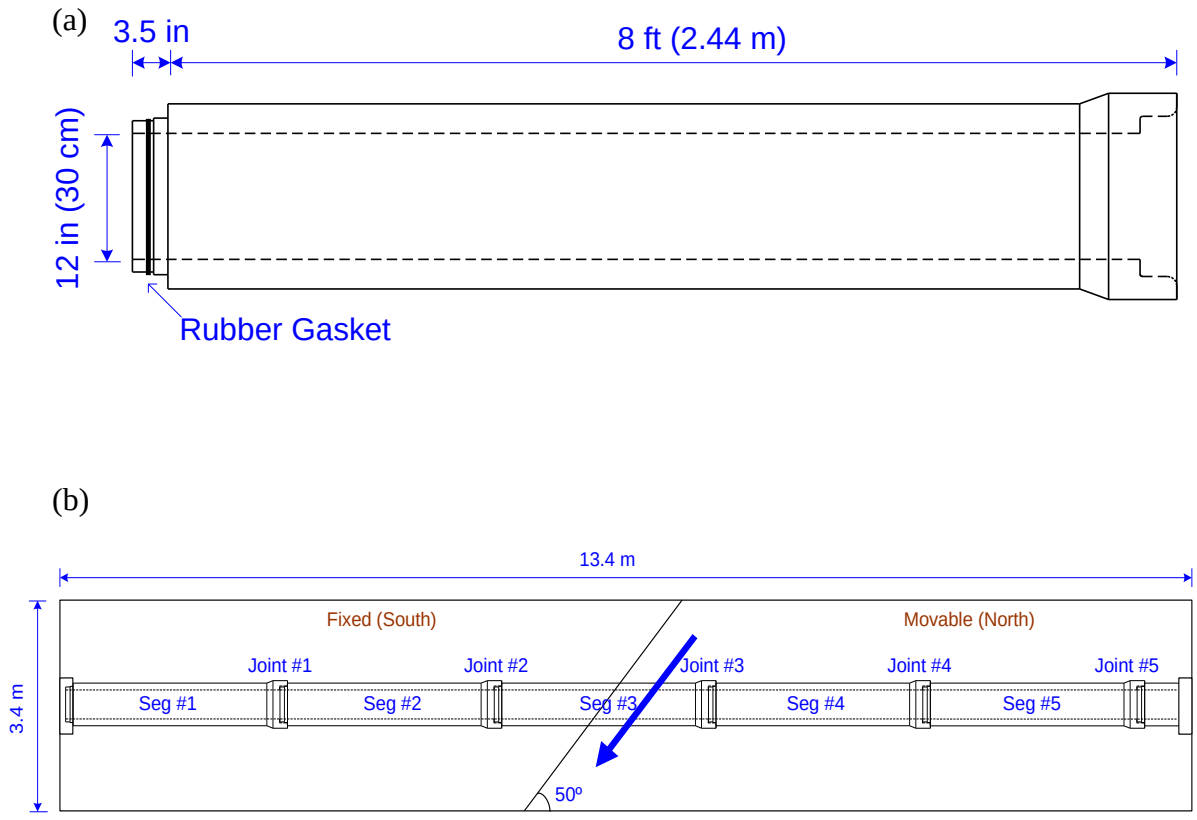

Figure 6.4. (a) Schematic of a typical commercial concrete pipe with dimensions (used in experiment #2), (b) schematic of the test basin.

During the tests, response from all sensors was monitored, and this information was used to assess the sequence of pipeline failure; the final information from the sensors was then compared with the visual inspection after excavation. Visual inspection indicated that pipeline failure was concentrated at the joints. In all four tests, two predominant modes of failures were observed, namely, compressive telescoping failure of joints and a combined failure by rotation and contraction. Fig. 6.5 shows two joints from the second test where these failures were detected. Compressive telescoping failure was observed at joint 1 and 4; combined rotation and contraction failure was observed at joints 2 and 3 (see Fig. 6.4 for joint numbering).

(a) (b)

Figure 6.5. Joint damage observed in pipeline test #2, (a) joint failure by combined rotation and contraction, and (b) compressive telescoping failure.

6.4 Finite Element Model of Buried Concrete Pipeline subjected to PGD

The FEM software ABAQUS ver. 6.10 was used to model the large scale test. The explicit solution scheme was chosen as it is highly efficient for solving three-dimensional contact problems with large deformations. The explicit procedure was originally developed to model high-speed impact events and hence the use of an explicit scheme to solve a quasi-static problem such as ground rupture requires special considerations. The minimum time increment in explicit solutions is usually quite small and hence most problems require a large number of increments increasing the computation time. To decrease the computation time, the simulations were run on parallel 2.4 GHz processors.. Different FEM models used for modeling the large scale tests had different demands on the processor RAM, and generally varied from 4 GB to 26 GB. The number of elements was the essential parameter that dictated the required RAM.

The soil was modeled as elastic-perfectly plastic. Isotropic elasticity was assumed with the Young's modulus E = 30 MPa and Poisson's ratio ν = 0.25. The Drucker-Prager (1952) function with no cohesive component was used to model soil yielding. The specifics of this yield criterion were discussed in Chapter 5. For the sand used in the experiment, the internal friction and dilatancy angles were taken equal to 40° and 5°, respectively. This translates in the following Drucker-Prager parameters: β = 58.6°, ψ^* = 10.2°, and K = 0.778. The value of 5° for the

dilatancy angle was selected, based on Bolton (1986), and it is likely to be a low estimate when related to the relative compaction of 80%.

Concrete in ABAQUS can be modeled using three different constitutive models -

1. Smeared crack concrete model in ABAQUS/Standard.
2. Brittle cracking model in ABAQUS/Explicit
3. Concrete damaged plasticity (CDP) model in both ABAQUS/Standard and ABAQUS/Explicit.

Since the explicit solution scheme was chosen, the smeared concrete model could not be used. The brittle cracking model assumes that concrete behavior is controlled by tensile cracking and compressive failure is not important. Visual inspection of the damaged pipes in the large scale tests showed both compressive and tensile failure of concrete. Hence this model was not used. The CDP model on the other hand assumes that compressive crushing and tensile cracking are the two main failure mechanisms of concrete. In the present analysis, CDP model is used.

6.4.1 Concrete Damage Plasticity (CDP) model

The CDP model is based on the model proposed by Lubliner et al. (1989) and incorporates the modifications proposed by Lee and Fenves (1998). A brief description of the model is provided in this section. The constitutive equations used in the CDP model aim to capture the irreversible damage occurring during the failure of concrete. An overview of the main components in the model is described here. For a more detailed discussion of the different aspects of this constitutive model the reader is referred to Lubliner et al. (1989) and Lee and Fenves (1998).

The constitutive equation of a material with scalar damaged elasticity takes the form (Lee and Fenves, 1998; ABAQUS Theory Manual, 2008)

$$\sigma_{ij} = (1-d)(D_o^{el})_{ijkl}(\varepsilon_{kl} - \varepsilon_{kl}^{pl}) = D_{ijkl}^{el}(\varepsilon_{kl} - \varepsilon_{kl}^{pl}) \tag{6.1}$$

where σ_{ij} is the Cauchy stress tensor, d is the scale stiffness degradation variable ($d = d_t$ in tension and $d = d_c$ in compression), ε_{kl} is the total strain tensor, ε_{kl}^{pl} is the plastic strain tensor, $\left(D_0^{el}\right)_{ijkl}$ is the initial undamaged elastic stiffness tensor of the material, while $D_{ijkl}^{el} = (1-d)\left(D_0^{el}\right)_{ijkl}$ is degraded elastic stiffness tensor.

The effective stress tensor $\bar{\sigma}_{ij}$ is defined from Equation (6.1) as

$$\bar{\sigma}_{ij} = (D_o^{el})_{ijkl}(\varepsilon_{kl} - \varepsilon_{kl}^{pl}) \tag{6.2}$$

Thus the Cauchy stress tensor is related to the effective stress tensor through the relation

$$\sigma_{ij} = (1-d)\bar{\sigma}_{ij} \tag{6.3}$$

The factor (1-*d*) represents the ratio of the effective load-carrying area (overall area minus the damaged area) to the overall section area. In the absence of any damage (*d* = 0), the effective stress ($\bar{\sigma}_{ij}$) is equal to the Cauchy stress (σ_{ij}). However when damage occurs, the effective stress is more representative of the Cauchy stress as the effective area carrying load is reduced due to damage of the material. Hence, the plasticity parameters in the CDP model are formulated in terms of the effective stress. In the formulation, the degradation variable (*d*) is governed by a set of hardening variables and the effective stress

$$d = d(\bar{\sigma}, \tilde{\varepsilon}^{pl}) \tag{6.4}$$

Damage states in tension and compression are characterized independently by two hardening variables, $\tilde{\boldsymbol{\varepsilon}}_{\boldsymbol{t}}^{\boldsymbol{pl}}$ (equivalent plastic strain in tension) and $\tilde{\boldsymbol{\varepsilon}}_{\boldsymbol{c}}^{\boldsymbol{pl}}$(equivalent plastic strain in compression). Micro-cracking and crushing in concrete can be represented by increasing the values of the hardening variables. These two variables control the evolution of the yield surface and the degradation of the elastic stiffness.

The yield function (*F*) and flow rule in the CDP model are also defined in the effective stress space

$$F(\bar{\sigma}, \tilde{\varepsilon}^{pl}) \leq 0 \tag{6.5}$$

Both hardening (in compression) and softening behavior is governed by a non-associative flow rule

$$\dot{\varepsilon}^{pl} = \dot{\lambda}\frac{\partial G(\bar{\sigma})}{\partial \bar{\sigma}} \tag{6.6}$$

where $\dot{\lambda}$ is a non-negative plastic multiplier. The flow potential *G* in the CDP model is the Drucker-Prager function

$$G = \sqrt{(\varepsilon \sigma_{to} \tan\psi)^2 + \bar{q}^2} - \bar{p}\tan\psi \tag{6.7}$$

where σ_{to} is the uniaxial tensile stress at failure, ε is eccentricity and it defines the rate at which the function reaches the asymptote, ψ is the dilation angle measured in the *p*-*q* plane. $\bar{p} = -\frac{1}{3}\bar{I}$ is the effective hydrostatic stress and $\bar{q} = \sqrt{\frac{3}{2}\bar{S}\cdot\bar{S}}$ is the Mises equivalent effective stress. $\bar{S}$ is the deviatoric part of the effective stress tensor $\bar{\sigma}$, and $\bar{I}$ is the first invariant of the effective stress tensor.

The uniaxial tensile and compressive behavior of concrete in the CDP model is characterized by plastic damage. In uniaxial tension (Fig. 6.6(a)), stress-strain response follows a linear elastic relationship until failure stress σ_{to} is reached, after which there is an onset of micro-cracks. The formation of micro-cracks is represented by a strain softening response. Under uniaxial compression (Fig. 6.6(b)), the response is linear until it reaches initial yield σ_{co}, after which stress hardening takes place till it reaches the ultimate stress, σ_{cu} after which strain softening takes place. Upon unloading the specimen from any point on the strain softening branch (in either uniaxial tension or compression), the response is weakened and the elastic stiffness of the material is degraded. This degradation in elastic stiffness is characterized by two independent damage variables, d_t and d_c ($0 \leq d_t, d_c \leq 1$). The damage variables take a value of 1 when the material is fully damaged and they are 0 for an undamaged material. Instead of modeling the steel reinforcement in the pipeline, a composite action of the pipe and steel was assumed. Figure 6.6 shows the stress strain curve of the concrete-steel composite assumed in the FEM models presented in this thesis.

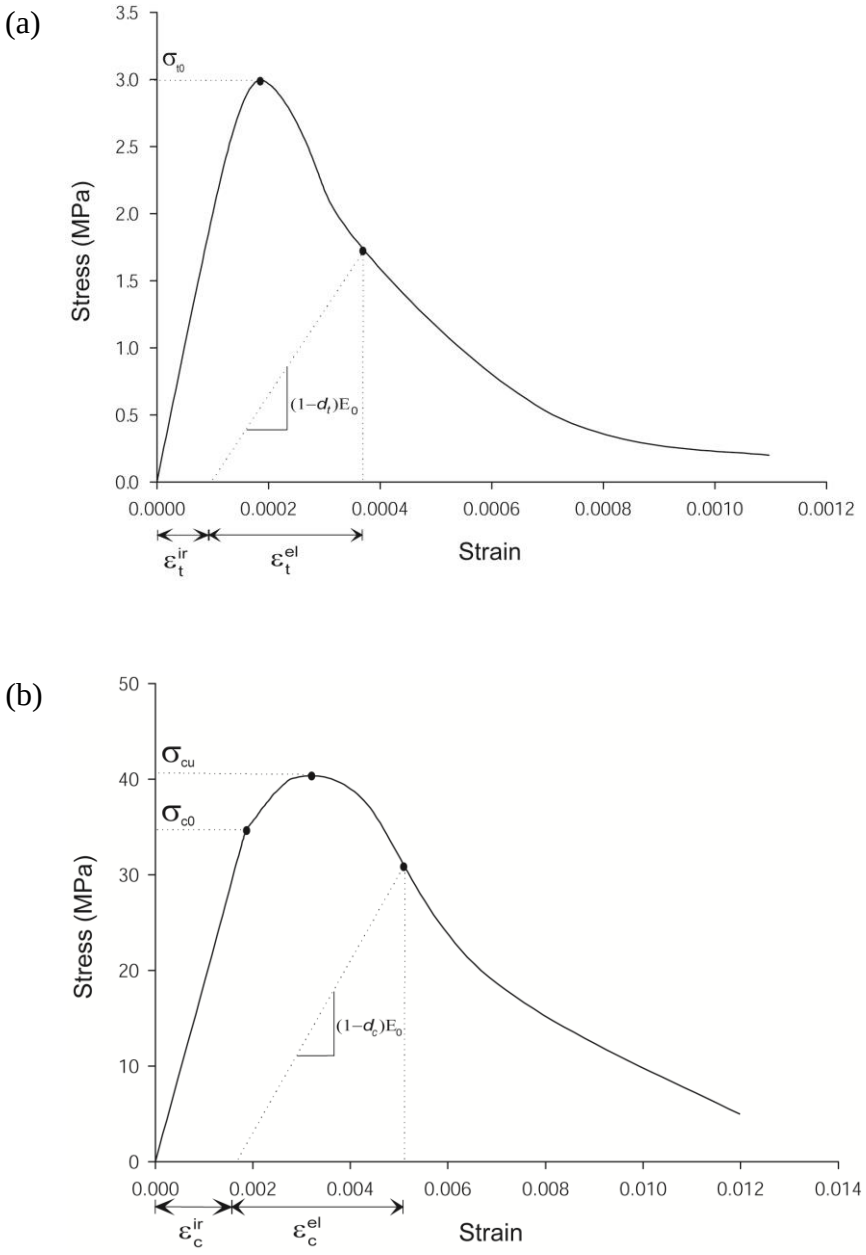

Figure 6.6. Stress-strain response of concrete under uniaxial stress in concrete damage plasticity model, (a) in uniaxial tension, and (b) uniaxial compression.

6.4.2 Modeling aspects in ABAQUS system

The soil-pipe contact was modeled as a master-slave contact (the pipe being the master; the nodes of the master surface can penetrate the slave surface but not vice versa). A refined mesh was used on the slave surface to minimize excessive penetration. The contact was unilateral, and no tensile stresses across the boundary were permitted. Isotropic surface friction was assumed, with coefficient of friction μ = 0.3, typical of clean sand–formed concrete interface (NAVFAC, 1986). The bell-spigot contact between two pipes was modeled in a similar manner (the spigot being the master surface).

Both the soil and pipe were modeled using 8 node brick elements with reduced integration and hour-glass control (C3D8R ABAQUS element). Significant mesh distortion problems were encountered near the fault during the simulations. To allow for large displacements in the mesh near the fault, Arbitrary Lagrangian-Eulerian (ALE) adaptive meshing scheme was used for the entire soil. In a purely Lagrangian analysis, the nodes are fixed with the material, and as the material is deformed, elements are also deformed. The material boundary coincides with the element boundary. By contrast, in an Eulerian analysis nodes are fixed in space and the material flows through the elements. The elements do not deform and so can be partially or completely void. The Eulerian mesh is typically a grid of elements that extend well beyond the material. The Eulerian material boundary must be computed during each time increment. The ALE meshing scheme uses an approach in between the pure Eulerian and pure Lagrangian analysis. The ALE technique uses a single mesh definition that is smoothed gradually within analysis steps. By doing this, a high quality mesh can be maintained throughout the analysis. By using the ALE technique excessive mesh distortions were prevented during the simulation.

Figure 6.7 shows a schematic of an isometric view of the test basin and pipeline with different boundaries. The gravity load was applied to the entire assembly in the negative Z direction. Displacement boundary conditions were prescribed on all faces of the boundary. Table 6.1 summarizes the boundary conditions used in the model. In Table 6.1, U_x, U_y, and U_z correspond to the displacements along X, Y and Z directions respectively. The gravity load was applied first and it determines the initial stresses in the soil. The displacement boundary conditions were applied subsequently. Due to dilation in the soil during PGD, it was assumed that the movable half of the box was displaced at an angle of 10° with respect the fault. Both the

gravity load and prescribed displacements were applied to the model using a "smooth-step" criterion to avoid exciting the model. In this criterion, the prescribed loads or displacements were applied using a ramp function starting from the value of zero.

Application of ABAQUS/Explicit to a quasi-static event like ground rupture (PGD) required special considerations. The time step in an explicit procedure is very small. It was computationally impractical to model the PGD in its natural time period (1 feet displacement in about 60 seconds). Literally millions, if not billions of time steps would be required to finish the simulation. Hence in the simulation, the PGD was attained in a much shorter time of 3 seconds.

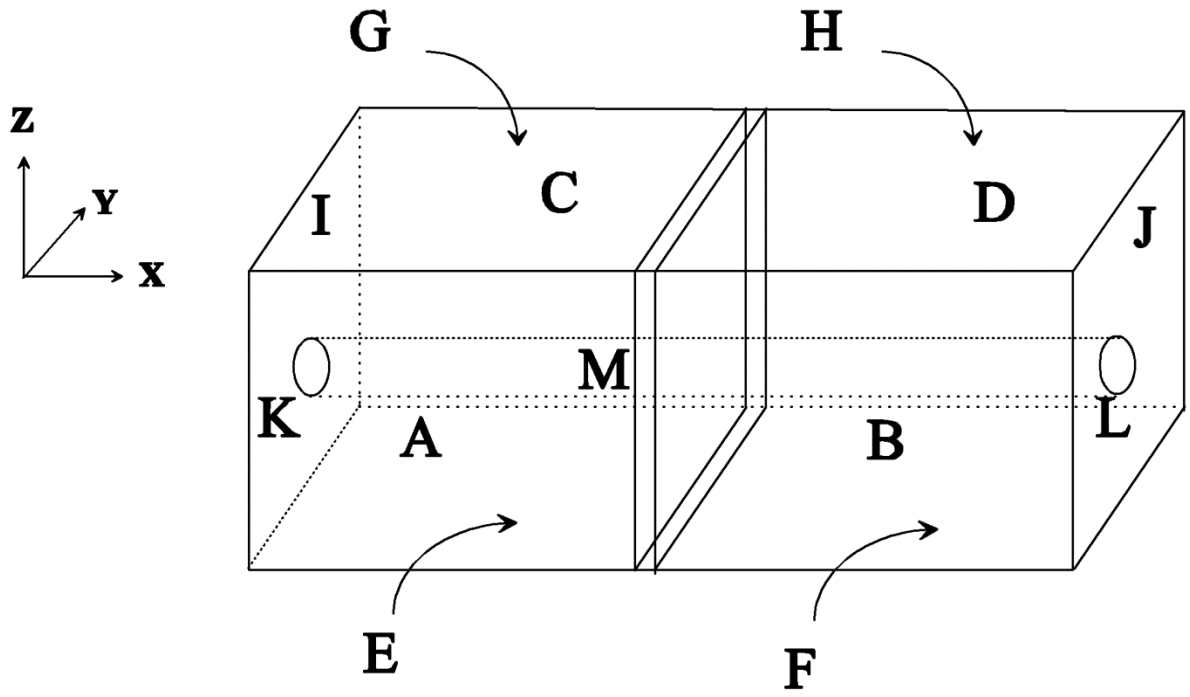

Figure 6.7. Schematic of soil bed with pipe showing the different boundary surfaces.

A total of five pipes and a 3-foot cut section of a pipe were used in the FEM simulations to model experiment No. 2 (see Fig. 6.4(b) for a schematic). Three discretization models with varying mesh sizes and geometrical features were developed in ABAQUS to understand the modeling complexity required to effectively capture the damage observed in large scale tests. A summary of the three discretization models is provided in Table 6.2.

Table 6.1. Prescribed boundary conditions in the finite element model.

Face	U_x (m)	U_y (m)	U_z (m)
A	Free	0	Free
B	Free	-0.2643	Free
C	Free	0	Free
D	Free	-0.2643	Free
E	Free	Free	0
F	Free	Free	0
G	Free	Free	Free
H	Free	Free	Free
I	0	Free	Free
J	-0.1524	Free	Free
K	0	Free	Free
L	-0.1524	Free	Free

Table 6.2. Summary of the three discretization models.

Model No.	No. of elements	No. of processors	Simulation time	Comments
1	20,000	3	1 day	Bell of pipe not modeled; Grout not modeled
2	700,000	3	10 days	Bell of pipe modeled; Grout modeled
3	3 million	5	24 days	Bell of pipe modeled; Grout modeled

In the first discretization model, the entire test assembly was made with about 20,000 elements. This was an extremely coarse mesh with the largest element dimension of about 0.5 m. Figure 6.8 shows the test basin. A finer mesh gradation (element size ~ 0.1 m) was used closer to the fault location. Instead of modeling the bell and spigots connection, a simpler slide-in connection was used (Fig. 6.9). The grout in between the pipes was also not modeled. The joints between the pipes were modeled to have a snug fit (no gap). Since the fault crosses the pipeline in between joints 2 & 3 (Fig. 6.8(b)), a finer mesh was used on pipe #3.

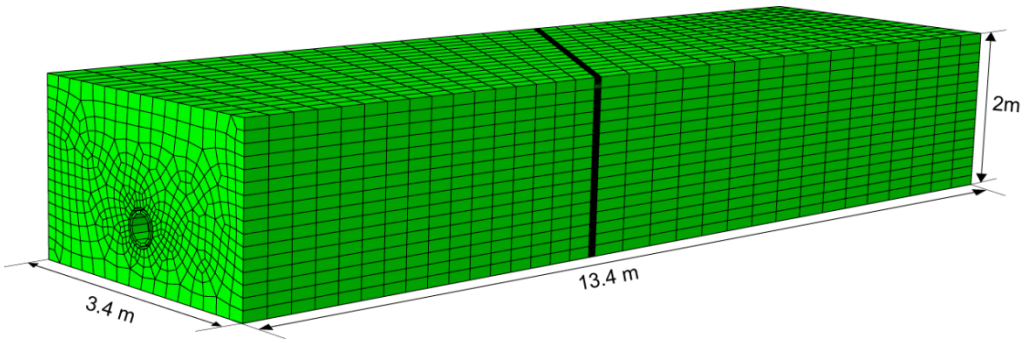

Figure 6.8. Simulated test basin with a coarse mesh.

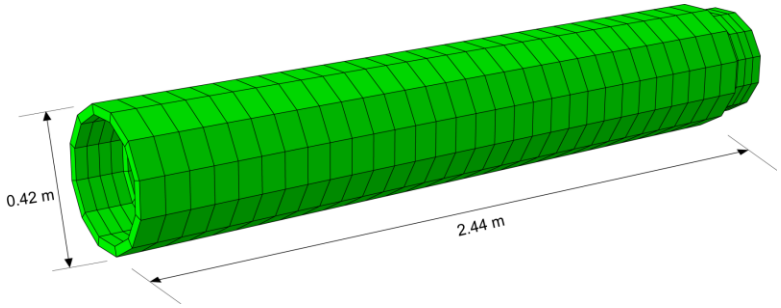

Figure 6.9. Simplified pipe model adapted in the first discretization model; the bell portion of the pipe was replaced by a flat slide-in connector.

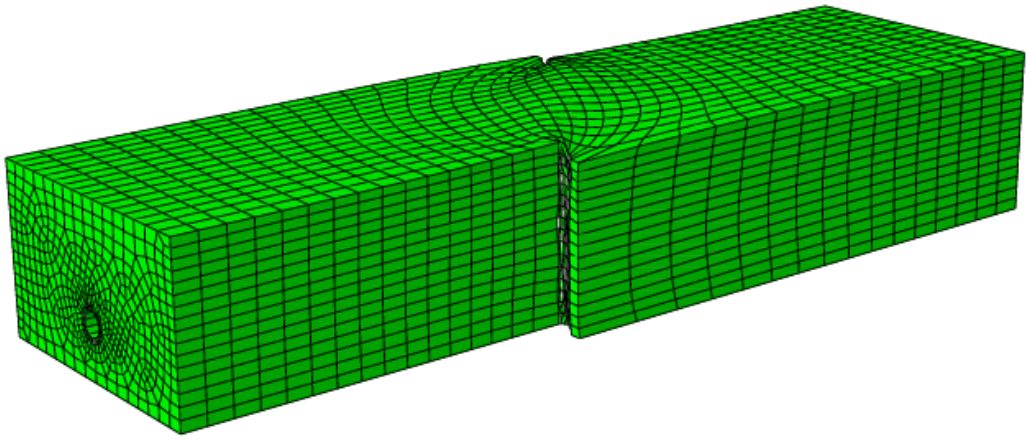

Figure 6.10. Deformed soil mesh after ground rupture.

The ALE technique helped in preventing excessive mesh distortions near the fault. Fig. 6.10 shows the deformed soil mesh after subjecting the simulated test basin to ground rupture. In the full scale test, the load from the pipelines was transferred through the reaction plates (Fig. 6.3) to the test basin frame and the force was monitored with four load cells at each end of the pipeline. Figure 6.11 compares the end reaction forces from the simulation and experiment on the North and South ends of the test basin.

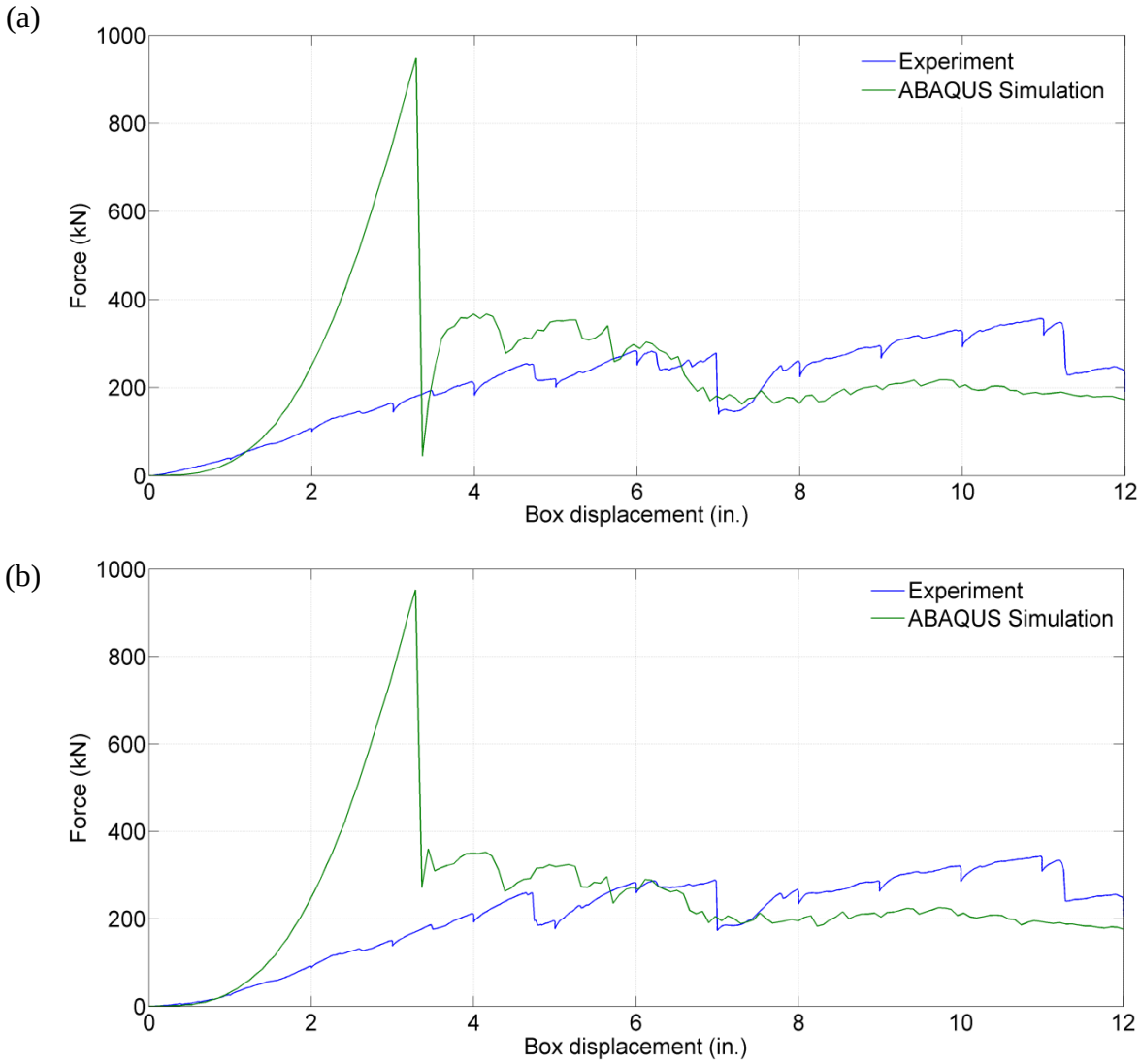

Figure 6.11. Comparison of pipeline end reaction forces from experiment and pipe simulation model #1, (a) north end reaction, and (b) south end reaction.

Since in the first simulation the joints were modeled without grout and as having a snug fit, the initial stiffness of the model pipeline exceeded the stiffness of the physical pipe assembly. Consequently, the calculated axial forces in the first 3 inches of PGD significantly exceeded the measured magnitudes. However, after some damage at the joints has occurred, the calculated forces dropped down to a level measured in the experiment.

Concrete strains were monitored on pipes #2, 3, and 4, with strain gages installed at three locations along each pipe on two opposite sides, as illustrated in Fig. 6.12(a). The average strain measured on pipe #2 at location SG1 and SG1' is illustrated in Fig. 6.12(b) as a function of the actuation step in the process of test tank displacement. The strain difference, indicative of curvature of the pipe, is given in Fig. 6.12(c). The respective values calculated from the finite element model are presented in Fig. 6.12(d) and (e). The discrepancy in the strain measured and calculated is more than threefold in the early stages of the test. The reason in this discrepancy was identified in the crude model of the joints that renders the system stiffer than the physical pipeline, resulting in axial forces exceeding significantly the true values.

Figure 6.13 shows a comparison of the deformed pipeline in the experiment and simulation. In the experiment (Fig. 6.13(a)), severe damage was observed in joints #2 and #3; joints #4 and 5 experienced moderate damage; no damage was observed in joints #1 and #6. The damage was also indicated in numerical calculations, with the tensile damage variable d_t illustrated in Fig. 6.13(b); the compressive damage was identical to the tensile damage. The damage observed in simulations extended from the joints to the body of the pipe. This, however, was not the case in the experiment. Further, the simulation showed damage at pipeline ends. This also was not seen in the experiment.

Based on these observations a second FEM model was developed with a bell on the pipe segments. The grout was also modeled. The strength of the grout in compression and tension was assumed to be 10 times lower than the strength of concrete. In the large scale experimental tests, when grouting the bell and spigot joints together, a foam (0.8 inch thick) was placed in the bell segment to prevent the grout from leaking into the pipe. This foam was modeled in FEM simulation as a linear elastic element with a very low stiffness. The second FEA model had 700,000 elements and took 10 days to run on three processors. Figure 6.14 shows the simulated test basin with the buried pipeline. The finite element discretization of the pipe is shown in

Fig. 6.15. Figure 6.16 shows a comparison of the deformed pipeline in the experiment and in the simulation.

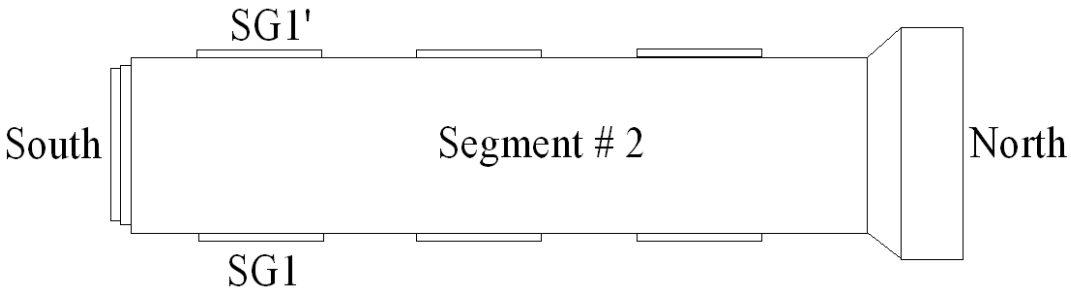

(a)

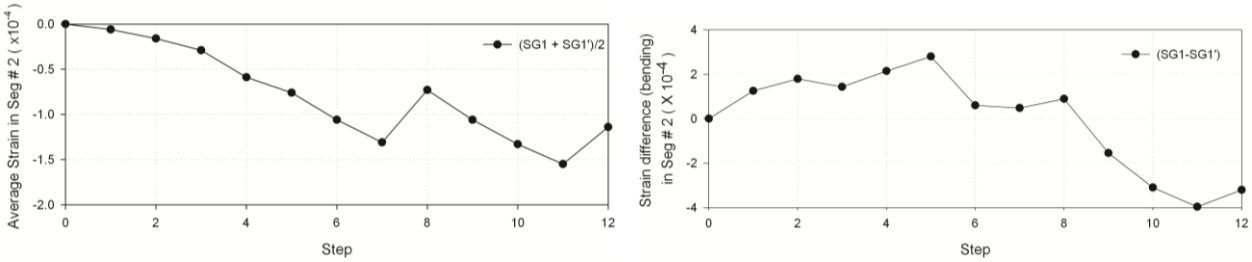

(b)

(c)

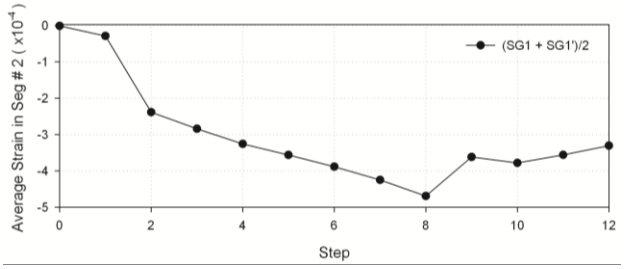

(d)

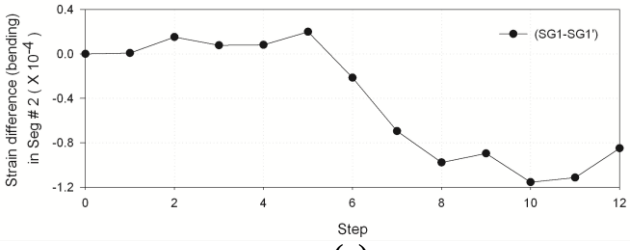

(e)

Figure 6.12. (a) Location of strain gages on segment #2, (b) measured average strain (compression negative), (c) measured strain difference, (d) calculated average strain, (e) calculated strain difference.

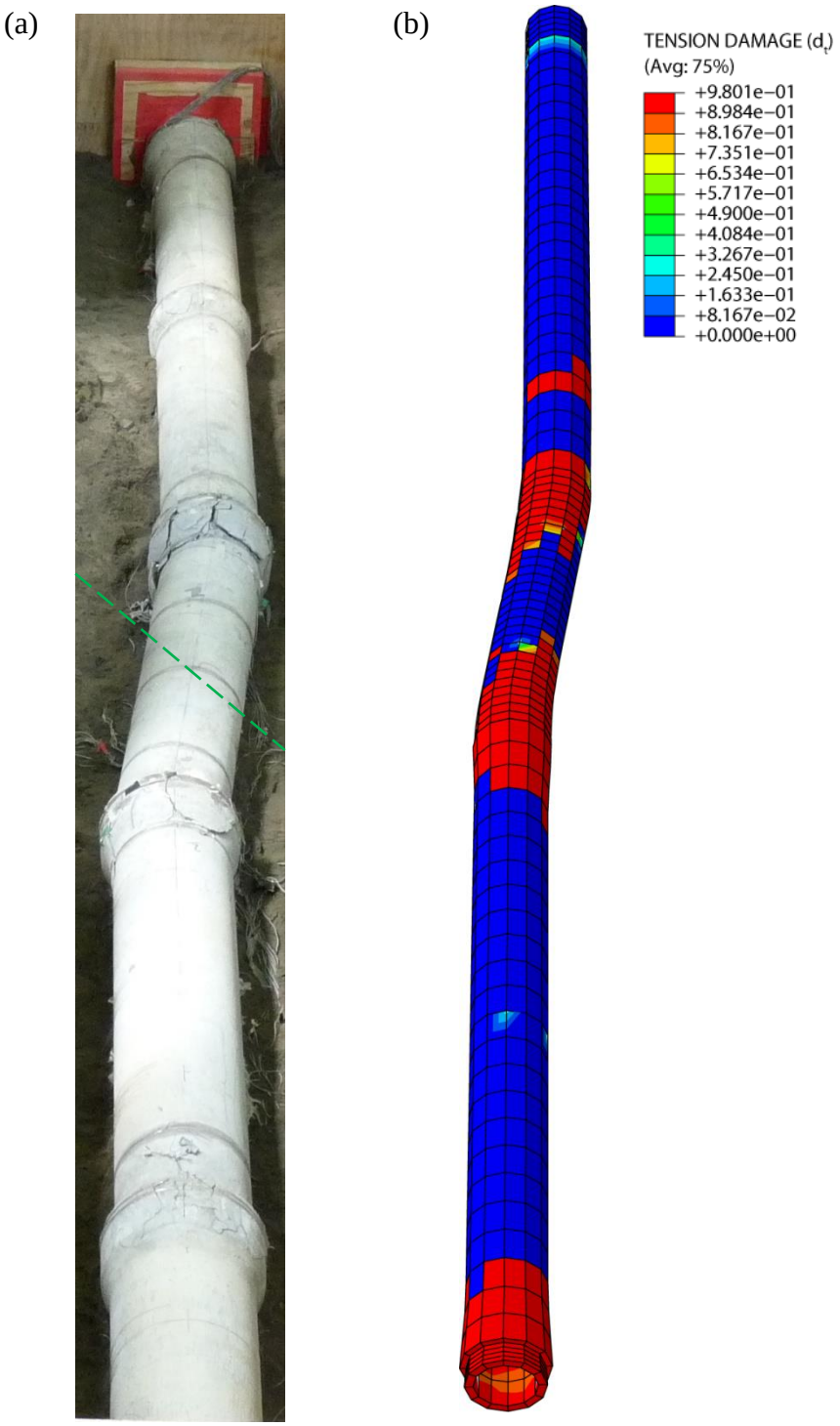

Figure 6.13. Comparsion of pipeline damage in experiment #2 and FEA simulation #1, (a) excavated pipeline after the test, and (b) numerically simulated damage showing the tensile damage parameter dt; dt = 0 means no damage and dt = 1 means complete damage.

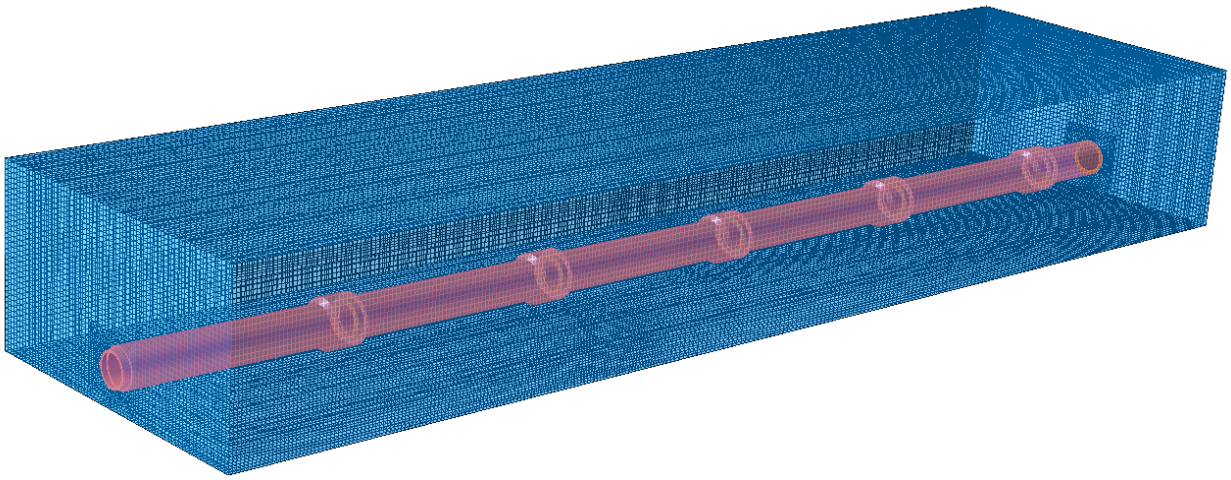

Figure 6.14. Simulated test bed with buried pipeline in the second FEM model.

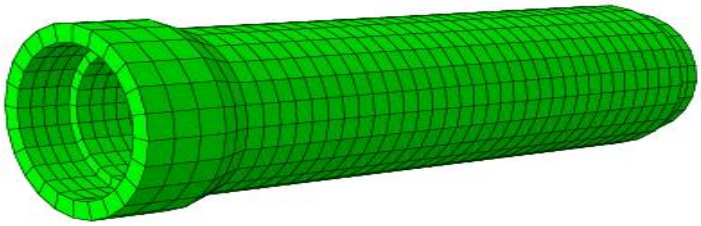

Figure 6.15. Pipe model with FEM mesh discretization used in the second FEM model.

The damage to concrete pipeline in simulation #2 (Fig. 6.16(b)) and #1 (Fig. 6.13(b)) was similar for most part. However in simulation #2 (Fig. 6.16(b)), no damage was observed at the ends of the pipeline. This was not the case in simulation #1(Fig. 6.13(b)). Figure 6.16 compares the damage observed in the full scale experiment #2 and simulation #2. The simulation #2 estimates the joint damaged areas much better than simulation #1. However, even in this simulation, the damage in the middle pipe (pipe crossing the fault in Fig. 6.16(b)) propagated from pipe joints far into the pipe body, and this was not seen in the experiment.

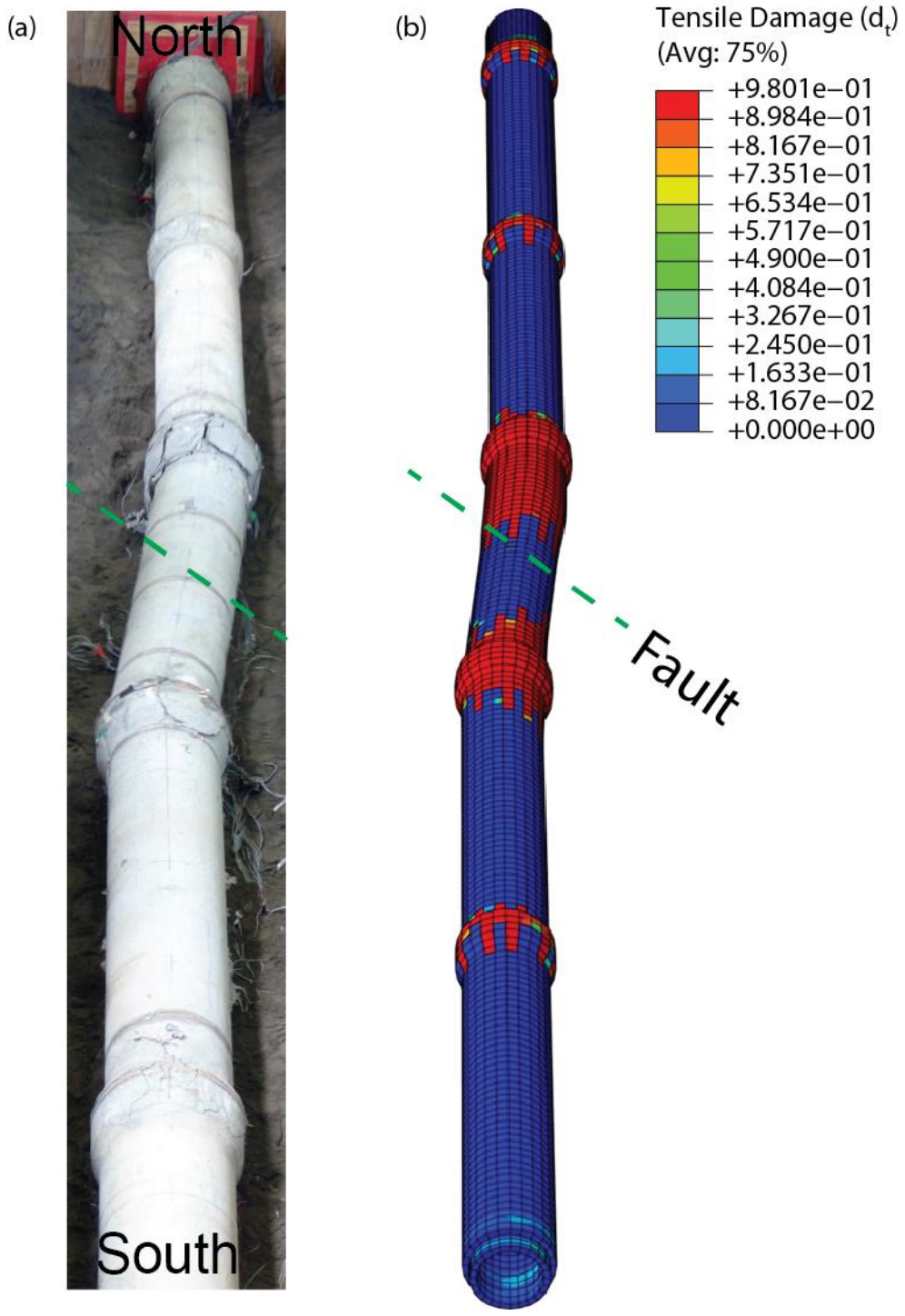

Figure 6.16. Comparison of pipeline damage in experiment #2 and FEA simulation #2, (a) excavated pipeline after the test, and (b) numerically simulated damage showing the tensile damage parameter d_t; $d_t = 0$ means no damage and $d_t = 1$ means complete damage.

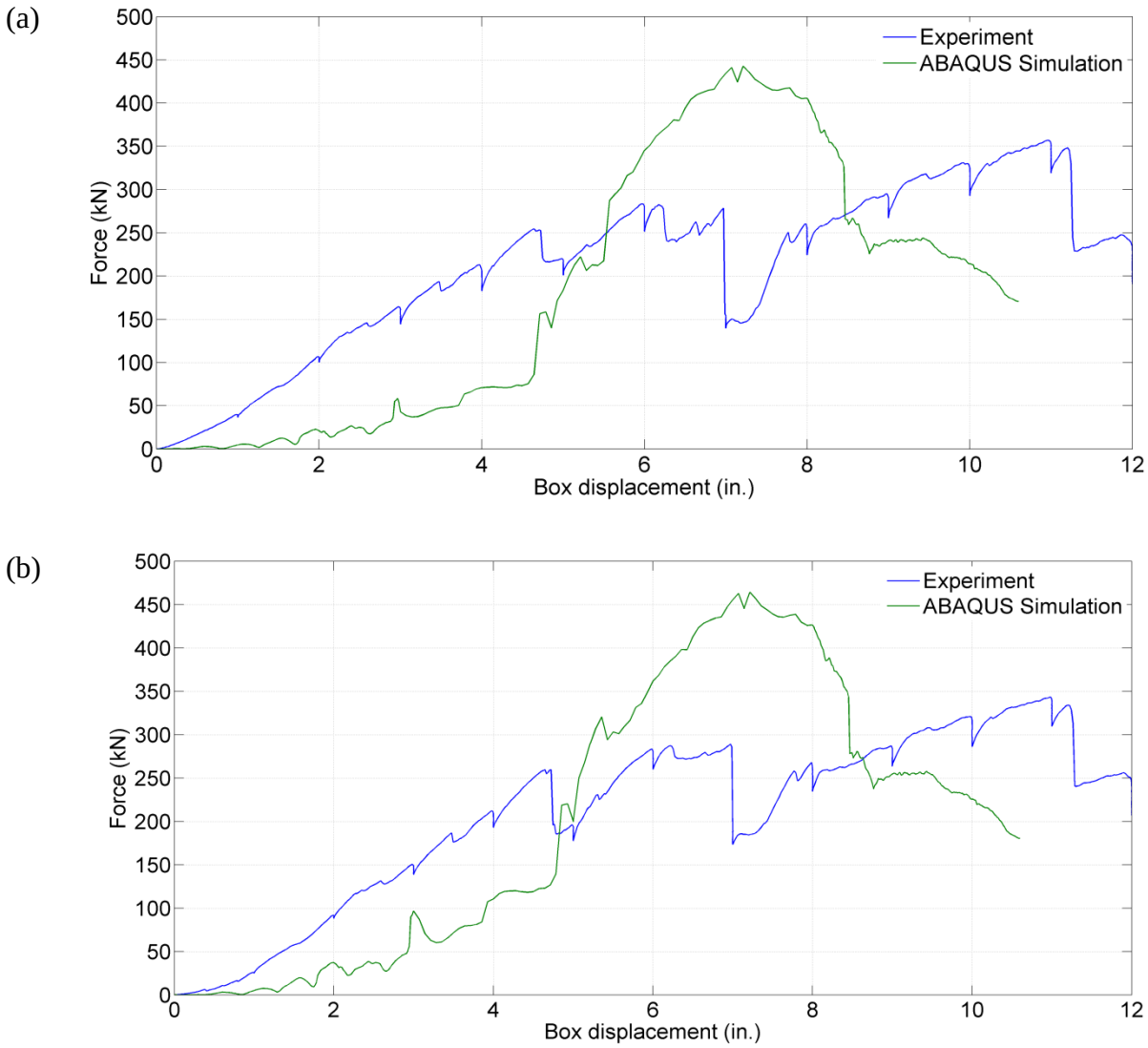

Figure 6.17. Comparison of pipeline end reaction forces from experiment #2 and FEA model #2, (a) north end reaction, and (b) south end reaction.

Figure 6.17 shows a comparison of the pipeline end reaction forces measured in the experiment and corresponding values from simulation #2. It was observed that in the first 4.5 inches of fault displacement the pipeline end reaction forces from simulation underestimated the experimental results. This is probably due to the foam in the simulation between the bell and spigot getting crushed. The foam 0.8 inch thick was placed at all the 5 pipe joints in simulation model #2 and hence had a combined thickness of about 4 inches. The foam acted as a compliant system in the pipeline assembly decreasing the stiffness of the pipe in the initial few inches of box movement. After the soft interface between the pipes was completely squeezed, the end

reaction forces increased quite rapidly in the simulation, but and after about 7 inches of displacement, a drop in the end reaction forces was observed. This drop occurred also in the experiment at about the same displacement.

While the second simulation model performed much better than the first model, it still overestimated the pipe damage and the end reaction forces. The overestimation of pipe damage could be due to the use of only one element across the pipe bell thickness (Fig. 6.15) during the finite element discretization process. Till now, the results from the two finite element concrete models were compared with the experimental test #2, while steel-reinforced concrete pipes were used. Since the steel reinforcement was not modeled, a composite action of steel and concrete was assumed. This assumption of a composite action of the steel and concrete might not have been reasonable and this could be one reason behind the discrepancy of test results from simulation and experiment. In the full scale experiment #4, the concrete pipes had steel fibers reinforcement, and an assumption of composite action for that experiment would be much more reasonable. Based on all these observations, a third FEM model was developed and results were compared with experiment #4.

The third FEM model had about 3 million elements and took about 24 days to run on 5 processors. Figure 6.18 shows mesh discretization used on the pipe. It can be seen that the bell of the pipe had three elements across its thickness instead of just one as in the simulation #1 & 2. Hence it was expected that this model should give a better estimate of pipe damage than the two previous FEM models. Since, it was decided to compare this simulation model (FEA model #3) with experiment #4 where steel fibers were used, the compressive and tensile strengths of concrete shown in Fig. 6.6 were increased by 20%.

Figure 6.19 shows a cross section of a bell and spigot joint in the FEM simulation. Four elements across the pipe wall thickness were used in the simulation model #3, as opposed to two in the previous simulation models.

Figure 6.20 shows the deformed soil mesh at the end of simulation. Figure 6.21(a) shows the deformed pipeline from experiment #4 after excavation. In the experiment, the damage to the pipeline in the experimental test was concentrated at the two joints closest to the fault (joint #2 & 3). Joints 1 and 4 experienced moderate damage in the bell sections in the form of longitudinal cracks. No damage however was observed at joint #5. Figure 6.21(b) shows the result from the FEM model #3. The simulation showed a little damage at joint #1 and 4. However this damage

did not propagate through the entire thickness of the bells and so was not visible in Fig. 6.21(b). Joint #5 was not damaged in the simulation as well.

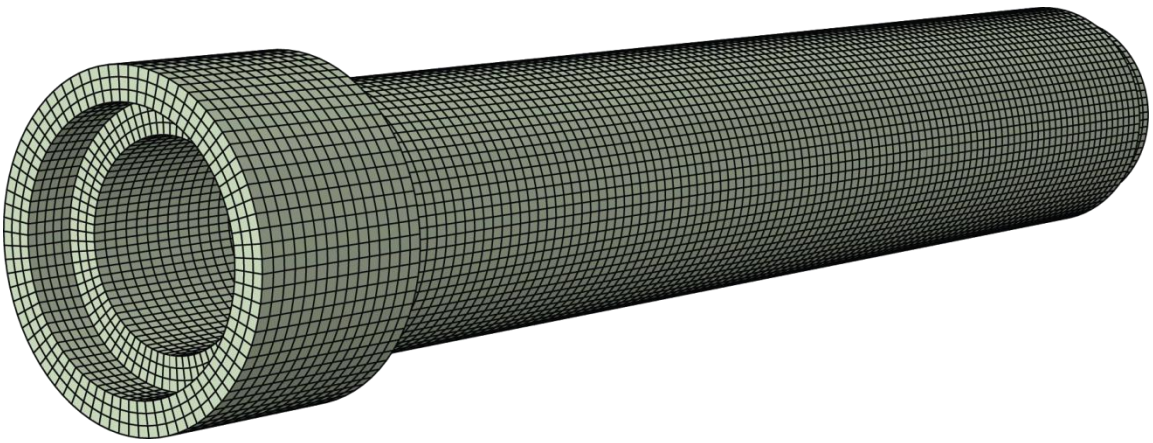

Figure 6.18. Finite element mesh discretization of concrete pipe used in simulation model #3 (pipe was 2.44 m long and inner diameter of 31 cm and outer diameter of 42 cm).

The damage to the joints 2 and 3 in the experiment was essentially due to longitudinal cracks propagating throughout the thickness of the pipe bell. This kind of damage was also observed in the simulation, Fig. 6.22. Figure 6.23 compares the end reaction forces obtained from experiment #4 and simulation #3.

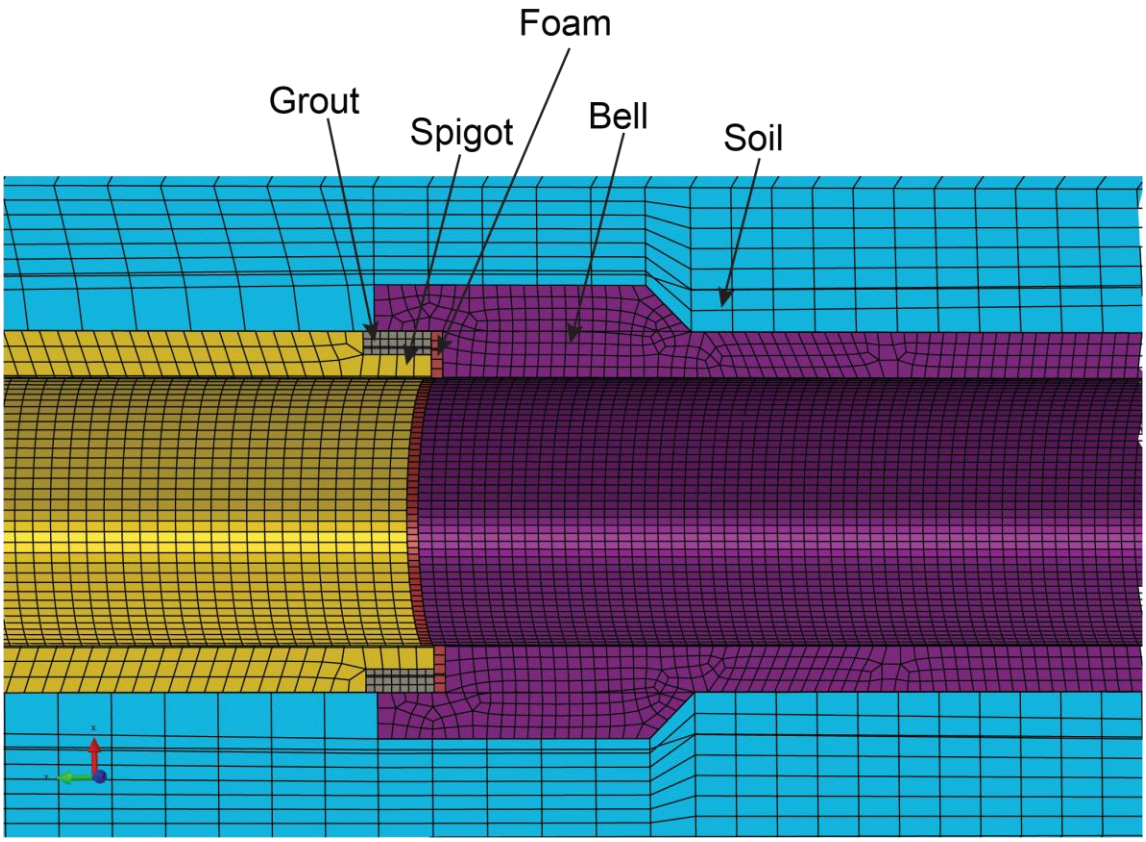

Figure 6.19. Cross-section of the bell and spigot joint showing different components in the simulation model #3.

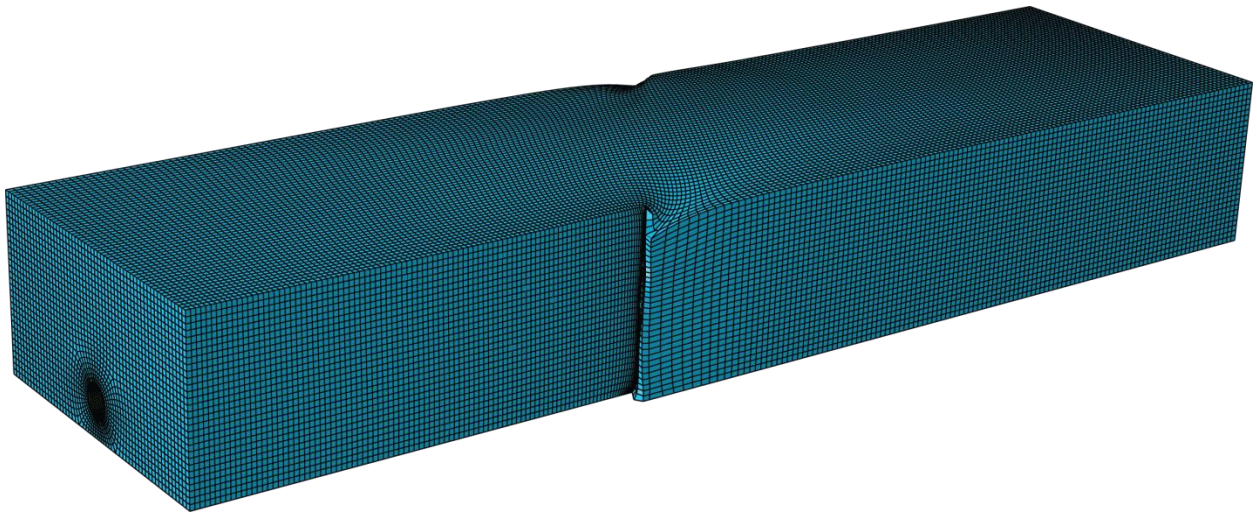

Figure 6.20. Deformed soil bed in the third simulation model; 3 million elements.

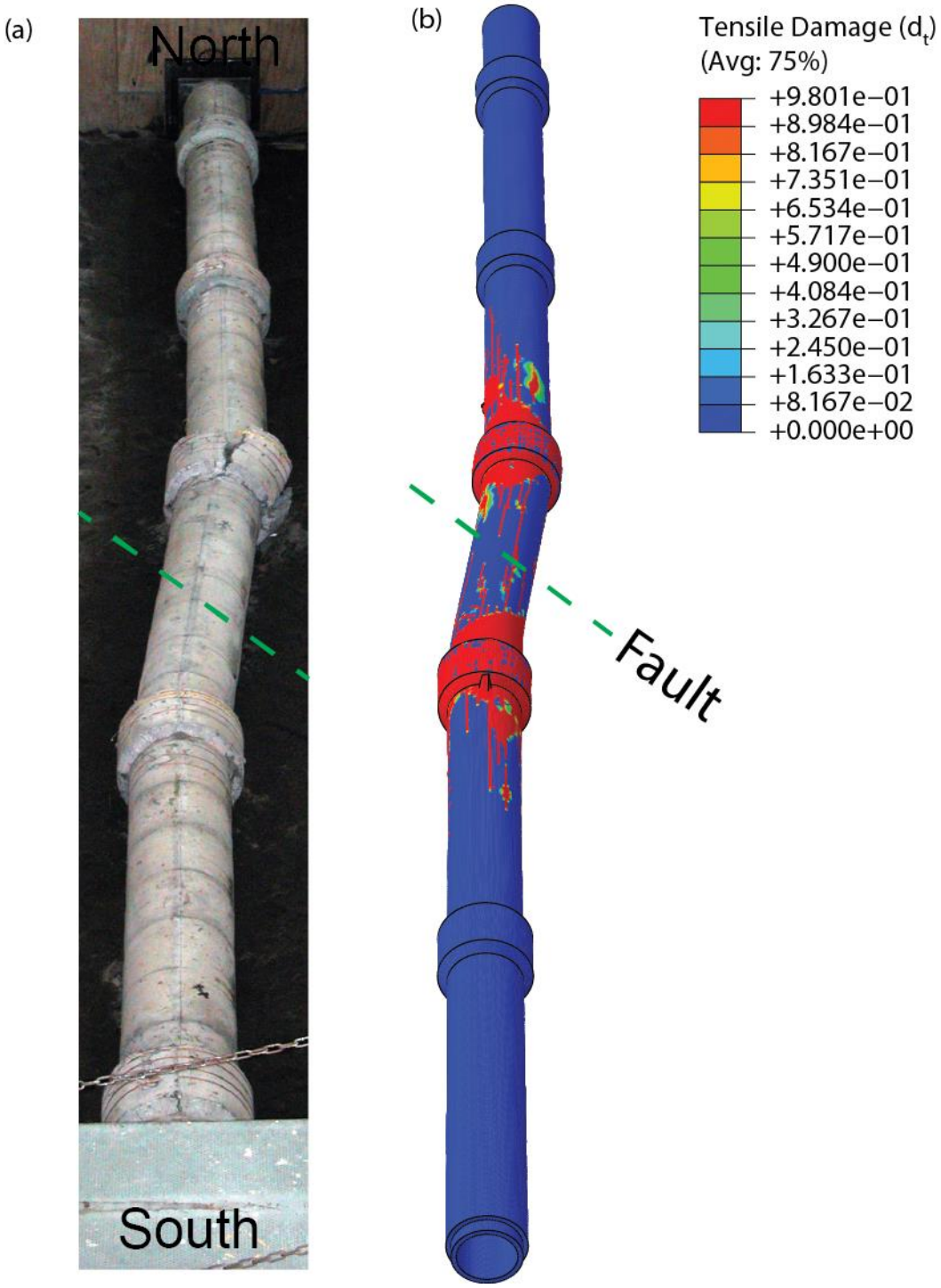

Figure 6.21. Comparison of pipeline damage in experiment #4 and FEA simulation #3, (a) excavated pipeline after the test, and (b) numerically simulated damage showing the tensile damage parameter d_t; $d_t = 0$ means no damage and $d_t = 1$ means complete damage.

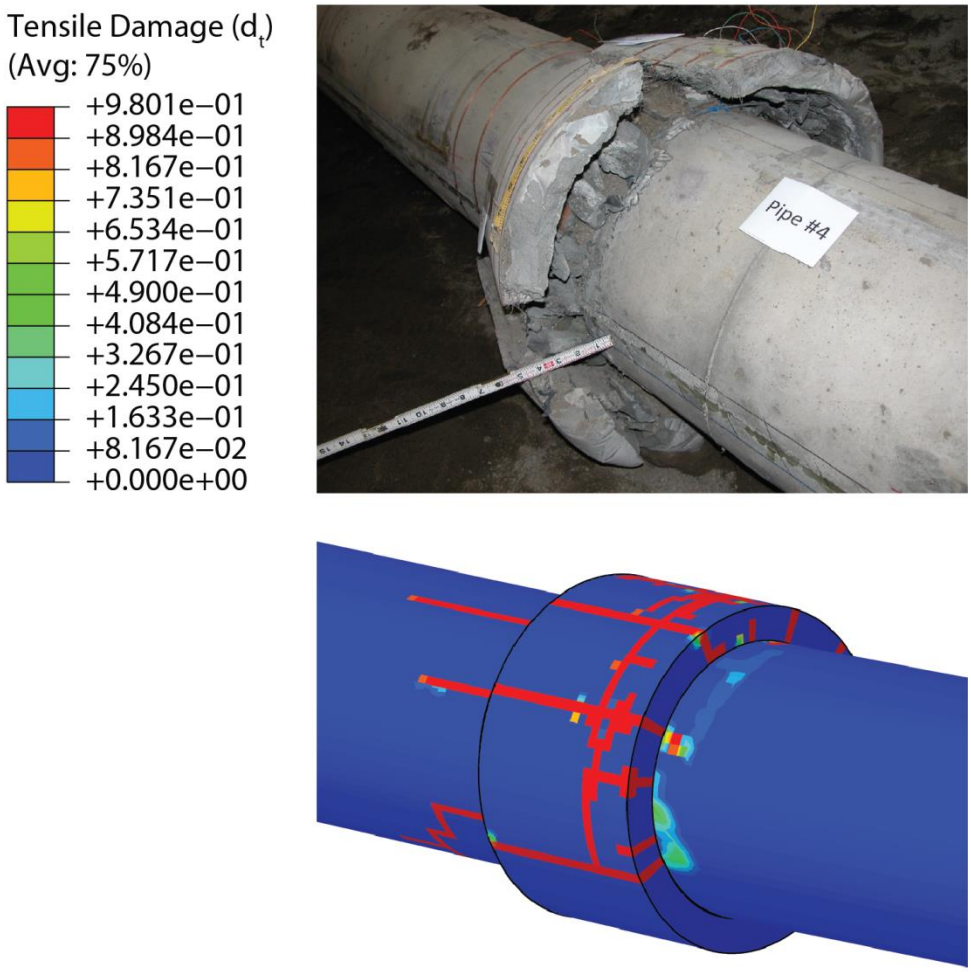

Figure 6.22. Comparison of cracking pattern at joint #3 from experiment #4 and finite element simulation #3; the longitudinal cracking pattern observed in the experiment was captured in the simulation model.

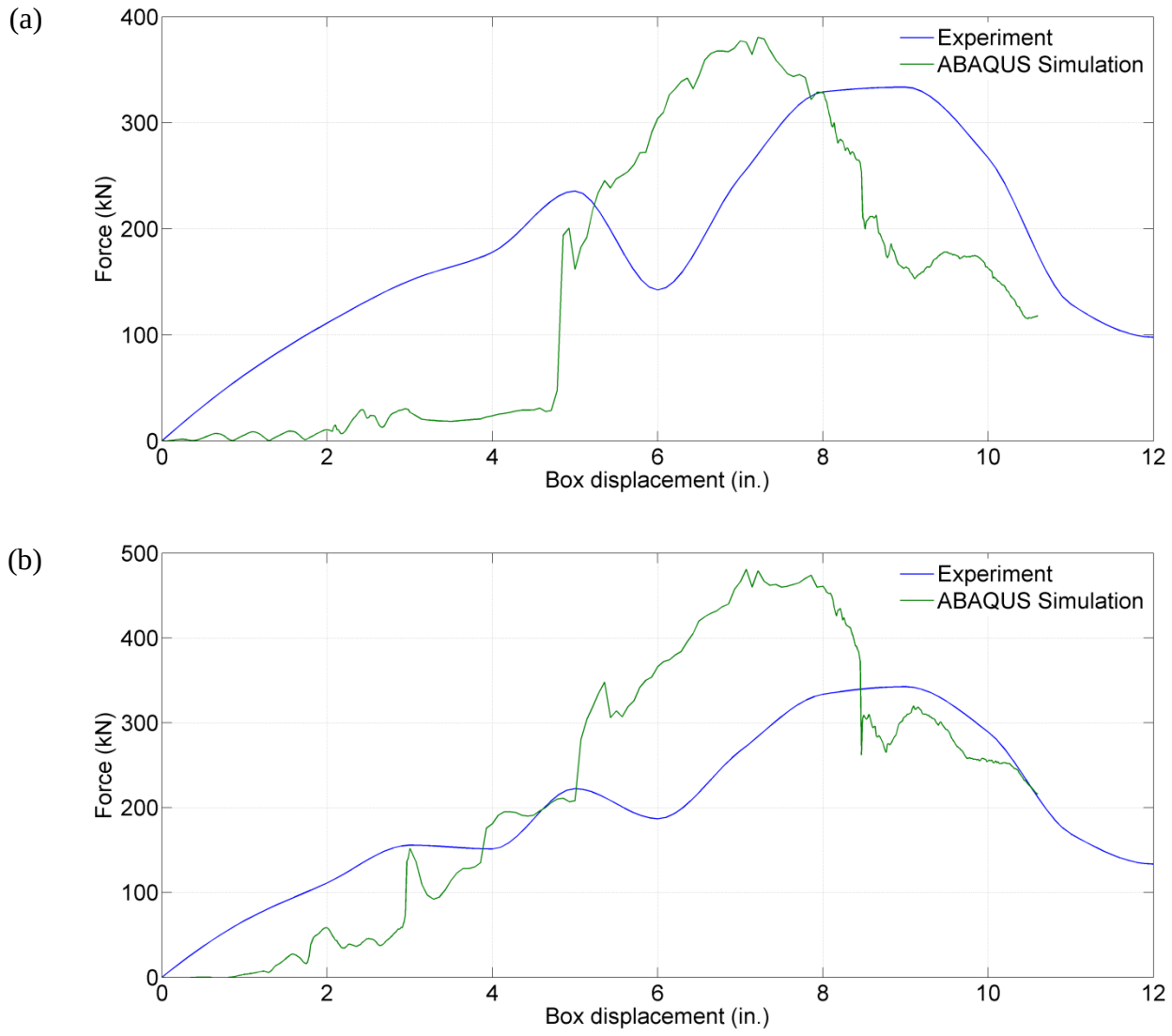

Figure 6.23. Comparison of pipeline end reaction forces from experiment #4 and FEA model #3, (a) north end reaction, and (b) south end reaction.

The results from the FEM simulation models #2 & 3 presented in this chapter match the experimental observations with reasonable accuracy.

Through the simulations, it was observed that depending on the amount of fault movement, the pipeline damage is either localized at the pipe closest to the fault or is distributed along the entire pipeline. During the first few inches of ground movement, the damage is localized at the joints closest to the fault. The initiation of damage occurs in the bells of the joints

due to circumferential tension. Very little damage was observed in the remaining joints during this time. When the fault movement continued, the damage propagates from the joints into the pipeline. The damage now occurs predominantly at the joints farther from the fault. Telescopic compression failure occurs at this time. On continuing the fault movement (simulation) the damage was seen to propagate to the body of the pipe.

6.5 Concluding remarks

3D FEA analysis of buried segmented concrete pipelines was computationally expensive. The bell-and-spigot joint was the component that needed the most refinement. Since the majority of the pipe damage was concentrated at the pipe joints, avoiding modeling of the pipe bell and grout overestimated the pipe end reaction forces. Refining the pipe model to four elements across the thickness of the pipe and modeling grout appeared to be important to reasonable predictions. Reported simulations constitute the author's contribution to this multi-investigator project, and they present only a small portion of the outcome of the entire project.

Chapter 7

SUMMARY AND CONCLUSIONS

The research presented in the thesis had two major objectives: (1) gain experimental evidence supporting the hypothesis that asperities on sand grain surfaces are prone to time-delayed fracture (*static fatigue*), and (2) demonstrate that *static fatigue* on grain surfaces is the predominant phenomenon that might be responsible for time effects observed in granular soils. Both experimental tests and numerical simulations were performed as part of the research. A summary of work accomplished during the study is given next, followed by the conclusions, and recommendation for future work.

7.1 Summary of research work and accomplishments

- Studies of surface morphology of sand grains were accomplished using Atomic Force Microscopy (AFM) and Scanning Electron Microscopy (SEM). Descriptors for quantifying the surface morphology were developed.
- Material properties characteristic of quartz sand grains (Ottawa 20-30 sand) were obtained using Nanoindentation test.
- Two devices were developed for performing micro-scale laboratory tests on a single inter-granular contact. Using the first device, qualitative information on grain movement under prolonged loading was obtained. The second device was capable of providing quantitative data on grain convergence during sustained load. A modified consolidometer for measuring radial stresses in soil was developed. This device was used to study the changes of lateral stress in granular soils (and steel shot) under prolonged loading conditions. Vertical deflections in the granular material as small as 100 nm were measured. Tests were performed on both dry and wet sands.

- Discrete Element Method (DEM) simulations were performed. A parametric study was carried out to study the effect of micro-parameters of the model on the macroscopic properties. DEM simulations were carried out to mimic the increase in horizontal stress associated with an increase in contact stiffness in confined sand, and the step-wise settlement observed in physically tested specimens.
- A Finite Element Model (FEM) of Cone Penetration Test (CPT) was developed, and changes to penetration resistance caused by static fatigue-induced soil stiffness increase were simulated.
- A plausible explanation for the initial (observed) drop in cone penetration resistance after dynamic compaction and subsequent (delayed) increase in CPT resistance was suggested. DEM and FEM simulations were performed to support the suggested explanation.
- Three finite element models of a segmented concrete pipeline buried in granular fill, subjected to ground rupture. Different levels of detail (mesh discretization and physical consistency) were used to obtain information on the degree of complexity required to obtain reasonable estimates of pipeline damage as observed in a full scale experimental test.

Major accomplishments are listed below:

- Scanning Electron Microscopy (SEM) and Atomic Force Microscopy (AFM) studies revealed rich surface morphology of sand grains. The elevations and slopes of the *hills and valleys* present on sand grain surfaces follow Gaussian-type distributions; this characteristic was encountered at different magnification levels. The roughness component of the surface texture of Ottawa 20-30 sand grains had a different signature compared to a Lake Michigan Dune sand grain. Even though statistical parameters such as Surface roughness, Skewness, Kurtosis could be used to describe sand grain surfaces, these parameters were dependent on the magnification level (scale). The fractal dimension of sand grain surface texture can be used as a metric to quantify the grain surface morphology.

- SEM images of Lake Michigan Empire Beach sand and Huron River sand showed the presence of micro-organisms on grain surfaces, most likely Diatoms. No micro-organisms were found on Ottawa 20-30 sand grains and Lake Michigan Dune sand.
- Nanoindentation tests revealed that the mechanical characteristics such as elastic modulus, hardness, and creep of quartz mineral, although similar within one grain, varied considerably from grain to grain. Further, the Young's Modulus of quartz mineral in sand grains is a function of depth; the modulus decreases with depth.
- The three-grain tests and grain-to-grain contact tests performed using Ottawa 20-30 sand grains under sustained loading confirmed that grain asperities are prone to static fatigue. Due to static fatigue, the grains "slip" and converge towards one another slowly in time. The larger the applied load, the greater the grain convergence; the sand grains converged by 1.9 μm in 21 days under 0.8 N force, they converged by 0.8 μm in 1.8 days under 2.9 N force. SEM imaging of grain surfaces after the tests showed crushed/fractured areas, and broken debris and crystalline fragments at grain contact locations.
- The modified consolidometer tests performed on dry Ottawa 20-30 sand and Lake Michigan Dune sand showed that the lateral stress in sand increases over time under a constant vertical stress under confined (nearly 1D) strain conditions. The rate of increase in lateral stress was faster (at the same vertical stress) for the Lake Michigan Dune sand than that for Ottawa 20-30 sand. The rate of increase in lateral stress was also influenced by the initial rate of loading and the magnitude of vertical stress; an increase in either resulted in a faster rate of increase in lateral stress. In all cases, the rate of increase in lateral stress decreased with time. Results from the wet consolidometer tests were more complicated to interpret and were influenced by the pH of pore water. The vertical settlement in both dry and wet consolidometer has a step-wise characteristic.
- The DEM model developed to mimic static fatigue supports the conjecture that during 1D strain conditions, increased contact stiffness and an associated slip result in an increased macroscopic elastic modulus, thereby increasing the lateral-to-vertical stress ratio of an assembly under lateral constraint. Further, the vertical strain during this process had a step-wise characteristic consistent with the physical tests (modified consolidometer tests). FEM simulations of CPT test showed that an increase in Young's Modulus and, and consequently, in lateral-to-vertical stress ratio during aging causes a delayed increase in

the tip resistance, which is very much in the range of measured increase in the field. The DEM and FEM simulations performed support the conjecture that the observed drop and delayed increase in CPT resistance following dynamic compaction could be caused by a change in stress state and not by a change in the soil strength (angle of internal friction) as commonly interpreted.

- Finite element modeling of the buried pipeline subjected to fault movement indicated that pipe bell, grout, and joints are the critical components of the pipeline assembly that require careful numerical modeling.

7.2 Conclusions

Even though *aging* in granular material has been reported by numerous investigators, no conclusive explanation behind the driving mechanism(s) was presented. The phenomenon was still called a *continuing Enigma* in 2008 (Mitchell 2008). "Particle rearrangement" and "structuration" are often cited as causing changes in granular assemblies leading to variation in properties (Mesri et al., 1990; Bowmann and Soga, 2003), and they have been used to explain the puzzling effect of delayed increase in cone penetration resistance in dynamically compacted sands. Rearrangement of particles and restructuring, however, are the results of an underlying process and cannot be considered as causes of this mystifying behavior. In this research it was hypothesized that the key mechanism contributing to time effects in sand is the delayed fracture of the micro-morphological features on surfaces of grains in contact (asperities, crystalline fragments, and mineral debris). The experimental evidence collected as part of research in this thesis supports the suggested hypothesis. The major conclusions are summarized below.

- Micro-scale tests performed on sand grains confirm that asperities on sand grain surfaces are prone to delayed fracture (*static fatigue*). The delayed fracturing of the asperities produces larger contact areas and stiffer (firmer) contacts. Thus, due to static fatigue at grain contacts and consequent grain convergence, the stiffness of contacts between two grains increases. This alters the major force chain network in granular assemblies, leading to changes in the intensity of the fatigue process at contacts. The increase in contact stiffness propagates through the spatial scales, and manifests itself as an increase in macroscopic elastic stiffness, and increase in lateral stress in confined sand. The increase

in lateral stress during aging in nearly 1D strain conditions was demonstrated using the modified consolidometer tests. The DEM simulations developed to mimic static fatigue support the conjecture of increased macroscopic modulus due to increased contact stiffness during aging.

- The delayed fracture of asperities is a 'catastrophic' event at the micro-scale. However, in a granular assembly, the fatigue process at a single contact does not cause deformation at the meso scale (granular assembly), because of redundancy of a single grain support through multiple contacts. Only when a large enough number of contacts have fatigued, an instability is possible in the granular system, which allows reconfiguration of grains, leading to strain (in an average sense). Once the assembly reaches a stable *self-organized* configuration, the process will repeat itself, after large number of contacts further fatigued. Due to this periodic process, the vertical subsidence under 1D strain conditions does not follow a smooth curve, but rather has a distinct step-wise characteristic in time. This step-wise characteristic was observed in all of the consolidometer tests, and was also mimicked in DEM simulations. Modified consolidometer tests performed in this research indicated that the vertical strains and changes in lateral stress during aging are very sensitive to external excitations. Hence it is recommended that any aging study performed in the laboratory should be free from external vibrations. The lateral stress in soils under nearly 1D increases strain conditions increases over time. The changes in lateral stress in wet samples are very much dependent on the pH of pore water, and the stress can either increase, decrease, or remain constant. This peculiar behavior is owed to mineral dissolution and possible softening of contacts. Changes in Total Dissolved Solids (TDS) during the wet consolidometer tests suggest that mineral dissolution (other than quartz) was occurring. After drying, the dissolved solids precipitate at grain contacts, forming hour-glass shaped bonds, which fuse the grains together. This was evident when large amount of solids were present in the solution (TDS = 353 ppm). This fusion of grains after drying was not evident in samples with fewer dissolved solids (TDS < 150 ppm). The increase in lateral stress during aging under 1D strain conditions obtained from the DEM model closely follows the result obtained from the modified consolidometer test. The model suggests that during aging, contact force homogenization occurs and the distribution of the force chains changes in the assembly. The mean contact

force on the grains and number of contacts were however almost the same before and after aging. This is in contrast to the aging model proposed very recently by Suarez (2012), who used the rate process theory in DEM, and found a decrease in mean contact force produced by aging, and increase in the number of contacts (however, the experimental test results in this thesis indicate that the model of Suarez, 2012, may be overestimating the rate of lateral stress increase).

- FEM and DEM simulations performed in this research suggest that the delayed increase in CPT resistance after dynamic compaction of sands is produced by gradual increase in stiffness (due to intergranular contact fatigue), causing, in turn, an increase in the horizontal stress in the sand bed. The time-delayed increase in penetration resistance is not caused by an increase in strength (strength increases immediately after the new, denser fabric is formed after compaction). DEM simulations of static fatigue also supported the conclusion that the soil strength changes insignificantly during; the elastic modulus and stress state, on the other hand, change during aging.
- 3D FEM modeling of the pipeline assembly subjected to ground rupture proved to be a computationally expensive procedure, even with the use of parallel computing options. The model outcome matched the experimental result from the steel fiber reinforced pipeline closely; but it requires a fine mesh, particularly for discretizing the pipes and the joints of the pipeline.

7.3. Recommendations for future research

During the course and development of this research, it became apparent that many aspects of time effects in sand, particularly those related to static fatigue at grain contacts are still not completely understood. Recommendations for future research are listed below.

- The AFM imaging of sand grain surfaces in this research revealed different signatures of roughness in sands of different origin (Ottawa 20-30 sand and Lake Michigan Dune sand). More research must be performed in this area to ascertain the significance of the micro-morphology in mechanical properties of sands. The use of fractal descriptors to describe grain surface morphology need to be investigated. This research could prove

beneficial to study extraterrestrial regolith to obtain information regarding the geological processes involved in the formation of grains.

- Grain-to-grain testing was performed in this research to measure the rate of grain convergence during aging. The tests performed in this research used dry sand grains. In-situ conditions are seldom dry and hence the grain-to-grain testing must be performed under moist/wet conditions to study the influence of environmental conditions on the fatigue process. Also, testing needs to be performed with different pH solutions. Further it is also recommended to perform testing under different loads and contact obliquity, to cover many possible configurations of contacts.
- It is recommended to build a model for asperity crushing in DEM. This can be achieved by building a grain surface with many particles bonded together. Using rate process theory, the loss in bond strength can be simulated resulting in delayed failure at the contact similar to stress corrosion cracking in rocks (e.g., Potyondy, 2007). The model could then be used to estimate the changes in contact stiffness and coefficient of friction at a contact during aging.
- During aging in the modified consolidometer tests, although dry sands experienced an increase in lateral stress over time, results from the wet tests were more complicated to interpret as the effects of water evaporation and capillarity could not be avoided. It is therefore recommended to develop an experimental system where evaporation of water and capillary effects are removed.

REFERENCES

ABAQUS /CAE (2008). User's Manual (v. 6.10-1). Dassault Systèmes Corp., Providence, RI, USA.

Afifi, S. S. and Richart, F.E.Jr. (1973). "Stress history effects on shear modulus of soils." *Soils and Foundations*, 13(1), 77-95.

Afifi, S.S. and Woods, R.D. (1971). "Long-term pressure effects on shear modulus of soils." *Journal of the Soil Mechanics and Foundations Division*, 97(SM10), 1445-1460.

Al-Shamrani, M.A. and Sture, S. (1994). "Numerical evaluation of time dependency of the coefficient of earth pressure at rest during secondary consolidation." *Developments in Theoretical and Applied Mechanics*, 17, 415-426.

Al-Sanad, H.A. and Ismael, N.F. (1996). "Effects of aging on freshly deposited or densified calcareous sands." *Transportation Research Record*, 1547, 76-81.

Anderson, D.G. and Stoke, K.H.II. (1978). "Shear modulus, a time-dependent soil property." *Dynamic Geotechnical Testing*, ASTM STP 654, 66-90.

ASME (2009). "Surface Texture (Surface Roughness, Waviness, and Lay)." Designation B46.1.

Ashford, S. A., Rollins, K. M., and Lane, J. D. (2004). "Blast-induced liquefaction for full-scale foundation testing." *Journal of Geotechnical and Geoenvironmental Engineering*, 130(8), 798-806.

ASTM (2008). "Standard Specification for Reinforced Concrete Culvert, Storm Drain, and Sewer Pipe." Designation: C 76-08a, ASTM International.

Axelsson, G. (2000). "Long Term Set-Up of Driven Piles in Sand." PhD thesis, Royal Institute of Technology, Stockholm, Sweden.

Baxter, C.D.P. (1999). "An Experimental Study on the Aging of Sands." Ph.D. dissertation, Virginia Tech, Blacksburg, VA.

Baxter, C.D.P. and Mitchell, J. K. (2004). "Experimental study on the aging of sands." *Journal of Geotechnical and Geoenvironmental Engineering*, 130(10), 1051-1062.

Binning, G., Quate, C.F., Gerber, Ch. (1986). "Atomic Force Microscope." *Physical Review Letters*, 56, 930-933.

Bolton, M.D. (1986). "The strength and dilatancy of sand." Géotechnique, 36(1), 65-78.

Bowman, E.T. and Soga, K. (2003). "Creep, ageing and microstructural change in dense granular material." *Soils and Foundations*, 43(4), 107-117.

Bhushan, B. (1999). "Handbook of micro/nanotribology." 2nd ed. CRC Press.

Bishop, A.W. (1958). "The test requirements for measuring the coefficient of earth pressure at rest." *Brussels Conference on Earth Pressure Problems*, Vol 1.

Castellanza, R. and Nova, R. (2004). "Oedometric tests on artificially weathered carbonatic soft rocks." *Journal of Geotechnical and Geoenvironmental Engineering*, 130(7), 728–739.

Charlie, W.A., Rwebyogo, M.F., and Doehring, D.O. (1992). "Time-dependent cone penetration resistance due to blasting." *Journal of Geotechnical Engineering*, 118(8), 1200-1215.

Charles, S.J. (1958). “Static fatigue of glass. I.” Journal of Appied Phycics, 29, No. 11, 1549-1553.

Chow, F.C., Jardine, R.J., Brucy, F., and Nauroy, J. F. (1998). "Effects of time on capacity of pipe piles in dense marine sand." *Journal of Geotechnical and Geoenvironmental Engineering*, 124(3), 254-264.

Cole, D.M., and Peters, J.F. (2007). “ A physically based approach to granular media mechanics: grain-scale experiments, initial results and implications to numerical modeling.” *Granular Matter*, 9(5), 309-321.

Cole, D. M., and Peters, J. F. (2007). “ Grain-scale mechanics of geologic materials and lunar simulants under normal loading.” *Granular Matter*, 10(3), 171-185.

Cuallar, E., Roberts, D. & Middleman, L. (1987). “*Static fatigue lifetime of optical fibers in bending.*” *Fiber and Integrated Optics*, 6(3), 203-213

Cundall, P.A. (1971). “A computer model for simulating progressive, large-scale movements in blocky rock system.” *Proceedings, Symposium of the International Society of Rock Mechanics*, 1, 129-136.

Cundall, P. A. (1987). “Distinct Element Models of Rock and Soil Structure,” in *Analytical and Computational Methods in Engineering Rock Mechanics*, Ch. 4,129-163, E. T. Brown, ed.

Cundall, P.A. and Strack, O.D.L. (1979). “A discrete numerical model for granular assemblies.” *Geotechnique*, 29, 47-65.

Daphalapurkar, N. P., Wang, F., Fu., B., Lu, H. and Komanduri, R. (2011). “*Determination of mechanical properties of sand grains by nanoindentation.*” Experimental Mechanics, 51, 719-728.

Daramola, O. (1980). “Effect of consolidation age on stiffness of sand.” *Geotechnique*, 30(2), 213-216.

DeJong, J.T., Fritzges, M.B., and Nüsslein, K. (2006). "Microbially induced cementation to control sand response to undrained shear." *Journal of Geotechnical and Geoenvironmental Engineering*, 132(11), 1381-1392.

Denisov, N.Y. and Reltov, B.F. (1961). "The influence of certain processes on the strength of soils." *Proc. 5th Int. Conf. Soil Mech. and Found. Engr.*, Paris, 75-78.

Dove, P.M. and Elston, S.F. (1992). "Dissolution kinetics of quartz in sodium chloride solutions: Analysis of existing data and a rate model for 25°C." *Geochimica et Cosmochimica Acta*, 56(12), 4147-4156.

Dowding, C. H. and Hryciw, R. D. (1986). "A laboratory study of blast densification of saturated sand." *Journal of Geotechnical Engineering*, 112(2), 187-199.

Drucker, D.C. and Prager, W. (1952). “Soil mechanics and plastic analysis or limit design.” Quart. Appl. Math., Vol. 10, No. 2, 157-165.

Dumas, J.C. and Beaton, N.F. (1988). “Discussion of “Practical Problems from Surprising Soil Behavior.” by J.K. Mitchell.” *J. of Geotech. Eng.*, 114 (3), 367-368.

Eguchi, R.T. (1982). “Earthquake performance of water supply components during the 1971 San Fernando Earthquake.” Technical Report 1396-2a, Wiggins JH Company, Redondo Beach, CA.

Eidinger, J. and Davis, C.A. (2012) “Recent Earthquakes: Implications for U.S. Water Utilities.” *Water Research Foundation*.

Fordham C.J., McRoberts, E.C., Purcell, B.C., and McLaughlin, P.D. (1991). “Practical and theoretical problems associated with blast densification of loose sands.” *Proceedings of the 44th Canadian Geotechnical Conference*, Canadian Geotechnical Society, Volume 2, 92.1-92.8.

Fischer-Cripps, A.C. (2011). “Nanoindentation.” Springer, New York.

Handford, G.T. (1988). “Densification of an existing dam with explosives,” *Proceedings of Hydraulic Fill Structures Specialty Conference*, Fort Collins, Colorado, 750–762.

Handy, R.L., Remmes, B., Moldt, S., Lutenegger, A.J., and Trott, G. (1982). “In situ stress determination by Iowa stepped blade.” *Journal of the Geotechnical Engineering Division, 108(11), 1405-1422.*

Hastings, H.M. and Sugihara, G. (1993). “Fractals, A User’s Guide For the Natural Sciences.” Oxford University Press.

Heubach, W.F. (2002) “Seismic screening checklists for water and wasterwater facilities.” *Technical Council on Lifeline Earthquake Engineering*, Monograph No. 22, ASCE.

Hryciw, R.D. (1986). “A Study of the Physical and Chemical Aspects of Blast Densification of Sand.” Ph.D dissertation, Northwestern University, Evanston, Illinois.

Human, C. A. (1992). "Time-Dependent Property Changes of Freshly Deposited or Densified Sands, Ph.D. Dissertation." University of California, Berkeley.

Itasca. (2008). Particle Flow Code in 3 Dimensions (PFC3D), Itasca Consulting Group, Inc., Minneapolis.

Jamiolkowski, M. and Manassero, M. (1995). “The role of in situ testing in geotechnical engineering – Thoughts about the future.” *Proceedings, International Conference in Advances in Site Investigation Practice*, 929-951.

Jefferies, M.G., Crooks, J.H.A., Becker, D.E. and Hill, P.R. (1987). “Independence of geostatic stress from overconsolidation in some Beaufort Sea clays.” *Canadian Geotechnical Journal*, 24(3), 342-356.

Jefferies, M.G. and Rogers, B.T. (1993). “Discussion of “Time-Dependence of lateral earth pressure,” by Schmertmann.” *Journal of Geotechnical Engineering*, 119(12), 2008-2012.

Joshi, R. C., Achari, G., Kaniraj, S. R., and Wijeweera, H. (1995). "Effect of aging on the penetration resistance of sands." *Canadian Geotechnical Journal*, 32(5), 767-782.

Jirathanathaworn, T. (2009). “Development of Photoelastic Methods Towards Study of Mechanical Aging of 2-Dimensional Granular Assemblies.” Ph.D. dissertation, University of Michigan, Ann Arbor, Michigan.

Karlsrud, K., Hansen, S.B., Dyvik, R and Kalnes, B. (1992). “NGI’s pile test at Tilbrook and Pentre - Review of testing procedures and results”, NGI publication no. 188, Oslo.

Kavazanjian, Jr, E. and Mitchell, J.K. (1984). “Time-Dependence of lateral earth pressure,” *Journal of Geotechnical Engineering*, 110(4), 530-533.

Kennedy, R. P., Chow, A. W., and Williamson, R. A. (1977), “Fault movement effects on buried oil pipelines,” Journal of the Transportation Engineering Division, ASCE, 103(TE5), 617-633.

Kim, J., Nadukuru, S. S., Pour-Ghaz, M., Lynch, J. P., Michalowski, R. L., Bradshaw, A. S., Green, R. A., Weiss, W. J. (2012). “Assessment of the behavior of buried concrete

pipelines subjected to ground rupture: Experimental study." *Journal of Pipeline Systems Engineering*, 3(1), 8-16.

Kolymbas, D. and Bauer, E. (1993). "Soft oedometer: A new testing device and its application for the calibration of hypoplastic constitutive laws." *Geotechnical Testing Journal*, 16, 263-270.

Krinsley, D.H. and Doornkamp, J.C. (1973), "Atlas Of Quartz Sand Surface Textures." Cambridge University Press.

Kroll, R.G. (1990). Alkalophiles. In: Edwards, C. (Ed.), "Microbiology of Extreme Environments." McGraw-Hill, New York, 55-92.

Kuhn, M.R. (1986). "Micromechanical Aspects of Soil Creep." Ph.D thesis, University of California, Berkeley.

Kuhn, M.R. and Mitchell, J.K. (1992). "The modeling of soil creep with discrete element method." *Engineering Computations*, 9(2), 277-287.

Kwok, C.Y. and Bolton, M. (2010). "DEM simulations of thermally activated creep in soils." *Geotechnique*, 60(6), 425-434.

Lade, P.V. and Karimpour, H. (2010). "Static fatigue produces time effects in granular materials." *GeoFlorida 2010: Advances in Analysis, Modeling & Design*, Geotechnical Special Publication 199, D. Fratta, A.J. Puppala, and B. Muhunthan, eds., 530-539.

Lade, P.V., Nam, J. and Liggio, C.D. (2010). "Effects of particle crushing in stress drop-relaxation experiments on crushed coral sand." *Journal of Geotechnical and Geoenvironmental Engineering*, 136(3), 500-509.

Lambe, T.W. and Whitman, R.V. (1969). "Soil Mechanics." John Wiley & Sons, Inc.

Lee, K.L. (1977). "Adhesion bonds in sands at high pressures." *Journal of the Geotechnical Engineering Division*, 103(GT8), 908-913.

Lee, J. and Fenves, G.L. (1998). "Plastic-damage model for cyclic loading of concrete structures." *ASCE Journal of Engineering Mechanics*, 124(8), 892-900.

Li, J., Du, Q., and Sun C. (2009). "An improved box-counting method for image fractal dimension estimation." *Pattern Recognition*, 42, 2460-2469.

Lubliner, J., Oliver, J., Oller,S. and Onate, E. (1989). "A plastic-damage model for concrete." *Int. J. Solids Struct*., 25(3), 299-326.

Mandelbrot, B.B. (1967). "How long is the coastline of Britan? Statistical self-similarity and fractional dimension." *Science*, 155, 636-638.

Mandelbrot, B.B. (1982). "The Fractal Geometry of Nature." W.H. Freeman, New York.

Mandelbrot, B.B. (1985). "Self-affine fractals and fractal dimension." *Phyica Scripta*, 32, 257-260.

Marchetti, S. (1980). "In situ tests by flat plate dialatometer." *Journal of Geotechnical Engineering Division*, 106(GT3), 299-321.

Mayne, P.W. and Kulhawy, F.H. (1982). "K_0 – OCR relationship in soil." *Journal of the Geotechnical Engineering Division*, 108(6), 851-872.

McLaskey, G.C. and Glaser, S. D. (2011). "Micromechanics of Asperity Rupture During Laboratory Stick Slip Experiments." *Geophysical Research Letters*, 38, L12302.

Mesri, G. and Castro, A. (1987). "C_α/C_c concept and Ko during secondary compression." *Journal of Geotechnical Engineering Division*, 113(GT3), 230-247.

Mesri, G., Feng, T.W., and Benak, J. M. (1990). "Postdensification penetration resistance of clean sands." *Journal of Geotechnical and Geoenvironmental Engineering*, 116(7), 1095-1115.

Mesri, G. and Hayat, T.M. (1993). "The coefficient of earth pressure at rest." *Canadian Geotechnical Journal*, 30, 647-666.

Michalowski, R.L. (2005). "Coefficient of earth pressure at rest." *Journal of Geotechnical and Geoenvironmental Engineering*, 131(2), 1429-1433.

Michalowski, R.L. and Nadukuru, S.S. (2012). "Static fatigue, time effects, and delayed increase in penetration resistance after dynamic compaction of sand." *Journal of Geotechnical and Geoenvironmental Engineering*, 138(5), 564-574.

Michalowski, R. L. and Park, N. (2004). "Admissible stress fields and arching in piles of sand." *Géotechnique*, 54(8), 529–538.

Mitchell, J.K. and Solymar, Z.V. (1984). "Time-dependent strength gain in freshly deposited or densified sand." *Journal of Geotechnical Engineering*, 110(11), 1559-1576.

Mitchell, J.K. and Santamarina, J.C. (2005). "Biological Considerations in Geotechnical Engineering." *Journal of Geotechnical and Geoenvironmental Engineering*, 131(10), 1222-1233.

Mitchell, J.K. (2008). "Aging of sand – a continuing enigma?" *6th Int. Conf. on Case Histories in Geotechnical Engineering*. Arlington, VA, Aug. 11-16, 2008, 1-21.

Nadukuru, S.S. and Michalowski, R.L. (2012). "Arching in distribution of active load on retaining walls." *Journal of Geotechnical and Geoenvironmental Engineering*, 138(5), 575-584.

Narsilio, G.A., Santamarina, J.C., Hebeler, T., and Bachus, R., 2009. "Blast densification: Multi instrumented case history." *Journal of Geotechnical and Geoenvironmental Engineering*, 135(6), 723-734.

"Strain gauge configuration types." National Instruments White Paper, 2006; accessed from www.ni.com (July 10, 2010).

NAVFAC (1986). Design Manual DM 7-02: Foundations and Earth Structures. September 1986.

Newmark, N.M., and Hall, W.J. (1975), "Pipeline design to resist large fault displacement", Paper UILU-ENG-75-2011, *US National Conference on Earthquake Engineering*, Ann Arbor, MI, 416-425.

Ng, T.T., and Dobry, R. (1994). "Numerical simulations of monotonic and cyclic loading of granular soil." *Journal of Geotechnical Engineering*, 120(2), 173-175.

Ng, E.S., Tsang S.K. and Auld B.C. (1988), "Pile foundation: The behavior of piles in cohesionless soils", *Federal Highway Administration Report* FHWA-RD-88-081.

Oliver, W.C., and Pharr, G.M. (1992). "An improved technique for determining hardness and elastic modulus using load and displacement sensing indentation experiments." *Journal of Materials Research*, 7(6), 1564-1583.

Oliver, W.C., and Pethica, J.B. (1989). "Methods for continuous determination of the elastic stiffness of contact between two bodies." US Patent No. 4,848,141, July 18.

O'Rourke, M.J. and Liu, X. (1999). "Response of buried bipelines subject to earthquake effects." *Multidisciplinary Center for Earthquake Engineering Research*, Monograph No. 3, Buffalo, NY.

O'Rourke, T.D. and Lane, P.A. (1989). "Liquefaction Hazards and their Effects on Buried Pipelines." National Center for Earthquake Engineering Research, Technical Report NCEER-89-0007, Buffalo, NY.

O'Rourke, T.D. and Palmer M.C. (1996). "Earthquake Performance of Gas Transmission Pipelines", *Earthquake Spectra*, 20(3), 493-527.

O'Rourke, M.J. (2003): Buried Pipelines, *Earthquake Engineering Handbook* (Chapter 23), CRC Press.

O'Sullivan, C. and Bray, J.D. (2004). "Selecting a suitable time step for discrete element simulations that use the central difference time integration scheme." *Engineering Computations*, 21(2), 278-303.

Pethica, J.B., Hutchings, R., Oliver, W.C. (1983). "Hardness measurement at penetration depths as small as 20 nm." *Philosophical Magazine A*, 48 (4), 593-606.

Pethica, J.B., Oliver, W.C. (1989). "Mechanical properties of nanometer volumes of material: Use of the elastic response of small area indentations", *Thin Films: Stresses and Mechanical Properties*, 130, 13-23.

Pharr, G.M. (1998). "Measurement of mechanical properties by ultra-low load indentation." *Materials Science and Engineering A*, 253, 151-159.

Radjai, F., Jean., M., Moreau, J.J. and Roux., S. (1996). "Force distributions in dense two-dimensional granular systems*." Physical Review Letters*, 77(2), 274-277.

Radjai, F., Roux., S. and Moreau, J.J. (1999). "Contact forces in granular packing,*" Chaos*, 9(3), 544-561.

Robertson, P.K. and Capanella, R.G. (1983). "Interpretation of cone penetration test – part 1 (Sand)." Canadian Geotechnical Journal, 20(4), 718-733.

Potyondy, D.O. (2007). "Simulating stress corrosion with a bonded particle model for rock." *International Journal of Rock Mechanics and Mining Sciences*, 41(8), 1329-1364.

Saftner, D.A. (2011). "Time-Dependent Strength Gain in Recently Disturbed Granular Materials." Ph.D. dissertation, University of Michigan, Ann Arbor, Michigan.

Sarkar, N. and Chaudhuri, B.B. (1994). "An efficient differential box-counting approach to compute fractal dimension of image." *IEEE Transactions on Systems, Man, and Cybernetics*, 24, 115-120.

Scholz, C.H. (1968a). "Mechanism of creep in brittle rock." Journal of Geophysical Research., 73(10), 3295- 3302.

Scholz, C.H. (1968b)."Microfractures, aftershocks, and seismicity." *Bulletin of the Seismological Society America*, 58(3), 1117-1130.

Scholz, C.H. (1972). "Static fatigue of quartz." *Journal of Geophysical Research*, 77(11), 2104-2114.

Seed, H.B. (1979). "Soil liquefaction and cyclic mobility evaluation for level ground during earthquakes." *Journal of the Geotechnical Engineering Division*, 105(GT2), 201-255.

Services TAMC (2010). "Chile earthquake and tsunami update. Hawaii: Tripler Army Medical Center." Center for Excellence in Disaster Management and Humanitarian Assistance

Services TAMC (2011). "Japan Earthquake and Tsunami Update Wednesday, April 20, 2011." Hawaii: Tripler Army Medical Center (TAMC). Center for Excellence in Disaster Management and Humanitarian Assistance.

Skempton, A.W. (1986). “Standard penetration test procedures and the effects in sands of overburden pressure, relative density, particle size, aging, and overconsolidation.” *Geotechnique*, 36(3), 425-447.

Schmertmann, J.H. (1964). “Generalizing and measuring the Hvorslev effective components of shear resistance.” *Symosium on Laboratory Shear Stregnth Testing of Soils*, ASTM, Philadelphia, PA, 147-162.

Schmertmann, J.H. (1983). “A simple question about consolidation.” *Journal of Geotechnical Engineering*, 109(1), 119-122.

Schmertmann, J.H. (1987). "Discussion of "Time dependent stregnth gain in freshly deposited or densified sand" by J. K. Mitchell and Z. V. Solymar." *Journal of Geotechnical Engineering*, 113(2), 173-175.

Schmertmann, J.H. (1991). “The Mechanical Aging of Soils.” *Journal of Geotechnical Engineering.* 117(9), 1288-1330.

Schmertmann, J.H. (1964). "Generalizing and measuring the Hvorslev effective components of shear resistance." *Symp. on Laboratory Shear Strength Testing of Soils*, ASTM, Philadelphia, PA, 147-162.

Schuh, C.A. (2006). “Nanoindentation studies of materials.” *Materialstoday*, 9(5), 32-40.

Shin, H. and Santamarina, J.C. (2009). “Mineral dissolution and the evolution of Ko.” *Journal of Geotechnical and Geoenvironmental Engineering,* 135(8), 1141-1147.

Skov, R. and Denver, H. (1988). “Time-dependence of bearing capacity of piles.” *Proceedings of the 3rd International Conference on Applied Stress Wave Theory to Piles*, 879-888.

Slatter, E.E., Fityus, S. G. and Smith, D. W. (2005). “Measuring lateral pressures during suction controlled one dimensional consolidation.” *Proceeding of the International Symposium on Advanced Experimental Unsaturated Soil Mechanics*, 117–124.

Stocks-Fischer, S., Galinat, J. K., and Bang, S. S. (1999). “Microbiological precipitation of CaCO3.” *Soil Biology and Biochemistry*, 31(11), 1563-1571.

Suarez, N.R. (2012). “Micromechanical Aspects of Aging in Granular Soils.” Ph.D. dissertation, Virginia Polytechnic Institute and State University, Blacksburg, Virginia.

Susila, E. (2005). “Finite Element Simulation of the Cone Penetration Test in Uniform and Stratified Sand.” PhD thesis, University of Michigan, Ann Arbor.

Susila, E. and Hryciw, R.D. (2003)."Large displacement FEM modeling of the cone penetration test (CPT) in normally consolidated sand." *International Journal for Numerical and Analytical Methods in Geomechanics* 27(7): 585-602.

Swartz, R. A., Jung, D., Lynch, J. P., Wang, Y., Shi, D. and Flynn, M. P. (2005). “Design of a wireless sensor for scalable distributed in-network computation in a structural health monitoring system.”*5th International Workshop on Structural Health Monitoring*, 1570-1577, Stanford, CA, 2005

Tavenas, F. and Audy, R. (1972). “Limitations of the driving formulas for predicting bearing capacities of piles in sand.” *Candian Geotechnical Journal.* 9, 47-62.

Thomann, T.G. and Hryciw, R.D. (1992). “Stiffness and strength changes in cohesionless soils due to disturbance.” *Canadian Geotechnical Journal*, 29, 853-861.

Thomann, T.G. (1990). “Stiffness and Strength Changes in Cohesionless Soils Due to Stress History and Dynamic Disturbance.” PhD dissertation, University of Michigan, Ann Arbor, Michigan.

Thronton, C. (1997). “Force transmission in granular media.” *KONA Powder and Particle*, 15, 81-90.

Ting, C.M.R., Sills, G.C., and Wijeyesekera, D. C. (1994), “Development of K_0 in soft soils.” *Geotechnique*, 44(1), 101-109

Tromas, C., Colin, J., Coupeau, C., Girad, J.C., Woirgard, J., and Grilhe, J. (1999). “Pop-in phenomenon during nanoindentation in MgO.” *The European Physical Journal Applied Physics*, 8(2), 123-128.

Troncoso, J.H. and Garcés, E. (2000). “Ageing effects in the shear modulus of soils.” *Soil Dynamics and Earthquake Engineering*, 19(8), 595-601.

Tsuji, Y., Kawaguchi, T. and Tanaka, T. (1993). “Discrete particle simulation of two-dimensional fluidized bed.” *Powder Technology*, 77, 79-87.

Vicsek, T. (1999). “Fractal Growth Phenomena.” World Scientific.

Voivret, C., Radjai., F., Delenne, J.Y. and El Youssoufi., M.S. (2009). “Multiscale force networks in highly poly disperse granular media.” *Physical Review Letters*, 102(17), 178-201.

Wang, L.R.L. and O'Rourke, M.J. (1978). “Overview of buried pipelines under seismic loading.” *Journal of the Technical Council*, ASCE, 104(TC1), 121-130.

Wang, Y.H. and Tsui K.Y. (2009). “Experimental characterization of dynamic property changes in aged sands.” *Journal of Geotechnical and Geoenvironmental Engineering*, 135(2), 259-270.

Wang, Y. H., Xu, D. and Tsui, K. Y. (2008). “ Discrete element modeling of contact creep and aging in sand.” *Journal of Geotechnical and Geoenvironmental Engineering*, 134(9), 1407-1411.

Wiederhorn, S.M. and Boltz, L.H. (1970). “Stress corrosion and static fatigue of glass.” *Journal of the American Ceramic Society*, 53(10), 543-548.

Williams, E.D. and Bartlet, N.C. (1991). “Thermodynamics of surface morphology.” *Science*, 251, 393-400.

Yoshisaki, K., O'Rourke, T.D., and Hamada, M. (2001): Large deformation behavior of buried pipelines with low-angle elbows subjected to permanent ground deformation, *Journal of Structural Mechanics and Earthquake Engineering*, JSME, 50(4), 215-228.